THERMAL PERFORMANCE COMPARISON BETWEEN MICROCHANNEL AND ROUND TUBE HEAT EXCHANGERS

By

OZKAN EMRE OZDEMIR

Bachelor of Science in Aerospace Engineering

Middle East Technical University

Ankara, Turkey

2006

Submitted to the Faculty of the
Graduate College of the
Oklahoma State University
in partial fulfillment of
the requirements for
the Degree of
MASTER OF SCIENCE
July, 2009

THERMAL PERFORMANCE COMPARISON

BETWEEN MICROCHANNEL AND

ROUND TUBE HEAT EXCHANGERS

Thesis Approved:

Dr. Lorenzo Cremaschi
Thesis Adviser

Dr. Daniel Fisher

Dr. David Lilley

Dr. A. Gordon Emslie
Dean of the Graduate College

ACKNOWLEDGMENTS

There are many people who have encouraged me in pursuing this Master's degree, and I would like to take this opportunity to thank all of them. First and foremost, it is essential to express my gratitude to my extremely supportive family. I want to thank them for showing me that my dreams are limitless as long as I work hard and never abandon my goals. They have instilled in me a fervent passion for learning, and they have also taught me how to learn from my mistakes. I would especially like to give thanks to my sister and brother in law because they were responsible for enlarging my vision as both a person and an engineer. They have supported me not only financially but also emotionally by sharing their vast experiences as former engineering students at the graduate level.

I would like to thank my professors who have shown me what it takes to become a passionate, hard-working and determined researcher. My advisor, Dr. Chremaschi, believed in my abilities as an engineer and had confidence in me to conduct extensive research regarding my thesis.

Last but certainly not least, I would like to thank my colleagues, specifically Shanshan, Ellisa, Sankar and Spencer, who have encouraged me to work diligently on this project. They have continued to support me through this trying process and have kept me motivated the whole way through. I would also like to thank all my friends who have made Stillwater a pleasant and memorable place for me.

TABLE OF CONTENTS

LIST OF TABLES

Table Page

Table Page

LIST OF FIGURES

Figure Page

Figure Page

Figure Page

Figure Page

CHAPTER I

Introduction

Developments in technology have been replacing itself with smaller, thinner, transportable and faster devices. On the other hand, these technological improvements also require more compact thermal solutions. Therefore, air conditioning industry has been trying to obtain higher efficiency level and greater equipment reliability. Before, producers used to meet the efficiency levels by improving the individual components such as more efficient compressors and increasing the overall heat transfer area of condensers and evaporators. However, when the aim becomes simultaneously reduce equipments size and limit the cost, manufacturers had difficulties to meet the energy efficiency requirements (Keogh, 2007). After Tuckerman and Pease's (1981) investigation of heat transfer in microstructures, microchannel heat exchangers (MCHEXs) became an innovative and developing method in thermal applications. For example, having a massive efficiency compared to its smaller geometry made MCHEXs an important practical solution in different industries such as: aerospace, mini-heaters and mini-heat exchangers, materials processing and manufacturing, etc (Peng et al, 1995).

Compared to conventional fin and tube type heating coils, the advantages of MCHEXs can be summarized as follows:

- Higher overall heat transfer coefficient with improved heat transfer and thermal hydraulic performance

- Increased thermal effectiveness due to multiple parallel tubes t configuration
- Smaller refrigerant charges due to reduce internal volume of the micro-tubes in the heat exchangers
- Smaller coil sizes that provide compact and transportable units
- Lesser amount of material that reduce the equipment cost

1.1Background

Starting in early 1990s, several studies were conducted to investigate the application of micro-scaled ports in air conditioning systems. In order to provide higher thermal efficiency with single or two phase refrigerant, the optimum configuration of microchannel heat exchangers was obtained by increasing number of parallel passages and decreasing channel length (Heun and Dunn 1996). Furthermore, by comparing numerous geometries, the square port was contributed the highest heat transfer capacity due to its optimum packing capability in a fixed volume (Muzychka, 2005). Further decrease in microchannel port diameter increases the heat transfer coefficient in compact condensers (Bandhauer et. al, 2006). In figure 1.1 straight microchannel tube geometry is demonstrated and corresponding geometric variables are defined in table 1.1.

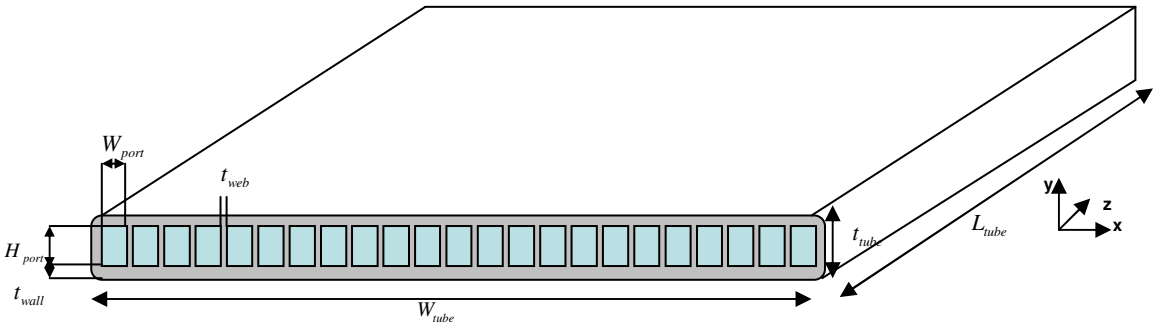

Figure 1.1: Straight Microchannel Tube Geometry

In addition to refrigerant side, air side performance of MCHEX as an indoor coil were also discussed by many researchers and louvered fin configuration was suggested to increase the air side thermal capacity (Webb and Jung., 1992). On the other hand, this high heat transfer capability caused a sudden frost growth on the air side of MCHEX when it is used as an outdoor coil. According to Xia et al.'s study (2006) a reduction in heat transfer coefficient and an increment in pressure drop were obtained due to frost blocks over the air gaps between microchannel tubes. In addition, Kim and Groll (2003) compared the outdoor coil performances of conventional fin and tube coil with a MCHEX. Results showed that, the cooling capacity and system performance of MCHEX are lower than fin and tube coil because of its higher frequency of defrost cycle. Recently, Padhmanabhan et al. (2008) has investigated the defrosting cycling performance of MCHEX, and in wet condition microchannel coil's frost growth was reported 50% faster than conventional fin and tube coil.

Table 1.1: Variable Definitions for Figure 1.1

W_{tube}	tube width
L_{tube}	tube length
t_{tube}	tube thickness
W_{port}	port width
H_{port}	port height
t_{wall}	port inner wall to tube outer wall thickness
t_{web}	port to port wall thickness

1.2. Objectives

Despite their higher performance as condensers, microchannel heat exchangers (MCHXs) are not widely used as outdoor evaporators in heat pump systems due to their frost growth rates and frequent defrost cycles required during cold and wet operating conditions. In literature, there are several studies that focus on the design and heat transfer performance of heat exchangers adopting straight microchannel tubes. However it seems that there is little work on alternative profiles of the microchannel tubes when these tubes are adopted primarily as outdoor evaporators of heat pump systems. In particular few researchers considered tube profiles that might reduce defrost cycles and increase the heating (frosting) service time in cold and wet operating conditions. The overall goal of this work is to develop an enhanced microchannel tube that overcomes the frosting performances of conventional fin and tubes during wet operating conditions and maintains high heat transfer performance during dry conditions. The baseline technology for dry conditions is the straight microchannel tubes heat exchanger while the most recent fin and tube coils are used as baseline for the wet condition performance comparison. In this study I took a first step toward this comparison and I numerically investigated the heat transfer and hydraulic performances of several types of round tube microchannel technology in heat pump applications.

The main objective of this study is to explore alternative profiles to straight microchannel tube geometry. Since the fin and round tube type heat exchangers have proved excellent frosting and defrosting performance, the idea is to start from a round tube geometry and apply gradually microchannel features to it. Based on this approach, the first specific objective of this work is to investigate the diameter that a round tube

with microchannel ports in it would required in order to achieve heat transfer rates similar to the ones in dry coils with straight vertical microchannel tubes. A second specific objective is to analyze and compare the thermal efficiency and pressure drop characteristics of the round microchannel tubes having different diameters and tube spacing with the performance of straight vertical microchannel tubes. This analysis aims to highlight current limitations and potential advantages of the round microchannel tube concept. In order to fulfill these objectives, the following methodology was used:

1. I reviewed previous experimental and numerical works that are related to design and heat transfer analysis of microchannel heat exchanger tubes and I identified geometric constraints in heat exchangers for heat pump systems. I also identified relevant analytical solutions and the most-up-to-date - computational approaches for this type of heat exchangers.

2. I numerically simulated tube in shell calorimeter heat transfer experiments to i) analyze the refrigerant side heat transfer enhancement if round microchannel tubes are used as outdoor evaporators, and ii) provide design guidelines for a suitable test apparatus.

3. I performed a parametric study of the air side heat transfer effectiveness of the round microchannel tubes and compared them with the ones of straight microchannel tubes.

4. I finally evaluated the hydraulic performances of round microchannel tubes by calculating the pressure drops assuming single phase fluid flow and for different geometries. I made a relative assessment by comparing the results with the ones from straight microchannel tubes exposed to similar operating conditions.

It should be noticed that even though two phase flow boiling of refrigerants (or refrigerant mixtures) occurs inside the actual outdoor evaporators, a relative assessment of the round microchannel tubes compared to straight microchannel tubes is still possible by using single phase fluid heated (or cooled) inside the microchannel ports by an air stream or by a water stream . Heat transfer and pressure drop correlations of single phase flow inside microchannel tubes are well known and available in the public domain. They can be implemented in commercially available computational fluid-dynamic software (CFD) and be accurate enough for conducting relative performance comparisons among different heat exchanger geometries. During my parametric investigation, single phase flow allowed to maintain reasonably low computational power and time. I was also able to point out current limitations and possible design improvements of the round microchannel tube concept. It is obvious that for further refinements of the results from this work, multi-phase and multi-components fluid flow simulators in microstructures should be considered as well as data from suitable experiments.

Based on the above-mentioned argument, I developed a numerical CFD model in FLUENT solver. This numerical model, which was also experimentally validated against data in the existing literature, was used to analyze the round microchannel tube geometries and to identify the effect from design modifications on the heat transfer and hydraulic performance of round microchannel tube heat exchangers.

Including the introduction chapter, this study is documented in nine chapters. Following chapter, chapter 2, presents a detailed literature review of previous experimental and computational studies. Then, in chapter 3 solution steps are given for FLUENT CFD solver. Chapter four discusses the accuracy of FLUENT CFD solver with

two validation models. Chapter five presents the refrigerant side analysis of commercially available round tube and straight microchannel tube models based on their 3D FLUENT simulations. Similarly, in chapter six, design and refrigerant side performance investigations of round microchannel tube are reported. Additionally, in chapter seven air side performance of round microchannel tube is presented according to its 2D FLUENT simulation. Chapter eight results are compared and a parametric study is presented to investigate the tube geometry impact on the heat transfer and pressure drop performances of round microchannel tube. Finally in chapter nine, conclusion of studies are summarized with future work suggestions.

CHAPTER II

Literature Review

Before starting to develop my computational model, a good understanding about the concept of fluid flow in microchannel tube is required. Therefore, by searching previous studies in the literature and analyzing their results, a detailed review was done about microchannel heat exchangers. It was observed that, researchers first experimentally investigated the heat transfer characteristics of microchannels and compared their efficiencies with conventional size correlations in the early 20^{th} century. Then during past decade more comprehensive results were obtained with computational research.

In this chapter an extensive summary regarding previous investigations are presented according to the improvements on their results. First, the experimental studies are summarized in order to provide a better perspective about the advantages of microchannel heat exchangers. Then in the second part of this chapter, numerical approaches are discussed to validate the accuracy of Navier-Stokes equations and demonstrate the micro-scale fluid flow applications in commercially available FLUENT CFD software packages. Finally, a brief conclusion is provided to outline the main results of fluid flow and heat transfer characteristics in microchannels.

2.1 Experimental Studies of Single Phase Forced Convection in Microchannels

Since the validation of my numerical model will be based on the data from literature, it was required to search relevant experimental data that summarize single phase heat transfer correlations in mircochannels. In this section each experimental work is discussed in details, and related single phase microchannel heat transfer studies and corresponding range of validity are presented in table 2.3.

Experimental investigation on the convective heat transfer characteristics in microscale tubes started in early 1980. Tuckermann at al.'s studies (1982, 1991) inspired a lot of researchers to identify fluid flow and its effects on convective heat transfer coefficient in microchannels. Previously, there have been many studies were published in literature regarding evaluation of the Nusselt number in conventional size duct which are given Zhigang et al.'s study (2007) as:

Shah Correlation (1978): $$Nu_{avg} = (4.364 + 0.0722\,\mathrm{Re}_f\,\mathrm{Pr}_f \frac{D_h}{L})(\frac{\mu_f}{\mu_w})^{0.14} \qquad (2.1)$$

Gnielinski Correlation (1975): $$Nu_{avg} = \frac{\frac{f}{2}(\mathrm{Re}_f - 1000)\,\mathrm{Pr}}{1 + 12.7(\frac{f}{2})^{\frac{1}{2}}(\mathrm{Pr}_f^{\frac{2}{3}} - 1)} \qquad (2.2)$$

where; $$f = \frac{1}{\left[3.64\log(\mathrm{Re}_f) - 3.28\right]^2} \quad \text{for } 3000 < \mathrm{Re}_f < 5\times10^6 \qquad (2.3)$$

Dittues – Boelter Correlation (1930): $$Nu_{avg} = 0.023\,\mathrm{Re}_f^{\,0.8}\,\mathrm{Pr}_f^{\,0.4} \qquad (2.4)$$

where; $0.6 < \mathrm{Pr}_f < 160$ and $\mathrm{Re}_f > 10000$

In table 2.1 variable definitions for above equations, 2.1, 2.2 and 2.3, are tabulated.

Some researchers believed that these correlations would be applicable for microchannel heat sinks. Others disagreed and suggested new approaches based on characteristics of microchannels such as, for example, the effect of small hydraulic diameter on the wall boundary layer fluid flow. A detailed review of previous experimental studies which are related to microchannel heat exchangers is presented next.

Table 2.1: Variable Definitions for Equation 2.1, 2.2, 2.3, 2.4 and 2.5

Symbol	Description
D_h	Hydraulic diameter [m]
f	Friction factor
L	Tube length [m]
μ_w	Dynamic viscosity, fluid [kg/m-s]
μ_f	Dynamic viscosity, wall [kg/m-s]
Nu	Nusselt number , fluid
Pr_f	Prandtl number, fluid
Re_f	Reynolds number , fluid

X.F. Peng and his coworkers reported a series of experimental investigations about forced convection in rectangular microchannels. Single phase forced-flow convection of water and methanol through rectangular microchannel ports was studied by B.X. Wang and X.F. Peng (1994). Experiments were conducted to investigate the effect of the geometry and thermal properties on the fluid flow through microchannels. Structure of the test tubes was made of stainless steel and hydraulic diameter was varied

between 0.31mm to 0.75 mm. In addition, uniform heat flux was applied to the lower plate surface. It was obtained that the large change in the fluid temperature with respect to small port geometry results a fully developed heat transfer regime starting at about Re= 1500-2000 in rectangular microchannel tubes. In addition, by using the experimental results Dittues- Boelter equation (Eq-2.4) was modified to correlate fully turbulent Nusselt number in microchannels as:

$$Nu_{avg} = 0.00805 \,\mathrm{Re}_{Dh}^{\,4/5}\,\mathrm{Pr}_{f}^{\,1/3} \qquad (2.5)$$

Another collective study between B.X. Wang and X.F. Peng with G.P. Peterson and H.B. Ma was aimed to further experimentally investigate the influence of liquid velocity, subcooling, property variations and microchannel geometric configuration on the heat transfer behavior and transition on the fluid flow mode (1994). Similar geometric properties in Wang et al.'s previous work (1994) were used and methanol was selected as a working fluid. Results showed that cooling performance of the microchannel ports can be enhanced with an increase in the liquid velocity regarding transition in the flow regime. Furthermore, an increase in heat transfer coefficient was reported due to subcooling effect. Compared to velocity effect, it was obtained that the wall temperature has a higher influence on the heat transfer rate of microchannel tubes. Finally, the number of the port effect on cooling capacity was studied and it was noted that increasing the channel port numbers has a significant control on the overall heat transfer performance, which was claimed as the most important parameter in Nusselt number correlation. In addition to their previous studies, Peng and Peterson investigated the rectangular microchannel port size effect on thermal properties of the fluid (1995). It was stated that due to the extreme size reduction in the channel port a sudden change can occur in

thermophysical properties, which increases the Reynolds number of the fluid flow. As a result, a transition from laminar to turbulent region can be observed at lower Reynolds number than conventional size channels.

Peng and coworkers expended their studies of the single phase forced convective heat transfer by using a binary mixture of water and methanol (1996b). The aim was to investigate the transition region of a binary mixture according to the change in hydraulic diameter from 0.133 to 0.367 mm and the variation of Reynolds number within 70 to 700. Similar to their previous studies, three distinct regions were observed in the flow regime. By comparing the experimental data it was obtained that when the size of the microchannel is decreased, the critical Reynolds number also reduces from 700 to 200 for the transition region. Additionally, mixture concentration effect on heat transfer was studied and critical mole fractions were analyzed. Compared to geometric influence on the fluid flow, it was concluded that the aspect ratio of the microchannel port has the most significant effect on the heat transfer and the fluid flow of the binary mixtures. In addition to their experimental studies, Peng and Peterson further investigated the effect of geometric parameters on microchannel flow and drove empirical correlations for the Nusselt number both in laminar and turbulent regions (1996a). Comparable experimental set up was used within hydraulic diameter range of 0.15 to 0.343 mm. In addition to aspect ratio, effect of port center to center distance on heat transfer was considered and included in the empirical formulations:

Laminar flow correlation: $$Nu_{avg} = 0.1165\left(\frac{D_h}{W_c}\right)^{0.81}\left(\frac{H}{W}\right)^{-0.79} \mathrm{Re}_{Dh}^{0.62} \mathrm{Pr}^{1/3} \quad (2.6)$$

Turbulent flow correlation: $$Nu_{avg} = 0.072\left(\frac{D_h}{W_c}\right)^{1.15}[1 - 2.421(Z - 0.5)^2]\mathrm{Re}_{Dh}^{0.8} \mathrm{Pr}^{1/3} \quad (2.7)$$

where; $$Z = \frac{\min(H,W)}{\max(H,W)} \quad (2.8)$$

Experimental results showed that geometric configurations have distinct effects in different flow regions. In laminar flow, the range deviation of the correlation (Eq-2.6) was obtained around ± 30%. In turbulent flow, it was concluded that additional geometric parameters are necessary for accurate heat transfer analysis compared to laminar flow. Therefore, a nondimensional parameter Z (Eq-2.8) was required to define for the turbulent Nusselt number correlation (Eq-2.7) which has a deviation around ±25%.

Similar to Peng at al.'s previous studies, Harms at al. theoretically and experimentally studied the single phase forced convection in two microchannel configurations: single channel system and multiple channel system (1997). Deionized water was applied as a working fluid within the Reynolds number range of 173 – 12900. By using different channel geometries, an enhancement was obtained in the heat transfer performance by decreasing the channel width and increasing the channel depth. In addition, a transition region was observed when Reynolds number was equal to 1500, which is smaller than conventional sized prediction. Compared to turbulent flow region, it was concluded that developing laminar flow region provides a better heat transfer performance.

A detailed literature survey about single phase convective heat transfer in microchannel structures was reported by Peng at al. (2002). Heat transfer correlation differences between conventional size channels and microchannels were presented by comparing previous studies. In laminar flow, different correlations were compared and the effect of geometry was discussed. It was mentioned that by analyzing the Peng et al.'s previous experimental results, the optimum aspect ratio which provides the maximum

heat transfer can be obtained when the port height is equal to three quarters of port width. On the other hand, in turbulent flow the optimum value for the port aspect ratio was reduced to 0.5. By comparing all previous studies, Peng et al. indicated that there hasn't been an unequivocal agreement in identifying the heat transfer parameters in noncircular microchannels.

As it mentioned earlier, some researchers experimentally applied conventional tube correlations to microchannel heat exchangers. For instance, Rahman and Gui investigated heat transfer characteristics for single phase (water and R11) and two phase (R-12) fluids in microchannels (1993). Two type of microchannel heat sink were presented: the I-channel and the U-channel. In the I-channel heat sink parallel channel configuration was used between inlet and outlet headers to show lower pressure drop effect. On the other hand, only a single passage was used in the U-channel to examine higher mass flow rate effect on heat transfer. In both channels' results experimental Nusselt numbers were evaluated higher than the conventional sized correlations. Surface roughness, which provides a repeated growth in the boundary layer thickness, was claimed as the main effect for the increase of heat transfer in microchannels. Furthermore, the gradual transition from laminar to turbulent flow was discussed due to small channel dimension, which gives the same order of magnitude as the turbulent length scale. In addition, compared to single phase flow, higher heat transfer coefficient was observed with liquid forced convection of two-phase flow in microchannels. In 2000, Rahman et al. further studied convective heat transfer in parallel pattern (I – Tube) and series pattern (U – tube) microchannel heat sinks (2000). Only water was used as a working fluid to investigate the variation of the Nusselt number and pressure drop. It was

concluded that for any given Reynolds number, the Nusselt number gets higher at the entrance than at the exit due to the beginning of boundary layer formation.

Another turbulent regime effect on heat transfer coefficient in microchannels was studied by Adams et al. (1997). Two copper circular microchannel tubes, which had 0.76mm and 1.09mm diameters, were experimentally tested within 2600 to 23000 Reynolds number range. Results were obtained higher than the Gnielinski's correlation (Eq-2.2). Therefore, further modifications were applied on Gnielinski's correlation based on the experimental results. Adam et al. further studied turbulent convection in non-circular microchannels to investigate the hydraulic diameter limit (1999). It was presented that the Gnielinski correlation could be applicable within the range of Reynolds Number 3.9x 10^3 to 2.14 x 10^4 and Prandtl Number 1.22-3.02, respectively. Furthermore, it was concluded that 1.2mm hydraulic diameter can be predicted as the lower limit to apply classical turbulent single-phase Nusselt number correlations to non-circular channels.

Celata et al. reported characteristics of laminar flow in circular microtubes within the diameter range of 0.528-0.05 mm (2006). The geometric scaling effect on convective heat transfer in microchannel was analyzed according to thermal entrance length, axial wall conduction and viscous heating. For the viscosity effect the proportion of viscosity heating to heat flux at the wall effect on total temperature rise, κ was presented as;

$$\kappa = \frac{\Delta T_{f-v}}{\Delta T_{f-q}} = \frac{1}{2} Br\, \Omega^* f \,\mathrm{Re} \qquad (2.9)$$

where Ω^* is the dimensionless cross-sectional area, $\Omega^* = \frac{\Omega}{D^2}$.

It was suggested that viscous heating can be neglected if the κ is smaller than 5%. Variable definitions for equation 2.9 are defined in table 2.2.

Additionally, it was stated that the rate of increase in the heat transfer coefficient is smaller than the decrease in the diameter range. Therefore, the decrease in Nusselt number can be observed more significantly in smaller diameter compared to conventional correlations. It was also noted that in smaller diameters the radial temperature profile deforms more than large ducts due to higher fluid velocity. Thus, the change in thermal properties becomes more important with the decrease in geometric properties.

Zhigang et al. studied the implementation of the conventional size correlations for microchannel tubes (2007). De-ionized water was used in 45, 92 and 141 μm diameter quartz glass channels. First, no axial heat conduction assumption was discussed for microchannels. It was claimed that axial conduction may cause uniformity in the wall temperature, which would reduce the heat transfer capacity. Thus, by referring Maranzana et al.'s previous study (2004), the axial conduction number of "*M*" was suggested to define an inequality to compare the axial conduction at the wall.

$$M = \left(\frac{k_w}{k_f}\right)\left(\frac{D}{L}\right)\left(\frac{A_w}{A_f}\right)\frac{1}{\mathrm{Re}_{Dh}\,\mathrm{Pr}_f} < 0.01 \qquad (2.10)$$

The axial conduction is recommended to be neglected when *M* is lower than 0.01. Variable definitions of equation 2.9 are listed in table 2.2.

Then, within the 100 to 3000 Reynolds number range experimental Nusselt number results were compared with the correlations of Shah (Eq-2.1) for laminar flow, Gnielinski (Eq-2.2) for transition regime, and Dittus – Boelter (Eq-2.4) for turbulent flow. First, in laminar region it was noted that the experimental Nusselt number becomes smaller than classical correlation. Similar to Peng et al.'s previous conclusion, variation

of thermophysical properties effect was claimed for the decrease in laminar Nusselt number. On the other hand, in turbulent region experimenal results sharply increased compared to the conventional correlations, which was also mentioned in Adams at al.'s previous study (1997). Viscous dissipation effects were discussed as an increasing factor on convective heat transfer in turbulent region. In addition, thinner conductive liquid layer, entrance and surface roughness were also described as a triggering factor on heating capacity.

Table 2.2: Variable Definitions for Equation 2.9 and 2.10

Symbol	Description
A_f	Area , fluid [m^2]
A_w	Area , wall [m^2]
Br	Brinkman number [$\mu U^2/q'_w$]
k_f	Thermal conductivity, fluid [W/m-K]
k_w	Thermal conductivity, wall [W/m-K]
ΔT_{f-v}	Temperature rise due viscous heating , [K]
ΔT_{f-q}	Temperature rise due heat flux , [K]
Ω	Cross sectional area , [m^2]

Early studies were pointing out disagreements between the classical correlations and the experimental results in microchannel heat exchangers. However, some recent studies have claimed that conventional size correlations would be applicable for microchannels too. For example, Lelea et al. presented the heat transfer of laminar distilled water flow in stainless steel microtubes with the diameters of 0.1, 0.3 and 0.5 mm (2004). First, the pressure drop was analyzed for each tube with and without input power and results were compared individually. It was suggested that for microchannel

tubes the multiplication value of friction factor f and the Reynolds number Re can be equal to the conventional constant, f. Re=64 , if the total length of the tube is heated. For partial heating, however, lower f. Re values were evaluated. Furthermore, compared to the experimentally obtained Nusselt number with classical correlations, it was found that conventional theories were in a good agreement for water flow within 0.1, 0.3 and 0.5 mm diameter microchannels. Consequently, Owhaib and Palm studied the single phase forced convection of circular microchannel (2004). R134a was used as working fluid within three different channel diameters; 1.7, 1.2 and 0.8 mm. Results were compared with conventional correlations and pervious microchannel correlations such as equatuion 2.2 and 2.4. It was obtained that classical correlations were in a good agreement with the experimental results. On the other hand, none of previously presented microchannel correlations had consistent results with their experimental study. Furthermore, below Re=5000, the heat transfer coefficients for each channel diameter were calculated equal to each other.

Recently, variations in previous heat transfer analysis between conventional size correlations and microchannel results have been discussed by Mokrani et al. (2009). First, a water tunnel was designed as an experimental set up which can define the boundary conditions more precisely. Then, conventional Nusselt number correlations were checked with the experimental data and it was found that Shah-London and Gnielinski's correlations agree with the experimental results in laminar and turbulent regions respectively. Consequently, it was concluded that if the measurements error can be decreased and the entrance zone effects can be clarified, it is applicable to use large channel correlations to identify the heat transfer analysis in microchannels.

Table 2.3: Summary of Experimental Studies of Single Phase Forced Convection in Microchannels

Reference Study	Boundary Conditions	Findings & Conclusions
Wang & Peng (1994)	Water and methanol inside stainless steel rectangular ports of 0.31mm< D_h < 0.75 mm at uniform heat flux	▪ Turbulent flow regime was observed when 1500<Re<2000 ▪ Dittus- Boelter equation (**Eq-2.4**) was modified for microchannels (**Eq-2.5**)
Peng et al. (1994)	Methanol inside stainless steel rectangular ports of 0.31mm< D_h < 0.65 mm	▪ Heat transfer coefficient was increased by increasing flow velocity , temperature difference and port number respectively
Peng & Peterson (1995)	Methanol inside stainless steel rectangular ports of 0.31mm< D_h < 0.75 mm	▪ In microchannels laminar to turbulent region transition was reported at lower Re than conventional size channels due to sudden change in fluid properties
Peng & Peterson (1996b)	Water-methanol mixture inside stainless steel rectangular ports of 0.133mm < D_h <0.367mm at 70<Re <700	▪ Critical Re reduced from 700 to 200 by decreasing the size of the microchannel
Peng & Peterson (1996a)	Water inside stainless steel rectangular ports of 0.15mm< D_h < 0.343mm at 50<Re <4000 with uniform heat flux	▪ Experimental Nu correlations were developed as a function of H/W , Re , D_h and Pr (**Eq-2.6** (laminar) **Eq-2.7** (turbulent))
Harms et al. (1997)	Deionized water inside silicon rectangular ports of D_h =0.4mm at 173<Re<12900	▪ Transition from laminar to turbulent was claimed when Re is equal to 1500 ▪ Compared to turbulent region , better heat transfer performance was obtained in developing laminar flow region
Rahman & Gui (1993)	Water and R11 (single phase) and R-12 (two phase) inside silicon parallel-I type and series-U type heat sinks	▪ Increase in heat transfer in mirochannels was reported due to repeated growth in the boundary layer thickness by it surface roughness
Adams et al. (1997)	Water inside copper circular ports of 0.76mm < D_h< 1.09mm at .6x10^3<Re<2.3x10^4	▪ Experimental Nu was obtained higher than Glenski's correlation **(Eq-2.2)**
Adams et al. (1999)	Water inside copper non-circular ports of D_h = 1.13mm at 3.9x 10^3< Re<2.14 x 10^4	▪ Within Re 3.9x10^3 <Re < 2.14 x10^3 and 1.22 <Pr < 3.02, Glenski's correlation (**Eq-2.2**) was suggested as applicable to predict Nu ▪ D_h =1.2mm was claimed as the lower limit to apply classical correlations
Celata et al. (2006)	Water inside circular ports of 0.528mm<D_h< 0.05mm at 50<Re<2775	▪ Inside microchannels increase in fluid temperature due viscous heating was suggested to be checked by ratio of κ (**Eq-2.9)**
Zhigang et al. (2007)	De-ionized water inside quartz glass ports of D_h = 45, 92 and 141 µm at 100<Re<3000	▪ The axial conduction effect may reduce the heat transfer capacity **(Eq-2.10)**
Lelea et al. (2004)	Distilled water inside stainless steel ports of D_h = 0.1, 0.3 and 0.5 mm at Re <800	▪ Multiplication of friction factor and Re (***f*. Re=64)** was reported as applicable if the total tube length is heated in microchannels
Owhaib & Palm (2004)	R134a inside stainless steel circular ports of D_h = 1.7 , 1.2 and 0.8 mm	▪ Classical correlations **(Eq-2.4 , Eq-2.5)** were agreed with the experimental results of microchannels but microchannel correlations didn't
Mokrani et al. (2009)	Water inside stainless steel rectangular ports of 0.1mm < D_h < 1mm at 100<Re <5000	▪ Classical correlations **(Eq-2.4-2.6)** can be applicable when the measurements errors are reduced

2.2 Numerical Analysis of Single Phase Forced Convection in Microchannels

The experimental uncertainty from the measurements and the limited microtube geometries studied in the literature show some inconsistencies and certain disagreements among researchers in the field. . Some researchers further investigated the thermal performances of microchannel heat exchangers using numerical approaches. The main purpose of the numerical studies was to find the optimum geometric parameters that minimize the thermal resistance and pressure drop and increase the heat transfer rate capability of the microchannel heat exchangers. During these studies, the following three-dimensional Navier-Stokes equations were used to define fluid flow and conjugate heat transfer in microchannels:

Continuity:
$$\frac{\partial \rho}{\partial t} + (\nabla \rho \vec{V}) = 0 \tag{2.11}$$

Momentum:
$$\frac{\partial (\rho \vec{V})}{\partial t} + \nabla .(\rho \vec{V}\vec{V}) = -\nabla P + \nabla .(\bar{\bar{\tau}}) + \rho \vec{g} + \vec{F} \tag{2.12}$$

where
$$\bar{\bar{\tau}} = \mu \left[(\nabla \vec{V} + \nabla \vec{V}^T) - \frac{2}{3} \nabla .\vec{V} I \right] \tag{2.13}$$

Energy:
$$\frac{\partial (\rho E)}{\partial t} + \nabla .(\vec{V}(\rho E + p)) = \nabla .\left(k_{eff} \nabla T - \sum_j h_j \vec{J}_j + (\overline{\overline{\tau_{eff}}} .\vec{V}) \right) + S_h \tag{2.14}$$

Where
$$k_{eff} = k + k_t \quad , \qquad E = h - \frac{p}{\rho} + \frac{V^2}{2} \tag{2.15, 2.16}$$

Variable definitions for equations 2.11 – 2.16 are defined in table 2.4

FLUENT become a popular commercial CFD solver which is commonly used in the literature to simulate different type of microchannel tubes. According to previous studies, the following assumptions were usually applied to simplify the governing equations:

1. Fully developed laminar / turbulent flow
2. Constant/temperature dependant fluid properties
3. Incompressible flow
4. Steady state process
5. No slip at the wall
6. Negligible body forces
7. Negligible radiation heat transfer and natural convective heat transfer

Table 2.4: Variable Definitions for Eq.s: 2.11, 2.12, 2.13, 2.14, 2.15 and 2.16

Symbol	Description
E	Total energy [J]
$\vec{F}$	Force vector [N]
$\vec{g}$	Gravitational acceleration [m/s^2]
ρ	Density [kg/m^3]
h	Sensible enthalpy [J /kg]
I	Unit tensor
$\vec{J}$	Diffusion flux [kg/m^2-s]
k	Thermal conductivity [W/m-K]
k_t	Turbulent thermal conductivity [W/m-K]
k_{eff}	Effective conductivity [W/m-K]
μ	Molecular viscosity [kg/m-s]
P	Pressure [Pa]
p	Static pressure [Pa]
S_h	Chemical reaction heat [W]
t	Time [s]
$\bar{\bar{\tau}}$	Stress tensor
$\vec{V}$	Overall velocity Vector [m/s]

Numerical analysis helped researchers to quantify the effect of different type of geometries and boundary conditions, and assisted to have a better physical understanding about the fluid flow and heat transfer phenomena in microchannel tubes. Since my model build up on the existing knowledge in this area, a detailed review about relevant numerical studies that focus on single phase convective flow boiling in microchannel tubes is presented next. Additionally, an overview of these numerical investigations is summarized in table 2.4 for quick glance to the existing knowledge in this area.

In the early 21st century, Federov and Viskanta studied three-dimensional conjugate heat transfer in microchannel based heat sinks numerically (2000). Incompressible laminar flow was analyzed by using Navier-Stokes equations of motion. By validating the numerical results with previous experimental data, it was stated that Navier-Stokes equations are capable to provide accurate numerical solutions for the laminar flow and conjugate heat transfer investigations in microchannels. Furthermore, higher heat transfer was reported at the channel inner side walls than bottom wall due to smaller thermal resistance effect. In addition to Federov and Viskanta's investigations, another numerical study of conjugate heat transfer in microchannel heat sinks was presented by Ambatipudi and Rahman (2000). Channel aspect ratio, Reynolds number and number of port effects on thermal performance were investigated individually. First, it was mentioned that microchannel heat sinks can provide a reduction in thermal resistance with shorter conduction paths between heats sources compared to conventional size heat exchangers. Then, numerical results were compared with previous experimental studies in literature. Higher Nusselt number at the entrance was reported due to the development of thermal boundary layer. In addition, with a higher channel dept and lesser material between

heater and cooler, a smoother temperature profile and a larger variation in the Nusselt number were observed. Furthermore, an enhancement in heat transfer coefficient was found at higher fluid velocity. It was concluded that the solid channel outlet temperature can be decreased with an increase in Reynolds number because of larger mass flow rate effect.

Another numerical study about three-dimensional fluid flow in rectangular micro-channel heat sinks was reported by Qu and Mudawar (2002). Their aim was to evaluate local and average heat transfer characteristics such as temperature, heat flux and Nusselt number in microchannels. In addition, Reynolds number and thermal conductivity of solid material's effects on heat transfer process were discussed. It was suggested that temperature rise in fluid and solid region of the microchannel heat sink can be approximated as linear. Similar to previous analysis, the Nusselt number and heat flux were reached their maximum value at the channel inlet and approached to zero near the channel corners. Furthermore, the enhancement in heat transfer was explained with the rise of the Reynolds number, which increases the fully developed region length. Finally, it was stated that the use of classical fin method, which offers the advantage of simplicity in calculations, can only give qualitative results for microcannel heat sinks.

Lee at al. and his group experimentally reported the validity of classical correlations for single phase internal flow (2005). During the experiments, Reynolds number and the hydraulic diameter were varied 300 to 35000 and 318 to 902 μm respectively. It was obtained that the inlet and the boundary condition differences between the microchannel experiments and the conventional correlations limit the model validations. In addition, numerical methods were applied by using commercial software

package FLUENT. By utilizing the symmetry boundary conditions, only quarter domain was simulated. Results showed that the 3D conjugate approach and simplified thin wall model can provide consistent results with the experimental data. Therefore, it was concluded that heat transfer capacity can be obtained numerically with both studies if inlet and boundary conditions were defined properly. In laminar regime, however, thin wall analysis was suggested to apply due to its computational efficiency. Furthermore, Liu and Garimella studied the thermal performance of single phase water flow in microchannel heat sinks both computationally (2005). Their aim was first set a CFD model with FLUENT and then, compare their five developed analytical approaches; 1D resistance model, a fin approach, two fin-liquid coupled models, and a porous medium approach. By assigning the port wall thickness as fin thickness, conjugate heat transfer solution, a simulations solution of convection and conduction, was analyzed to obtain variation in thermal resistance. It was reported that compared to other four models, 1D resistance model can able to present the physics of the heat transfer problem accurately without including any complexity in its equations. Therefore, it was suggested to use 1D model for the design and optimization of practical microchannel heat sinks.

Unlike incompressible flow analysis, Chen et al. numerically studied three dimensional heat transfer characteristics of compressible flow in microchannels (2005). Due to the advantages of having shorter computational time and smaller memory usage, reduced Navier Stokes equations were developed to evaluate the thermal characteristics of long microchannels. First, the numerical program was validated with the simulation of incompressible flow in conventional size channels and results were obtained in a good agreement with the classical correlations. Then, constant heat flux boundary condition in

long microchannel wall was simulated with compressible flow of air. It was found that the local Nusselt number of the microchannel has a continuous decrease along the channel axes due to absence of fully developed region. In addition, constant surface temperature boundary condition was illustrated numerically and it was reported that after decreasing at the channel inlet, local Nusselt number starts to increase through the flow direction which stays constant for incompressible flow. Fluid compressibility and the energy transfers between kinetic energy, internal energy and flow work were claimed as an explanation for the differences between compressible and incompressible fluid flow in microchannel tubes.

Li et al. presented the "synergy principle" which is the combined action between velocity and temperature gradients (2005). This numerical study was consisted of laminar flow heat transfer in noncircular microchannels. Water was used as a working fluid and two types of geometry were selected as port cross-section; trapezoidal and triangular. Numerical results were compared with previous experimental studies and it was found that the fully developed heat transfer velocity and temperature gradient have a better synergy at lower Reynolds number (Re <100). Furthermore, it was obtained that in fully developed region the Nusselt number, which stays constant in conventional size ducts, has an increase with the increase of Reynolds number in microchannels. In addition, compared to both cross-sectional geometries, higher fully developed heat transfer coefficient was obtained with trapezoidal cross-sectional geometry.

Furthermore, Saidi and Khiabani reported the number of layers effect on thermal efficiency of microchannel heat sinks (2007). In addition, analytically and numerically obtained results were compared to obtain the effects of aspect ratio, porosity, channel

width and the solid properties on the thermal resistance of microchannel heat sinks. First, it was found that the increase in aspect ratio reduces the thermal resistance by increasing both the channel cross-section and the heat transfer area between solid and fluid interiors. However, an optimum value of the channel aspect ratio couldn't obtain due to the construction limitations. On the other hand, in order to reduce the thermal resistance, an optimum surface porosity was achieved by keeping the balance between fluids – channel base distance and channel wall – channel base distance. Furthermore, additional decrease in thermal resistance was investigated with the increase in channel width, and channel layer number effects on microchannel thermal resistance were discussed. It was presented that increasing the channel layers up to four or five can effectively decrease the overall thermal resistance of microchannel heat sink. In addition to Saidi and Khiabani's study, Xie et al. investigated the turbulent heat transfer and pressure drop in minichannel heat sinks numerically (2007). Single phase water was used as a coolant and effect of geometric properties such as channel height, width, vertical wall and bottom plate thicknesses were reported parametrically. The aim of the study was to obtain the optimum channel geometry which provides a smaller pressure drop and maximum allowable heat flux with the minimum thermal resistance in 20x20mm minichannel heat sink. It was obtained that pressure drop and thermal resistance can be diminished with the increase of the channel height which was calculated as 5mm for an optimum value. Additionally, channel width effect was studied and in order to keep a good balance between pressure drops and maximum heat flux with lower thermal resistance, the ideal for channel width value was obtained as 0.5mm. Then, the effect of vertical wall thickness was analyzed and results showed that the thermal resistance reaches it turning

point by increasing the vertical thickness up to 0.3mm, which was accepted as the optimum value. Finally, the effect of channel bottom wall thickness was studied at previously obtained favorable geometric specifications. It was found that the thermal resistance reduced to its minimum value at 0.2mm channel thickness. In conclusion, in spite of its higher pressure drop penalty a narrow and deep channel was suggested to use for a better thermal performance rather than wide and swallow one.

Recently, Wang and his coworkers have presented their numerical study of forced convection in a microchannel with negligible axial heat conduction and results were compared with their experimental data (2009). The aim of their current study was to investigate the capability of the classical Navier Stokes and energy equations .The commercial software package of FLUENT was used for the numerical simulations of trapezoidal microchannels and deionized water was selected as working fluid. It was noted that the numerical results have a good agreement with the experimental wall temperature and local Nusselt number distributions. Therefore, it was concluded that classical Navier Stokes equations can be applicable to evaluate the thermal performance of the microchannel heat exchanger having a hydraulic diameter as small as 155 μm.

Table 2.5: Summary of Numerical Analysis of Single Phase Forced Convection in Microchannels:

Reference Study	Computational Simulation	Findings & Conclusions
Federov & Viskanta (2000)	Conjugate heat transfer study inside three dimensional rectangular microchannel of D_h = 0.086mm	▪ Higher accuracy was reported with Navier-Stokes equations in numerical solutions
Ambatipudi & Rahman (2000)	Water flow analysis inside silicon rectangular single and multiple port microchannels	▪ Channel aspect ratio, Re and number of port effects on thermal performance were investigated individually
Qu & Mudawar (2002)	3D heat transfer analysis of water flow inside silicon rectangular microchannel heat sink with D_h = 0.086m	▪ Increased heat transfer was observed at higher Re due to increase in fully developed region length ▪ Linear temperature rise were reported in solid and fluid region of microchannel heat sink
Lee et al. (2005)	Deionized water inside rectangular microchannels of 0.194mm< D_h <534 mm at 300< Re <3500	▪ Numerical predictions by **FLUENT CFD** solver based on a 1/4 domain of microchannel heat exchanger showed only 5% deviation compared to experimental studies
Liu & Garimella (2005)	Comparison of analytical procedures of water flow inside rectangular mirochannel ports with its numerical results by using **FLUENT CFD** solver	▪ Compared to other analytical methods , 1D resistance model was suggested based on its accuracy in its solutions and non-complexity in its equations
Chen et al. (2005)	Comparison of compressible and incompressible fluid flow heat transfer in rectangular microchannels 0.03mm < Dh < 0.05 mm	▪ The energy transfers between kinetic energy, internal energy and flow work were claimed as the main differences between compressible and incompressible fluid flow in microchannels
Li et al. (2005)	Investigation of water flow inside silicon trapezoidal D_h = 0.102mm and triangular D_h =0.084mm microchannels	▪ Fully developed heat transfer velocity and temperature gradient were reported as having a better "synergy" at lower Reynolds number (Re <100)
Saidi & Khiabani (2007)	Rectangular multi-layer microchannel heat sink performance analysis by numerical simulations	▪ Increasing the channel layers up to four or five was effectively decreased the overall thermal resistance of microchannel heat sink
Xie et al. (2007)	3D water flow simulation in rectangular minichannels of 0.8mm< D_h <1.41 mm	▪ In spite of its higher pressure drop penalty, a narrow and deep channel was suggested to use for a better thermal performance rather
Wang et al. (2009)	Laminar deinoized water flow inside silicon trapezoidal microchannels of D_h = 0.155mm was studied experimentally and numerically by **FLUENT CFD** solver	▪ It was concluded that classical Navier Stokes equations can be applicable to evaluate the thermal performance of the microchannel heat exchanger with D_h =0.155 mm

2.3 Literature Summary

By searching previous applications within the past thirty years, a comprehensive literature review is presented and some important conclusions are emphasized next. First, the reduction of critical Reynolds number for micro-flow was mentioned in many studies. The most logical and generally accepted explanation was the effect of sudden changes in fluid thermal-physical properties is due to smaller channel diameters. For instance; a laminar inlet flow which has a Reynolds number around 500 was observed fully turbulent at the exit of the microchannel due to the dramatic increase in fluid temperature (Wang et al, 1994). However, since each study shows certain differences, an universal micro-scaled critical Reynolds number for laminar flow hasn't been obtained yet. For this study, Peng and Peterson's commonly accepted suggestion was selected for the laminar critical Reynolds number as $R_{critical}$ =400.

Another remark was the effect of thermal boundary layer development on the heat transfer of microchannel heat exchangers. In the text, the thermal boundary layer was defined as a result from free stream and surface temperature difference. Therefore, thicker the boundary layer provides a higher impact in the heat transfer coefficient. For example, the highest temperature difference occurs at the tip section of microchannels. As a result, many researchers reported that the maximum Nusselt number occurs at the channel inlet. In addition, some studies also mentioned the effect of boundary layer length. Considering the role of thermal gradient in convective heat transfer, a longer thermal entry length would be preferred to have a higher heat transfer. For internal flows, the laminar thermal entry length can be estimated by Langhaar's correlation (1942) which is given in Introduction to Heat Trasnfer text book (Incropera et al.,2007) as :

$$L_{th} = 0.05\,\mathrm{Re}_D\,\mathrm{Pr}\,D \tag{2.17}$$

From the equation, it can be clearly observed that at higher Reynolds number, microchannel heat exchangers can provide more heat transfer with their longer thermal length. According to previous studies from Celata et al. (2006) and Zhigang et al. (2007), the axial heat conduction and viscous dissipation effects should be considered during the heat transfer analysis in microchannel structures. The correlations Eq-2.9 and 2.10 also confirm this conclucion.

In addition to characteristic effects of the fluid flow, geometric specifications were also discussed in the literature. To decrease the thermal resistance and increase the maximum heat transfer capacity with lower pressure drop channel height, width, aspect ratio and depth were discussed in the literature. It is concluded that, maximum heat transfer in microchannels can be obtained by decreasing the port area and keeping the tube length close to its thermal entry length. Therefore, a narrow and deep channel was recommended to obtain better heat transfer performance.

In conclusion, with the help of this literature review, certain fluid flow assumptions, geometric effects on heat transfer capacity and several microchannel design methods were identified. This experience from the previous studies is the basis of the numerical model developed in this thesis to study the round microchannel tube model design. The following sections will present the computational analysis of each simulation model by using FLUENT CFD software package.

CHAPTER III

Fluent CFD Modeling

One can define Computational Fluid Dynamics (CFD) as a computational technology which makes the analysis of complicated fluid dynamics possible with a higher accuracy[1]. Therefore, in thermal design applications CFD became an important tool in terms of its various advantageous. For instance, by using CFD it is possible to design a virtual prototype and analyze its performance before its prototyping and manufacturing. With sufficiently high computing power CFDs are able to provide faster predictions regarding the performance of heat exchangers, which recently makes it a powerful tool for the energy efficiency analysis.

FLUENT CFD code is a common commercial software package. As it mentioned in the literature review, it has been used in many numerical application and provided coherent results by solving 3D Navier-Stokes continuity, momentum and energy equations. In this study FLUENT was selected as a computational tool to perform the numerical heat transfer analysis in microchannels. Throughout my research each model was analyzed by three main solution steps namely; Gambit pre-processing, FLUENT solution and FLUENT post-processing. In this section each step is explained and important solution methodologies are presented.

[1] From FLUENT website at http://www.fluent.com/solutions/whatcfd.htm.

3.1 Gambit Pre-processing

The first step of the computational study is to generate an appropriate model by using a computer aided design (CAD) packages. For FLUENT CFD solution, Gambit is provided as a preprocessing tool to create the heat exchanger geometry. By using Gambit's user friendly comments, journal files were generated for each heat exchanger tube design, which helped to apply further modifications in a time saving manner. Regarding to current study, the Gambit journal files can be found in appendices of A, B and C.

There are some specific Gambit operations which were applied during the pre-processing step for each heat exchanger tube respectively. First of all, for all 3D models only small sectional portions of the geometries were created by using symmetric and periodic boundary conditions. For example, for microchannel tubes only the central port section was modeled in Gambit, and for round tube only quarter section was generated. Despite neglecting the edge effects in straight microchannel tubes, this numerical modeling approach is reasonably sound and feasible by using a computer with Intel Dual Core Xeon Processor at 2.83GHz. and 4GB of RAM. In order to provide complete solutions with these partial geometries, "SYMMETRY" boundary conditions were applied for each sectional face cuts as shown in figure 3.1.

Type of meshing is another important Gambit operation which affects directly the FLUENT solver results and convergence. In this study since the flow was in the laminar region, equally spaced grid was preferred to simulate the continuity of the flow regime. In addition, to control the skewed cell volume in round geometry, quadrilateral elements were chosen which has the skew level between 0.98-1. Thus, "map" mesh type was preferred especially for the fluid flow interiors. In addition to its size, the number of grid

also affects computational calculations in terms of its accuracy and convergence time. For example, in this study iteration time to resolve the velocity and temperature field was ranged between 2 hours to 10 days depending on the mesh quality and grid numbers. Besides, in order to ensure the results are independent from the mesh used, a grid dependency study was conducted. By refining the grids and comparing their results, grid dependency was checked for three dimensional and two dimensional models individually.

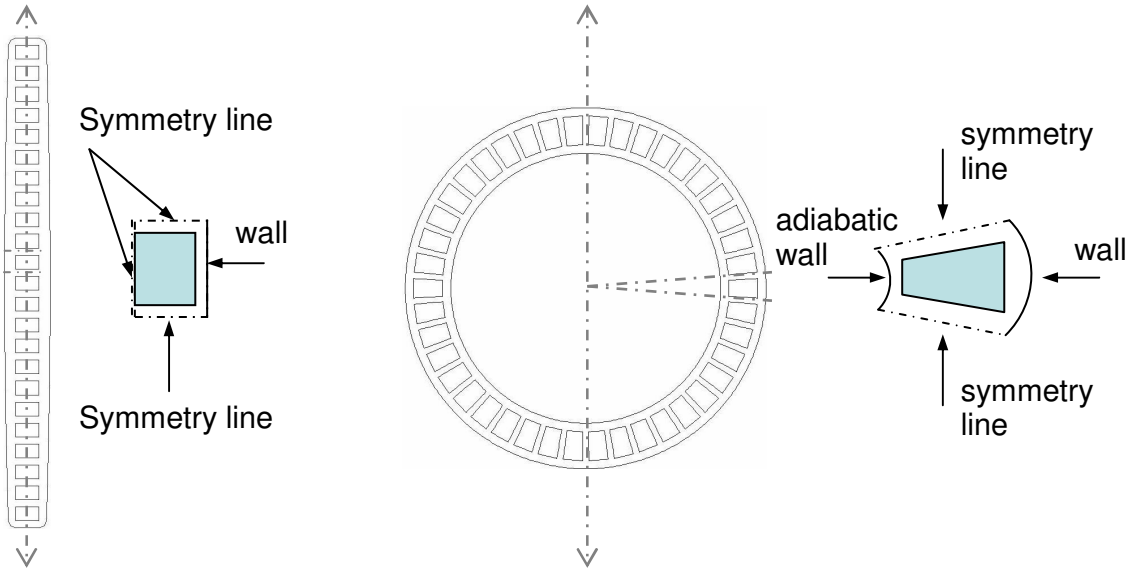

Figure 3.1: Sectional Simulation Symmetry Boundaries

Another practical Gambit operation, which is applied during the pre-processing of the simulation, is the "scale function" command. To create a continuous and smooth meshing quality, I created the geometries using dimensional values in millimeter. Once the geometry and the meshing were completed, "scale function" command was applied. By dividing each length into 1000, models were converted to metric scale. In order to avoid any error due to scaling, "check topology" and "check geometry" commands were further applied to examine deformation in the mesh qualities.

Finally, beside "SYMMETRY" boundary condition, "MASS_FLOW_INLET" was used to define tube inlets due to available experimental data. Tube outlets, on the other hand, were defined as "PRESSURE_OUTLET" in order to obtain a better convergence and avoid backflows during FLUENT convergence. In figure 3.2, a 3D quarter tube in tube counter heat exchanger geometry and boundary conditions are demonstrated.

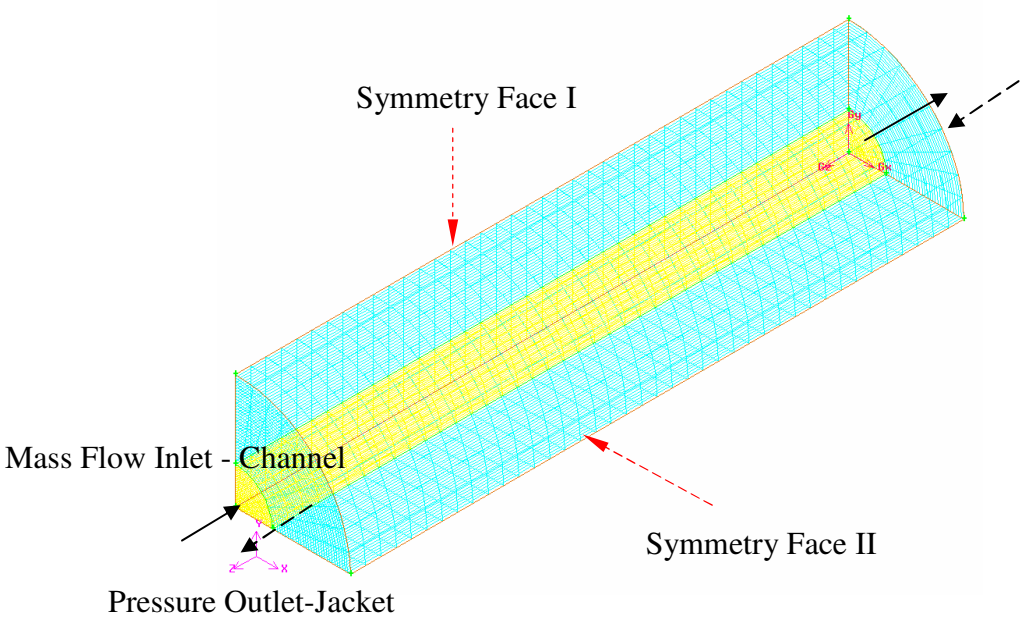

Figure 3.2: Boundary Conditions shown in the 3D Model of the Tube in Tube Calorimeter Counter Flow Heat Exchanger

After creating the geometry, scaling its unit to the metric system and examine its mesh quality, and assigning appropriate boundary conditions Gambit pre-processing step was completed by generating a case file (MODEL-NAME.msh) which is ready to run using the FLUENT solver procedure.

3.2 Fluent Solver

3.2.1 Fluent Solver Setup and Iterative Procedure

The next procedure in CFD simulation is the application of FLUENT solver to the meshed Gambit geometry. After reading the case file, the first step in FLUENT is to perform a grid check over the entire geometry to avoid any solver problems due to invalid mesh connectivity. Once the grid check is satisfactory, FLUENT solver type can be defined accordingly. There are two type solvers available for 2D and 3D simulations; single-precision and double-precision solvers. It is recommended to use double-precision solver for long and small diameter pipes with high aspect ratio grids in connection with heat transfer analysis (FLUENT 6.3 User's Guide, 2006). Therefore, in my study double-precision solver was applied in 2D and 3D analysis of microchannel heat exchangers.

Before moving to the next steps, it is necessary to discuss computational solution method of FLUENT to have a better understanding on the results. The method of CFD can be explain as simulation of a continues problem domain with a discrete domain usually by using Finite-Difference method over a computational grid. According to Bhaskaran and Collins' "Introduction to CFD basics" notes (2002) a simple Finite-Difference illustration can be given with following 1-D example;

$$\frac{du}{dx} + u^m = 0; \quad 0 \le x \le 1; \quad u\ (0) = 1 \tag{3.1}$$

By keeping the m=1, equation can be simplified as linear. As it shown in figure 3.3.a, with four equally-spaced grid points, the linear equation can be defined as;

$$\left(\frac{du}{dx}\right)_i + u_i = 0, \tag{3.2}$$

where the subscript *i* represents grid point's value. By using Taylor Series Expansion, Eq-3.1 can be shown as;

$$\left(\frac{du}{dx}\right)_i = \frac{u_i - u_{i-1}}{\Delta x} + \mathrm{O}(\Delta x) \ , \tag{3.3}$$

where $\mathrm{O}(\Delta x)$ is the truncation error which makes the solution first order accurate. By substituting Eq-3.3 into Eq-3.2, following discrete equation is obtained for the given algebraic equation 3.1.

$$\frac{u_i - u_{i-1}}{\Delta x} + u_i = 0 \tag{3.4}$$

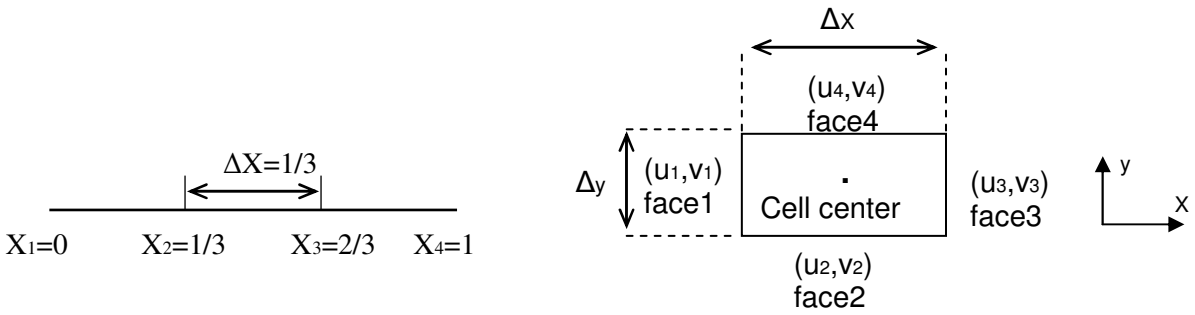

(a) Equally spaced grid points (b) sample rectangular cell

Figure 3.3: Computational Finite-Difference Grid Arrangement (Bhaskaran et al., 2002)

FLUENT applies the discretization by using finite volume method for the solution of conservation of mass, momentum and energy equations. The meshed GAMBIT geometry consists of many quadrilaterals. In finite volume approach these quadrilaterals are defined as cells and grid points are as nodes. Each cell defines a control volume and the integral form of the conservation equations are applied at each control volume to get discrete equations for finite difference solution. For instance, a steady, incompressible flow's continuity equation can be shown in an integral form as;

$$\int_s \vec{V}.\hat{n}\ dS = 0 \ , \tag{3.4}$$

where S is the surface of control volume and $\hat{n}$ is the normal vector of the surface. This equation implies that the total mass flow within the control volume is equal to zero.

In FLUENT, finite volume approach is used to solve equation of motions at each cell location. Considering previous integral equation 3.4 and assigning each face velocity as $\vec{V} = u_i\hat{i} + v_i\hat{j}$ over the rectangular cell geometry, which is shown in figure 3.3-b, resultant finite volume method solution becomes;

$$-u_1\Delta y - v_2\Delta x + u_3\Delta y + v_4\Delta x = 0 \tag{3.5}$$

Equation 3.5 is the discrete form of the continuity equation for one cell. Similar to this approach, conservation of mass, momentum and energy equations are solved at center of cell in FLUENT solver engine by applying the boundary conditions.

In the exact solutions the left hand side (LHS) of each discrete equation is shown as equal to zero. However, in iterative solutions LHS cannot reach to zero and usually be equal to small numbers, which is called the residuals. Therefore, in FLUENT convergence of solution is controlled by the residual of each discrete conservation equation. At every iteration, FLUENT calculates and reports the residuals of each continuity variable for overall cells. In this study every heat exchanger tube model was analyzed with LHS=10^{-6} convergence requirement as it is suggested in FLUENT 6.3 User's Guide (2006).

After the grid check, FLUENT default solver should be modified regarding the specifications of the simulation. There are two types of solution methods available in FLUENT; pressure based and density based solvers. In current study pressure based solver, which calculates the pressure value by continuity equations and controls the accuracy of the velocity field, was selected based on the FLUENT 6.3 User's Guide's

(2006) suggestion for the low speed incompressible channel flow simulation. In addition, "The Pressure–Based Segregated Algorithm", which solves each continuity equations individually, was used due to its computational memory efficiency. An example of segregated algorithm is shown in figure 3.4. Implicit formulation was applied because of its faster convergence in steady state than explicit formulation. Finally, "Green-Gauss Cell Based" was utilized as a gradient option because of easy implementation in a quadrilateral map meshing quality of the heat exchanger tubes.

Following solver definition, solution controls should be specified in order to have accurate and rapid convergence in iterative results. In the steady state solution algorithm following iterative results (ψ_{new}) are calculated by the current results (ψ_{old}) and its difference with the previous iterations ($\Delta\psi$). This relation is controlled by the Under Relaxation Factors (URF) within the FLUENT solver algorithm. In other words, ψ_{new} can be expressed as:

$$\psi_{new} = \psi_{old} + (URF \times \Delta\psi) \tag{3.6}$$

By default, FLUENT assigns the optimum largest URF for each variable in the solver. According to FLUENT 6.3 User's Guide's (2006) these values are applicable for several simulations. On the other hand, in this study, in order to obtain a stable convergence at the solution and reduce the reversed flows inside the small port channels, pressure and momentum URLs were gradually reduced to 0.1 and 0.3 respectively for every model. In addition, pressure-velocity coupling and discretization inputs were kept as the default values at first. Then, in order to increase the accuracy and to finalize the iterations second order upwind discretization factors were applied for momentum and energy equations.

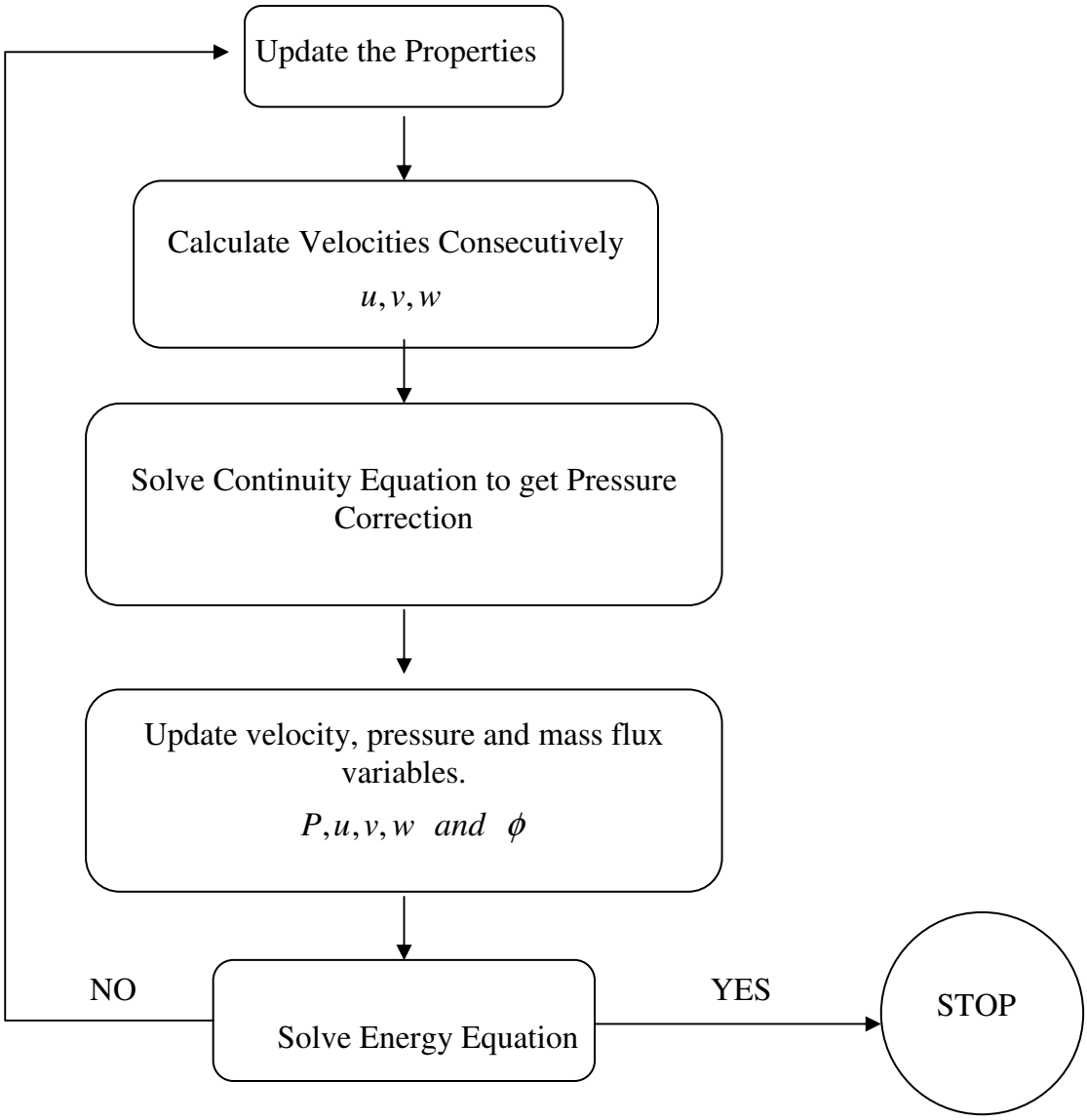

Figure 3.4: Pressure Based Segregated Algorithm (FLUENT 6.3 User's Guide, 2006)

3.2.2 Material Properties and Boundary Condition Setup

FLUENT provides a variety of fluid and solid material properties in its database. Moreover, it is also possible to create or customize the materials according to simulation requirements. For microchannels, aluminum was used as a solid material and the default constant material properties were applied in CFD simulations. For the fluid flow, water

and air were used as a working fluid respectively in different models. As it mentioned in previous chapter, sudden temperature rise in microchannels reduces the critical Reynolds number based on its influence on fluid properties. To imply a more realistic simulation, temperature dependant fluid variables were required to use in FLUENT. As a result, two parametric studies were applied to investigate the temperature effect on water and air thermal properties by using Engineering Equation Solver (EES). Results are plotted in appendix D. By applying curve fitting method over thermal property-temperature graphs, each variable is define as a 3rd order polynomial function of temperature as ;

For water:

$$\rho_{water}(T) = 1.52435e-5T^3 - 0.0182791T^2 - 6.58465\mathrm{T} + 254.689 \quad (3.7)$$

$$Cp_{water}(T) = -4.90704e-5T^3 + 0.0595573T^2 - 22.9131\mathrm{T} + 7020.88 \quad (3.8)$$

$$k_{water}(T) = 6.23e-9T^3 - 1.58186e-5T^2 - 0.009472\mathrm{T} - 0.98291 \quad (3.9)$$

$$\mu_{water}(T) = -2.44e-9T^3 - 2.54378e-6T^2 - 0.00089\mathrm{T} + 0.104451 \quad (3.10)$$

For air:

$$\rho(T) = -3.30992\mathrm{e}-08T^3 + 0.0000427651T^2 - 0.0206492\mathrm{T} + 4.41603 \quad (3.11)$$

$$Cp(T) = 4.19664\mathrm{e}-07T^3 - 0.0000508663T^2 - 0.0337043\mathrm{T} + 1008.06 \quad (3.12)$$

$$k(T) = 4.63995\mathrm{e}-12T^3 - 2.90213\mathrm{e}-08T^2 + 0.0000904396\mathrm{T} + 0.00100233 \quad (3.13)$$

$$\mu(T) = 4.91694\mathrm{e}-14T^3 - 8.11006\mathrm{e}-11T^2 + 8.20472\mathrm{e}-08\mathrm{T} - 6.88378\mathrm{e}-08 \quad (3.14)$$

In addition to material properties, FLUENT CFD solver also provides detailed boundary conditions which enable to simulate momentum and energy equations together. For instance, at each interfaced wall section FLUENT generates wall “shadow”, which separates each wall into two faces and makes them possible to analyze individually. In this study, it is required to define fluid/solid interface with a suitable boundary condition

to get a conjugated solution for convection and conduction. Therefore, “couple” option was selected under wall thermal boundary condition to solve energy equations for the wall and its shadow simultaneously.

Finally, after selecting the solver, assigning the solution controls and defining particular boundary conditions, FLUENT model can be initialized according to selected boundary condition. Initializing process assigns the starting values for the continuity equations before its iterative solution. Therefore, in order to have faster convergence initial values should be selected advisedly. In this study, channel inlet boundaries were selected to initialize the momentum and the energy equations. Moreover, to further decrease the iteration time and reduce the temperature effect on the reversed flow, first the momentum equation was solved alone to obtained the fully developed velocity profile. Once the momentum profile is converged, energy equation was included to the solver and further iterations were applied until both momentum and energy equations are converged. Additional result analysis methods will be discussed in the following section.

3.2.3 Fluent Journal File

In Fluent solver, journal files were created for each study to have more practical simulation models. The main procedure in the journal file is to modify given default FLUENT parameters according to model’s initial conditions and previous assumptions. In appendices of E and F, journal files of all simulation models were given. In this section, the procedure to create a RMC tube counter flow heat exchanger simulation journal file is explained by using FLUENT 6.3 Command List manual (2006) as follows:

- First the meshed case file was read by defining the location in the computer:

  file rc

case file name: C**:RMC\RMC-M.msh**

- Then, the material properties were modified based on the refrigerant selection. In my simulation single phase water was used as a working fluid and thermal properties were defined as a 4^{th} order temperature dependent polynomial function as $P(T) = A_0 + A_1T + A_2T^2 + A_3T^3$. Each polynomial coefficient was previously defined by using EES software library which were given in equations 3.7 – 3.10:

define materials change-create

from material-name: **air**

to material name: **water**

change density (kg/m3) [Cp (j/kg-K) / thermal conductivity (w/m-K) / viscosity (kg/m-s)]? : **y**

methods: **polynomial**

number of coefficients: **4**

coeff 1: $\mathbf{A_0}$

coeff 2: $\mathbf{A_1}$

coeff 3: $\mathbf{A_2}$

coeff 4: $\mathbf{A_3}$

change molecular weight: **y**

value (kg/kgmol): **18.0152**

change L-J characteristic length? : **y**

value (angstrom): **0**

change L-J Energy Parameter? : **n**

change thermal expansion coefficient? : **n**

change degrees of freedom? : **n**

change speed of sound? : **n**

change/create mixture and overwrite air?: **y**

- After the refrigerant properties each inlet and outlet boundary conditions were generated based on given initial variables in the following order:

define boundary-conditions mass-flow-inlet port-inlet [jacket inlet]

mass flow specification method: mass flow rate: **y**

mass flow-rate (kg/s): **3.59722E-05**

use profile for total temperature? : **n**

total temperature (K): **274.6**

use profile for supersonic/initial gauge pressure? : **n**

supersonic/initial gauge pressure (Pascal) : **0**

direction specification method: direction vector: **y**

reference frame: absolute: **y**

coordinate system: Cartesian (x, y, z) : **y**

use profile for x-component of flow Direction? : **n**

x-component of flow direction: **0**

use profile for y-component of flow direction? : **n**

y-component of flow direction: **0**

use profile for z-component of flow direction? : **n**

z-component of flow direction: **1 [-1]**

define boundary-conditions pressure-outlet port-outlet [jacket outlet]

use profile for gauge pressure? : **n**

gauge pressure (Pascal) : **15803.2057**

use profile for backflow total temperature? : **n**

backflow total temperature (k) : **274.6**

backflow direction specification method: direction Vector : **n**

backflow direction specification method: normal to boundary : **y**

radial equilibrium pressure distribution : **n**

specify targeted mass flow rate : **n**

- Before start the iterative procedure, micrchannel cell values were initialized according to its inlet boundary condition:

solve/initialize compute-defaults mass flow inlet

zone id/name : **port-inlet**

solve initialize initialize-flow

- Due to counter flow heat exchanger simulation, water jacket flow cell values were initialized separately based on its inlet velocity:

solve patch

cell zone id/name: **(2)**

variable : **z-velocity**

patch absolute velocity? : **n**

value : **-.048674769**

solve patch (2) z-velocity n -0.048675769

- Convergences of continuity momentum and energy equations were set to E-06 requirement:

solve monitors residual convergence-criteria

continuity residual convergence criterion : **1.0e-6**

x-velocity residual convergence criterion : **1.0e-6**

y-velocity residual convergence criterion : **1.0e-6**

z-velocity residual convergence criterion : **1.0e-6**

energy residual convergence criterion : **1.0e-6**

- Energy equations were excluded to obtain the fully developed velocity profile first and estimated 15000 numbers of iterations were applied until the solution converged and results were written into RMC-G1-Conv.cas file:

solve set equations temp

solve Energy equation(s)? : **n**

solve set equations temp n

solve iterate 15000

file write-case-data RMC-M-Conv.cas

- Since the momentum equation was previously converged its residual value was reduced to E-07 to be able to start to iterations. After 5 iterations, residuals were re-set to E-06 level and additional 5000 iterations were applied including the energy equation.

solve monitors residual convergence-criteria 1.0e-7 1.0e-6 1.0e-6 1.0e-6 1.0e-6

solve set equations temp

solve Energy equation(s)? : n

solve iterate 5

solve monitors residual convergence-criteria 1.0e-6 1.0e-6 1.0e-6 1.0e-6 1.0e-6

solve iterate 5000

file write-case-data RMC-M-0.cas

- To be able to reach the convergence requirement within the simulation, under relaxation factors for momentum and pressure solutions were reduced 0.4 and 0.1 respectively in 1000 additional iterations. In every gradual URL reduction, simulation was saved by numbering from 1 to 5 accordingly:

solve set under-relaxation mom 0.6

solve iterate 1000

file write-case-data RMC-M-1.cas

solve set under-relaxation mom 0.5

solve iterate 1000

file write-case-data RMC-M-2.cas

solve set under-relaxation mom 0.4

solve iterate 1000

file write-case-data RMC-M-3.cas

solve set under-relaxation pressure 0.2

solve iterate 1000

file write-case-data RMC-M-4.cas

solve set under-relaxation pressure 0.1

solve iterate 5000

- To increase the accuracy in the solution, final 10000 iterations were applied by increasing the discritization factor and final results were written to RMC-G1-2nd.cas file:

file write-case-data RMC-M-5.cas

solve set discretization-scheme mom 1

solve set discretization-scheme temp 1

solve monitors residual convergence-criteria 1.0e-7 1.0e-6 1.0e-6 1.0e-6 1.0e-6

solve iterate 5

solve monitors residual convergence-criteria 1.0e-6 1.0e-6 1.0e-6 1.0e-6 1.0e-6

solve iterate 10000

file write-case-data RMC-M-2nd.cas

Based on listed test commands which were presented in bold letters journal file was written as:

file rc C:RMC\RMC-M.msh

define materials change-create air water y polynomial 4 254.689 6.58465 -0.0182791 1.52435E-05 y polynomial 4 7020.88 -22.9131 0.0595573 -4.90704E-05 y polynomial 4 -0.9829 0.009472 -1.58786E-05 6.23E-09 y polynomial 4 0.104451 -0.00089 2.54378E-06 -2.44E-09 y 18.0152 y 0 n n n n y

define boundary-conditions mass-flow-inlet port-inlet y 3.59722E-05 n 274.6 n 0 y y y n 0 n 0 n 1

define boundary-conditions mass-flow-inlet jacket-inlet y 5.78E-04 n 323 n 0 y y y n 0 n 0 n -1

define boundary-conditions pressure-outlet port-outlet n 15803.2057 n 300 n y n n

define boundary-conditions pressure-outlet jacket-outlet n 1.758830455 n 300 n y n n

solve initialize compute-defaults mass-flow-inlet port-inlet

solve initialize initialize-flow

solve patch (2) z-velocity n -0.048675769

solve monitors residual convergence-criteria 1.0e-6 1.0e-6 1.0e-6 1.0e-6 1.0e-6

solve set equations temp n

solve iterate 15000

file write-case-data RMC-M-Conv.cas

solve monitors residual convergence-criteria 1.0e-7 1.0e-6 1.0e-6 1.0e-6 1.0e-6

solve set equations temp y

solve iterate 5

solve monitors residual convergence-criteria 1.0e-6 1.0e-6 1.0e-6 1.0e-6 1.0e-6

solve iterate 5000

file write-case-data RMC-M-0.cas

solve set under-relaxation mom 0.6

solve iterate 1000

file write-case-data RMC-M-1.cas

solve set under-relaxation mom 0.5

solve iterate 1000

file write-case-data RMC-M-2.cas

solve set under-relaxation mom 0.4

solve iterate 1000

file write-case-data RMC-M-3.cas

solve set under-relaxation pressure 0.2

solve iterate 1000

file write-case-data RMC-M-4.cas

solve set under-relaxation pressure 0.1

solve iterate 5000

file write-case-data RMC-M-5.cas

solve set discretization-scheme mom 1

solve set discretization-scheme temp 1

solve monitors residual convergence-criteria 1.0e-7 1.0e-6 1.0e-6 1.0e-6 1.0e-6

solve iterate 5

solve monitors residual convergence-criteria 1.0e-6 1.0e-6 1.0e-6 1.0e-6 1.0e-6

solve iterate 10000

file write-case-data RMC-M-2nd.cas

3.3 Fluent Post-processing

The final step in a CFD study is the method of analysis and interpretation of the iterative results. Before starting the post-processing, it is important to reach the desired convergence in each continuity variable. As it suggested in FLUENT 6.3 User's Guide (2006), in this study each model was iterated until its residual equals to 10^{-6}. Additionally, a further continuity check was applied on heat and mass balances by keeping the maximum flux difference within 1%.

There are several post-processing techniques available in FLUENT that users can chose to present their results such as displaying velocity vector and path lines, create temperature maps and plotting quantitative results. In this study, based on data reduction procedure, wall temperature, fluid temperature and total surface heat flux values were plotted in FLUENT to investigate changes in local properties. There are two types of field values available in FLUENT plotting namely cell and node values. FLUENT solves every equation at each cell and store as a cell value. Node values, however, are obtained by further averaging the surrounding cell values (Bhaskaran, 2002).In spite its high

memory occupancy, cell averaging method was used to have the local finite value effect in simulation results.

Furthermore, FLUENT also provides surface and volume integration for averaged results at a specific face or volume. In this study, “area–weighted average” and “mass average” options were applied for the calculation of averaged surface variables and outlet properties respectively. In addition to FLUENT post-processing tools, during this investigation Microsoft Excel spreadsheet was used to create comparison plots for all heat exchanger models and to apply further heat transfer analysis from the computational results given by FLUENT. In the excel spreadsheet, local variables were stored in each column. By doing so, averaging operation and numerical integration along the entire array elements became easy to perform. An example of excel spreadsheet is given in the appendix G.

CHAPTER IV

Fluent Validation

Before computing the simulation results for the thermal and hydraulic performance of straight and round microchannel tube heat exchangers, I conducted an extensive model validation of the program created using the FLUENT environment. This validation estimates the accuracy of the simulation results compared to experimental data and/or analytical solutions available in the public domain. The model was applied to tube geometries and operating conditions that are close or share common traits with the straight and round microchannel tube cases. It was also verified that the numerical simulations provided sound trends and the main characteristics of local heat flux and pressure drops at the fluid to wall surface boundaries were captured by the model. Experimental studies were searched in literature to obtain relevant reference data and analytical solutions to compare with my FLUENT simulation approach.

There were two experimental studies selected based on their close similarities with the work in this thesis. First, Monrad and Pelton's parallel flow investigation in annular spaces (1947) was simulated in FLUENT and experimental results were compared with their computational responses. Additionally, Peng and Peterson's experimental study (1996a), which was related to thermal performance analysis of

microchannel heat exchanger plate, was selected to investigate with FLUENT solver and to confirm its computational ability in smaller geometries. In this section, these two FLUENT validation models are presented individually.

4.1 Validation of Model 1: Convective Heat Transfer in Single Phase, Parallel Fluid Flow inside small diameter Tube and Tube Heat Exchanger

Monrad and Pelton experimentally studied the heat transfer coefficient of concentric annulus by using water as a working fluid in turbulent region (1947). In their study, two annular flow areas were created by using brass and copper concentric cylindrical tubes in diameters of 0.27, 0.625 inches respectively. In addition, due to lack of information, 1.53 inches external tube's material was chosen as the Aluminum and outer surface was assumed to be isolated. During the experiments, temperature measurements were taken at five distinct locations within the copper tube surface and from these averaged values heat transfer rate and heat transfer coefficients were calculated at different Reynolds number. From the tabulated results, four data points which have similar initial conditions and smaller in Reynolds number were selected to replicate their geometry and experimental boundary condition with my FLUENT solver. In the following section, geometric specifications and boundary conditions are explained in details.

4.1.1 Validation of Model 1 (Small diameter Tube in Tube HX):

Gambit Pre-Processing and Boundary Conditions

Before start to analyze the computational validation in FLUENT, experimental geometry was transferred to three dimensional computational domains with equally spaced grid points. In order to create fine rectangular cells, the central brass pipe diameter was used

as a reference length to estimate tube spacing grid numbers. Geometric specifications and assigned numbers of grid points are tabulated in table 4.1.

Table 4.1: Geometric Specifications and Related Grid Numbers of Validation Model-1

Geometry	Length [in] (Monrad et al., 1947)	Number of Nodes (N_{node})
$R_{1/4"Brass-Pipe}$	0.27	10
$R_{Copper-Tube}$	0.625	26
$R_{2"Al-Pipe}$	1.53	67
L_{pipe}	67.5	72

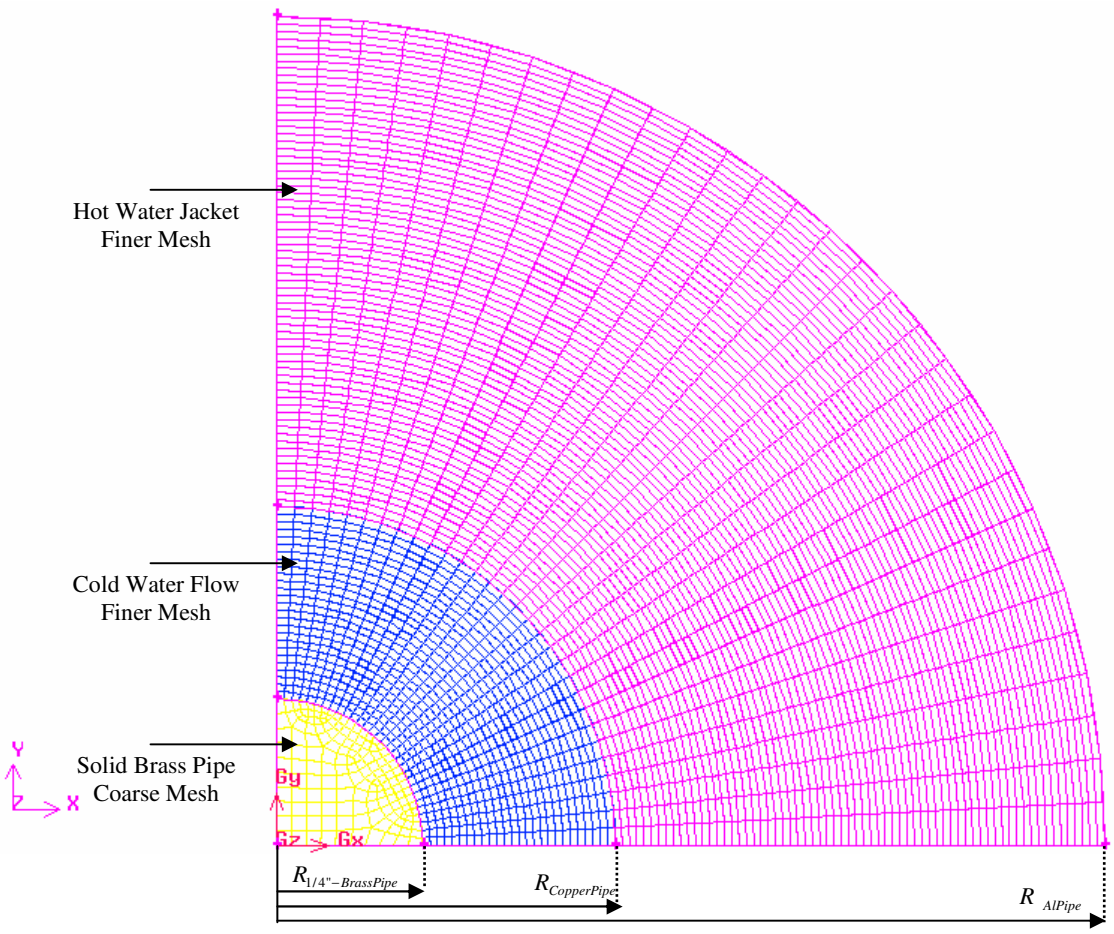

Figure 4.1: Face Mesh Quality of Validation of Model 1

(Small diameter Tube in Tube HX)

Due to its negligible radial conductive heating, coarse type meshing was applied to the solid brass pipe face. For the fluid flow regions, however, finer mesh was used to increase the accuracy in the FLUENT model. Moreover, in order to increase the computational efficiency, quarter geometry was created by using symmetry face boundary conditions at the sectional face cuts. By doing so, the sectional computational solution approach, which will be used in my round tube microchannel heat exchanger model, was tested. In order to provide a better illustration, face mesh quality and corresponding geometric specifications with node numbers (N_{node}) are presented in figure 4.1.and table 4.1 respectively.

In Monrad et al.'s study, increase in Reynolds number effect on heat transfer capacity was studied by changing the initial mass flow rate of the annular inlets. Therefore, mass flow inlet and pressure outlet boundary conditions were used to apply the given initial conditions.

4.1.2 Validation of Model 1 (Small diameter Tube in Tube HX): Fluent Solution

Experimental boundary conditions were applied to my FLUENT journal files, which are given in appendix A-1, by using four selected data points respectively. Monrad et al. specified these initial conditions in British Units System. In FLUENT solver, however, data points are required to be defined in SI Units. Therefore, each experimental value was converted to metric system by using EES's library. As it can be seen in table 4.2, selected data points were obtained in fully turbulent region for both annular spaces. A suitable turbulent model was required to apply for the solution of continuity equations. Based on FLUENT 6.3 user's guide suggestion (2006), two equation "Standard k-ε Model" was

selected due to its practical calculations and reasonable accuracy in fully turbulent flow simulations.

Table 4.2: Initial Experimental Conditions (Monrad and Pelton, 1947)

Exp	T_{hot} [K]	$\dot{m}_{hot}$ [kg/s]	Re_{Dh}	T_{cold} [K]	$\dot{m}_{cold}$ [K]	Re_{cold}
1	331.89	0.48	11300	277.17	0.26	4661
2	332.44	0.57	13700	276.89	0.26	4620
3	332.44	0.82	19300	276.89	0.26	4553
4	332.44	1.07	25300	277.44	0.20	3544

In addition to given parameters, further calculations were required to define assigned boundary conditions. For example; in "pressure outlet" flow exit condition an average pressure loss is necessary to define as gauge pressure between inlet and outlet. Therefore, in turbulent flow analysis, Colebrook function was selected to evaluate the Darcy friction factor (f) in turbulent flow and the Darcy–Weisbach equation was to evaluate to evaluate a reasonable pressure difference for each annulus as :

Colebrook function (1938):
$$\frac{1}{\sqrt{f}} = -2\log\left(\frac{\varepsilon/D_h}{3.7} + \frac{2.51}{\mathrm{Re}\sqrt{f}}\right) \qquad (4.1)$$

where Re > 4000 and ε is equal to 0.0015 mm for copper and brass tubing.(Cengel, 2004)

Darcy–Weisbach equation as given in Incropera (2007):
$$\Delta P = f.\frac{L}{D_h}\frac{\rho V^2}{2} \qquad (4.2)$$

which is applicable both for laminar and turbulent flow in smooth tubes. The to Darcy friction factor, *f*, must be correlated based on the flow regime (Incropera et al. 2007).

In equation 4.1, an iterative study is required to obtain the friction factor of f . By using EES program, friction factor coefficient was evaluated as a function of Reynolds number for each flow. Then, by substituting f into equation 4.2, gauge pressures were estimated at each outlet boundaries.

In addition to pressure drop, turbulent quantities are required to be specified in order to make standard k-ε model applicable in FLUENT. Thus, the turbulent intensity, the ratio of root-mean-square of the velocity fluctuations u' to the mean flow velocity u_{avg} , I was evaluated based on FLUENT 6.3 user's guide (2006) empirical correlation as follows:

Turbulent intensity: $$I = \frac{u'}{u_{avg}} = 0.16(\mathrm{Re}_{Dh})^{-1/8} \qquad (4.3)$$

Resultant friction coefficient, gauge pressure and turbulent intensity values are shown in table 4.3.

For the material properties, FLUENT database was used and default solid properties of copper and aluminum were selected. However, since it is not provided by default in FLUENT, EES library was used to define the brass material properties. Once specification of boundary conditions and material properties are finalized, four flow simulations were carried out by using identical meshed geometry.

In the iterative solution of FLUENT, first, convergence in momentum equations was reached in order to have fully developed velocity profile in heat transfer analysis. Then, energy equations were included in to the solver and additional iterations were applied. Compared to other iterative parameters, momentum equations were observed higher in residual due to turbulence within the flow field. Therefore, to reduce the

previous turbulent solution's effect on current calculation, URL factors of momentum and pressure values were decreased gradually at additional 100 iterations.

Table 4.3: Friction Coefficient, Gauge Pressure and Turbulent Intensity of Fluids

Exp	f_{hot}	$P_{gauge-hot}$ [Pa]	I_{hot} %	f_{cold}	$P_{gauge-cold}$ [Pa]	I_{coldt} %
1	0.03	8.22	4.96	0.04	298.22	5.57
2	0.03	11.39	4.84	0.04	299.00	5.57
3	0.03	21.15	4.64	0.04	291.61	5.58
4	0.02	33.81	4.48	0.04	183.54	5.76

Consequently, momentum residual was reached to level of 10^{-6} around 3000 iterations. Then, by increasing solver discretization to the second order upwind, each simulation was further iterated in order to increase its accuracy. Results were saved when the total number of iteration was reached to 10000 in number. In table 4.4, the change in residuals with respect to number of iteration is given.

Table 4.4: Change in Momentum Residual during Iterative Study

Number of Iterations	Exp 1	Exp 2	Exp 3	Exp 4
Momentum Convergence - 750	3.71E-07	4.26E-07	4.92E-07	8.70E-08
1st Order -Default URL - 2000	8.08E-06	1.25E-05	1.16E-05	1.41E-05
1st Order - Reduced URL - 3000	3.37E-06	5.40E-06	4.86E-06	6.15E-06
2nd Order - Reduced URL -10000	3.77E-06	5.97E-06	5.35E-06	6.79E-06

After completing the iterative study, results were analyzed by FLUENT post-processing tools. In the following section, each solution method will be presented and compared with the experimental data.

4.1.3 Validation of Model 1 (Small diameter Tube in Tube HX): Fluent Post-processing

In the experimental study, temperature changes were presented according to measured points and their averages such as; $T_{hot-avg}$, $T_{wall-avg}$, T_{hot-in} , $T_{hot-out}$ etc. Based on these temperature profiles, heat transfer rates ($\dot{Q}$) and related heat transfer coefficients (h) were tabulated for each Reynolds number. In order to provide a sound comparison between computational and experimental results the following data reduction was applied.

1. Since each fluid region was defined in 3D, volumetric integration was required on averaging the entire zone properties. In addition, during each simulation, cell mass flow rates were affected by volume temperatures due to variable fluid density. Thus, for the hot fluid zone average fluid temperature was obtained by using "Mass-Weighted Average" option in FLUENT, which calculates the average temperature by dividing the summation of the product of each cell density (ρ_i) , cell volume (V_i) and its temperature (T_i) by the summation of the product of cell density and volume as:

Mass-Weighted Average (volumetric):

$$T_{fluid-avg} = \frac{\int T\rho dV}{\int \rho dV} = \frac{\sum_{1}^{n} T_i \rho_i |V_i|}{\sum_{1}^{n} \rho_i |V_i|} \qquad (4.4)$$

2. Similar to fluid volume, fluid inlet and outlet average temperatures were calculated based on mass flow rate. In addition, since the boundaries were consisted of face surfaces, temperatures were averaged by dividing the summation of the product of each cell temperature and dot product of face area ($\vec{A}_i$) and momentum vectors ($\vec{v}_i$) by summation of the dot product of face area vector and it momentum flux as:

Mass-Weighted Average (area): $$T_{inlet/outlet-avg} = \frac{\int T\rho\left|\vec{v}.d\vec{A}\right|}{\int \rho\left|\vec{v}.d\vec{A}\right|} = \frac{\sum_1^n T_i\rho_i\left|\vec{v}_i.\vec{A}_i\right|}{\sum_1^n \rho_i\left|\vec{v}_i.\vec{A}_i\right|} \quad (4.5)$$

3. For the solid surface, however, properties and the motion of the solid region were stationary. Therefore, average surface temperature was obtained by dividing the summation of the surface face temperature and its area (A_i) by the total surface area (A) as:

Area-Weighted Average: $$T_{surface-avg} = \frac{1}{A}\int TdA = \frac{1}{A}\sum_1^n T_i \left|A_i\right| \quad (4.6)$$

4. Then, substituting the averaged inlet and outlet temperature values ($T_{hot-in}, T_{hot-out}$) with given mass flow rate ($\dot{m}$) and calculating the specific heat (Cp) at the inlet temperature, overall heat transfer rate of hot fluid flow was obtained as:

Heat transfer rate: $$\dot{Q} = \dot{m}\ Cp\ (T_{hot-in} - T_{hot-out}) \quad (4.7)$$

5. Finally, by dividing the heat transfer rate by the multiplication of total surface ($A_{surface}$) heat transfer area and fluid to surface temperature difference, heat transfer coefficient (h) was evaluated as:

Heat transfer coefficient: $$h = \frac{\dot{Q}}{A_{surface}(T_{fluid-avg} - T_{surface-avg})} \quad (4.8)$$

By following these five steps, overall heat transfer rate and related heat transfer coefficients were calculated for each set of experimental conditions of tables 4.2 and 4.3. Comparative results are presented in tables 4.5 and 4.6., and the discrepancy between my FLUENT program and experimental data is plotted in figure 4.2.

Table 4.5: Comparisons of Computational Heat Transfer Coefficient with Experimental Data:

Exp	Re_{Dh}	$h_{avg\,\exp}$ [btu/hr-ft2-F]	$h_{avg\,FLUENT}$ [btu/hr-ft2-F]	Difference %
1	11300	216	205	5.1
2	13700	254	238	6.3
3	19300	300	292	2.6
4	25300	388	376	3.2

Table 4.6: Comparisons of Computational Heat Transfer Rate with Experimental data:

Exp	Re_{Dh}	$Q_{\exp}$ [btu/hr]	Q_{FLUENT} [btu/hr]	Difference %
1	11300	20700	21299	2.9
2	13700	23800	23776	0.10
3	19300	25400	26811	5.6
4	25300	25800	26628	3.2

Compared to experimental studies, computational results in FLUENT solver was provided a good agreement in thermal analysis of annular tube in tube parallel flow heat exchanger. In FLUENT solver the maximum error was obtained 6.3 % for the heat transfer coefficient calculation. As it can be seen in figure 4.2, similar trend as the

experimental data was observed for the heat transfer coefficient if the Reynolds number increases from 10^3 to $25x10^3$. In my FLUENT program the overall heat transfer capacity was calculated for each Reynolds number and the comparison with the experimental values indicated the maximum deviation as 5.6 %.

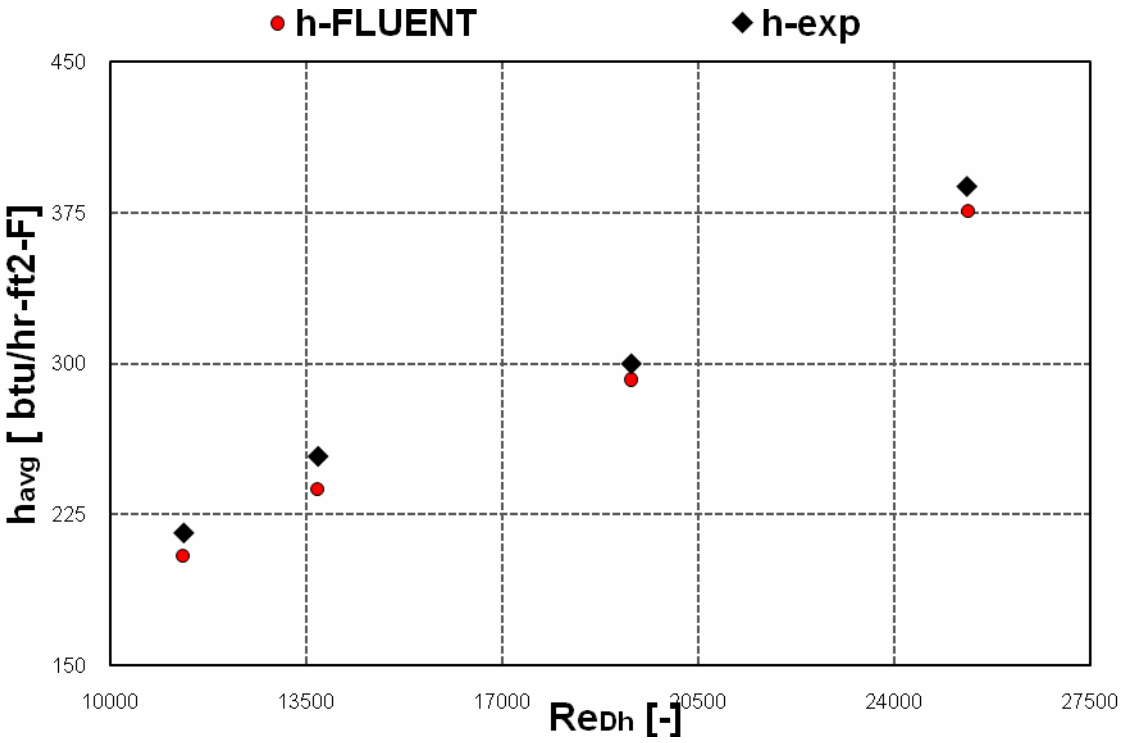

Figure 4.2: FLUENT Validation of Model 1: Average Heat Transfer Coefficient of Parallel Flow inside small diameter Tube in Tube Heat Exchangers

4.2 Validation of Model 2: Convective Single Phase Heat Transfer Rate in Fluid Flow inside Microchannel Tubes

Beside fluid to fluid heat transfer analysis, additional validation was required to test my FLUENT program in terms of its capability in simulation of micro-scaled fluid flow and

it thermal performance in laminar region. Peng and Peterson's experimental study (1996) their empirical correlation (Eq-2.5) were used for this validation.

Peng and Peterson's correlation: $$Nu = 0.1165\left(\frac{D_h}{W_c}\right)^{0.81}\left(\frac{H}{W}\right)^{-0.79} \mathrm{Re}_{Dh}^{0.62} \mathrm{Pr}_f^{1/3}$$

During their study, twelve different heat transfer plates were designed for the experimental set up and each plate had certain geometry characteristics. The hydraulic diameter ranged between 0.15 to 0.343 mm, and laminar, single phase water flow was investigated. In figure 4.3, which was presented in Peng and Peterson's study (1996), experimentally measured Nusselt numbers at each plate and the resultant correlation is shown.

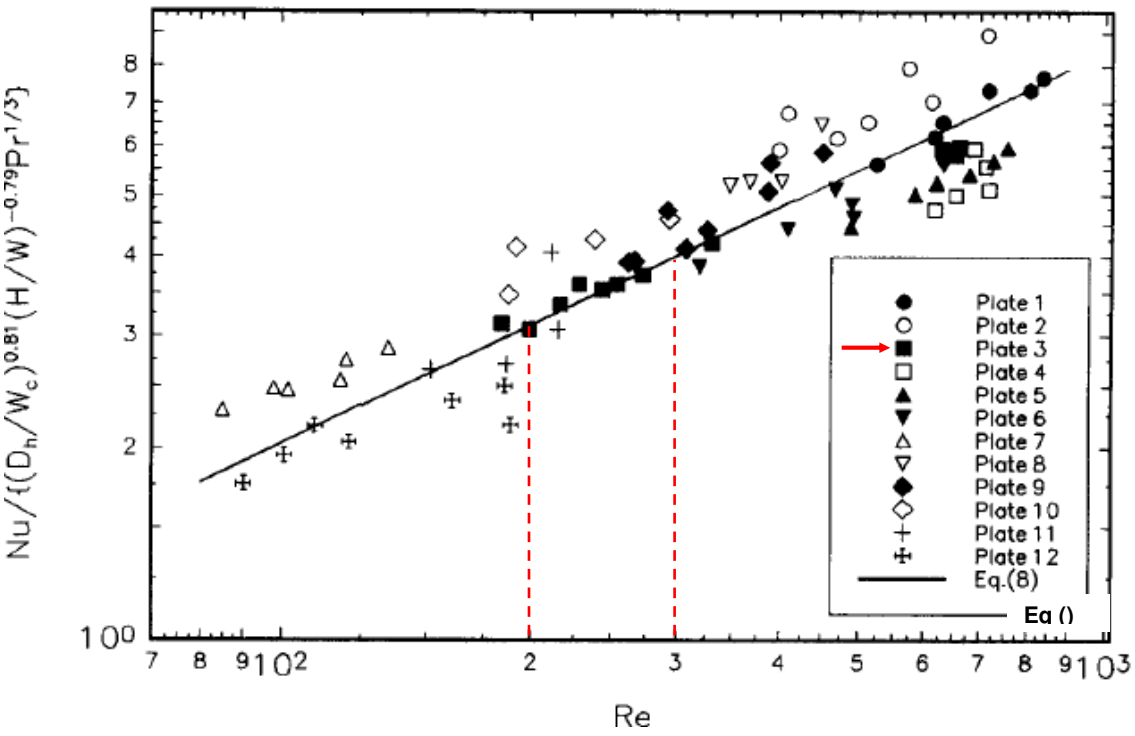

Figure 4.3: Peng and Peterson's Experimental Results (1996) on Convective Heat Transfer Nusselt Number in Single Phase Fluid Flow inside Microchannel Tubes

According to figure 4.3, it was obtained that the equation 2.4 has its highest accuracy on experimental measurements of "plate-3" within the Reynolds number range of 200 to 300. Therefore, by using plate-3's geometry and evaluating the initial conditions within the same Reynolds number range, five cases were studied using my FLUENT program to validate the accuracy of mesh and solver approach.

4.2.1 Validation of Model 2 (Convective Single Phase Heat Transfer Rate inside Microchannel Tubes): Gambit Pre-Processing and Boundary Conditions

Similar to first validation model, a sectional geometry was created according to plate-3's geometric specifications which are listed in table 4.7. In order to increase the accuracy on fluid flow simulation in microchannels, finer mesh quality was created on port faces based on plate-3's port aspect ratio, H/W =0.75. On solid surface, however, due to its stationary position, higher grid size was used to have an efficient computational model. Figure 4.4 illustrates the geometry and grid size differences between two faces.

Table 4.7: Geometric Parameters and Node Numbers of Validation of Model-2

Parameter	Length [mm] (Peng et al. , 1996)	Node Numbers
W	0.4	16
H	0.3	12
W_c	2	80
W_t	18	360
L	45	30

Mass flow inlet and pressure outlet boundary conditions were used to define inlet and outlet boundaries in microchannel flow. To simulate the complete geometry,

symmetry axes were used at the sectional walls. After assigning the solid and fluid volumes, pre-processing was completed by writing VALIDATION2.msh file in Gambit. Corresponding journal file is presented in appendix A-2.

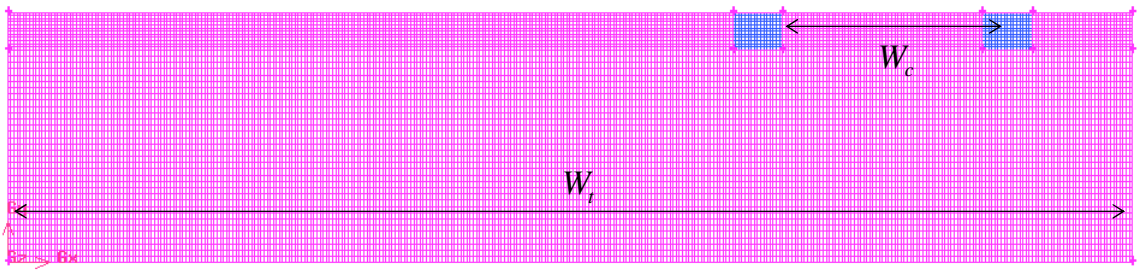

(a) Partial geometry of plate-3

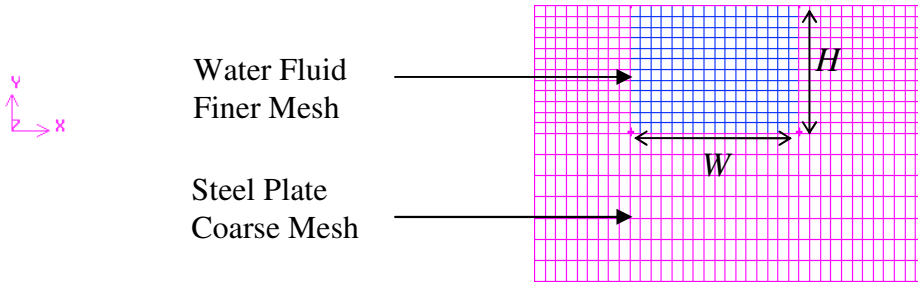

(b) Face mesh quality

Figure 4.4: Geometric Variables of Validation of Model-2 (Convective Single Phase Heat Transfer Rate inside Microchannel Tubes)

4.2.2 Validation of Model 2 (Convective Single Phase Heat Transfer Rate inside Microchannel Tubes): Fluent Solution

According to Peng and Peterson's experimental procedure (1996), FLUENT solver was used to create 5 different cases within the Reynolds number from 200 to 300. These case studies are similar to my CFD models which will be developed for microchannel heat exchangers. Thus, this validation study will help me to verify my FLUENT code based on its applicability and accuracy of the meshing techniques and its CFD solver approach for micro-structures.

In order to define suitable initial parameters, some prior calculations were required. First, water mass flow rate was calculated based on given Reynolds number as:

$$\dot{m} = \frac{\mathrm{Re}\, A_{port} \mu}{D_h} \tag{4.9}$$

where D_h is the hydraulic diameter: $D_h = \frac{4(cross-\sec tion\ area)}{wetted\ \ perimeter} = \frac{2WH}{W+H}$ (4.10)

For pressure outlet boundary condition, the Darcy–Weisbach correlation, equation 4.2, was used to estimate the pressure loss and the friction factor was estimated according to the correlation in laminar flow $f = \frac{64}{\mathrm{Re}_{mc-tube}}$, where Re*mc-tube* is the Reynold number calculated based on the flow inside one port of the tube This approach to estimate the pressure loss inside microtubes was previously suggested in Lelea et al.'s study (2004). It provided good estimates of the main pressure losses of laminar fluid flow inside microchannel tubes, expecially if the tube is heated for its entire length.

Table 4.8: Initial Conditions of Each Simulation Based on Reynolds Number:

Simulation	Re_{Dh}	$\dot{m}$ [kg/s]	P_{gauge} [Pa]
1	200	7.04E-05	7244.16
2	225	7.92E-05	8149.68
3	250	8.80E-05	9055.19
4	275	9.68E-05	9960.71
5	300	1.06E-04	10866.23

In Peng et al.'s experimental study (1996), microchannel heat exchanger plate was heated by an electrical heater which provides low voltage (V) and high electric current (I). Since the plate has a uniform cross-sectional area, the heat flux along the plate was assumed to be to be uniform and calculated as:

$$\overset{"}{q} = \frac{Q}{A_{plate}} \tag{4.11}$$

Where the total heat input and plate area were defined as:

$$Q = I \times V \tag{4.12}$$

$$A_{plate} = W_t L \tag{4.13}$$

According to the experimental study, voltage and electric current were selected as V =0.15 [V] and I =50 [A]. Then, by using above equations (4.11, 4.12, 4.13), resultant heat flux was obtained as $\overset{"}{q}$ = 9259.26 [w/m^2] and applied to the lower surface of the plate as a constant heat flux boundary.

Additionally, based on the experimental procedure, the port inlet fluid temperature was selected as $T_{port-in}$=293 [K]. In order to investigate the sudden temperature change effect on fluid thermal properties in microchannel, fluid properties were defined as a polynomial function of temperature.

Once all the boundary conditions were set, each validation model was initialized by port inlet values and iterative study was started. In order to reach convergence in the iterative study, URL factors of momentum and pressure equations were decreased gradually to decrease the residuals. In addition, second order upwind discretization was

applied to increase the accuracy of the results. In the following section, these iterative results will be analyzed and compared with Peng et al.'s experimental correlation.

4.2.3 Validation of Model 2 (Convective Single Phase Heat Transfer Rate inside Microchannel Tubes): Fluent Post-processing

The aim of second validation model was to obtain a computational Nusselt number by FLUENT and compare it with Peng et al.'s experimental correlation. In the paper, log mean temperature difference (LMTD) method was suggested to evaluate the average temperature difference between channel wall and fluid flow. Therefore, during pos-processing, similar data reduction was applied to have a reasonable comparison.

$$\Delta T_m = \frac{\Delta T_{in} - \Delta T_{ex}}{\ln\left(\Delta T_{in} \big/ \Delta T_{ex}\right)} \tag{4.14}$$

where;

$$\Delta T_{in} = T_{wall-in} - T_{fluid-in} \tag{4.15}$$

$$\Delta T_{ex} = T_{wall-ex} - T_{fluid-ex} \ . \tag{4.16}$$

To evaluate LMTD method, local temperatures were needed such as; $T_{wall-in}, T_{wall-out}$ etc. By using Fluent "XY Plot" post-processing tool water fluid and wall temperatures were plotted along microchannel length, *L*. In 3D simulation, plotted local values were calculated at the x-y faces along the z direction. Therefore, at each z location resultant values, which were equal in number of grid points, were presented in x-y plot. By writing plotted values in data files, results were averaged in Excel spreadsheet based on number of points and comprehensible temperature profiles were obtained for each

simulation. In Figure 4.5, (a) shows the FLUENT x-y plot results and (b) gives the averaged Temperature profile which is plotted Excel spreadsheet.

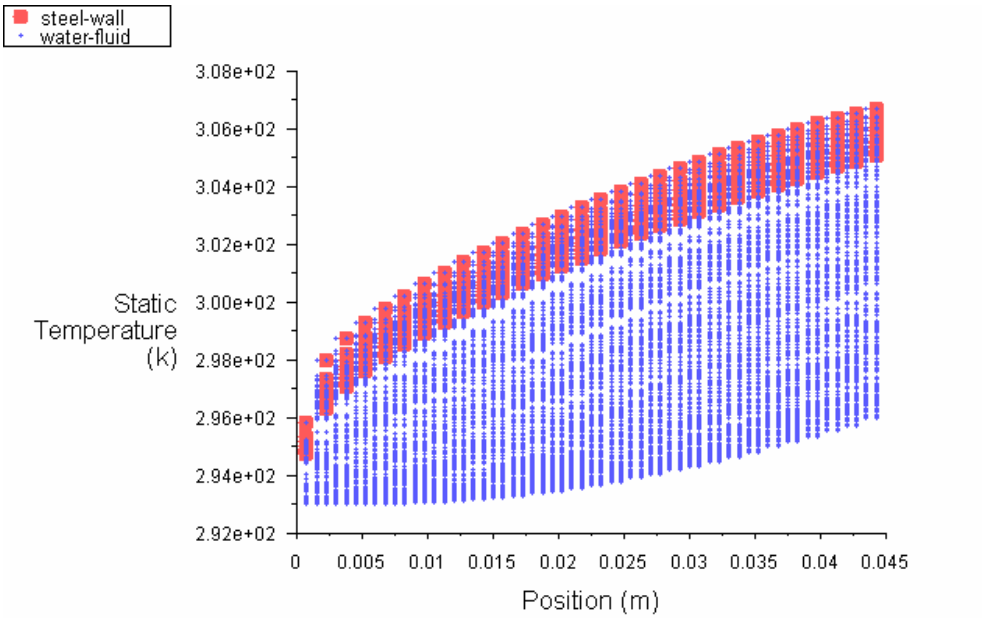

(a) FLUENT x-y

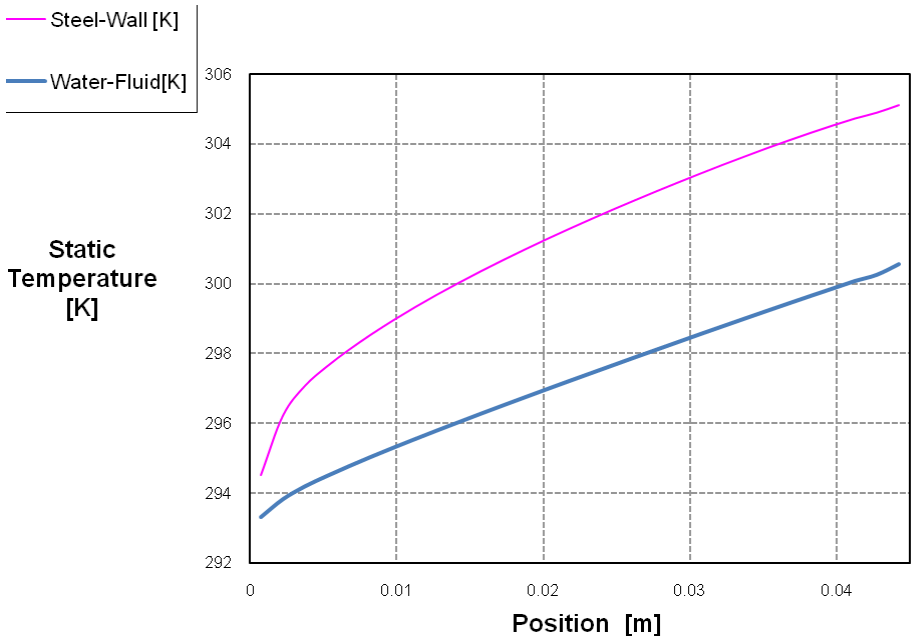

(b) Averaged Temperature plot of FLUENT xy plot (a)

Figure 4.5: Temperature Profile along Fluid Flow Direction of Validation of Model-2 (Convective Single Phase Heat Transfer Rate inside Microchannel Tubes)

In addition to number of point averaging, further calculations were required for the wall temperature analysis. During its flow, water was in contact with four different channel surfaces. Since the top wall of the plate was isolated, two side walls and the bottom wall were considered as convective surfaces and the resultant average wall temperature was evaluate as:

$$T_{wall-avg}(z) = \frac{T_{swall-side1}(z) + T_{wall-btm}(z) + T_{wall-side2}(z)}{3} \tag{4.17}$$

Then, by using averaged local temperature profiles, overall heat transfer coefficient and averaged Nusselt number were calculated for each simulation as:

$$h_{avg} = \frac{q''}{\Delta T_m} \tag{4.18}$$

$$Nu_{avg} = \frac{hD_h}{k} \tag{4.19}$$

where k is the thermal conductivity of water which was evaluated by EES at inlet temperature : k= 0.59 [w/m-K] at $T_{inlet-fluid}$=293 [K].

Computational resultant values and corresponding Peng and Peterson's experimental correlations of Nusselt numbers are given in table 4.9. Based on correlated data points, percentage differences were calculated to measure the accuracy of computational results. In addition, the increase in Nusselt number with respect to the increase in Reynolds is shown in figure 4.6 and compared with Peng and Peterson's work.

Table 4.9: Comparisons of Computational Nusselt Number with Experimental Data:

Exp	Re_{Dh}	$Nu_{avg\,exp}$ [-]	$Nu_{avg\,FLUENT}$ [-]	Difference %
1	200	1.81	1.95	7.8
2	225	1.94	2.01	3.5
3	250	2.07	2.07	0.1
4	275	2.20	2.14	2.9
5	300	2.32	2.50	7.8

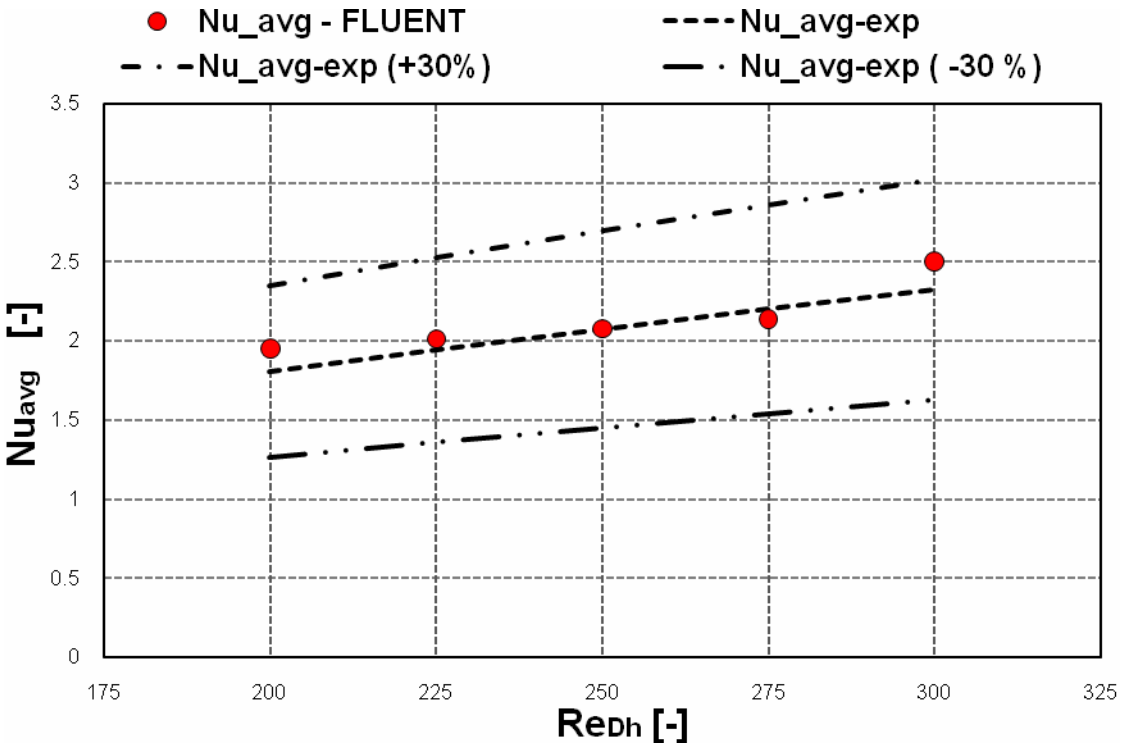

Figure 4.6: Experimental and Averaged Numerical Nusselt Number of Validation of Model-2 (Convective Single Phase Heat Transfer Rate inside Microchannel Tubes)

As it can be seen both in table 4.9 and figure 4.6, FLUENT provides a good agreement with Peng and Peterson's experimental correlation, for which the authors reported approximately ±30% accuracy deviation with their experimental data. Between

Peng and Peterson's predictions and the estimates of the average Nusselt number given by the FLUENT code of this work, the differences were within 7.8 %.

4.3 Validation Study Conclusion

According to previous experimental studies, FLUENT solver was validated and results were in agreement with experimental analysis within an error in the range from 0.1 to 7.8%. Therefore, it is concluded that the meshing technique and the my numerical solution method applied trough the Gambit and FLUENT programs can provide coherent results for micro-scaled fluid to fluid thermal analysis typical to microchannel heat exchangers. In addition, each validation model helped to create an iterative study technique and to understand both pre and post processing methods.

CHAPTER V

Analysis of the Refrigerant Side Convective Heat Transfer Coefficient for Microchannel Tubes inside a Counter Flow Tube Heat Exchanger

In literature, there are several methods available to evaluate the heat transfer coefficient or the Nusselt number for fin and tube heat exchangers. For microchannel tube, however, there is not a comprehensive well known theory to calculate the thermal performance as the methods available for conventional fin and tube heat exchangers. Before designing a round microchannel tube model in my study, I would like to develop a method to measure heat transfer parameters of commercially available round tube and straight microchannel tube geometries and compare the similarities and the differences if any between different geometries. For this reason, I numerically investigated the refrigerant side heat transfer coefficient and the air side heat transfer coefficient separately and independently from each other. Then, I combined the results from each side to estimate the overall performance.

In this chapter, refrigerant side heat transfer characteristics were studied by simulating a tube in tube counter-flow type heat exchanger, similar to actual tube calorimeter apparatus, which is commonly used for experimental data. By using FLUENT CFD solver, a computational 3D virtual domain was created to test each heat exchanger tube in terms of its internal cooling capacity. As a test simulation, tube in tube

counter flow heat exchanger configuration was conducted by my FLUENT code. Since the counter flow design provides higher temperature difference between hot and cold fluids, I could analyze the maximum heat transfer capacity of heat exchanger tubes with my FLUENT model.

Based on Padhmanabhan et al's study (2008) conventional size round tube and straight microhannel tube geometries were created in computational domain. In addition, identical single phase, laminar, counter flow, water jacket was simulated around each tube as a test environment. By doing so, every heat exchanger tube's cooling effect was measured according to the changes within the surrounding water jacket flow and iterative results were compared to identify heat exchangers internal thermal performance. In this section, first the test simulation procedure and then corresponding round tube and straight microchannel tube 3D counter flow studies are discussed respectively.

5.1 Counter Flow Heat Exchanger Simulation Procedure

As it mentioned earlier, Padhmanabhan et al.'s work (2008) was selected as a reference study to define the heat exchanger tube geometries and to set boundary conditions. For the outer water jacket, a suitable design was required in order to have a reasonable comparison. According to commercially available products, I defined a counter flow heat exchanger model, which could be applicable in FLUENT solver. Within my code following geometric parameters and previously validated assumptions were applied to simplify the Navier Stokes continuity, momentum, and energy equations:

1. The material and the diameter of the water jacket were defined by commercially available product of aluminum tube with 30mm diameter.

2. Since the tube length of L_{tube} =1.2 m is longer than the hydrodynamic entrance region (L_h) based on Langhaar et al.'s correlation (1942) given in the textbook (Introduction to Heat Transfer, Incropera et al.,2007) water flow was assumed to be fully developed and laminar. The L_h value was obtained according to Re_{Dh} and D_h as:

$$L_h \cong 0.05\,\mathrm{Re}_{Dh}\,D_h \tag{5.1}$$

3. Isolating the outer water jacket surface, radiation heat transfer and natural convective heat transfer are neglected

Additionally;

1. Incompressible flow
2. Steady state process
3. No slip at the wall
4. Negligible body forces assumptions were further applied to simplify continuity equations.

As it illustrated in figure 5.1, counter flow heat exchanger configurations were simulated in FLUENT by inserting round tube and straight microchannel tube in to an identical counter water flow. Within laminar region, water jacket was cooled by and local changes in its thermal properties along tube length (L_{tube}) were reported.

In this study, a 3D computational domain was used for the refrigerant side microchannel tubes. A 3D model is necessary because neither the geometry nor the thermal fluid conditions are axialsymmetric. If a 2D longitudinal cross section of the microchannel tube is selected as computational domain, the inner ports along heat

exchangher tube would not be able to directly exchange any heat transfer rate with the jacket water. Only the first and last ports at the top and bottom of the tube, respectively, would exchange heat with the water jacket. The others ports of the tubes would receive heat by conduction only through the top and bottom sections. Depending on the boundary conditions imposed to the microchannel tube with internal ports in it and on the algorithm used to estimate the heat transfer rates of the entire microchannel tube from the results of a 2D model, the calculated heat transfer rates for the entire microchannel tube in the tube shell were in a wide range of values. I did not find a consistent methodology to estimate the heat transfer rate of the entire microchannel tube from the predictions of a 2D model and I was unable to identify a general and physically sound algorithm to transfern the information from the 2D cases to the 3D geometry of the tube with microchannel ports in it. The predictected heat transfer rates would depend strongly on the post-processor operations (averaging and integration) and on boundary conditions imposed to the 2D cases. To overcome this ambiguity, I decided to opt for a 3D approach and I use a simplified geometry of the microchannel tube in the water jacket shell. While a 2D approach could be used in axialsymmetric flows such as the one inside a single round tube, a 3D model was required if microchannel ports are present inside the tube. In the next sections each heat exchanger tube simulation model will be discussed in details.

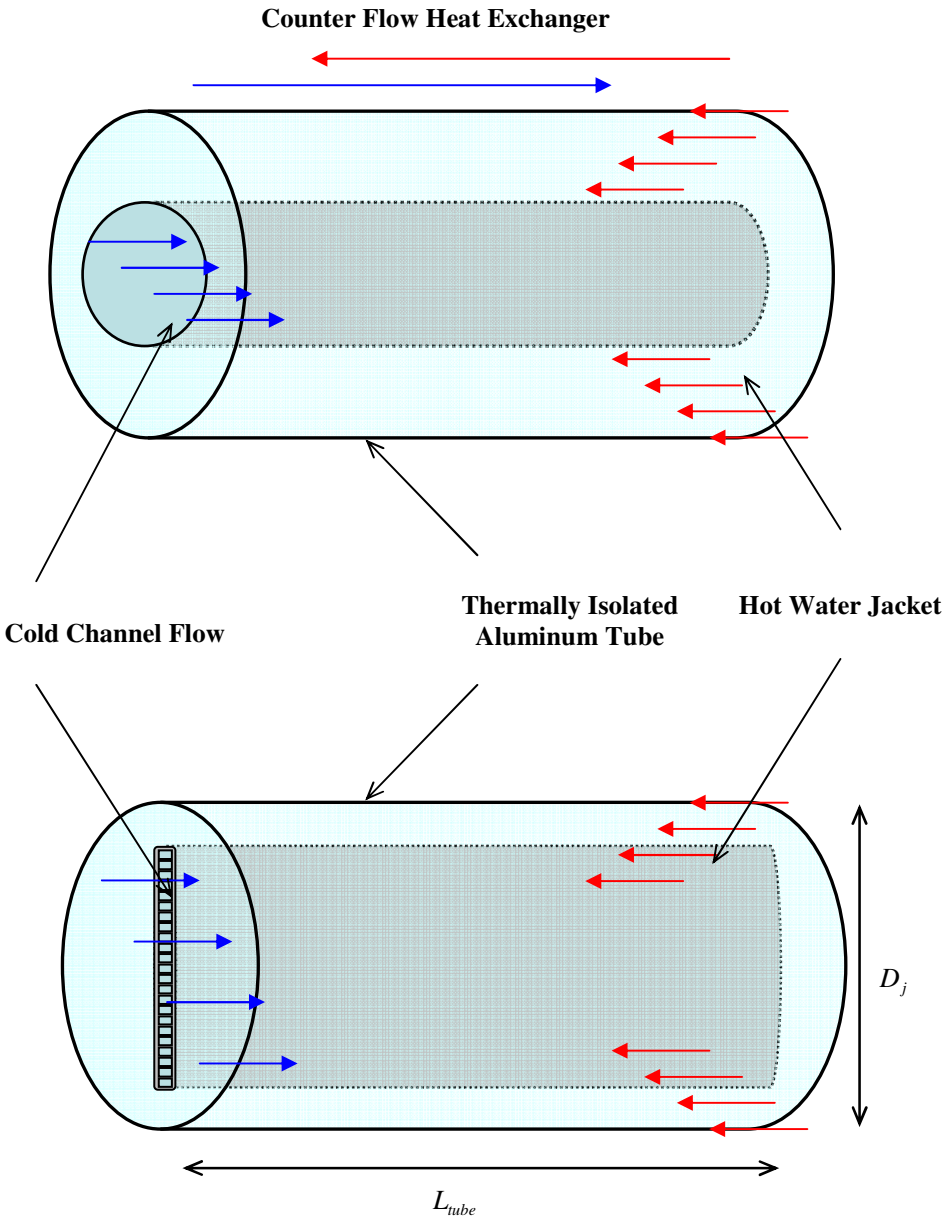

Figure 5.1 Sketches of the Counter Flow Tube Heat Exchanger with Full Round Tube (no microchannel) inside (top) and with one Straight Microchannel (SMC) Tube inside (bottom)

5.2 Model 1: Full Round Tube (no microchannel) inside Counter Flow Tube Heat Exchanger

5.2.1 Model 1: Gambit Pre-Processing and Boundary Conditions

Similar to "Validation of Model 1", quarter geometry was created by using symmetry boundary conditions. Additionally, equally spaced grid points were applied based on round tube's inner radius ($R_{Round-Tube\ in}$) and jacket radius (R_{jacket}) to round tube thickness ($t_{Round-Tube}$) ratio respectively. For the arc length, round tube outer length ($L_{Round-Tube}$) to channel thickness ratio was applied to create equal tangential grid spacing.

Grid dependency study was required to eliminate the grid distance effect in the iterative results, thus three different grid qualities were created by decreasing the grid distance accordingly. In table 5.1 number of node points (N_{Node}) and geometric properties are tabulated for each grid quality (coarse, medium and fine). Based on this table, Gambit journal files were generated and an example is presented in appendix B-1. Resultant mesh qualities for each grid study are presented in figure 5.2 respectively.

Table 5.1: Model 1, Geometric Specifications and Node Numbers

Geometry	Length [mm]	Coarse- N_{Node}	Medium - N_{Node}	Fine - N_{Node}
$R_{Round-Tube\ in}$	4.84	48	64	80
$t_{Round-Tube}$	0.30	3	4	5
$D_{h\ jacket}/2$	9.86	98	130	162
$L_{Round-Tube}$	8.08	24	32	40
L_{tube}	1200	30	40	50

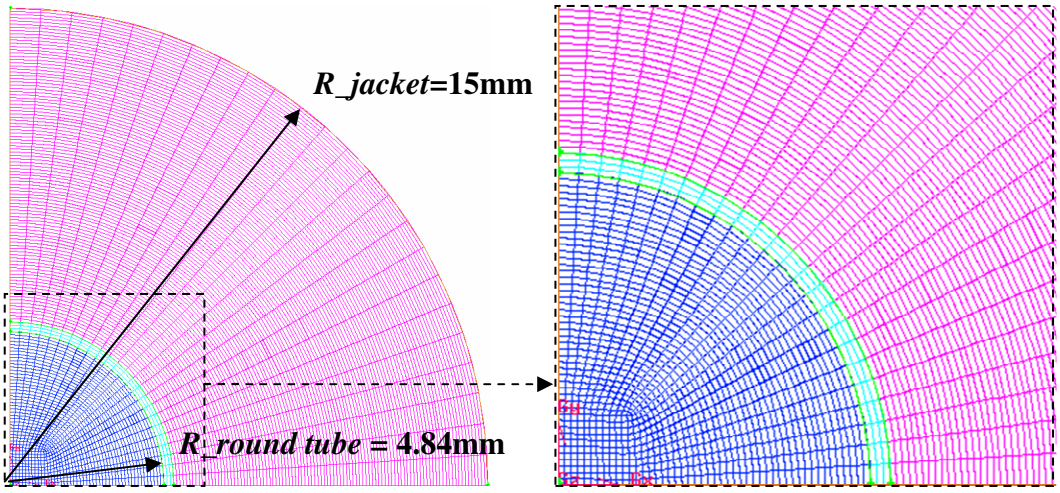

(a) Coarse Meshing (48x98 elements)

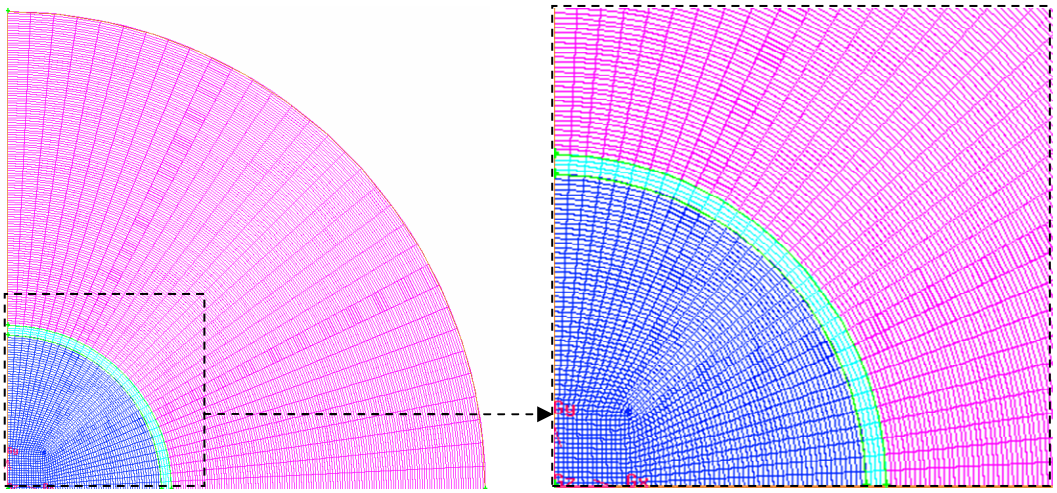

(b) Medium Meshing (64x130 elements)

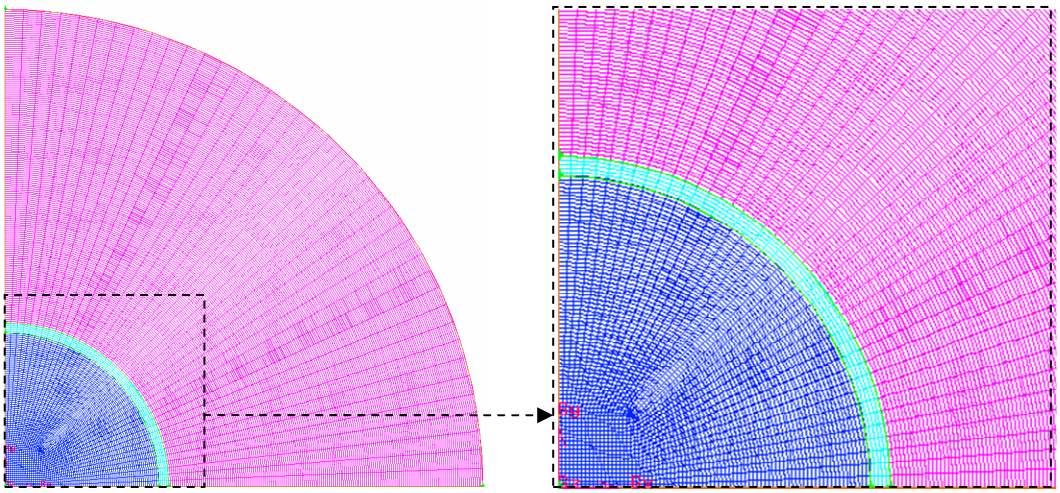

(c) Fine Meshing (80x162 elements)

Figure 5.2: Model 1, Face Mesh Qualities of Grid Study 1, 2 and 3

5.2.2 Model 1: Fluent Solution

In order to have a comparable simulation model it was important to represent fin and tube working condition precisely in FLUENT solver. Based on Johnson Control Inc.'s 4 ton heat pump system data for fin and tube heat exchanger, I calculated the round tube mass flow rate ($\dot{m}_{Round-Tube}$) by dividing the given fin and tube refrigerant mass flow rate ($\dot{m}_{Fin-Tube}$) in to its total circuit's number ($N_{circuit}$) , 0.12kg/s and 6 respectively, as :

$$\dot{m}_{Round-Tube} = \frac{\dot{m}_{Fin-Tube}}{N_{circuit}} \tag{5.2}$$

For the outer water jacket, I selected the mass flow rate according to critical Reynolds number for laminar region constrains for cylindrical tubes (Re_{lamiar}<2300) and kept it constant in each counter flow heat exchanger simulation. Additionally, round tube and outer water jacket initial temperatures were defined based on indoor and outdoor test conditions of Padhmanabhan et al.'s experimental study (2008), which were 70 ^{o}F and 32/36 ^{o}F, respectively. Resultant initial conditions are listed below in table 5.2.

Table 5.2: Model 1, Initial Conditions

	T_{in} [^{o}K]	V [m/s]	$\dot{m}$ [kg/s]	Re	f	P_{gauge} [Pa]
Tube	274.7	0.27	0.02	1560	0.041	187
Jacket	323	0.03	0.02	1152	0.056	1.76

In order to have a practical CFD solution, FLUENT journal files were written by using the tabulated boundary conditions. An example journal file for this study is

presented in appendix E-1. Moreover, as it mentioned in Chapter 2, temperature dependent thermal properties were used for water. Additionally, an identical iterative procedure, which was developed in previous validation studies, was applied for each grid quality. In my FLUENT code first the residual of each equation was set to E-06 convergence requirement, and only momentum equation was applied in order to reach fully developed velocity profile. After its convergence, energy equations were included into the solver and further iterations were applied by reducing pressure and momentum under relaxation factor gradually. Final results were recorded by using second order discretization solver.

Compared to other equations, the highest residual value was obtained in momentum equation results. In addition, in smaller grid distance, this value was reduced to E-05 level. Based on same iterative procedure with all meshing qualities, momentum residual values and corresponding iteration times are presented in table 5.3.

Table 5.3: Model 1, Grid Dependency Study Residual Comparison

Mesh Quality	Momentum Residual	Number of Iterations	Iteration Time
Coarse	5.0E-06	1200	4:48
Medium	1.1 E-05	12588	8:14
Fine	1.8 E-05	13300	19:47

First, by comparing iterative results, the most computationally efficient meshing quality was selected. Then, by using the optimum meshing further iterations were applied until the momentum residual converges to E-06 level. By doing so, Model 1 FLUENT

simulation was completed and iterative results were saved. In the following section, these results are presented in details by using FLUENT post processing tools accordingly.

5.2.3 Model 1: Fluent Post-processing

In this study my aim was to report the cooling effect of round tube heat exchanger inside a counter flow water jacket. Thus, heat transfer properties were measured from the jacket side of the heat exchanger with each mesh quality to investigate the different grid distance effect in the FLUENT solver results.

First, numerical results were organized by Excel spreadsheet program and each data was stored in different columns. By doing so, I could calculate local values by averaging the numerical results based on number of grid points. Additionally, in order to simplify results and eliminate the measured units in the solution, each local value was non-dimensionalized as:

Non-dimensional Length: $$\xi = \frac{z}{L_{tube}} \tag{5.3}$$

Non-dimensional Temperature: $$\theta(\xi) = \frac{T(z) - T_{\min}}{T_{\max} - T_{\min}} \tag{5.4}$$

Non-dimensional Heat Flux: $$q''^{*}(\xi) = \frac{q''(z)}{q''_{\max}} \tag{5.5}$$

Based on above equations, first the non-dimensional water jacket temperature profile was ($\theta(\xi)_{jacket}$) calculated for each meshing quality and results were presented in figure 5.3. All mesh types could provide similar trend in temperature change, however,

compared to fine mesh quality 2% difference was reported with coarse meshing at the flow exit region. Similarly, dimensionless local heat flux ($q''^{*}(\xi)$) values were evaluated by using equation 5.5 and results were plotted for every meshing quality. By doing so, I investigated the cooling effect in water jacket for each grid study. From figure 5.4, unlike temperature variation, separated curves were obtained at the jacket inlet region. Due to lack of element number, 3.6 % difference was obtained between coarse and fine meshing results at the exit region. Medium meshing on the other hand, showed around 99% similarity with fine meshing in both dimensionless results.

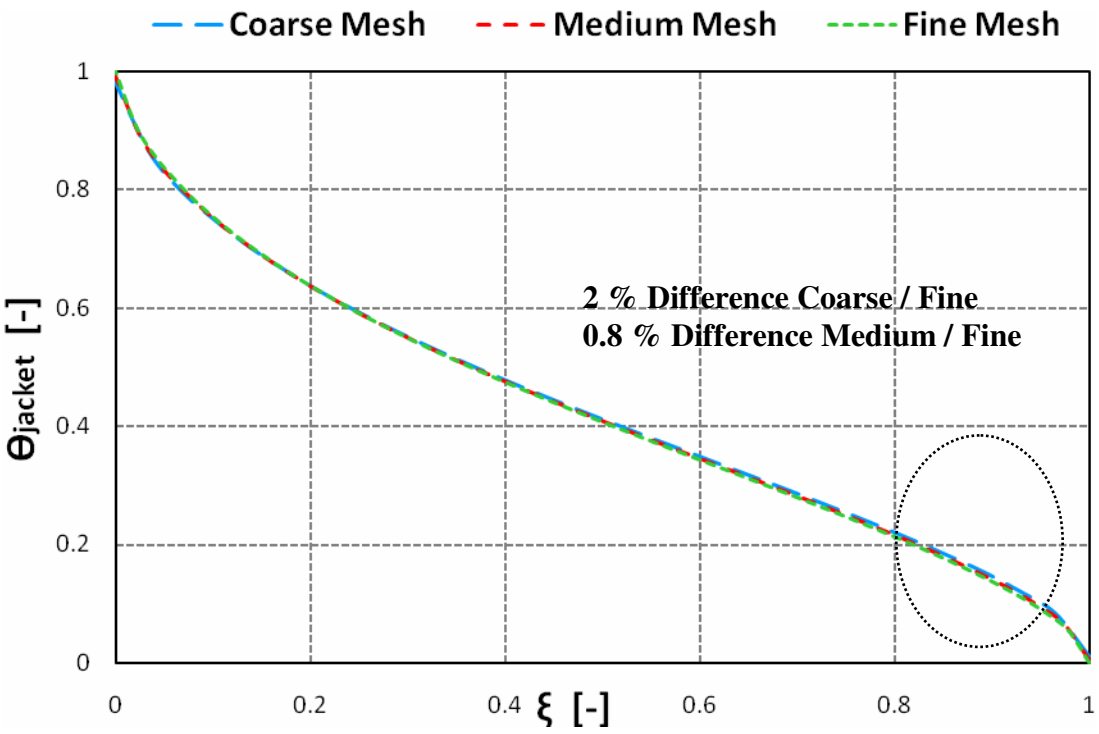

Figure 5.3: Model 1, Grid Dependency Study Dimensionless Temperature Distribution

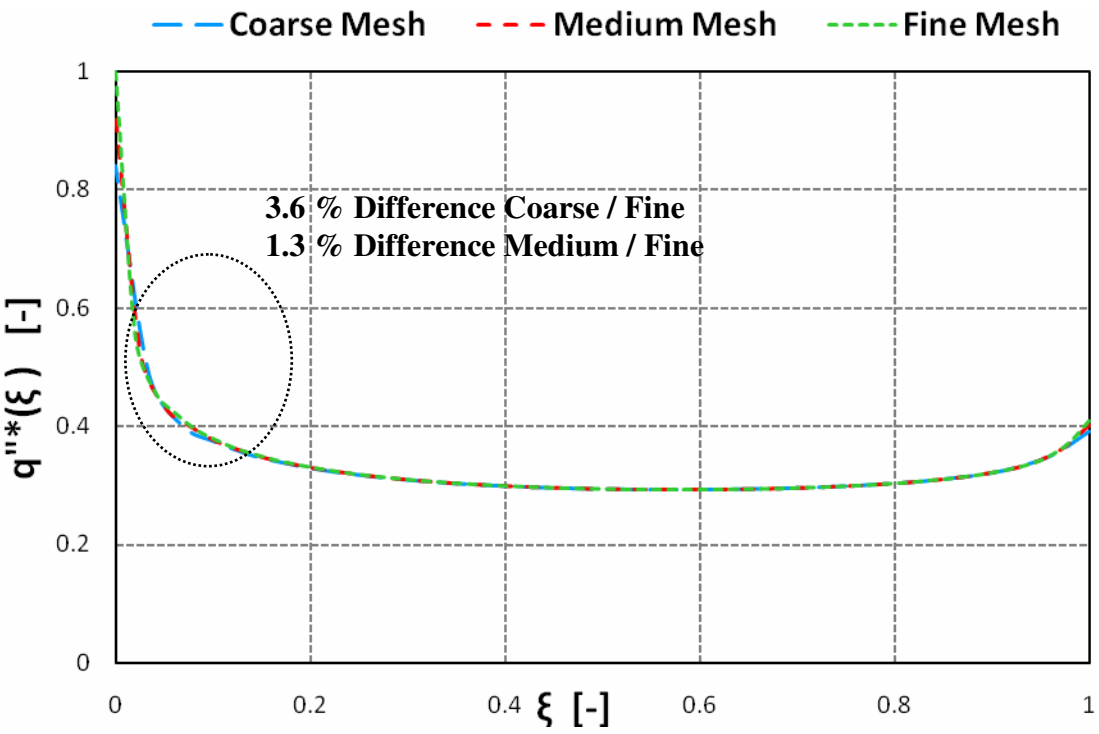

Figure 5.4: Model 1, Grid Dependency Study Dimensionless Heat Flux Distribution

In CFD applications, reducing the grid distance and increasing number of element provide more detailed iterative study which also require additional calculations in computational simulations. In my study, despite its lower grid distance compared to fine meshing, similar results were obtained with medium meshing quality. Additionally, based on residual comparison, medium meshing reached to lower residual value faster than fine meshing. Coarse meshing, on the other hand, showed 2 – 4 % difference in its results. Thus, medium meshing selected as the most computationally efficient and grid independent meshing and it was used for further iterations.

By reducing the under relaxation factor of momentum equation to 0.3, additional iterations were applied until the E-06 convergence requirement was obtained in all residuals. By using FLUENT post-processing tools each local value were obtained and

stored in Excel spread sheet. Based on these converged iterative results, I calculated the average ratio between convective to conductive heat transfer across the round tube jacket ($Nu_{j-FLUENT\ avg}$) by following four step data reduction procedure:

1. Dimensionless local temperature change was calculated by using equation 5.4. As it presented in figure 5.5, temperature difference between water jacket ($\theta(\xi)_{jacket}$) and channel surface ($\theta(\xi)_{wall}$) change was obtained according to counter flow configuration.

2. By applying equation 5.5, non-dimensional local heat transfer rates from water jacket to channel surface ($q''^{*}(\xi)$) were evaluated for each surface node point. Results are presented in figure 5.6.

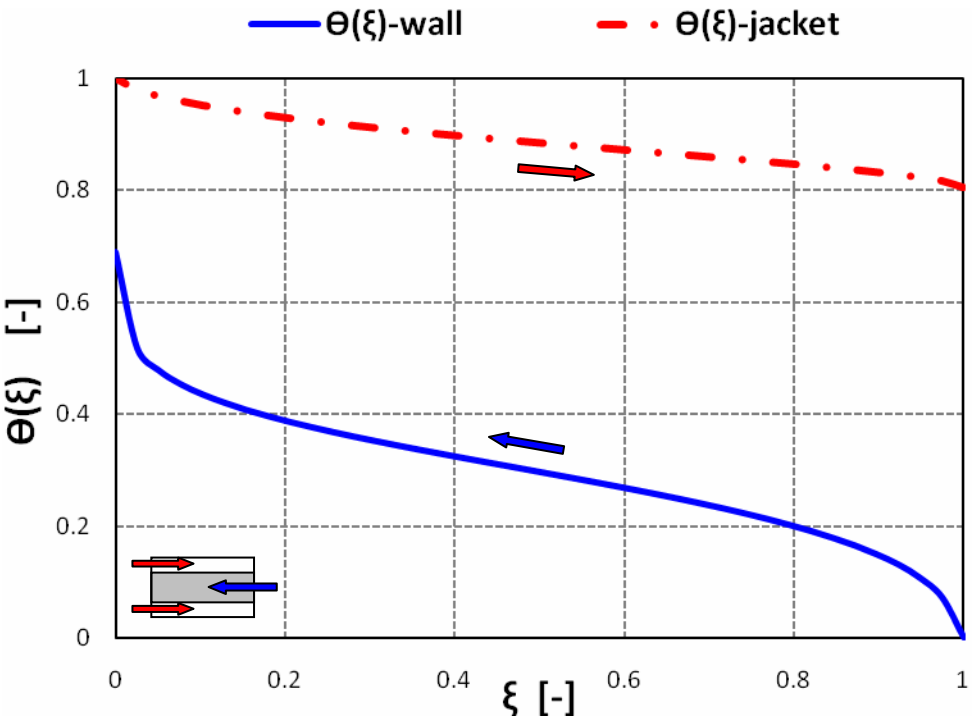

Figure 5.5 : Model 1, Dimensionless Local Water Jacket and Wall Temperatures

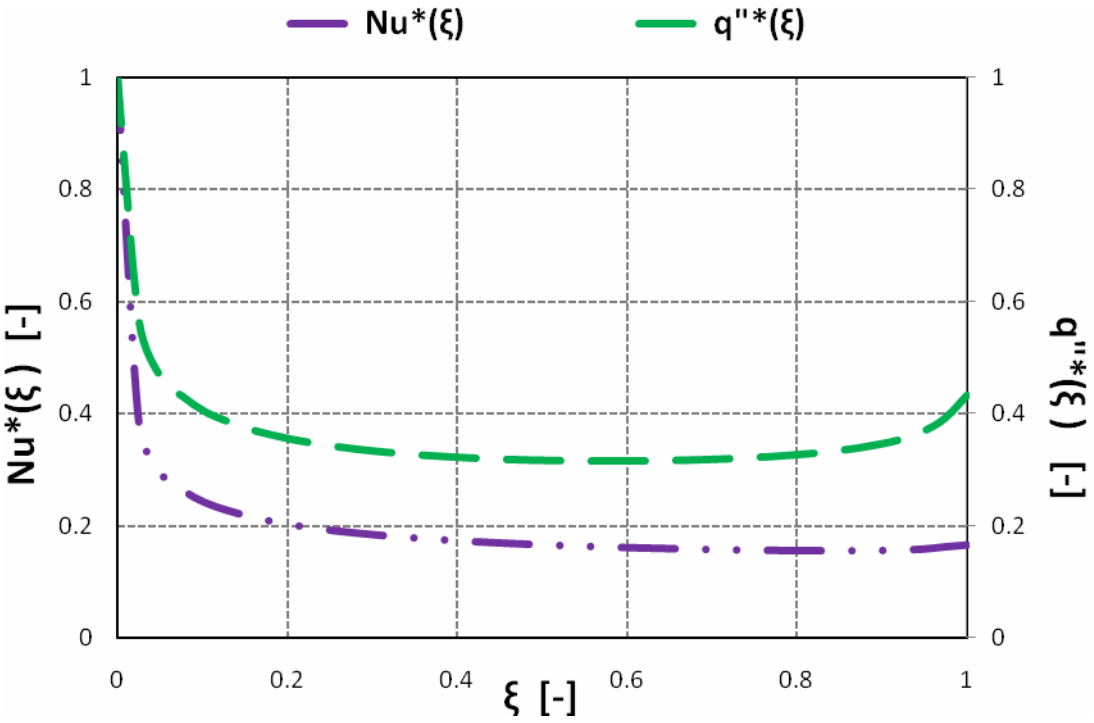

Figure 5.6 : Model 1, Dimensionless Local Heat Flux and Nusselt Number Distribution

Using resultant local $q''^{*}(\xi)$, $\theta(\xi)_{jacket}$ and $\theta(\xi)_{wall}$ values, dimensionless local Nusselt number ($Nu^{*}(\xi)$) variation along the tube length was evaluated as:

Non-dimensional Nusselt Number: $Nu^{*}(\xi) = \dfrac{Nu(z)}{Nu_{\max}}$ (5.6)

where, $$Nu(z) = \left(\frac{q''(z)}{T_s(z) - T_f(z)} \right) \frac{D_h}{k_f} \quad (5.7)$$

Based on equation 5.6 and 5.7, variation of dimensionless local Nusselt number is shown in figure 5.6.

3. Finally, averaged Nusselt number of the jacket was evaluated by numerically integrating the discrete values over the tube length, L. The trapezoidal rule was applied by using previously calculated averaged local Nusselt number values (Eq-5.7) as:

$$Nu_{avg\ jFLUENT} = \frac{1}{L}\int_{Zo}^{Zn=L} Nu(z)dz = \frac{\Delta z}{L}\left[\frac{Nu(z_0)+Nu(z_n)}{2}+\sum_{k=1}^{n-1} Nu(z_k)\right] \qquad (5.8)$$

where, Δz is the equally spaced grid point distance and n is the total number of grid points and resultant average Nusselt number was evaluated as:

$$Nu_{avg\ j-FLUENT} = 10.54$$

4. In order to validate my FLUENT code, I compared my computational results with corresponding Dirker and Meyer's analytical Nusselt number correlation for concentric annuli (2005), as:

$$Nu_{avg\ j-analytical} = C_0\ \mathrm{Re}_{D_h}^{C_1}\ \mathrm{Pr}_f^{\,1/3}\left(\frac{\mu_f}{\mu_{wall}}\right)^{0.14} \qquad (5.9)$$

where;

$$C_0 = \frac{0.003a^{1.86}}{0.063a^3 - 0.674a^2 + 2.225a - 1.157}\ ,\quad C_1 = 1.013e^{-0.067a}$$

$$\mathrm{Re}_{D_h} = \frac{\rho_f V D_h}{\mu_f}\ ,\ D_h = (D_{jacket} - D_{Round\_Tuhe-out})$$

and, $$a = D_{jacket} \Big/ D_{Round\_Tube-out}$$

By calculating volumetric mass weighted average fluid temperature (T_f) and area weighted average channel wall temperature (T_{wall}) in FLUENT solver, corresponding

fluid properties ($\rho_f, \mu_f, \mathrm{Pr}_f$ and μ_{wall}) were defined by using EES library. Then, substituting these variables into given analytical correlation (Eq-5.9), annular jacket side Nusselt number was calculated as:

$$Nu_{avg\ j-analytical} = 9.25$$

The difference between computationally obtained Nusselt number ($Nu_{avg\ j-FLUENT}$) and its corresponding analytical correlation ($Nu_{avg\ j-analytical}$) was reported as 12%. Based on Dirker and Meyer's experimental correlation (Eq-5.9) FLUENT sensitivity analysis was studied and results are presented in the next section.

5.2.3 Model 1: Fluent Sensitivity Analysis

In previous sections the iterative methodology and the data reduction process of my FLUENT code was presented based on given boundary conditions. Before analyzing the calculated results, it was required to investigate the sensitivity of the code and understand which variable effects more the heat transfer performance of the water to water, single phase, laminar, counter flow heat exchanger simulation. Thus according to variation of both jacket and round tube Reynolds number within laminar region, a sensitivity analysis was studied to measure its effect on averaged water jacket Nusselt number.

First, the jacket Reynolds number effect was measured by repeating the same procedure with two different jacket mass flow rates, which resulted higher and lower Reynolds number than initial value ; $\mathrm{Re}_{jacket} = 1084$. Based on iterative results, previously presented four step data reduction procedure was applied to calculate the Nusselt number variations. Additionally, Dirker and Meyer's experimental Nusselt number correlation, which can predict the averaged Nusselt number value in 3%

uncertainty, were used to measure the difference between their analytical solution and my FLUENT code. According to table 5.4, an average 50 % increase in water jacket Reynolds number was enhanced the Nusselt number around 15 %. Compared to experimental correlation, in figure 5.7 a similar trend was obtained in Nusselt number variation with 20% averaged disparity.

Table 5.4: Model 1, Sensitivity Analysis of Jacket Reynolds Number in Heat Transfer

Re_{jacket}	$Nu_{avg\ FLUENT}$	$Nu_{avg\ j-analytical}$
527	8.89	5.11
1084	10.54	9.25
1645	12.26	13.08

Similarly, increase in round tube mass flow rate effect in its cooling performance were investigated by reiterating my FLUENT simulation at different Round tube Reynolds number; $\mathrm{Re}_{Round-Tube}$. Based on table 5.5 an average 35 % change in the round tube Reynolds number could only affect the jacket heat transfer 1.6 %, which was noticed as 1 % in the experimental correlation.

Table 5.5: Model 1, Sensitivity Analysis of Tube Reynolds Number in Heat Transfer

$\mathrm{Re}_{Round-Tube}$	$Nu_{avg\ FLUENT}$	$Nu_{avg\ j-analytical}$
1039	10.49	9.2
1556	10.62	9.25
2079	10.83	9.33

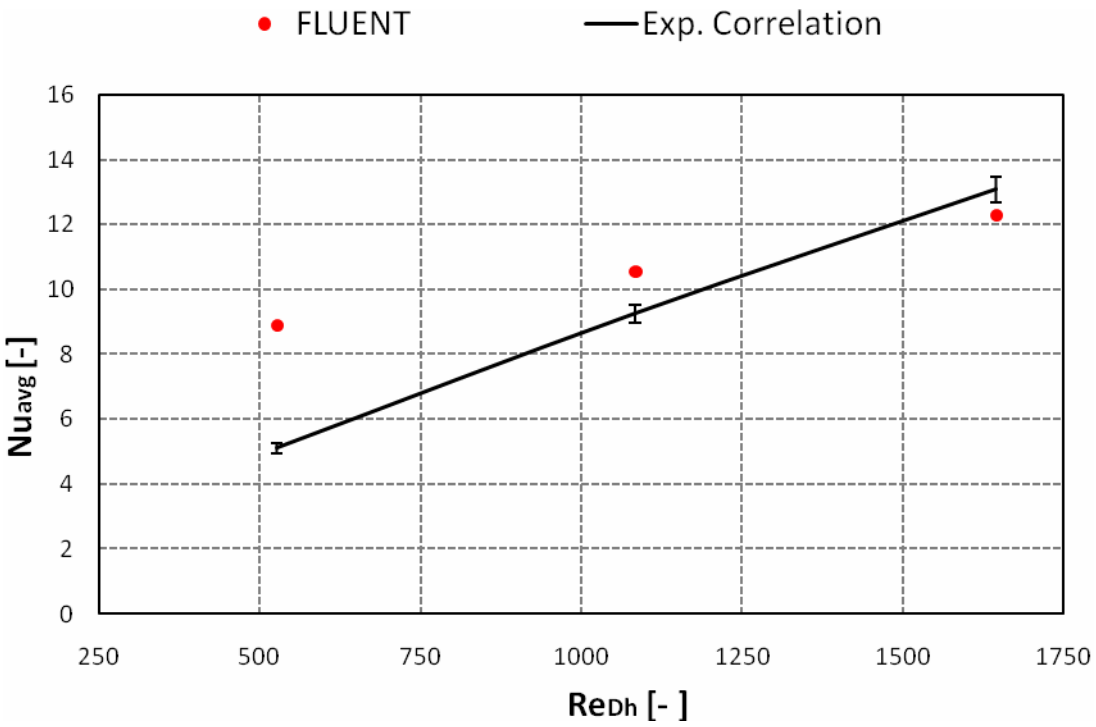

Figure 5.7: Sensitivity of Water Jacket Nu to Jacket Re, FLUENT Results Comparison

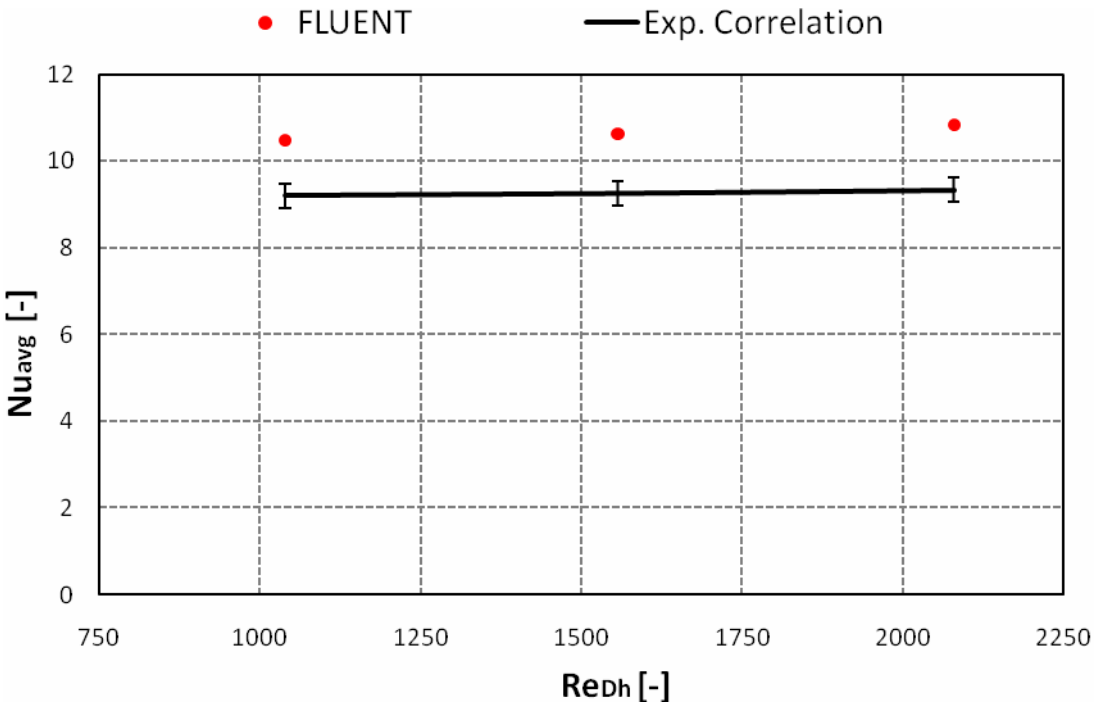

Figure 5.8: Sensitivity of Water Jacket Nu to Tube Re, FLUENT Results Comparison

According to figure 5.7 and 5.8 results, the ratio between averaged change in Nusselt number to corresponding Reynolds number increase ($\alpha = \Delta Nu / \Delta \mathrm{Re}$) was evaluated for each for each case . In conclusion, compared to internal round tube flow, 7.5 times higher sensitivity was calculated in round tube in tube simulation by only increasing the water jacket mass flow rate, which was calculated as:

$$\frac{\alpha_{Round-Tube} - \alpha_{jacket}}{\alpha_{Round-Tube}} = 7.5$$

5.2.4 Model 1: Discussion

Important remarks based on plotted results can be listed as:

1. In figure 5.5, $\theta(\xi)_{wall}$ profile varies between round tube and jacket inlet temperatures and despite its linear profile at the tube mid section, sudden changes were reported at flow inlet sections due to constant initial temperature boundaries.

2. According to figure 5.6, highest heat transfer intensity was observed at the water jacket inlet section due to sudden decrease in the fluid temperature. After stabilizing its heat transfer rate in the mid section, additional increase was investigated in jacket cooling rate at the flow exit, similarly, due to sudden decrease in wall temperature.

3. Based on equation 5.6, maximum Nusselt number value was evaluated at the inlet region as a result of beginning of thermal boundary layer formation.

4. Compared to Dirker and Meyer's experimental correlation (Eq-5.9) 12% disparity was reported in FLUENT results.

5. According to sensitivity analysis of my FLUENT simulation, increase in water jacket mass flow rate developed the heat transfer 7.5 times more than round tube mass flow rate.

6. Finally, based on fin and tube configuration, average refrigerant pressure drop within one circuit of round tube length ($L_{circuit}$) was calculated by using equation 4.2 as:

$$\Delta P_{Round-Tube-Coil} = 1457 \text{ Pa}$$

In table 5.6, a summary of simulation Model 1 full round tube (no microchannel) inside counter flow tube heat exchanger study is presented in terms of its aim, geometry, boundary conditions, results and conclusion.

Table 5.6: Simulation Model 1 Full Round Tube (no microchannel) inside Counter Flow Tube Heat Exchanger Summary Table:

Aim	Geometry		Boundary Conditions		Results		Conclusion
To test the 3/8 in size full round heat exchanger tube in terms of its internal cooling capacity based on the single phase water to water, laminar counter-flow tube in tube heat exchanger simulation by FLUENT CFD solver (Gambit Journal File: appendix B-1 FLUENT Journal File: appendix E-1)	$D_{Round-Tube\ out}$	10.3 [mm]	$T_{in\ Round-Tube}$	274.7 [^{o}K]	$\theta(\xi)_{wall}$	Figure 5.5	The maximum Nusselt number value was evaluated at the inlet region as a result of beginning of thermal boundary layer formation.
	$D_{Round-Tube\ in}$	9.7 [mm]	$\dot{m}_{in\ Round-Tube}$	0.02 [kg/s]	$\theta(\xi)_{jacket}$	Figure 5.5	
	$D_{h\ jacket}$	19.7 [mm]	$V_{in\ Round-Tube}$	0.27 [m/s]	$q''^{*}(\xi)$	Figure 5.6	
	L_{tube}	1.2 [m]	$\mathrm{Re}_{Dh\ Round-Tube}$	1560 [-]	$Nu^{*}(\xi)$	Figure 5.6	
	$A_{surface}$	0.036 [m^2]	$P_{gauge\ Round-Tube}$	187 [Pa]	$Nu_{avg\ j-FLUENT}$	10.54	
			$T_{in\ jacket}$	323 [^{o}K]	$\Delta P_{Round-Tube-Coil}$	1457 Pa	
			$\dot{m}_{in\ jacket}$	0.02 [kg/s]			
			$V_{in\ jacket}$	0.03 [m/s]			
			$\mathrm{Re}_{Dh\ jacket}$	1152 [-]			
			$P_{gauge\ jacket}$	1.76 [Pa]			

5.3 Simulation Model 2: Straight Microchannel Tube inside a Counter Flow Tube Heat Exchanger

5.3.1 Model 2: Gambit Pre-Processing and Boundary Conditions

Compared to round tube model, straight microchannel tube has more complexities in its geometric configuration. As it mentioned in literature review, previous studies were reported an early transition from laminar to turbulent region in microchannel flow due to sudden changes in fluid temperature. Thus, in order to have an accurate replication of fluid flow inside microchannels, it was required to use smaller grid distance both on port faces and trough flow direction. In my study, due to computational limitations it was not possible to apply fine grid quality for a complete multi-port microchannel configuration. Thus, a sectional simulation was needed to have computational efficiency.

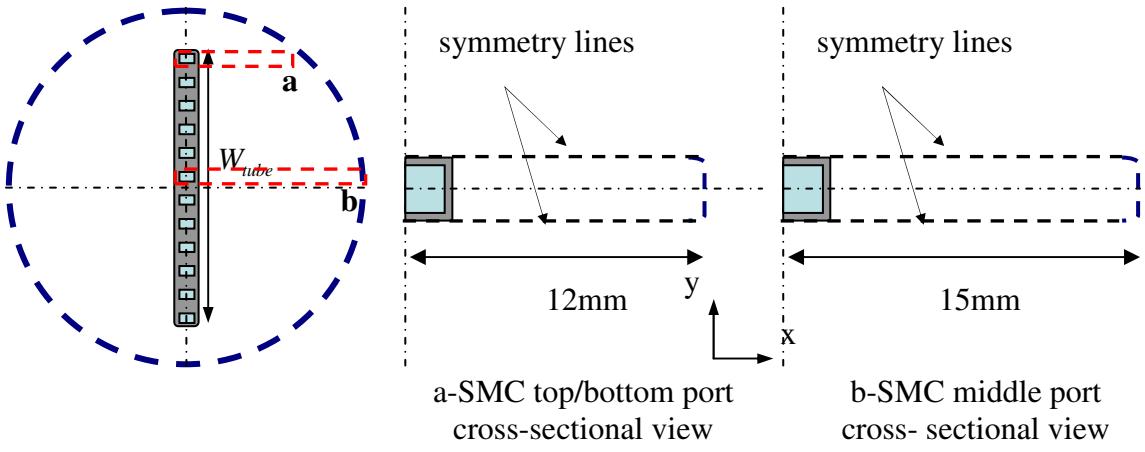

Figure 5.9: Schematic comparison of water jacket flow area at top/bottom (a) and mid section (a) of SMC tube inside a Counter Flow Heat Exchanger

In figure 5.9, top and middle sections of straight microchannel tube are shown. In order to estimate the effect that the distance between the outer tube wall and the microchannel tube wall has on the refrigerant side heat transfer coefficient calculated in

the numerical simulations, a preliminary study was conducted in FLUENT by simulating the cross-section in figure 5.9 (a) and the cross section in figure 5.9 (b). The first cross section represents the top (or bottom) section of the microchannel tube while Figure 5.9 b represents the middle section of the microchannel tube. Similar numbers of elements were created in each sectional geometry by using equivalent coarse grid size in Gambit. Additionally, 10^{-5} residual convergence criteria were applied in the FLUENT solver and constant initial velocity of about 1 m/s was imposed in both jacket sections. The cross section in the middle (Figure 5.9b) has 34 % more water jacket flow area with respect to the top section of figure 5.9 (a). This leads to Reynolds number of the water jacket of about 21 % higher in the middle section compared to the end section. As it can be seen in figure 5.10, in the middle port section 11 % higher average Nusselt number was found compared to tube top and bottom sections. This is consistent with the higher Reynolds number calculated in the domain of the water jacket for the middle section.

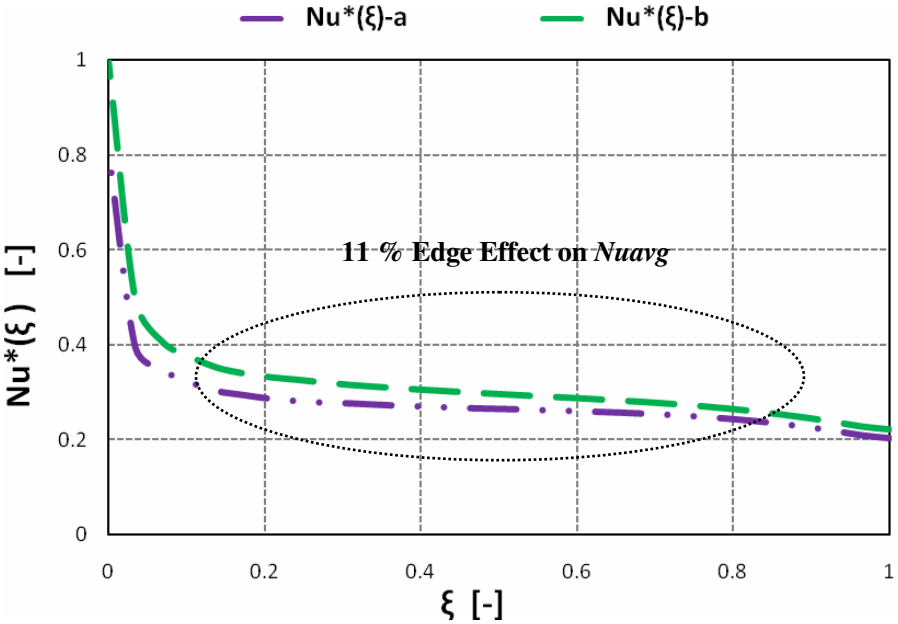

Figure 5.10: Comparison of Nusselt number at water jacket top/bottom and mid section of of SMC tube inside a Counter Flow Heat Exchanger

From the later assumption, the round outer jacket is actually transformed to a square channel as shonw in figure 5.11 (b). If end edge effects at the top and bottom sections of the microchannel tube are neglected, a further simplification is given in Figure 5.11 c. This is the simplified model choosen for numerically investigate the heat transfer performance of the microchannel tubes in the shell tube counterflow heat exchanger. It is a 3D model in x, y, and z directions, with z being the flow direction and x-y the cross sectional plane as indidicate in figure 5.11c.

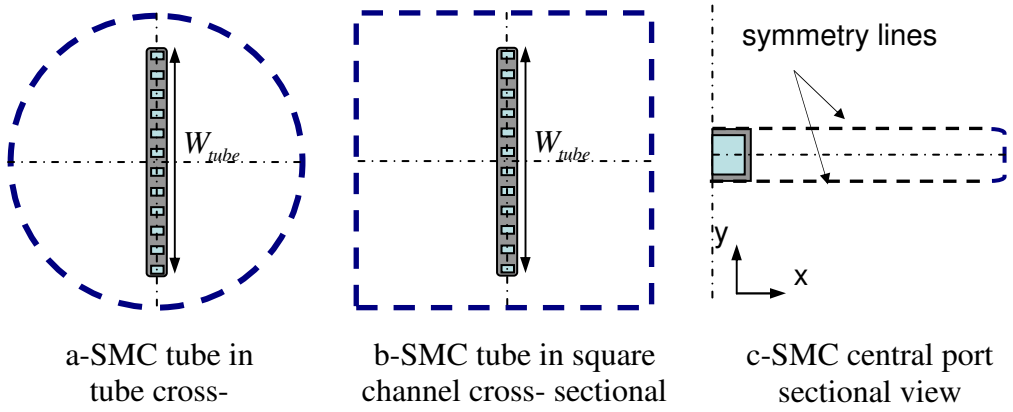

Figure 5.11: Model 2, Sectional Simulation Boundaries of SMC Tube Heat Exchanger

According to Padhmanabhan et al.'s study (2008), geometric configuration of central port section, which is shown in figure 5.11(c), was defined in Gambit. Based on port width (W_{tube}), equally spaced grid points were calculated for each geometric property. By doing so, reverse flow warning in FLUENT residual was prevented and continues flow profile was obtained. Furthermore, three different grid qualities, coarse, medium and fine, were created by increasing the node number accordingly to measure the

grid dependency in FLUENT solver. Geometric properties and related grid numbers were presented in figure 5.12 and table 5.7 respectively.

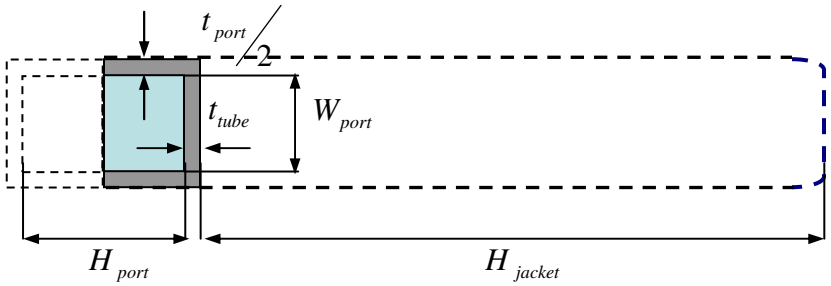

Figure 5.12: Model 2, SMC Tube Sectional Geometric Properties

Table 5.7: Model 2, SMC Tube Geometric Specifications and Node Numbers

Geometry	Length [mm]	Coarse- N_{Node}	Medium - N_{Node}	Fine - N_{Node}
W_{port}	0.51	12	19	25
$H_{port}/2$	0.41	10	15	20
$t_{port}/2$	0.13	3	5	6
t_{tube}	0.24	6	9	12
H_{jacket}	14.35	350	525	700
L_{tube}	1200	30	40	50

Based on tabulated geometric properties and number of nodes, Gambit journal files were created for each grid size and an example is presented in appendix B-2. With the decrease in grid distance, number of cell volumes was increased at each surface face. In figure 5.13 resultant port face mesh qualities of coarse, medium and fine are shown.

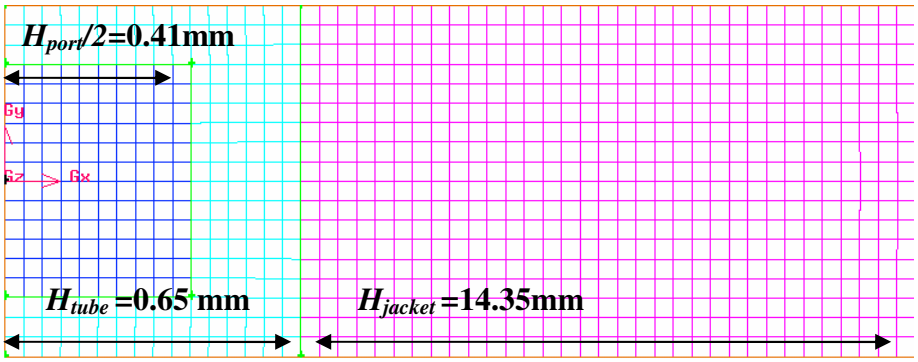

(a) Coarse Meshing (10x12 elements)

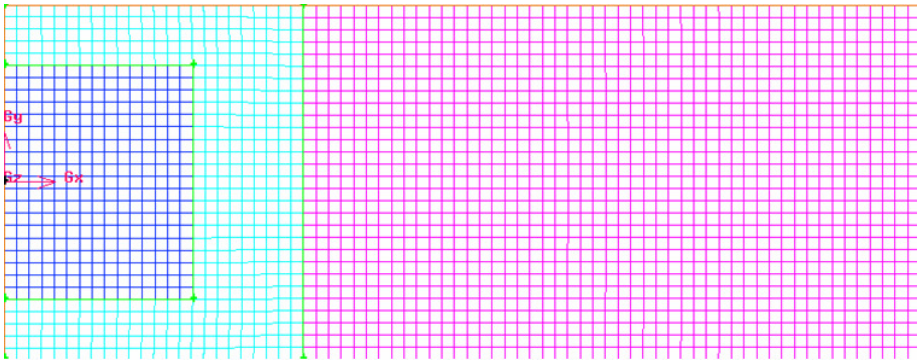

(b) Medium Meshing (19x15 elements)

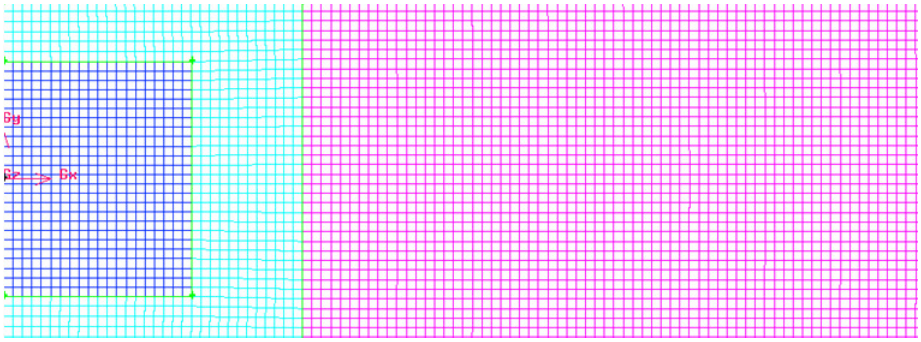

(c) Fine Meshing (25x20 elements)

Figure 5.13: Model 2, Face Mesh Qualities of Grid Study 1, 2 and 3

5.3.2 Model 2: Fluent Solution

Similar to previously defined round tube model, initial conditions were evaluated according to Padhmanabhan et al.'s study (2008) for SMC tube in tube counter flow heat exchanger model. With equally distributed fluid flow assumption, single port mass flow rate ($\dot{m}_{port}$) was evaluated based on Johnson Control Inc.'s 4 ton heat pump system data for microchannel heat exchanger unit ($\dot{m}_{SMC\,ref}$), as:

$$\dot{m}_{port} = \frac{\dot{m}_{SMC\,ref}}{N_{tube} \times N_{port}} \tag{5.10}$$

Additionally, by calculating the rectangular port hydraulic diameter corresponding Reynolds number was evaluated at port inlet temperature as:

$$\mathrm{Re}_{Dh\,port} = \frac{\dot{m}_{port}\, D_{h\,port}}{A_{port}\ \mu} \tag{5.11}$$

where ;

$$D_{h\,port} = \frac{2W_{port}H_{port}}{W_{port} + H_{port}} \tag{5.12}$$

and

$$A_{port} = W_{port}H_{port} \tag{5.13}$$

For the water jacket flow, previously specified inlet conditions were applied to have a logical comparison between each heat exchanger. In table 5.8, resultant initial conditions are given which were defined in FLUENT journal files. In appendix E-2 an example journal file is given for this simulation.

Table 5.8: Model 2, Initial Conditions

Geometry	T_{in} [^{o} K]	V [m/s]	$\dot{m}_{tube}$ [kg/s]	Re_{Dh}	f	P_{gauge} [Pa]
SMC Port	274.7	0.04	4 E-4	15	4	6546
Jacket	323	0.03	0.02	1107.2	0.06	1.45

In the literature, viscous heating effect was reported at lower Reynolds number in microchannels due to its extreme size reduction (Celata et al., 2006). Therefore it was required to check the temperature increase due to viscous heating before neglecting it in the FLUENT solver. Based on Celeta et al's suggestion viscosity effect κ equation (Eq-2.9) was modified for rectangular channel port as:

$$\kappa_{SMC} = \frac{\Delta T_{f-v}}{\Delta T_{f-q}} = \frac{1}{2}\left(\frac{\mu_f V^2}{k_f (T_w - T_f)}\right)\left(\frac{W_{port} H_{port}}{D_h{}^2}\right) f\,\mathrm{Re}_{Dh} \qquad (5.14)$$

When the fluid temperature at $T_f = T_{j_{in}}$, temperature increase was obtained $4\text{x}10^{-5}$ %, which is negligibly small. Thus, viscous heating wasn't included in FLUENT solver.

As it mentioned earlier, by using this sectional simulation, variations of temperature and heat transfer values were assumed to be only in flow direction, i.e. $T = T(z)$ and $Q = Q(z)$. However, in reality, these variations can show differences in tube width direction ($\vec{y}$) due to port to port heat transfer. To support this assumption, conductive heat transfer through port thickness was checked according to Maranzana et al.'s previous study (2004). The axial conduction number of "*M*" (Eq-2.10) was calculated for rectangular microchannel ports as:

$$M_{SMC} = \left(\frac{k_w}{k_f}\right)\left(\frac{D_h}{L_{tube}}\right)\left(\frac{t_{port}}{W_{port}}\right)\frac{1}{\mathrm{Re}_{Dh}\,\mathrm{Pr}_f} \tag{5.15}$$

Resultant axial conduction number was calculated as 0.002, which is smaller than recommended value (0.01). Based on this comparison axial conduction was neglected.

According to these assumptions first the grid dependency was checked by simulating the same boundary conditions with previously created three different grid qualities. Similar to round tube heat exchanger simulation, within similar iterative study the largest residual was obtained in momentum solution in each simulation. In table 5.9, numerical performance of each meshing quality was compared based on its residual value and convergence speed. Compared to iterative results and its performance, computationally most efficient meshing was selected. Then, by applying further iterations, final results were saved when the residual value was converged to E-06 level.

Table 5.9: Model 2, Grid Dependency Study Residual Comparison

Mesh Quality	Momentum Residual	Number of Iterations	Iteration Time [h:m]
Coarse	7.3502e-06	32915	40:46
Medium	1.8848e-05	39010	122:28
Fine	2.2607e-05	40000	2 weeks

5.3.3 Model 2: Fluent Post-processing

Before evaluating the averaged Nusselt number of water jacket flow around a SMC tube, it was necessary to minimize the grid distance effect on the iterative results. As it mentioned before, in CFD studies reducing the grid distance increases the number of

iteration points which improves the accuracy of the solutions and also requires more time to converge the residuals.

In order to make sure that decreasing the grid distance does not have significant changes in the iterative results, three meshing qualities (coarse, medium and fine) were created and simulated in FLUENT by applying an identical iterative procedure. Before applying any data reduction procedure, FLUENT results were compared in terms of their variation in the flow field. First, based on equation 5.4, dimensionless jacket side water temperature profile ($\theta(\xi)_{jacket}$) is presented along the tube length (ξ) in figure 5.14. By comparing coarse, medium and fine meshing simulation results with each others, similar $\theta(\xi)_{jacket}$ variations were found.

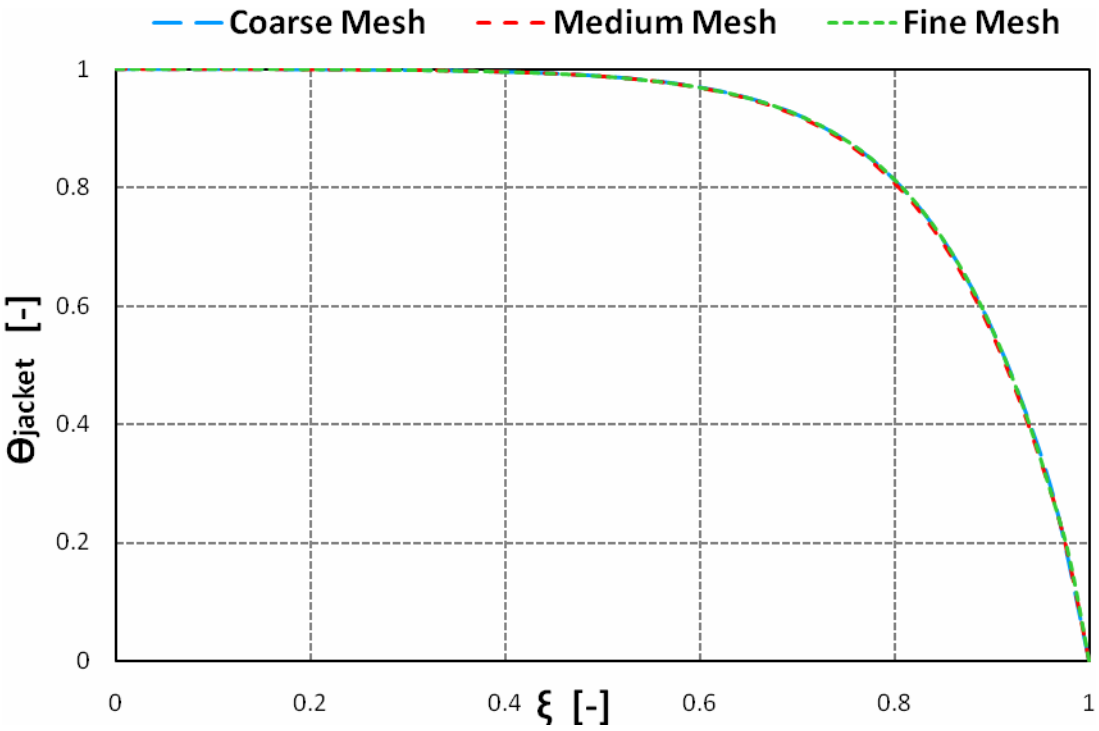

Figure 5.14: Model 2, Grid Dependency Study Dimensionless Temperature Distribution

Additionally, by using equation 5.5, dimensionless heat flux ($q''^{*}(\xi)_{jacket}$) variation in the flow direction results were compared for all meshing qualities. Unlike temperature variation, separate $q''^{*}(\xi)_{jacket}$ profiles were obtained near jacket exit which is shown in figure 5.15.

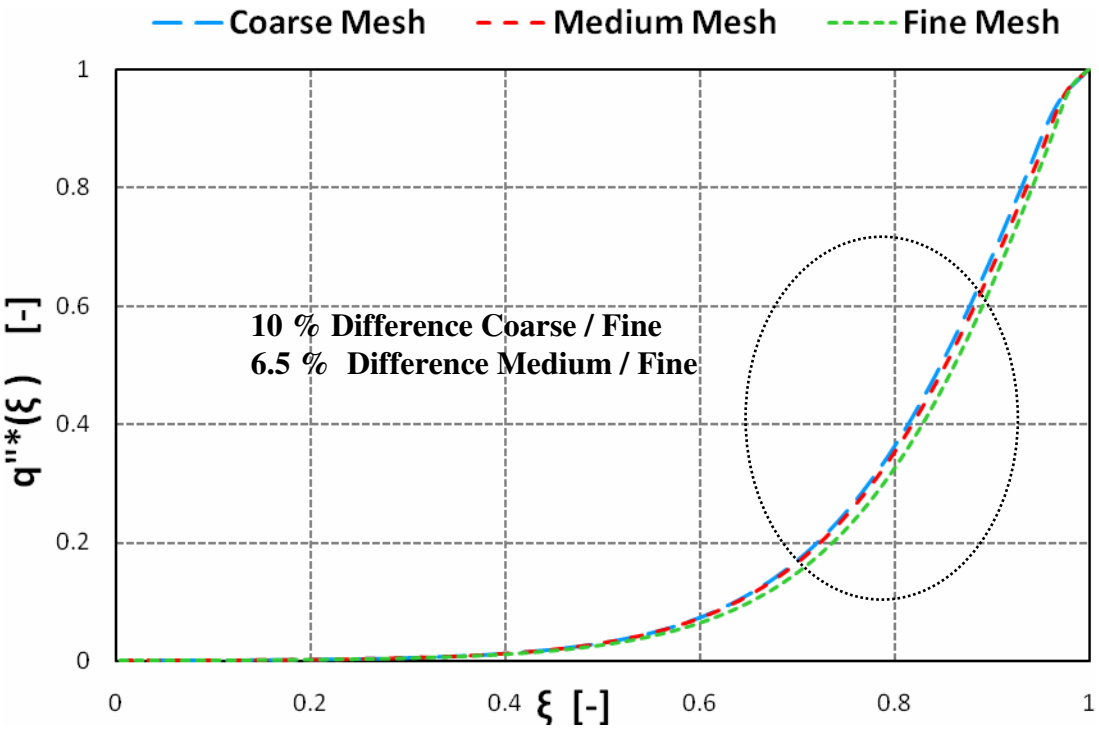

Figure 5.15: Model 2, Grid Dependency Study Dimensionless Heat Flux Distribution

Compared to coarse meshing, smaller separation were reported between medium and fine meshing results. Additionally, since medium meshing was more economical than fine meshing based on its convergence time, it was selected as the most computationally efficient and less grid dependent meshing quality. Thus, by using medium meshing and reducing the momentum URL value to 0.3, additional iterations were applied until the

residuals were converged. Similar to previous Model 1, four step data reduction procedure were applied to evaluate the average Nusselt number as:

1. Local $\theta(\xi)_{jacket}$, $\theta(\xi)_{wall}$ values were obtained by using Eq-5.4 respectively.

2. Similar to temperature variables, iterative FLUENT results were non-dimensonlized by using equation 5.5 and local $q^*(\xi)$ formation along tube length was presented in figure 5.17.

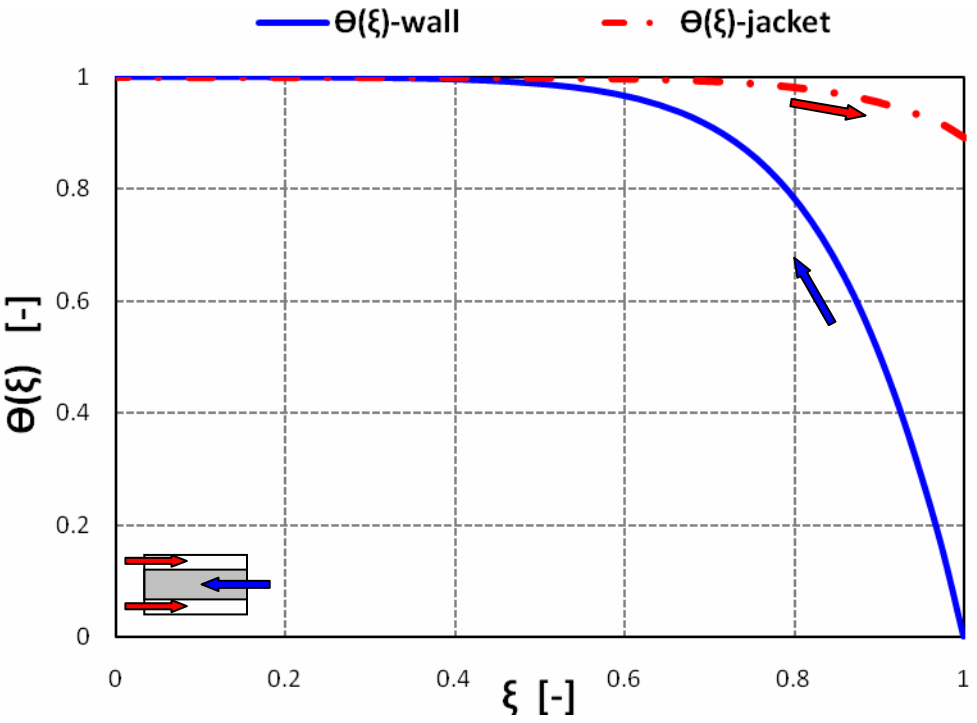

Figure 5.16: Model 2, Dimensionless Local Jacket and Wall Temperatures

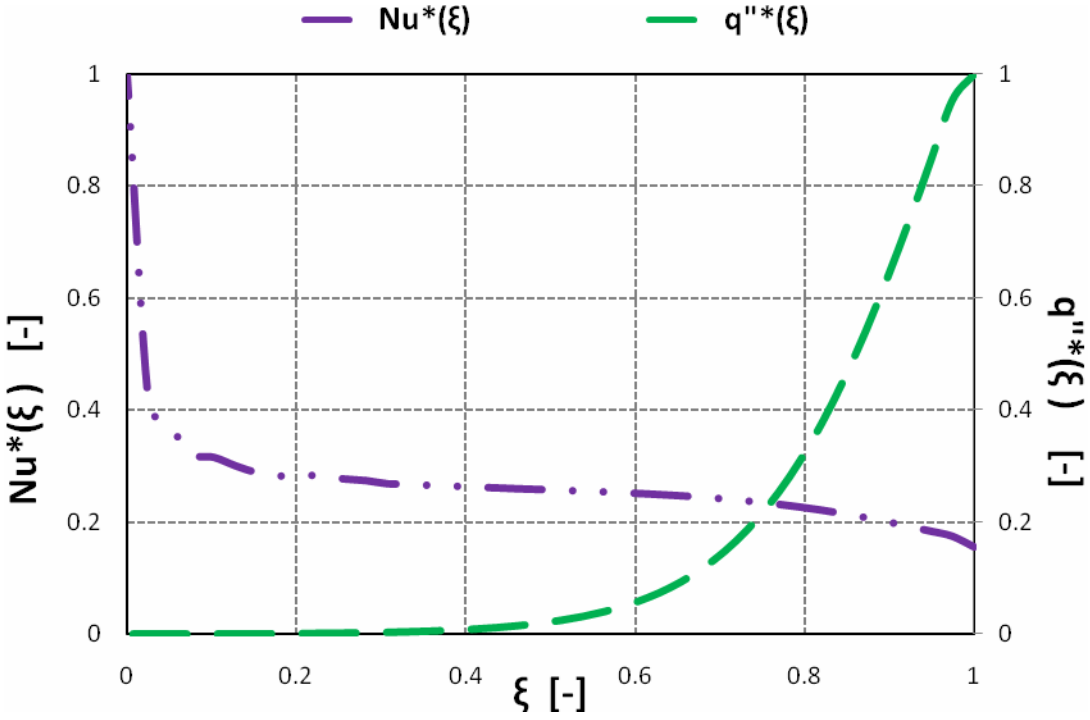

Figure 5.17 : Model 2, Dimensionless Local Heat Flux and Nusselt Number Distribution

3. Based on figure 5.16 results and heat flux variaton in figure 5.17 dimensioneless local Nusselt numbers ($Nu^*(\xi)$) were evaluated by using equation 5.6 and results were illusterated in figure 5.17.

4. Finally, averaged Nusselt number of the jacket, $Nu_{j-FLUENT_{avg}}$, was calculated numerically by using equation 5.8 and resultant Nusselt number was obtained as:

$$Nu_{j-FLUENT_{avg}} = 15.33$$

Following the four step procedure , data reduction study was completed for the straight microchannel tube counter flow heat exchanger simulation and corresponding results are be discussed in the next section.

5.3.4 Model 2: Discussion

According to plotted results following comments were made:

1. From dimensionless temperature profiles ($\theta(\xi)_{wall}$, $\theta(\xi)_{jacket}$) in figure 5.16 , it was obtained that microchannel wall temperature reaches the water jacket temperature, within the mid-section of the channel length. Compared to round tube in tube heat exchanger (Model 1) this fast wall temperature increase can be expalined by the lower refrigerant volume to surface area ratio of straight microchannel heat exchanger. Based on this fact, heat transfer from jacket water flow to channel surface starts to develop within the same tube length. Then, it reaches its maximum value at the flow exit due to maximum temperature difference between SMC tube surface and jacket fluid profile as it is shown in figure 5.16.

2. Unlike heat flux profile, highest local Nusselt number was obtained at the water jacket inlet because of thermal boundary layer formation, which was also observed in Model 1 simulation. After stabilizing in the mid section, a slight decrease was investigated in the Nusselt number value at the jacket outlet, since the wall temperature changes were more rapid compared to water jacket temperature near the jacket exit.

3. Based on vertical microchannel heat exchanger configuration, average pressure drop along coil height (H_{Coil}) was obtained by using equation 4.2 with laminar flow assumption as:

$$\Delta P_{SMC-Coil} = 5039 \text{ Pa}$$

4. Despite its higher pressure drop compared to fin and tube configuration, 45% higher Nusselt number was evaluated in SMC tube coil configuration model by using 61% less refrigerant.

In summary, numerical investigation of round tube and straight microchannel tube simulations and corresponding iterative results were individually presented in this section. Similarly, by applying the same FLUENT code and data reduction procedure, internal cooling performance of round microchannel tube study is presented in the next chapter.

In table 5.10, a summary of simulation Model 2 straight microchannel tube inside a counter flow tube heat exchanger is presented in terms of its aim, geometry, boundary conditions, results and a brief conclusion.

Table 5.10: Simulation Model 2 Straight Microchannel Tube inside a Counter Flow Tube Heat Exchanger Summary Table

Aim	Geometry		Boundary Conditions		Results		Conclusion
To test the straight microchannel (SMC) heat exchanger tube in terms of its internal cooling capacity based on single phase water to water, laminar counter-flow tube in tube heat exchanger simulation by FLUENT solver (Gambit Journal File: appendix B-2 FLUENT Journal File: appendix E-2)	W_{port}	0.51 [mm]	$T_{in\ port}$	274.7 [^{o}K]	$\theta(\xi)_{wall}$	Figure 5.14	Unlike $q''^{*}(\xi)$, $Nu^{*}{}_{MAX}(\xi)$ was obtained at the water jacket inlet section due to beginning of thermal boundary layer formation, which was also reported in Model 1 simulation
	H_{port}	0.82 [mm]	$\dot{m}_{in\ port}$	1.7 E-5 [kg/s]	$\theta(\xi)_{jacket}$	Figure 5.14	
	$D_{h\ port}$	0.6 [mm]	$V_{in\ port}$	0.04 [m/s]	$q''^{*}(\xi)$	Figure 5.15	
	N_{port}	23 [-]	$\mathrm{Re}_{Dh\ port}$	15 [-]	$Nu^{*}(\xi)$	Figure 5.15	
	$D_{h\ jacket}$	20.7 [mm]	$P_{gauge\ port}$	6546 [Pa]	$Nu_{avg\ j-FLUENT}$	15.33	
	L_{tube}	1.2 [m]	$T_{in\ jacket}$	323 [^{o}K]	$\Delta P_{SMC-Coil}$	5039 Pa	
			$\dot{m}_{in\ jacket}$	0.02 [kg/s]			
			$V_{in\ jacket}$	0.03 [m/s]			
			$\mathrm{Re}_{Dh\ jacket}$	1107.2 [-]			
			$P_{gauge\ jacket}$	1.45 [Pa]			

CHAPTER VI

Round Microchannel Tube Design and Analysis

To reduce the frost growth rate on microchannel heat exchanger in wet conditions, my study was aimed to develop an alternative design prototype based on conventionally available fin and tube and microchannel tube heat exchangers' design constrains. Previously, round tube and straight microchannel tube (Model 1 and Model 2) refrigerant side thermal behaviors were presented. By computationally simulating both tubes in an identical outdoor condition (counter flow water jacket), results were obtained by measuring the changes from the exterior environment. In this third model, Round Microhannel (RMC) tube internal heat transfer behavior was investigated by applying the same tube in tube counter flow heat exchanger simulation approach which was explained in chapter 5.

Before analyzing the heat transfer variation of the water jacket flow along the tube length, first the geometric design properties and corresponding boundary conditions are given in the following section.

6.1 Simulation Model 3: Round Microchannel Tube inside a Counter Flow Tube Heat Exchanger Design Constraints and Boundary Conditions

According to Previous investigations, fin and tube coil configuration has lower defrost cycle, which increases its performance as an outdoor coil compared to conventional microchannel heat exchanger. On the other hand, microchannel heat exchanger provides higher heat transfer performance since micro-scaled parallel port configuration decreases the refrigerant to surface ratio compared to fin and tube heat exchangers. By integrating these individual advantages in a single heat exchanger, my study was intended to investigate a round microchannel tube design, which could be applicable in fin and tube coil configuration. By doing so, it is aimed to have an alternative microchannel coil model which would have longer defrosting cycle than straight microchannel tube and higher heat transfer performance than a fin and tube heat exchanger within a reasonable pressure drop fault. Thus, according to round tube and straight microchannel geometries, following design constraints were applied to obtain RMC tube configuration:

1. The main question in the design procedure of RMC tube was its outer diameter in order to provide comparable heat transfer as SMC tube. Since there weren't any analogous study available in the literature, previously studied 3/8" in size round tube heat exchanger's outer diameter (D_o=10.3mm) was selected as an initial diameter value, to have a proportional design constrain.

2. Besides D_o, equal hydraulic diameter of SMC tube (D_h=0.6mm) was used for RMC tube port, which was given in the previous chapter.

3. According to Heun and Dunn's study (1996), rectangular port geometry is more advantageous due to its optimum packing capability which increases it heat transfer rate in SMC tubes. Based on this investigation, to increase the port capability on a round tube's circular configuration, previously given rectangular port geometry was modified to trapezoidal port shape. In an equivalent port height (H), port width (W) was changed (W_a, W_b) by keeping hydraulic diameter (D_h) constant. In figure 6.1, modified trapezoidal port shape and related geometric properties are shown.

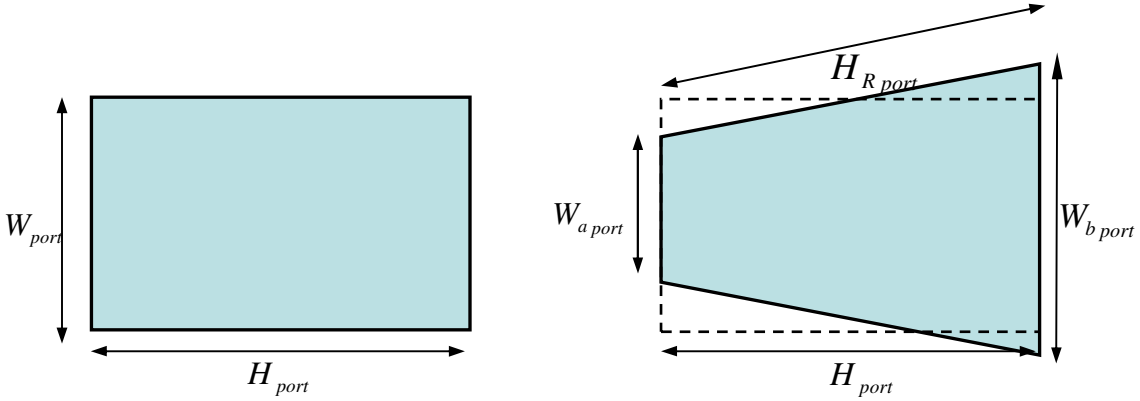

(a) SMC Tube Rectangular Port (b) RMC Tube Trapezoidal Port

Figure 6.1: Model 3, Rectangular and Trapezoidal Port Geometries

4. With the help of trapezoidal port geometry, uniform port thickness (t_{port}) was obtained in the tangential direction and defined as same as the SMC tube's port to port distance.

5. Similar to t_{port}, uniform tube thickness (t_{tube}) was used based on SMC tube geometry.

6. Internal tube surface was assumed to be adiabatic

Table 6.1: Model 3, RMC Tube Design Constrains

D_o [mm]	D_i [mm]	A_s [m^2]	t_{port} [mm]	t_{tube} [mm]
10.3	7.69	0.04	0.25	0.24

Based on given design constrains, which are shown in table 6.1, inner diameter and total number of port values were calculated for the RMC tube. In figure 6.2 (b) a closer look of RMC tube and in table 6.2 resultant geometric specifications are presented.

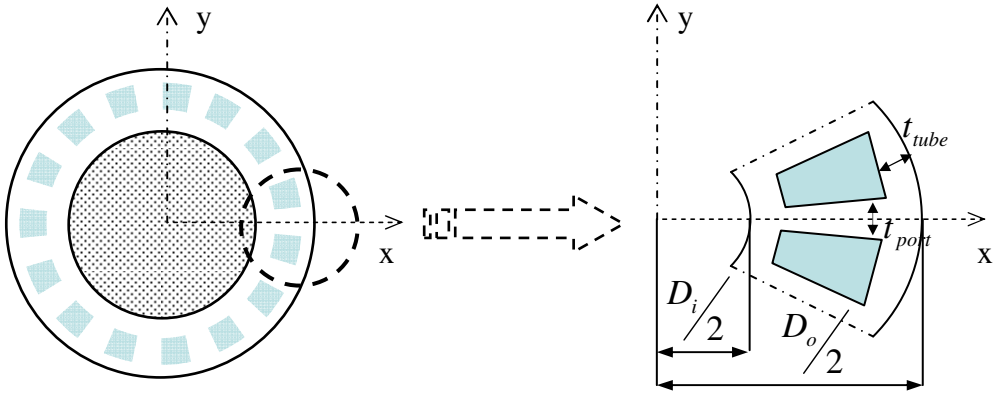

(a) RMC Tube (b) RMC Tube Sectional View

Figure 6.2: Model 3, RMC Tube Cross-sectional Profile

According to table 6.2, despite 14 % reduction in RMC tube outer heat transfer area, 57% more number of ports was achieved compared to SMC tube geometry.

Table 6.2: Model 3, RMC Tube Geometric Properties

$H_{R\,port}$ [mm]	$W_{a\,port}$ [mm]	$W_{b\,port}$ [mm]	$D_{h\,port}$ [mm]	N_{port} [-]
0.82	0.56	0.46	0.6	36

6.2 Model 3: Gambit Pre-Processing and Boundary Conditions

Similar to previous heat exchanger Model 1 and Model 2 studies, a sectional geometry was created to increase the simulation accuracy of the trapezoidal microchannel flow. Unlike SMC tube, in this approach there weren't any additional assumption needed due to RMC tube axis-symmetric geometry. By applying symmetry boundary conditions at the sectional cuts, single port geometry was created in GAMBIT. Additionally, since the RMC tube's inner gap was assumed as adiabatic, no meshing was applied in this region.

Corresponding to SMC tube simulation, equally spaced quadrilateral cells were created to reduce the skewness in the meshing. Based on figure 6.3, uniform grid spacing was generated according to the ratio of radial tube height ($H_{R\ tube}$) and radial jacket height ($H_{R\ jacket}$) with radial port height ($H_{R\ port}$) were taken respectively

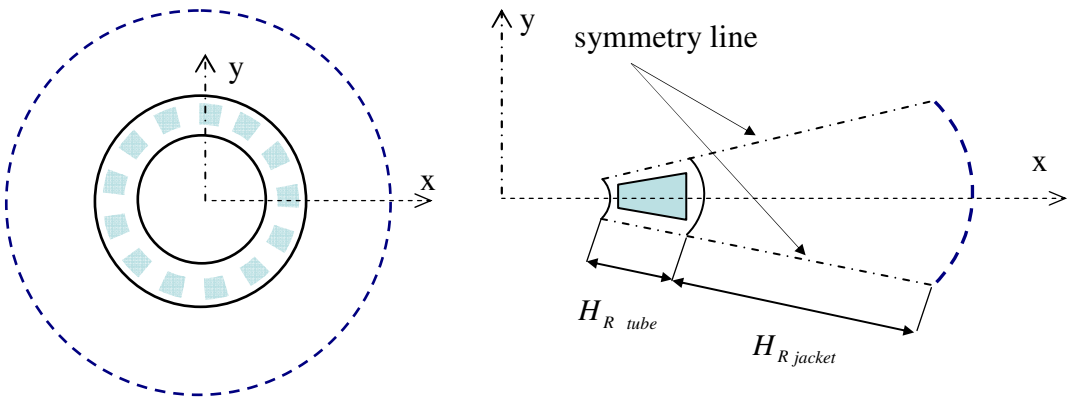

(a) RMC Tube in tube Cross-sectional View (b) RMC One Port Sectional View

Figure 6.3: Model 3, Single Port Simulation Geometry

Additionally, by increasing the node numbers and decreasing the grid distance, three different meshing qualities (coarse, medium and fine) were created to investigate the grid distance effect on iterative results. In table 6.3 geometric properties of RMC tube in tube simulation and number of node variation in each meshing are shown. According to this variation, resultant face meshing qualities; coarse, medium and fine are presented in figure 6.4.

Table 6.3: Model 3, Geometric Specifications and Node Numbers

Geometry	Length [mm]	Coarse- N_{Node}	Medium - N_{Node}	Fine - N_{Node}
$W_{a\ port}$ $(W_{b\ port})$	0.56 (0.46)	10	15	18
$H_{R\ port}$	0.82	20	30	36
$H_{R\ \ tube}$	1.3	32	48	58
$H_{R\ jacket}$	9.86	240	360	432
$H_{tube\ arc}$	0.9	18	27	32

For all meshing qualities, GAMBIT journal files were prepared and an example is given in appendix B-3. After creating quality.msh files, pre-processing step was completed. In the next section, RMC heat exchanger configuration and FLUENT solution is reported.

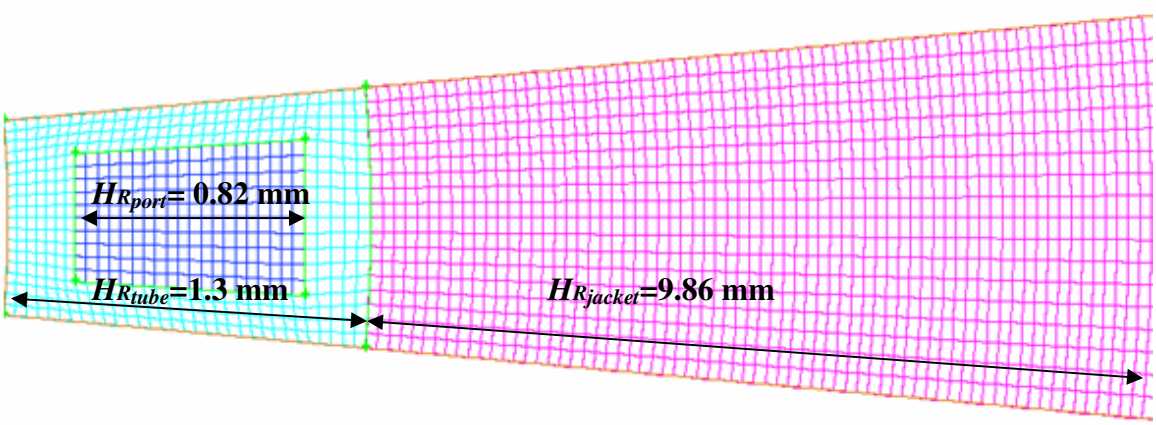

(a) Coarse Meshing (10x20 elements)

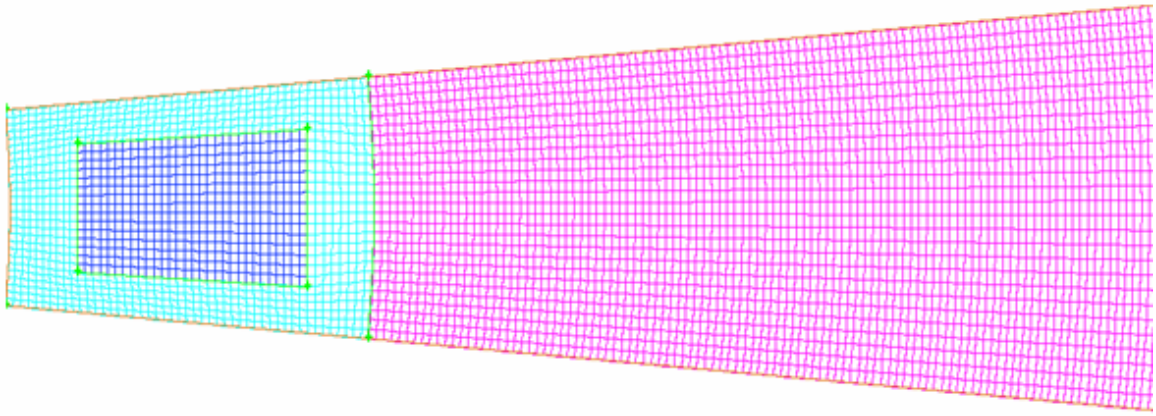

(b) Medium Meshing (15x30 elements)

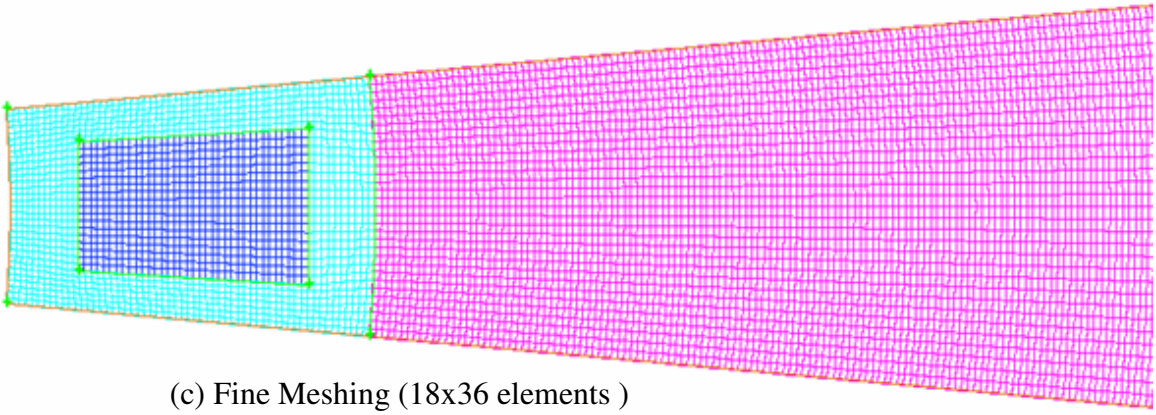

(c) Fine Meshing (18x36 elements)

Figure 6.4: Model 3, Face Mesh Qualities of Grid Study 1, 2 and 3

6.3 Model 3: Fluent Solution

In my study, in order to increase its thermal performance as an outdoor coil , fin and tube coil arrangement were used for the RMC tube heat exchanger configuration, i.e. by replacing the round tubes with RMC tubes inside a fin and tube coil, similar defrosting performance is aimed to be achieved. On the other hand, unlike fin and tube coil, a parallel tube configuration was used to reduce the refrigerant pressure drop in RMC tube heat exchanger. As figure 6.5 example illustration, within same fin and tube's coil height (H_{coil}) and coli width (W_{coil}), equivalent fin and tube row numbers of parallel ports were placed by keeping tube to tube distance constant. The corresponding fin and tube geometric properties were obtained by Padhmanabhan et al.'s previous study (2008).

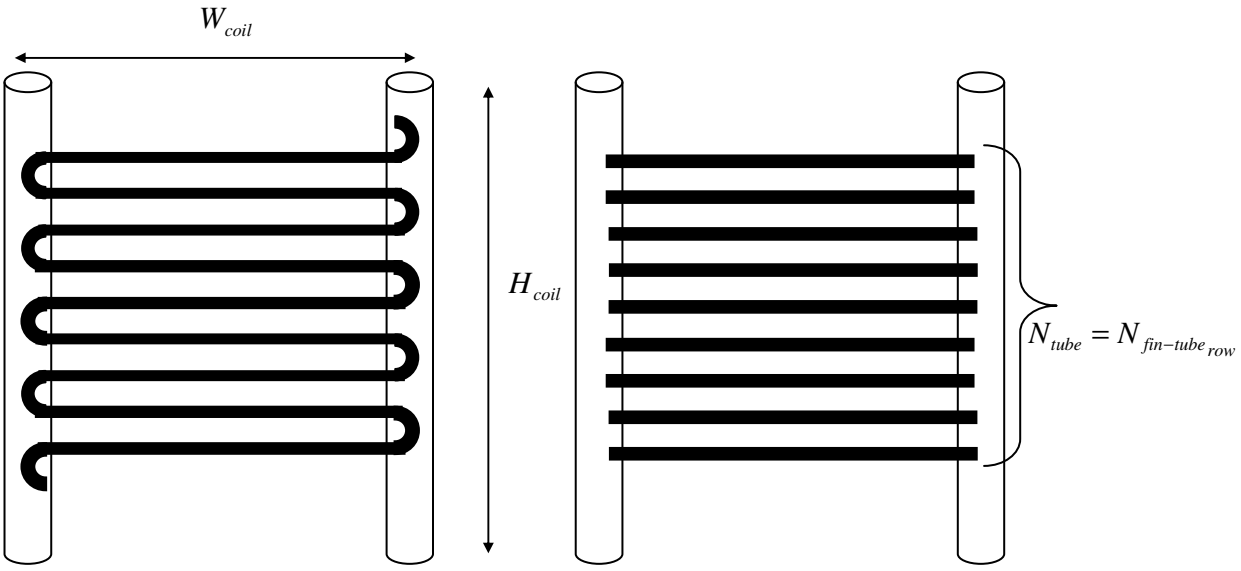

(a) Fin and Tube Coil Arrangement (b) RMC tube Coil Arrangement

Figure 6.5: Fin and Tube (a) and RMC Tube Coil (b) Configurations

Based on this parallel fin and tube heat exchanger configuration, boundary conditions for Model 3 were evaluated. Additionally, in order to have a reasonable comparison between two microchannel geometries, RMC port mass flow rate was calculated at the same refrigerant capacity of SMC tube which is given in equation 6.1.

$$\dot{m}_{port} = \frac{\dot{m}_{RMC\,ref}}{N_{tube} \times N_{RMC\,port}} \tag{6.1}$$

where ; $\dot{m}_{RMC\,ref} = \dot{m}_{SMC\,ref}$ and $N_{tube} = N_{fin-tube\,row}$

Beside port mass flow rate, the thermal boundaries were defined according to Padhmanabhan et al.' previous study (2008) and corresponding boundary conditions of RMC tube in tube heat exchanger simulation is presented in table 6.4.

Table 6.4: Model 3, Initial Conditions

Geometry	T_{in} [^{o} K]	V [m/s]	$\dot{m}_{tube}$ [kg/s]	Re_{Dh}	f	P_{gauge} [Pa]
SMC Port	274.7	0.09	0.001	32	2	140088.6
Jacket	323	0.03	0.020	1107.2	0.058	1.76

According to given initial conditions, FLUENT journal files were created to manipulate the iterative study. An example journal file for Model 3 simulation is given in appendix E-3. To simplify the continuity, momentum and energy equations, I applied the same assumptions with SMC tube simulations, which were defined in Chapter 5. According to the iterative approach, first the grid dependency was checked by comparing the computational performance of each meshing quality which is given in table 6.5.

Comparing the grid distance effect on iterative results and computational performances, the most convenient meshing quality was selected and additional iterations were applied until all residuals were converged to E-06 level. In the next section, data reduction procedure and the iterative results are presented.

Table 6.5: Model 3, Grid Dependency Study Residual Comparison

Mesh Quality	Momentum Residual	Number of Iterations	Iteration Time [h:m]
Coarse	2.6448e-06	28505	22.37
Medium	1.0286e-05	31616	60.:10
Fine	1.3210e-05	33560	101:38

6.4 Model 3: Fluent Post-processing

Similar to Model 1 and Model 2 studies, a preliminary grid dependency study was performed to check the grid distance influence in the iterative results. Thus, after completing an identical iterative procedure with coarse, medium and fine meshing, smaller grid distance effect was examined by comparing FLUENT solver results. As in previous tube in tube heat exchanger models' solution approach, first the dimensionless local water jacket temperature variation along tube length ($\theta(\xi)_{jacket}$) was plotted for each meshing quality. As it can be seen in figure 6.6, a uniform $\theta(\xi)_{jacket}$ profile was observed with all meshing qualities.

Additionally, non-dimensionless heat flux variation over the RMC tube surface ($q''^{*}(\xi)$) were plotted for all grid sizing. As it can be seen in figure 6.7, unlike uniform temperature variation, separate profiles were obtained in each meshing quality.

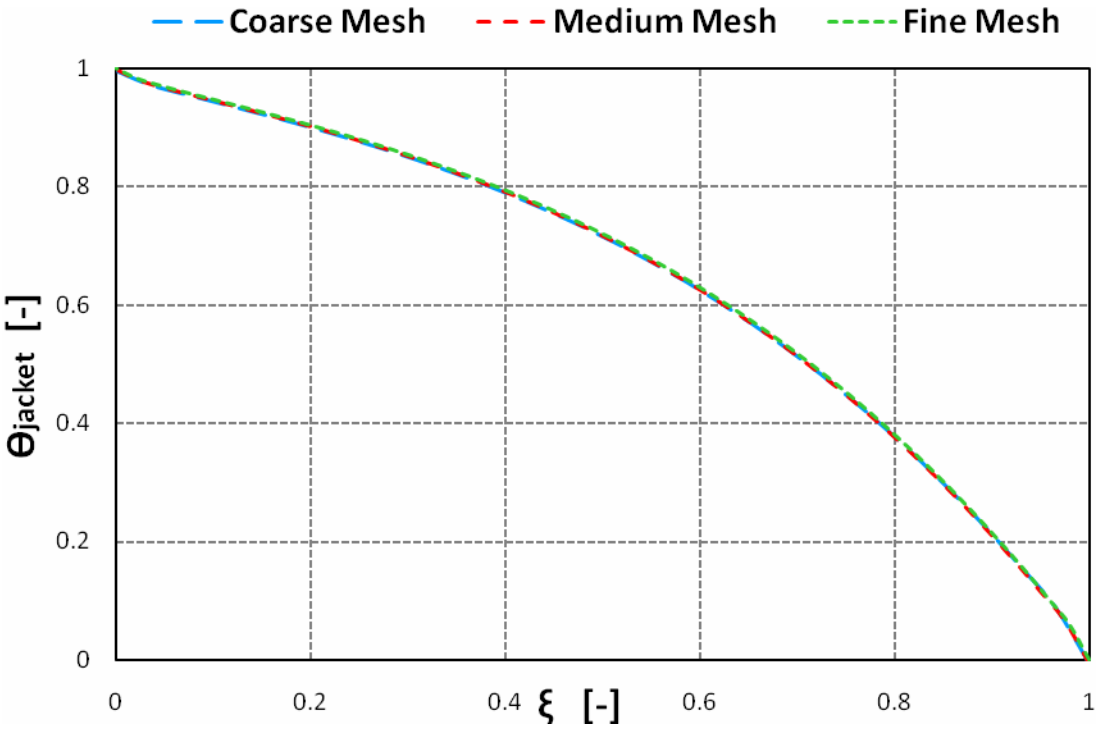

Figure 6.6: Model 3, Grid Dependency Study Dimensionless Temperature Distribution

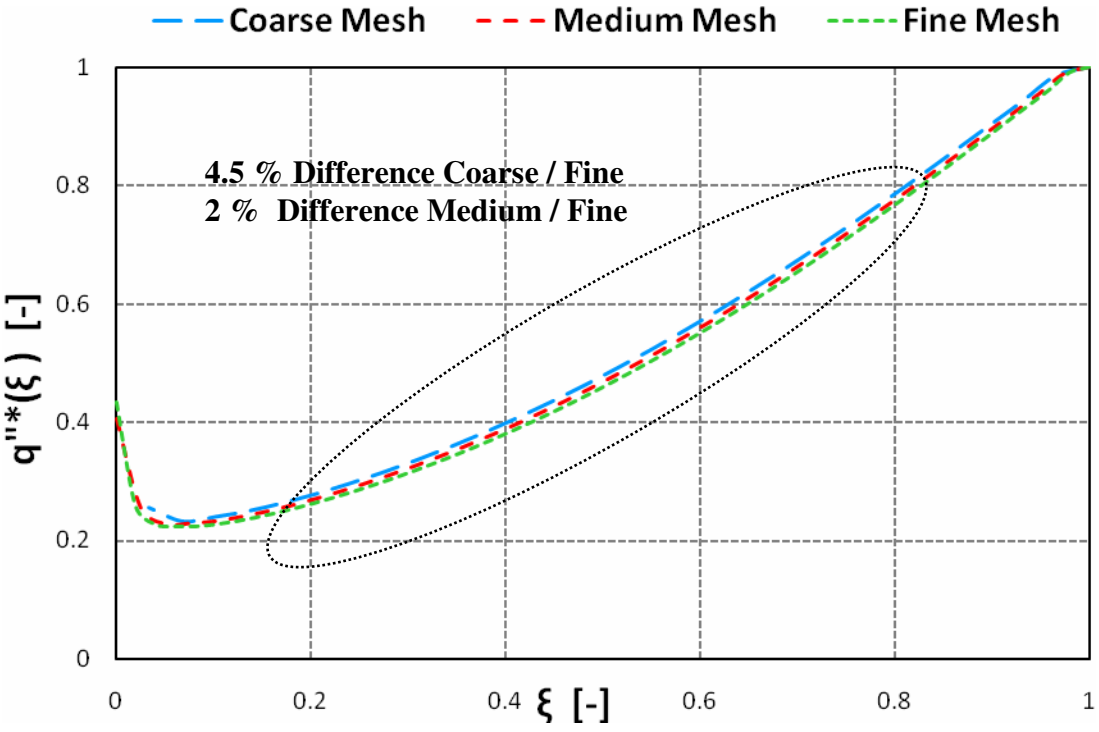

Figure 6.7: Model 2, Grid Dependency Study Dimensionless Heat Flux Distribution

Compared to coarse meshing, lower difference in average $q''^{*}(\xi)$ was found between fine and medium meshing. According to table 6.5, medium meshing provided better computational performance than fine meshing with more rapid convergence. Therefore, medium meshing quality was selected to apply further iterations.

The four step data reduction procedure, which was explained in Chapter 5, was used to calculate average Nusselt number as follows:

1. Variations in $\theta(\xi)_{jacket}$, $\theta(\xi)_{wall}$ values were evaluated by using equation 5.4 and results were shown in figure 6.8.

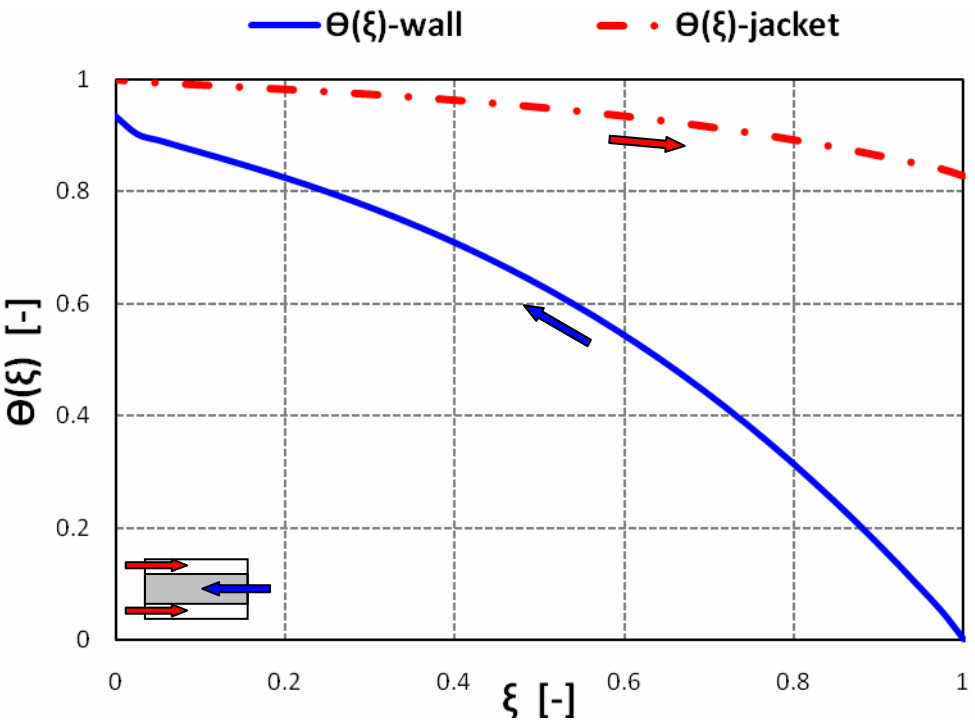

Figure 6.8: Model 3, Iterative Results of Dimensionless Jacket and Wall Temperatures

2. As temperature variatons , $q''^{*}(\xi)$ variation along the flow direction were plotted by nondimensionlizing iterative FLUENT results according to equation 5.5. Resultant profile is presented in figure 6.9.

3. Then , by applying equation 5.6 and 5.7, non-dimensional local Nusselt number values ($Nu^{*}(\xi)$) were calculated at each grid points. Formation of $Nu^{*}(\xi)$ is presented in figure 6.9.

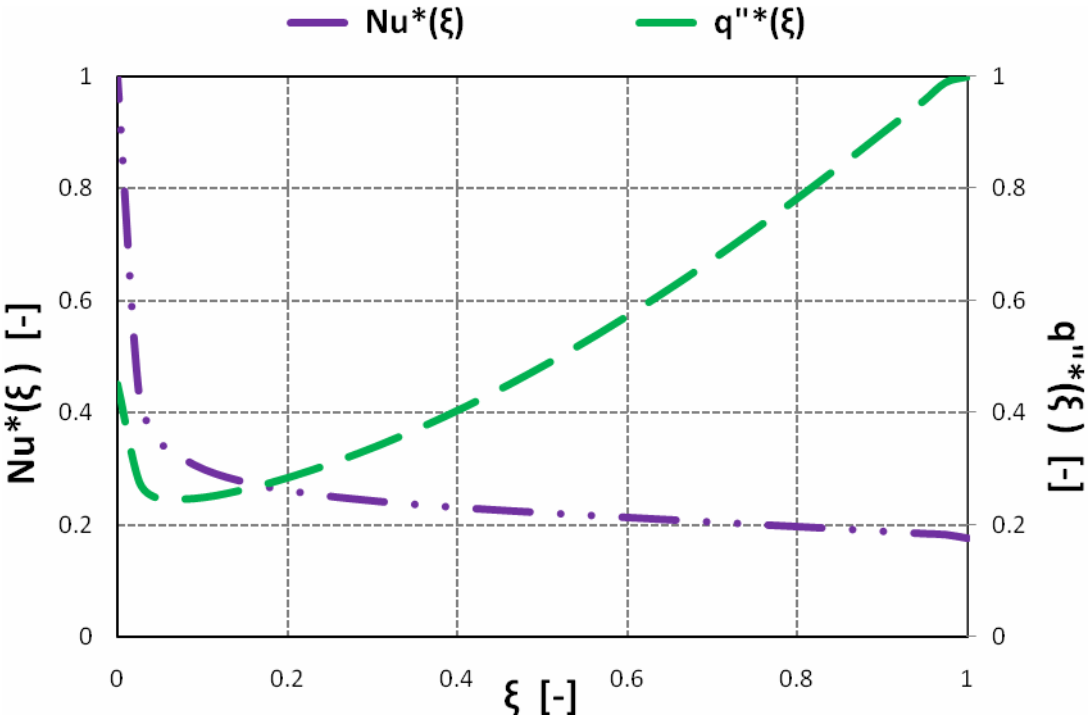

Figure 6.9: Model 3, Dimensionless Local Heat Flux and Nusselt Number Distribution

4. Lastly, I calculated the average Nusselt number ($Nu_{j-FLUENT_{avg}}$) by integrating the local Nusselt numbers numerically and dividing it in to total surface length which was defined in equation 5.8. By doing so, result was obtained as:

$$Nu_{avg\ j-FLUENT} = 13.06$$

By using four step data reduction procedure, comperable results were obtained for round microchannel heat exhcnager model. In the next section important remarks are discussed based on presented results.

6.5 Model 3: Discussion

By using the same iterative approach and data reduction procedure following observations were made:

1. According to counter flow heat exchanger configuration, in figure 6.8 an increasing temperature difference variation was obtained between jacket flow and inner RMC tube wall ($\theta(\xi)_{jacket} - \theta(\xi)_{wall}$), which attained its maximum value at the flow exit. Unlike SMC tube model (figure 5.14), dispites its higher port number, RMC tube's $\theta(\xi)_{wall}$ couldn't reach to $\theta(\xi)_{jacket}$ value due to its adiabatic inner surface.

2. In figure 6.9, variation in dimensionless heat flux profile along flow direction ($q''^{*}(\xi)$) was shown. Based on temperature profiles, first a sudden decrease in $q''^{*}(\xi)$ was reported at the channel inlet due to rapid change in $\theta(\xi)_{wall}$ value. Then, $q''^{*}(\xi)$ started to increase almost linearly and reached its highest value at the channel inlet where the flow and wall temperature difference is the maximum.

3. Similar to previous models, maximum local dimensionless Nusselt number ($Nu^{*}(\xi)$) was calculated at the flow inlet where the thermal boundary layer starts to develop. On the other hand, unlike previous Model 1 and 2 simulation results, a continues

decrease in the flow direction was found because of similar degree of change in both temperature and heat flux variation.

3. Compared to SMC tube, within an equivalent refrigerant capacity 15 % lower averaged Nusselt number was investigated with RMC tube.

4. Based on RMC tube coil arrangement, which is shown in figure 6.5, average pressure drop along coil width (W_{Coil}) was obtained by using equation 4.2 as:

$$\Delta P_{RMC-Coil} = 18280 \text{ Pa}$$

According to these results, in spite of the fact that RMC tube could provide similar refrigerant side internal heat transfer performance compare to SMC tube, it requires 2.61 times higher pressure drop to compensate. In order to reduce higher pressure drop defect in RMC design, a sensitivity analysis was applied based on number of port effect and results are presented in the next section.

6.6 Model 3: Fluent Sensitivity Analysis

In this section, the number of port effect is studied based on comparison on the iterative Nusselt number results and estimated heating coil pressure drop. First, according to previously given 36 port round tube geometric specifications, channel numbers were increased to 42 by decreasing port thickness (t_{port}) around 40 %. Based on medium meshing quality, which was investigated as the most computationally efficient earlier, a sectional geometry was created in Gambit. Then, within the same initial conditions, identical iterative procedure was applied in FLUENT solver.

According to equation 4.2, corresponding pressure drop in 42 ports RMC tube coil was obtained smaller than 36 ports RMC tube model, however, it couldn't compensate the pressure difference between SMC tube configuration. Thus, further increase in the port number was required to be studied. Within equivalent tube diameters (D_o and D_i) and tube thickness (t_{tube}) of RMC tube, I created an Annular Micro Channel (AMC) geometry to measure the ultimate number of port effect. Similarly, by using medium meshing quality a sectional geometry was simulated in FLUENT solver within identical iterative process. By using four step data reduction procedure average Nusselt numbers were evaluated for both simulations.

In table 6.6, calculated coil pressure drops and corresponding average water jacket Nusselt number results of RMC tube with 42 ports and AMC tube are presented against to SMC tube and 36 ports RMC tube. According to table 6.6, results were non-dimensionlized based on SMC tube's Nusselt number and Pressure drop respectively. Resultant values were shown in figure 6.10.

Table 6.6: Sensitivity Analysis Results in Round Microchannel

Model Name	Re	ΔP_{coil} [Pa]	Nu_{avg}
RMC tube with 36 ports	32.1	18280	13.1
RMC tube with 42 ports	27.5	15650	12.9
AMC Tube	54.5	4548	12.9
SMC Tube with 23 ports	15.0	5039	15.3

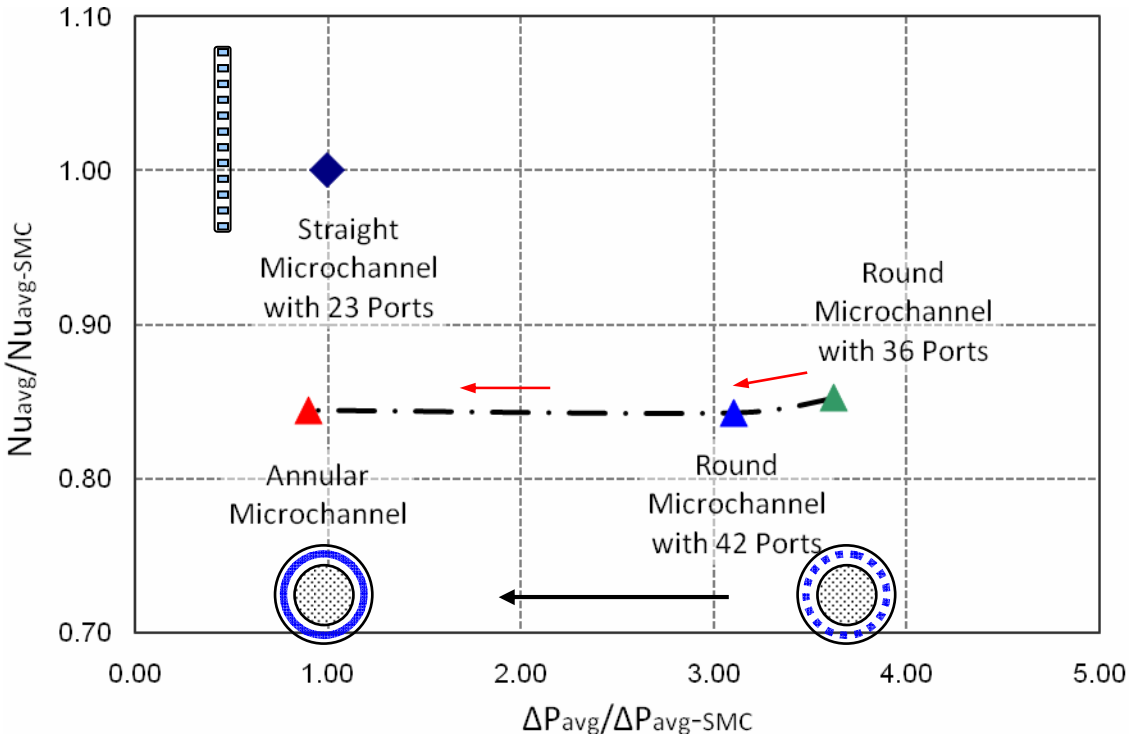

Figure 6.10: Comparison map of the Single Phase Pressure Drop and of the Convective Refrigerant Side Heat Transfer Nusselt Number between Straight Microchannel Tube (baseline geometry) and three Round Microchannel Tube Geometries

As it can be seen in figure 6.10, despite the smaller reduction in the averaged Nusselt number results, increase in port number of RMC tube helped to reduce the pressure drop in general. Moreover, compared to SMC tube around 10 % less pressure drop was reported with annular round microchannel coil configuration. Thus, it was concluded that in a 3/8" size round tube, annular port geometry can provide the optimum cooling performance with less pressure drop in a fin and tube coil configuration

In table 6.7, a summary of simulation Model 3 round microchannel tube inside a counter flow tube heat exchanger is presented in terms of its aim, geometry, boundary conditions, results and conclusion.

Table 6.7: Simulation Model 3 Round Microchannel Tube inside a Counter Flow Tube Heat Exchanger Summary Table

Aim	Geometry		Boundary Conditions		Results		Conclusion
To test the 10.3 mm outer diameter round microchannel (RMC) heat exchanger tube in terms of its internal cooling capacity based on single phase water to water, laminar counter-flow tube in tube heat exchanger simulation by FLUENT solver (Gambit Journal File: appendix B-3 FLUENT Journal File: appendix E-3)	$W_{a\ port}$	0.46 [mm]	$T_{in\ port}$	274.7 [^{o}K]	$\theta(\xi)_{wall}$	Figure 6.8	Compared to SMC tube, within an equivalent refrigerant capacity 15 % lover averaged Nusselt number was investigated with RMC tube.
	$W_{b\ port}$	0.56 [mm]	$\dot{m}_{in\ port}$	3.6 E-5 [kg/s]	$\theta(\xi)_{jacket}$	Figure 6.8	
	$H_{R\ port}$	0.82 [mm]	$V_{in\ port}$	0.09 [m/s]	$q''^{*}(\xi)$	Figure 6.9	
	$D_{h\ port}$	0.6 [mm]	$\mathrm{Re}_{Dh\ port}$	32 [-]	$Nu^{*}(\xi)$	Figure 6.9	
	N_{port}	36 [-]	$P_{gauge\ port}$	6546 [Pa]	$Nu_{avg\ j-FLUENT}$	13.06	
	$D_{h\ jacket}$	19.7 [mm]	$T_{in\ jacket}$	323 [^{o}K]	$\Delta P_{Round-Tube-Coil}$	18280 Pa	
	L_{tube}	1.2 [m]	$\dot{m}_{in\ jacket}$	0.02 [kg/s]			
			$V_{in\ jacket}$	0.03 [m/s]			
			$\mathrm{Re}_{Dh\ jacket}$	1152.4 [-]			
			$P_{gauge\ jacket}$	1.76 [Pa]			

CHAPTER VII

Air Side Heat Transfer Analysis for Refrigerant to Air Cross Flow Heat Exchangers using Microchannel Tubes

In the previous chapters, the refrigerant side heat transfer performance of round microchannel tube was evaluated for water single phase, laminar fluid flow inside a counter flow tube heat exchanger. Additionally, the major pressure drops were calculated based on parallel fin and tube heat exchanger configuration. Beside refrigerant side, air side performance is also required to investigate how efficient the new geometry compares to straight microchannel (SMC) tube. Thus, in this chapter my aim was to analyze the heat transfer capacity of round microchannel (RMC) tubes under cross flow of dry air streams by comparing their air side heat transfer capacity with the ones for SMC tubes. In the following sections, first the simulation procedures, and then the numerical results of air side heat transfer rates of round (microchannel) tube and straight microchannel tubes in cross flow configuration are discussed in details.

7.1 Refrigerant to Air Cross Flow Heat Exchanger Simulation Procedure

In order to have a complete understanding, air side performance study was applied to have an inclusive comparison between vertical SMC coil and horizontal RMC coil arrangements, which are shown in figure 7.1. By using Padhmanabhan et al.'s pervious.

work (2008), I obtained the coil geometries of RMC and SMC heat exchangers, which are given in table 7.1. Based on these geometric properties, a virtual domain was intended to conduct in FLUENT to evaluate the performance measurements numerically

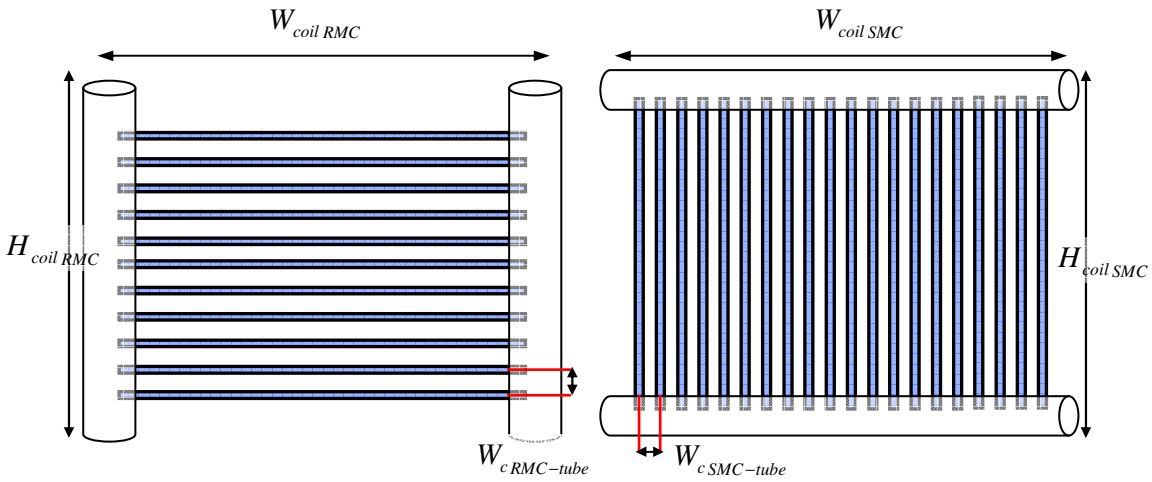

Figure 7.1: 3D Round and Straight Microchannel Coil Configurations

Table 7.1: Model 3, Geometric Specifications of RMC and SMC Coil Configurations

Coil Type	H_{coil} [mm]	W_{coil} [mm]	$W_{c\,tube}$ [mm]	N_{tube}
RMC Coil	965.2	1557	27	36
SMC Coil	923.9	1532	13	121

To increase the efficiency of iterative simulations, following simplifications were applied in the FLUENT model:

1. In order to obtain the geometry effects in the air flow profile such as flow separations and vortex formations, complete coil simulations were required for both heat exchangers. However, due to limitations in my computer system power, it was not

available to analyze whole tube geometries in 3D. Therefore, based on uniform air flow distribution assumption along tube height for RMC ($\frac{d}{dx}=0$) and tube width for SMC ($\frac{d}{dy}=0$), simulations were simplified in to 2D by taking corresponding cross-sections.

2. Based on parallel tubing arrangement, coil configurations were reduced to a single tube simulation within corresponding tube to tube distance, which is shown in figure 7.2. To obtain a complete solution with this simplified geometry, symmetry lines were used at the flow boundaries.

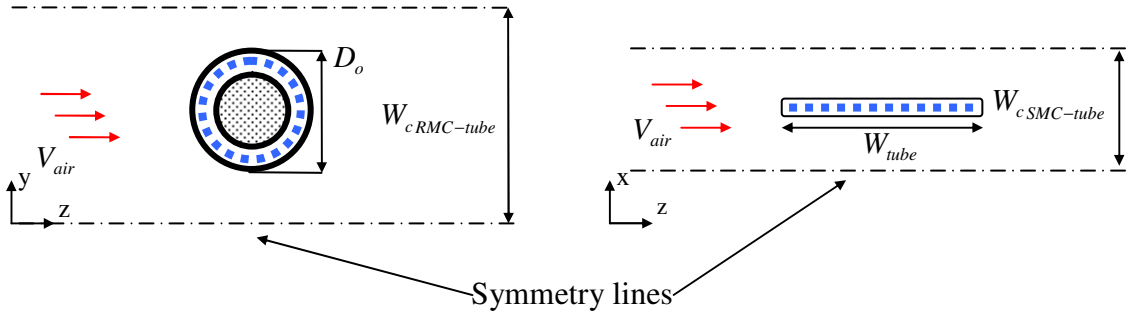

(a) 2D Single RMC Tube Geometry (b) 2D Single SMC Tube Geometry

Figure 7.2: Cross sections of the Round and Straight Microchannel Tubes in refrigerant to air cross flow heat exchangers

3. For the mircoahannel ports, refrigerant was assumed to be at the saturation level. Based on Padhmanabhan et al.'s study, R22 saturation point was used to define the constant refrigerant temperature which were applied to all microchannel port as:

$$T_{R22\,sat} = T_{port} = 275\ ^{o}\text{K}\ (\ 35\ ^{o}\text{F})$$

4. Similarly, based on experimental airside condition, a uniform air flow was defined with the initial conditions of V_{air} = 1 m/s and T_{air} 281.5 ^{o}K (47 ^{o}F) for both microchannel simulations.

According to the assumptions, I aimed to obtain an analogy between SMC and RMC tubes' air side performance. With the help of geometric simplifications, 2D simulations were conducted in FLUENT. In the next sections, each model is analyzed individually and corresponding results are presented in details.

7.2 Simulation Model 4: Round Microchannel Tube Heat Exchanger in Air Cross Flow Heat Exchanger

7.2.1 Model 4: Gambit Pre-Processing and Boundary Conditions

Similar to internal flow studies, to obtain continues external flow simulations smooth meshing qualities were applied by equally spaced grid points. Based on tube spacing ($W_{s\,tube}$) and tube surface length, i.e. tube perimeter (p_{tube}) uniform grid spacing were created by using Gambit post-processing tool. In order to eliminate the effect of meshing quality on FLUENT result, a grid dependence study was required. By decreasing the grid distance gradually, three meshing qualities were generated as: coarse meshing, medium meshing and fine meshing and an example Gambit journal file is given in apndix C-1. Acording to figure 7.3, orders of increase in the node points of W_{stube} and p_{tube} are given in table 7.2, and corresponding meshing qualities are presented in figure 7.4.

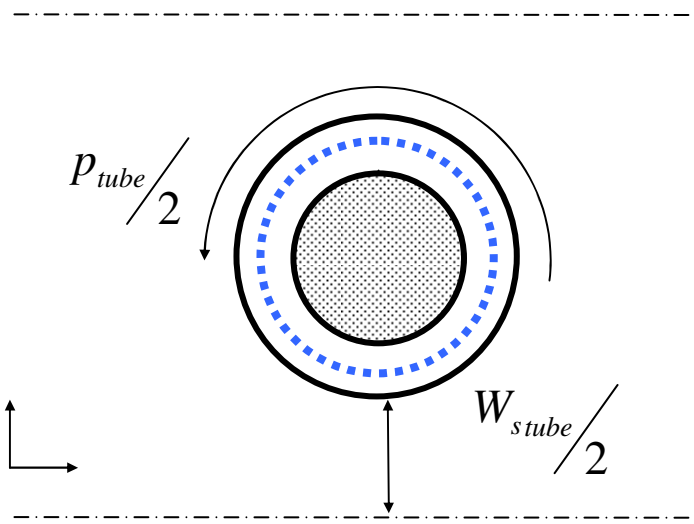

Figure 7.3: Model 4, Single Round Microchannel Tube Simulation Geometry

Table 7.2: Model 4, Geometric Specifications and Node Numbers

Geometry	Length [mm]	Coarse- N_{Node}	Medium - N_{Node}	Fine - N_{Node}
$W_{s\,tube}/2$	8.5	40	60	80
$p_{tube}/2$	16.2	210	360	504

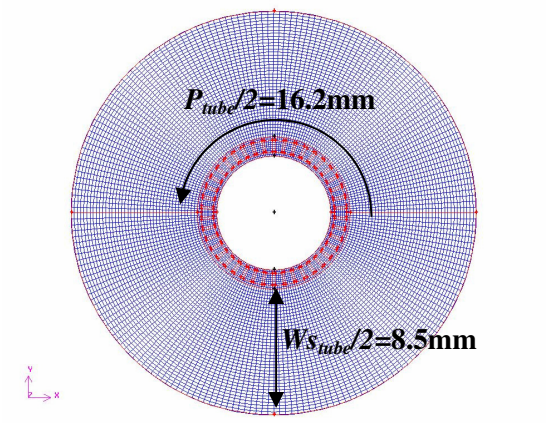

(a) Coarse Meshing (40x210 elements)

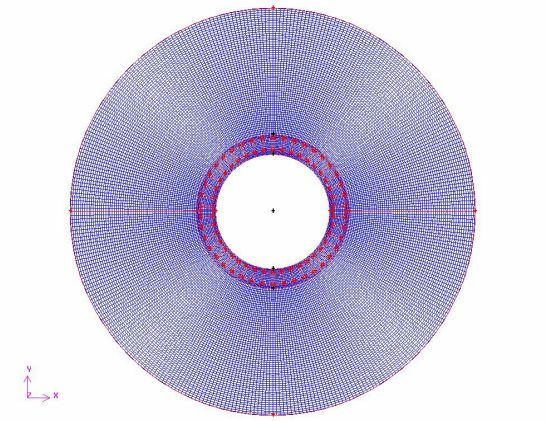

(b) Medium Meshing (60x360 elements)

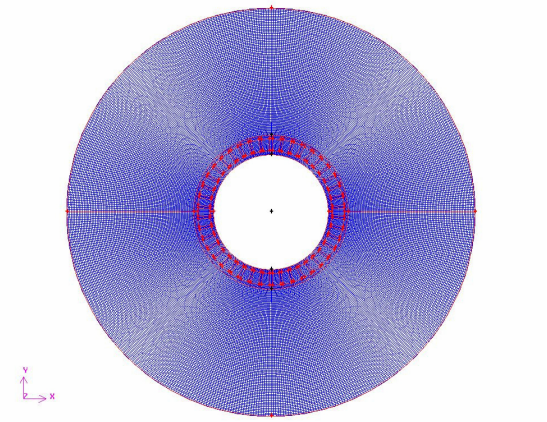

(c) Fine Meshing (80x504 elements)

Figure 7.4: Model 4, Face Mesh Qualities of Grid Study 1, 2 and 3

7.2.2 Model 4: FLUENT Solution

Similar to internal flow analysis, an iterative procedure was developed to perform an external flow simulation and control the convergence of the residuals as:

1. In computation simulations, iterative solver should be selected according to the flow consideration which can be defined by the critical Reynolds number. In the literature, external flow over a circular tube analogy states that the boundary layer remains laminar if the Reynolds number is smaller than 2 x 10^5 (Incropera et al., 2007). In my study, the flow regime was characterized by calculating the Reynolds number based on outer diameter (D_o) of RMC tube as:

$$\mathrm{Re}_{D_o} = \frac{\rho V D_o}{\mu} \tag{7.1}$$

where the initial temperature of air was used to define the fluid properties. According to equation 7.1, Reynolds number was evaluated as; $\mathrm{Re}_{RMC} \approx 729 < 2 \times 10^5$, thus laminar FLUENT solver was selected.

2. By using equation 3.7-3.14, water and air thermal properties were defined as 3rd order polynomial function of temperature. By doing so, sudden temperature change effect on fluid flow included into the solver.

2. Unlike internal flow simulation, unstable residual changes were obtained during iterations due to separation of the laminar boundary layer. To be able to control uncertainty of the solution, momentum URL was decreased to 0.4 accordingly and continues convergence to E-06 level was reached in each residual.

3. In the previous simulations, in order to obtain fully developed flow profile and reduce the iteration time, only momentum equation was solved before including the

energy equation. In this study, same principle was applied to achieve fully developed vortex region, i.e. continues vortex generations in the wake region, before include the energy equations.

By following these observations, a numerical procedure was developed for 2D cross-flow RMC study and to manipulate the iterations FLUENT journal files were created and given in appendix F-1. Based on this iterative procedure, first each meshing quality was simulated and their numerical performances are presented in table 7.3.

Table 7.3: Model 4, Grid Dependency Study Residual Comparison

Mesh Quality	Momentum Residual	Number of Iterations	Iteration Time [h:m]
Coarse	1.42E-07	17100	4:05
Medium	6.09E-08	17100	7:38
Fine	1.34E-08	16111	9:16

Compared to each meshing results, most efficient grid sizing was selected and additional iterations were applied to converge the momentum residual E-07 level. In the following section, grid dependency results and corresponding data reduction procedure is reported.

7.2.3 Model 4: FLUENT Post-processing

After finalizing the iterative procedure of grid dependency study, first, the surface heat flux variation along surface length ($q''(s)$) were obtained by using FLUENT x-y plot post-processing tool. By storing local heat flux data into Excel spreadsheet's columns,

dimensionless local heat flux profiles ($q''^{*}(\xi)$) along upper and lover surfaces were obtained using equation 5.4, where $\xi = \frac{s}{(p_{tube}/2)}$.

As it can bee seen in figure 7.5, heat transfer from air flow to tube wall was showed differences at particular locations on each surface which could be explained by boundary layer separation and unstable vortex formation.

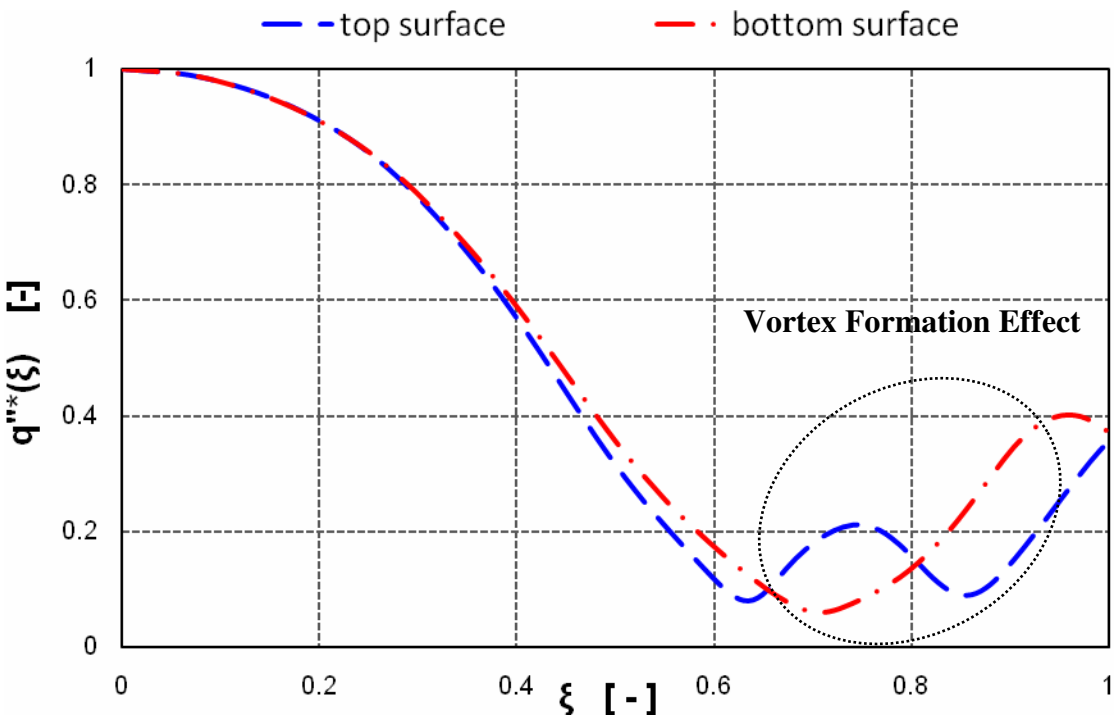

Figure 7.5: Model 4, Dimensionless Local Heat Flux Variation

In RMC tube, it was observed that the positions of the vortices within the wake region changes with further iterations. In addition, differences in the mesh density also affected the vortex formation profile which differ the heat flux on each surface. As a results, it was required to develop and additional data reduction procedure to obtain

reasonable comparisons between each models. Based on numerical results, an average cooling performance was evaluated by following three step procedures:

1. To eliminate the surface area effect, local heat flux values were integrated numerically over upper and lower surface length (s), respectively:

$$\frac{Q_{top}}{L_{tube}} = q'_{top}(s) = \int_0^{s_n} q''_{top}(s)ds = \Delta s\left[\frac{q''_{top}(s_0) + q''_{top}(s_n)}{2} + \sum_{k=1}^{n-1} q''_{top}(s_k)\right] \tag{7.2}$$

$$\frac{Q_{bottom}}{L_{tube}} = q'_{bottom}(s) = \int_0^{s_n} q''_{bottom}(s)ds = \Delta s\left[\frac{q''_{bottom}(s_0) + q''_{bottom}(s_n)}{2} + \sum_{k=1}^{n-1} q''_{bottom}(s_k)\right] \tag{7.3}$$

where; $s_n = p_{tube}/2$ and $L_{tube} = W_{RMC-coil}$

2. By using equation 7.2 and 7.3, calculated local heat transfer values along upper and lower surface lengths ($q'_{top}(s)$, $q'_{bottom}(s)$) were summed and average cooling capacity variation was obtained as:

$$Q_{avg}(s) = \sum Q(s) = L_{tube}\left(\int_0^{p_{tube}/2} q''_{top}(s)ds + \int_0^{p_{tube}/2} q''_{bottom}(s)ds\right) \tag{7.4}$$

3. Additionally, in order to eliminate the measured units, results were non-dimensionalized by:

$$\Phi(\xi) = \frac{Q_{avg}(s)}{Q_{\max}} \tag{7.5}$$

According to this data reduction procedure, dimensionless average cooling capacity variation $\Phi(\xi)$ along RMC tube surface length was obtained for each meshing quality and results are presented in figure 7.6. Compared to fine meshing results, coarse meshing

had 4% difference due to its lack of number of elements. Medium meshing, however, provided more than 99% similarity with the fine meshing cooling capacity results.

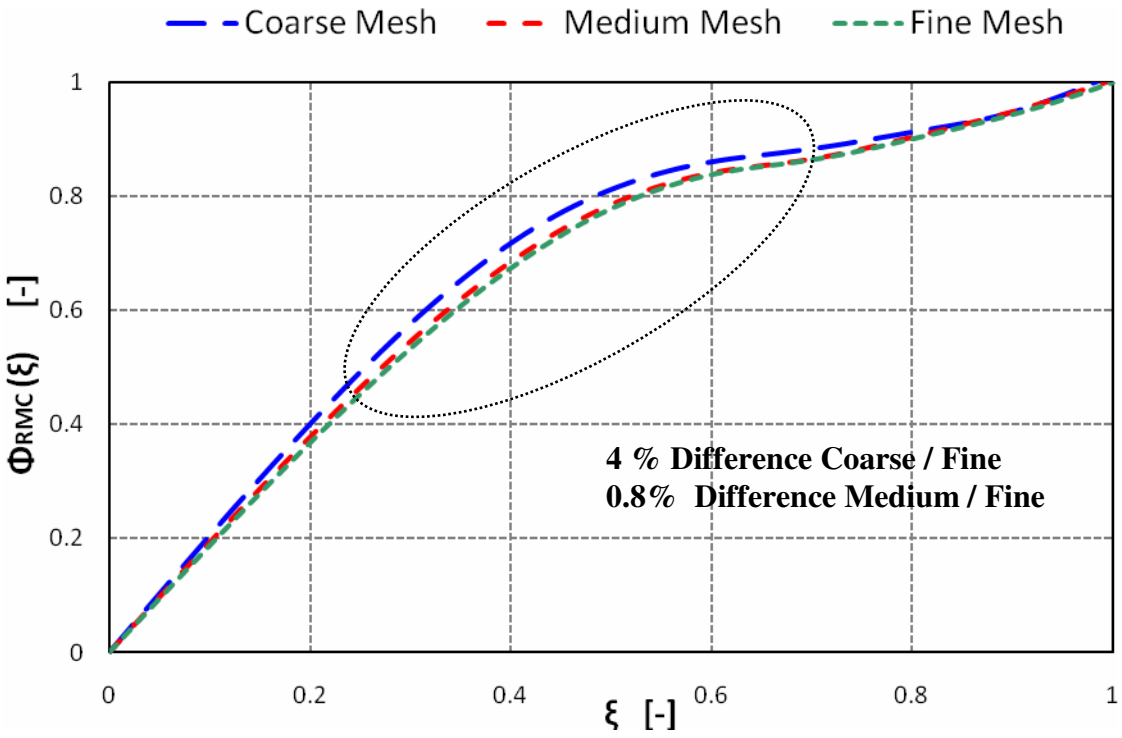

Figure 7.6: Model 4, Grid Dependency Study Dimensionless Cooling Distribution

Additionally, according to table 7.3, medium meshing provided faster computational performance than fine meshing. Thus, by using medium grid sizing further iterations were applied to reduce its residual value and to investigate the vortex region effect on RMC tube cooling performance. Besides, velocity and temperature maps were plotted by using FLUENT post-processing tools and results are presented in figure 7.7 and 7.8 accordingly.

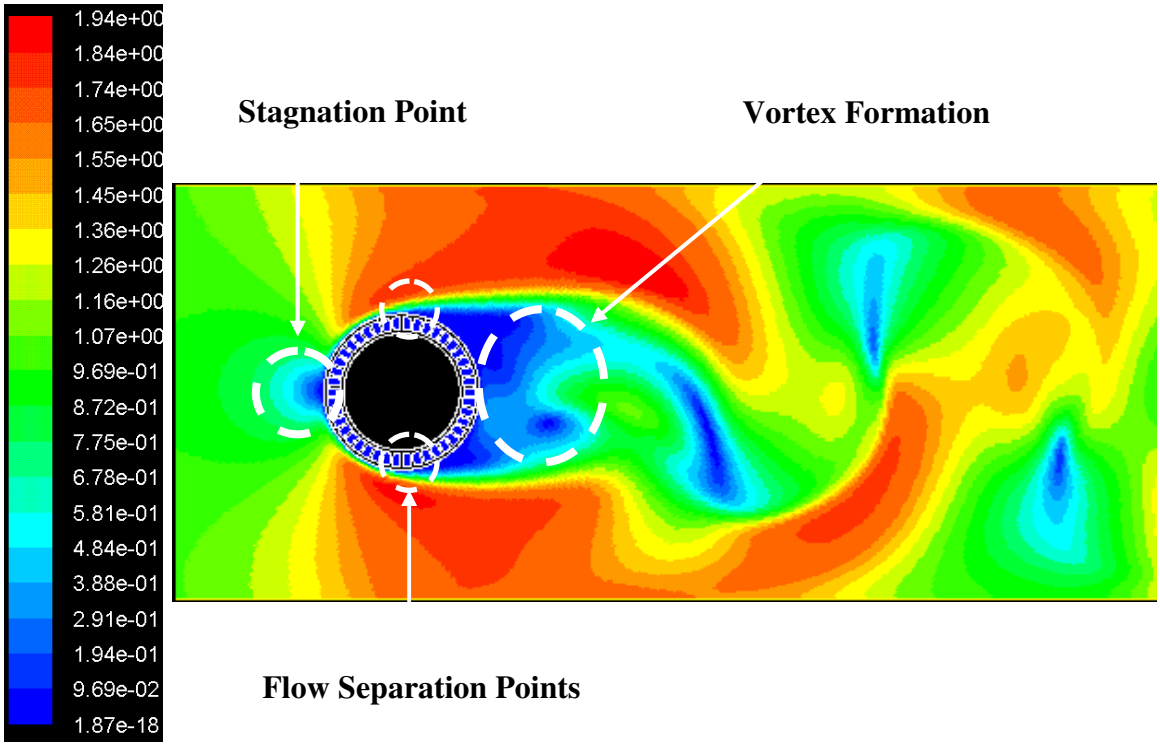

Figure 7.7: Model 4, Velocity Profile of Air Cross Flow over Do: 10.3mm AMC Tube

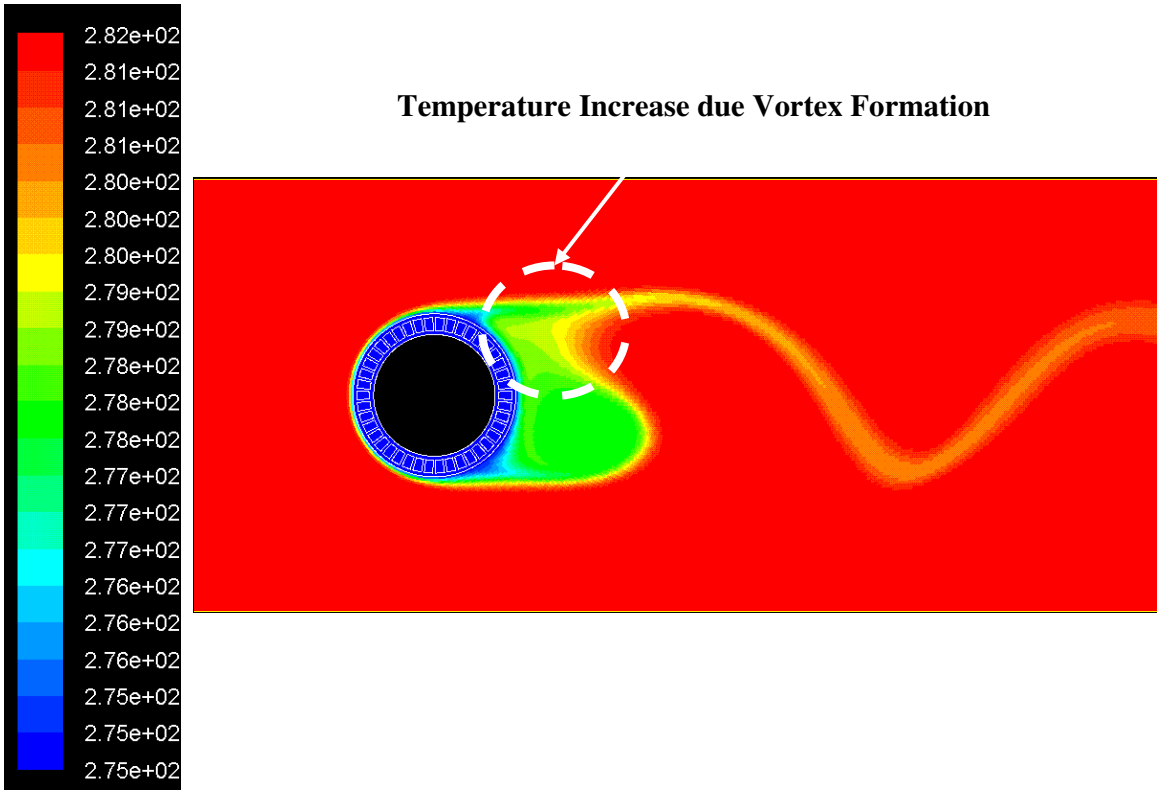

Figure 7.8: Model 4, Temperature Map of Air Cross Flow over Do: 10.3mm AMC Tube

According to external flow over circular cylinder analogy (Incropera et al, 2007), in figure 7.7, after stagnation point flow started to accelerate because of favorable pressure gradient ($\frac{dP}{ds} < 0$) and the laminar boundary layer started to develop over the tube surface. Then, based on increase in the pressure gradient, air flow started to decelerate due to adverse pressure gradient ($\frac{dP}{ds} > 0$) and reached to zero. At this point, flow separation was occurred near the surface since flow momentum was insufficient compared to higher pressure gradient. As a result, laminar boundary layer was separated and vortex formation started in the downstream region which is called wake region. To have a better understanding, flow stream lines were plotted by FLUENT solver and presented in figure 7.9.

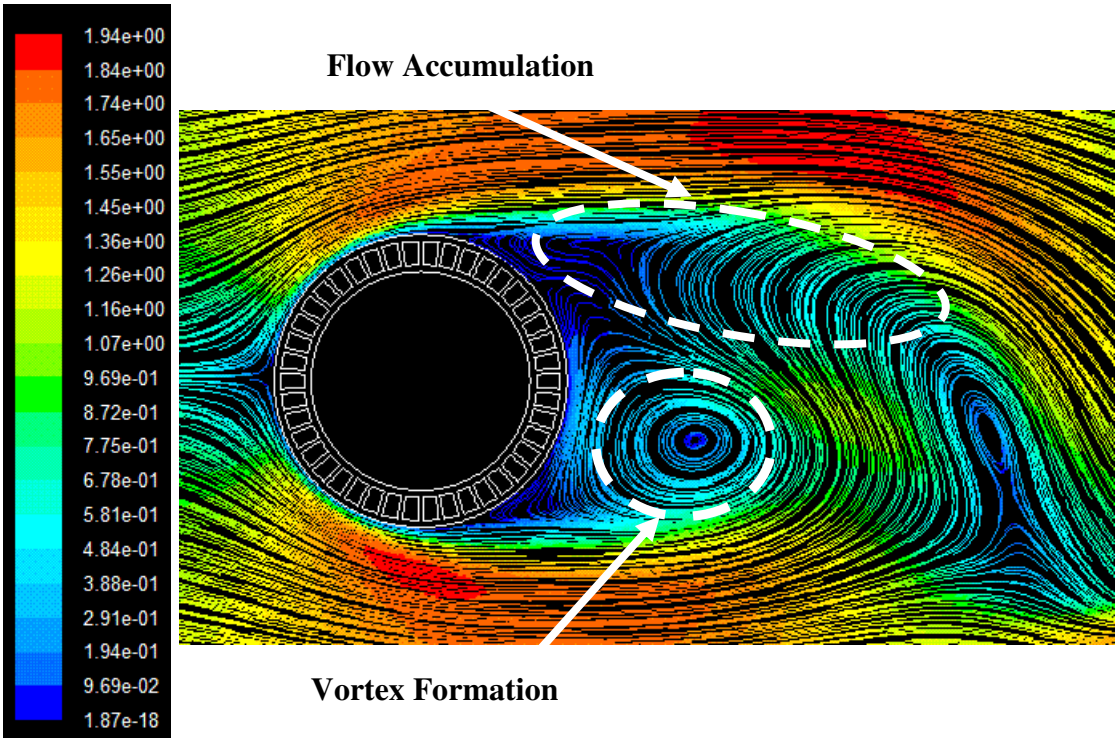

Figure 7.9: Model 4, Stream Lines of Air Cross Flow over Do: 10.3mm AMC Tube

Because of vortex formation, an accumulation from hot air to tube surface was reported and shown by figure 7.9. These sudden changes of the flow field and the temperature variations strongly affected the heat transfer performance of RMC tube. Based on this fact, three distinct regions were observed at the heat transfer variation and defined as laminar convection, boundary layer separation and vortex region, which are shown in figure 7.10.

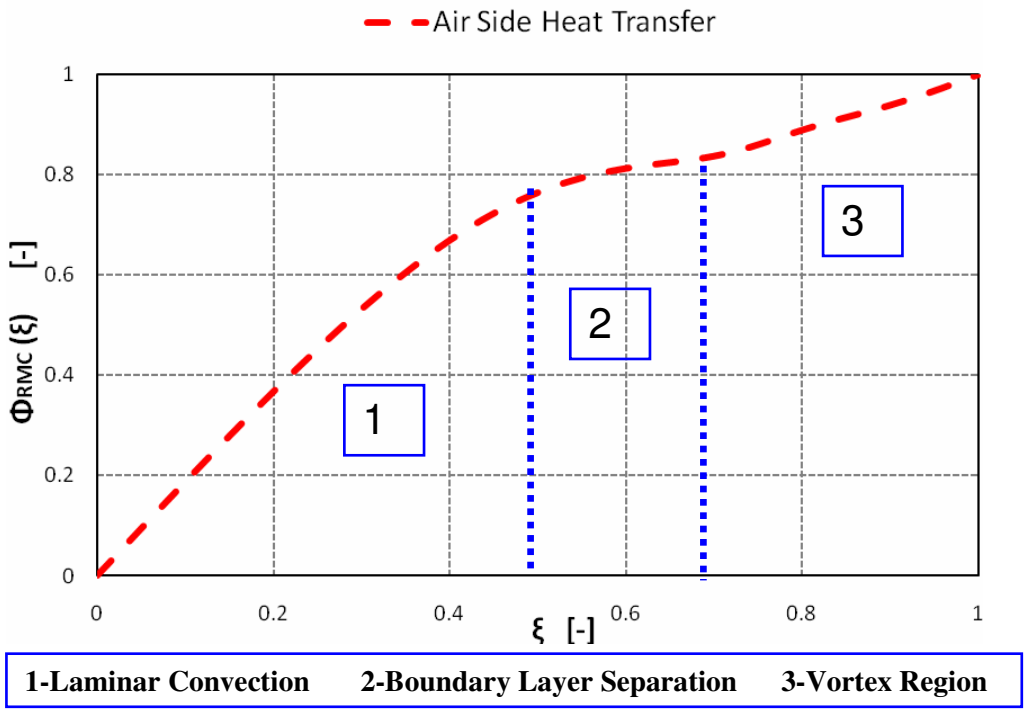

Figure 7.10: Model 4, Dimensionless Local Cooling Capacity Distribution

Finally, by assuming uniform heat transfer in each tube, averaged 36 parallel tubes -RMC coil cooling capacity was calculated based on its coil width (W_{coil}) and obtained as:

$$Q_{RMC-coil\,avg} = 458.2 \text{ W}$$

With this conclusion, air side performance analysis of 10.3 mm outer diameter RMC tube was completed. In the next section, SMC tube results are discussed in details.

7.3 Simulation Model 5: Straight Microchannel Tubes in Refrigerant to Air Cross Flow Heat Exchangers

7.3.1 Model 5: Gambit Pre-Processing and Boundary Conditions

Similar to previous external flow analysis, by using tube spacing ($W_{s\,tube}$) to SMC tube perimeter (p_{tube}), which are defined in figure 7.11, equally spaced grid points were generated to obtain continues flow simulations. To reduce the grid sizing effect on iterative procedure, three different grid sizing were created by increasing the node points of W_{stube} and p_{tube} accordingly, which are given in table 7.4. Resultant meshing qualities, i.e. coarse, medium and fine meshings are presented in figure 7.12.

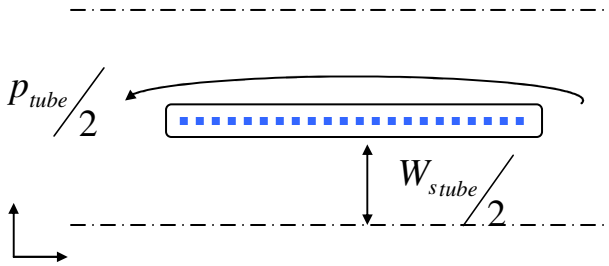

Figure 7.11: Model 5, Single Tube Simulation Geometry

Table 7.4: Model 5, Geometric Specifications and Node Numbers

Geometry	Length [mm]	Coarse- N_{Node}	Medium - N_{Node}	Fine - N_{Node}
$W_{s\,tube}/2$	5.7	25	50	80
$p_{tube}/2$	19.6	180	360	480

To manipulate the meshing process, Gambit journal files were created an example is given in appendix C-2.

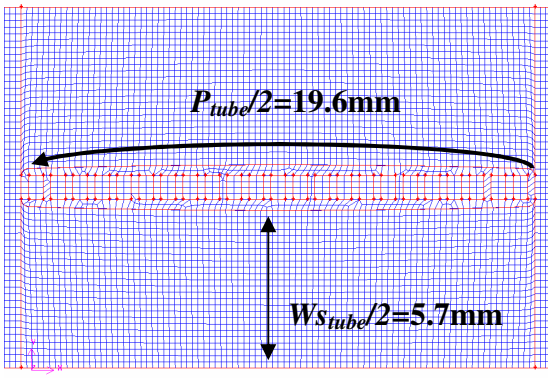

(a) Coarse Meshing (25x180 elements)

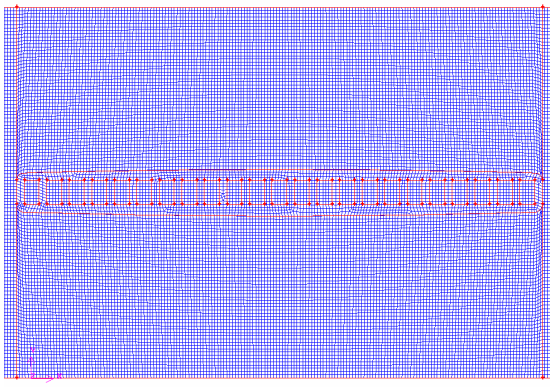

(b) Medium Meshing (50x360 elements)

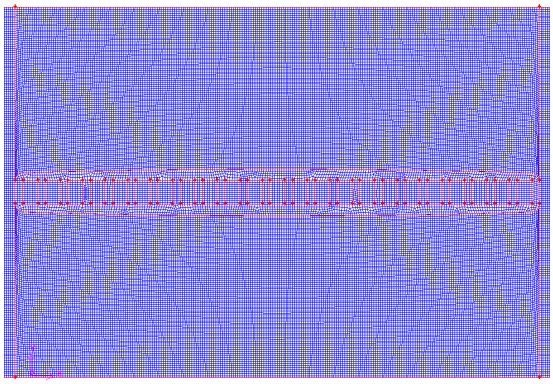

(c) Fine Meshing (80x480 elements)

Figure 7.12: Model 5, Face Mesh Qualities of Grid Study 1, 2 and 3

7.3.2 Model 5: FLUENT Solution

According to previously defined equation 7.1, corresponding Reynolds number of air flow over SMC tube surface were calculated based on external flow over a flat plate analogy, where tube length was used as characteristic length:

$$\mathrm{Re}_L = \frac{\rho\, V L_{tube}}{\mu} \tag{7.6}$$

By substituting previously defined air velocity ($V_{air} = 1 m/s$) and calculating the thermal properties at inlet temperature, resultant Reynolds number were obtained as $\mathrm{Re}_{SMC} \approx 1275 < 5 \text{ x } 10^5$ (Incropera et al, 2007), thus laminar FLUENT solver was selected. By following the same iterative procedure, which was defined in previous RMC simulation, FLUENT journal files were created and an example is given in appendix F-2. In order to reach fully developed velocity profile, convergence level was set to E-11 to have enough number of iteration in each SMC simulation.

Before analyzing the heat transfer performance of SMC tube in details, I investigated the grid dependency in my FLUENT code by simulating three different meshing qualities within the same iterative procedure and presented their numerical performances in table 7.5. In the following section, corresponding grid dependency results and average heat transfer capacity of SMC tube coil are presented in details.

Table 7.5: Model 5, Grid Dependency Study Residual Comparison

Mesh Quality	Momentum Residual	Number of Iterations	Iteration Time [h:m]
Coarse	3.01E-11	12939	1:00
Medium	5.83E-11	13740	2:19
Fine	5.67E-11	14598	4:34

7.3.3 Model 5: FLUENT Post-Processing

In order to have a comparable results with RMC tube simulation, same three step data reduction procedure were applied to evaluate average external cooling capacity profile of SMC tube along its tube surface (s) as :

1. By using equation 7.2 and 7.3 local heat flux values were integrated numerically over upper and lower surface lengths. By doing so, surface area effect was reduced to tube length (L_{tube}).

2. Substituting resultant heat transfer integrations over upper and lower surfaces into equation 7.4 , average cooling capacity formation along tube length ($Q_{avg}(s)$) were obtained was obtained .

3. Finally, each local value was non-dimensionalized ($\Phi(\xi)$) by using equation 7.5 to neglect the measured units in the results.

Following the three step procedure , first grid sizing effect were investigated by comparing coarse, medium and fine meshing results. As it can be seen in figure 7.13, despite their similar linear trends in the cooling capacity profile, 2.6 % difference were calculated between coarse and fine meshing results. Medium meshing, however, had 99% similarity in its results compared to fine meshing. Additionally, according to iterative performances of each meshing quality, medium meshing was more computationally economic than fine meshing regarding its smaller iteration time. Thus, additional iterations were applied by using medium grid sizing to reduce the residual values at E-12 level and corresponding velocity and temperature maps were plotted by using FLUENT post processing tools which are shown in figure 13 and 14, respectively.

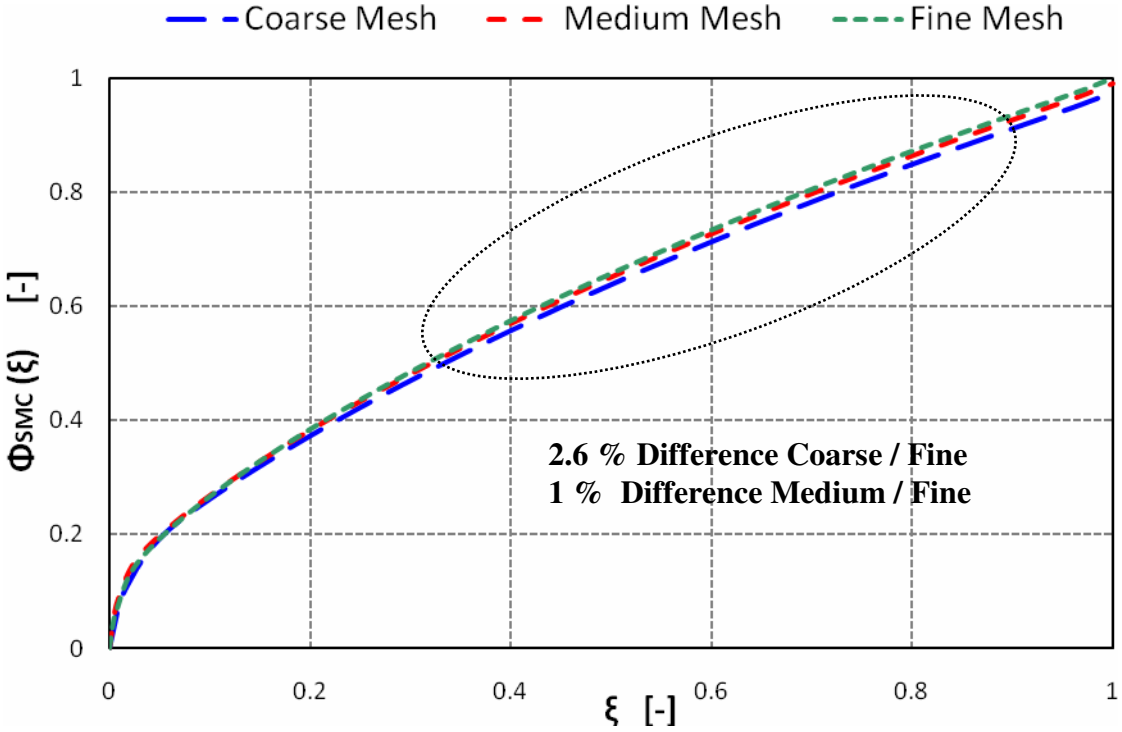

Figure 7.13: Model 5, Grid Dependency Study Dimensionless Cooling Distribution

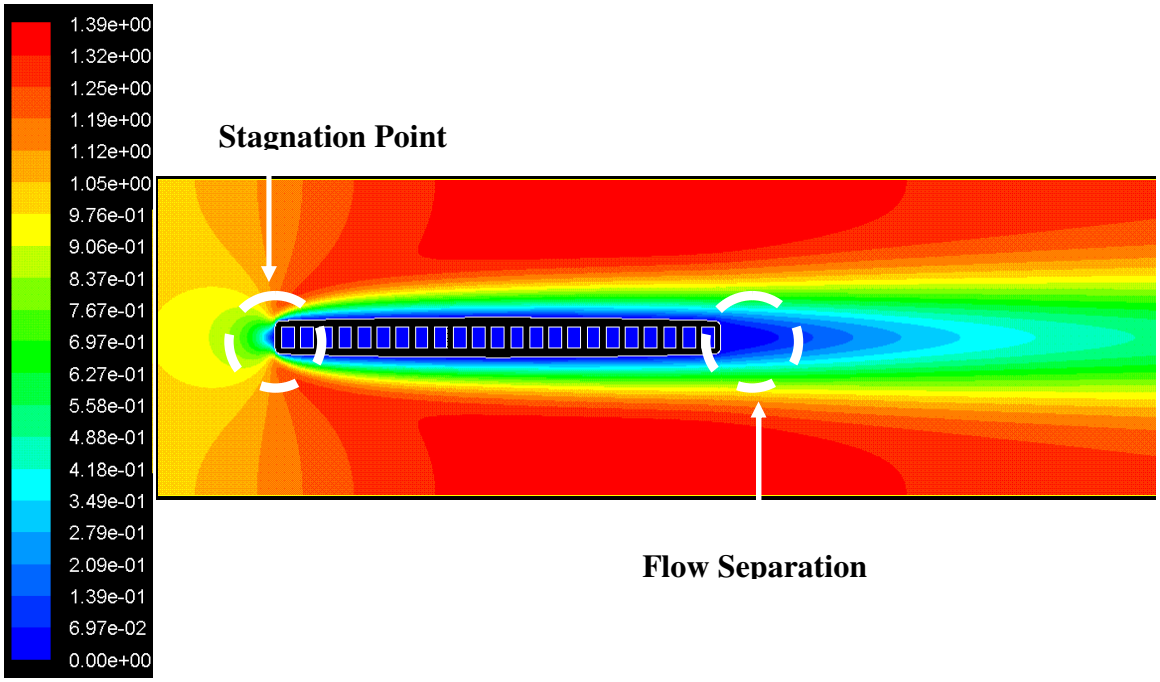

Figure 7.14: Model 5, Velocity Profile of Air Cross Flow over SMC Tube

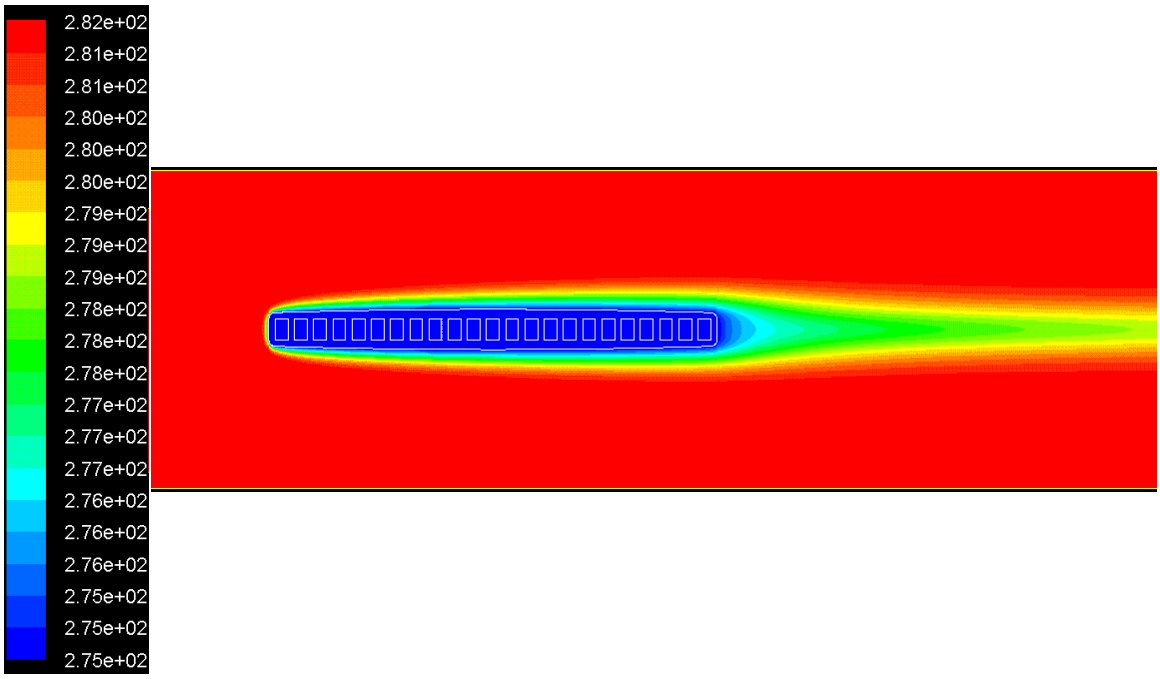

Figure 7.15: Model 5, Temperature Map of Air Cross Flow over SMC Tube

Unlike RMC tube, smooth air flow motion which was controlled by the viscous forces was obtained in SMC tube simulation because of its geometric configuration. Compared to RMC tube, negligible vortex formations were obtained at the flow separation region which is shown in figure 7.16. Additionally, corresponding dimensionless increased in averaged cooling capacity is shown in figure 7.17.

Finally , according to previously applied uniform heat transfer assumption in each tube , averaged 121 parallel tubes - SMC coil cooling capacity was evaluated based on its coil height (H_{coil}) as :

$$Q_{avg\ SMC-coil} = 765.32 \text{ W}$$

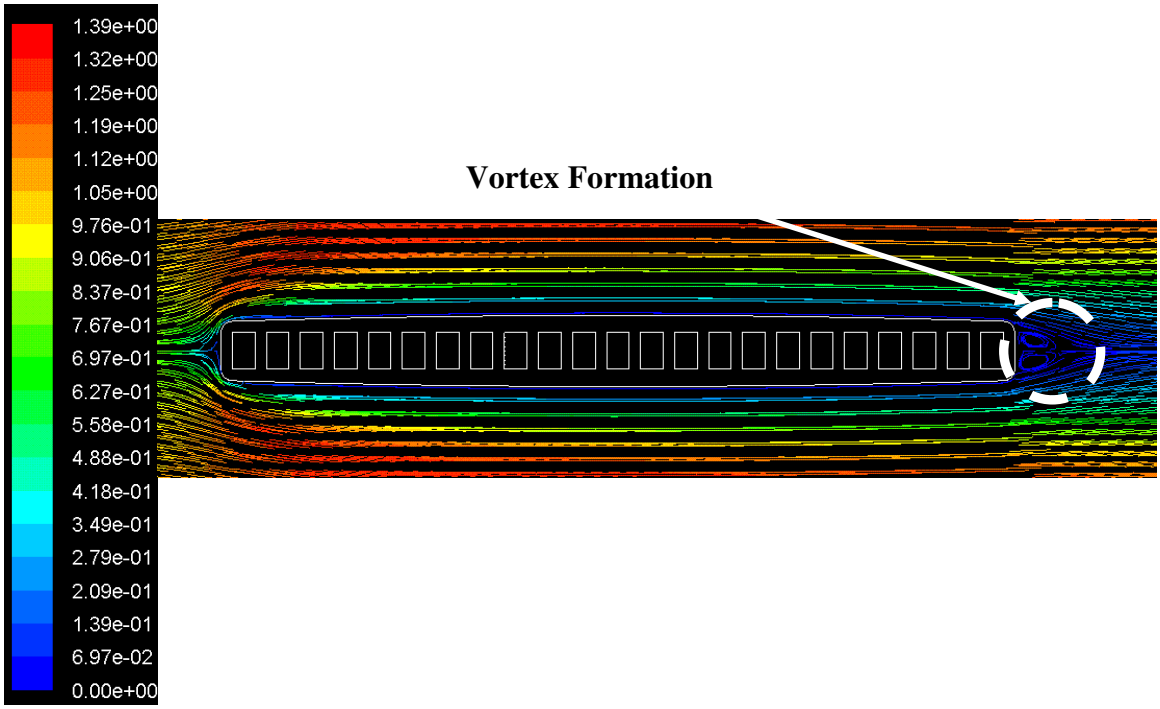

Figure 7.16: Model 5, Stream Lines of Air Cross Flow over SMC Tube

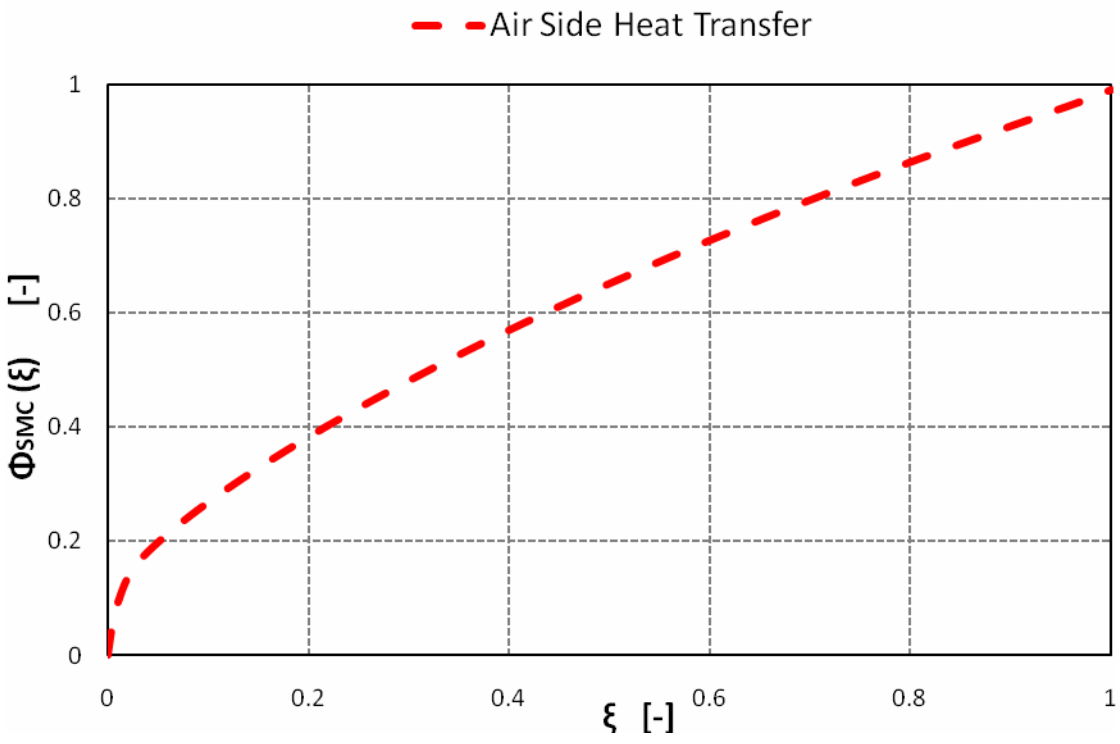

Figure 7.17: Model 5, Dimensionless Local Cooling Capacity Distribution

7.4 Discussion of the Simulation Results of the Refrigerant to Air Cross Flow Heat Exchangers Using Microchannel Technology

Based on Model 4 and Model 5 numerical results, following remarks were obtained:

1. According to figure 7.10, compared to rate of increase in laminar convection, around 65% decreases were calculated due to boundary layer separation within the mid section of RMC tube surface. On the other hand, because of flow accumulation from hot air side to downstream, additional 31 % increase were evaluated in the vortex region compared to flow separation section.

2. As a results of its symmetric and continues temperature decrease, almost linear heat transfer were investigated in air flow during its external flow over SMC tube surface, which is shown in figure 7.17

3. In spite of having larger tube lenght (L_{tube}), compared to SMC coil 40 % less cooling capacity were obtained with RMC coil due to its limited tube number and higher tube spacing.

In table 7.6 and 7.7 summaries of simulation Model 4 round microchannel tube and Model 5 straight microchannel tube inside air cross flow heat exchangers are presented in terms of its aim, geometry, boundary conditions, results and a brief conclusion.

Table 7.6: Simulation Model 4 Round Microchannel Tube inside Air Cross Flow Heat Exchanger Summary Table

Aim	Geometry		Boundary Conditions		Results		Conclusion
To analyze the heat transfer capacity of round microchannel (RMC) tube under cross flow of dry air streams by comparing its air side heat transfer capacity with straight microchannel tube (Gambit Journal File: appendix C-1 FLUENT Journal File: appendix F-1)	D_o	10.3 [mm]	$T_{in\ port}$	275 [^{o}K]	Velocity Profile	Figure 7.7	Sudden changes in the air flow strongly affected the heat transfer performance of RMC tube. Because of vortex formations in the vortex region additional 31 % increase were evaluated compared to its flow separation section.
	$W_{s\ tube}$	17 [mm]	$T_{in\ AIR}$	281.5[^{o}K]	Temperature Map	Figure 7.8	
	$W_{c\ tube}$	27 [mm]	$V_{in\ AIR}$	1 [m/s]	Stream Line Profile	Figure 7.9	
	N_{tube}	36 [-]	$\mathrm{Re}_{Do\ AIR}$	729 [-]	$\Phi(\xi)$	Figure 7.10	
					$Q_{avg\ RMC-coil}$	458.2 W	

Table 7.7: Simulation Model 5 Straight Microchannel Tube inside Air Cross Flow Heat Exchanger Summary Table

Aim	Geometry		Boundary Conditions		Results		Conclusion
To analyze the heat transfer capacity of straight microchannel (SMC) tube under cross flow of dry air streams to compare its air side heat transfer performance with round microchannel (RMC) tube (Gambit Journal File: appendix C-2 FLUENT Journal File: appendix F-2)	W_{tube}	1.3 [mm]	$T_{in\ port}$	275 [^{o}K]	Velocity Profile	Figure 7.14	Despite of having smaller tube length than RMC tube, 40 % more cooling performance were obtained with SMC coil due to its advance tube numbers.
	$W_{s\ tube}$	11 [mm]	$T_{in\ AIR}$	281.5[^{o}K]	Temperature Map	Figure 7.15	
	$W_{c\ tube}$	13 [mm]	$V_{in\ AIR}$	1 [m/s]	Stream Line Profile	Figure 7.16	
	N_{tube}	121 [-]	$\mathrm{Re}_{L\ AIR}$	1275 [-]	$\Phi(\xi)$	Figure 7.17	
					$Q_{avg\ SMC-coil}$	758.2 W	

CHAPTER VIII

Results and Discussion

In the previous sections microchannel heat exchanger numerical models were created by using the FLUENT CFD solver and a sensitivity analysis of calculated local heat flux from both refrigerant and air sides was given with respect to the grid size. Next, I summarize the numerical results from the simulations of the previous chapters and I present a parametric study that highlights the tube diameter and tube spacing impact on the heat transfer and pressure drop performances of round microchannel tube type heat exchangers.

8.1 Results of the Refrigerant Side Convective Heat Transfer Study for Microchannel Tubes inside a Counter Flow Tube Heat Exchanger

From the simulated results of laminar flow inside a counter-flow type tube heat exchanger, single phase refrigerant side Nusselt numbers and pressure drops are reduced in dimensionless form by dividing each data point by the maximum value of the straight microchannel (SMC) tube. This is chosen as baseline tube profile for the heat exchanger and, thus, a value of 1 is assigned by definition to the dimensionless Nusselt number (or dimensionless pressure drop) calculated inside vertical straight microchannel tubes.

As shown in figure 8.1, the local single phase Nusselt number of round microchannel (RMC) tube was estimated to be about 15% lower than SMC tube and about 24% higher than conventional diameter round tubes. The reduced Nusselt number of the round microchannel tube is due to its adiabatic inner surface, which decreases the ratio of the secondary heat transfer area on the refrigerant flow rate carried within the coil itself.

A compactness factor (*CF*) is calculated as shonw in Eq 8.1 and the values for the coils considered in this thesis are given in Table 8.1 below:

$$CF = \frac{A_{coil\,\mathrm{sec}\,ondary}}{\dot{m}_{coil}} \tag{8.1}$$

where ;

$$A_{coil\,\mathrm{sec}\,ondary} = p_{tube} \times L_{tube} \times N_{tube} \tag{8.2}$$

Table 8.1: Compactness (coil heat transfer area per coil refrigerant) of Heat Exchanger Coils

Heat Exchanger	p_{tube} [m]	L_{tube} [m]	N_{tube} [-]	$\dot{m}_{coil}$ [kg/s]	$A_{coil\,\mathrm{sec}\,ondary}$ [m^2]	CF [m^2/ (kg/s)]
SMC Tube	0.04	0.92	121	0.05	4.19	90
RMC Tube (D_o 10.3mm)	0.03	1.56	36	0.05	1.81	39
AMC Tube (D_o 10.3mm)	0.03	1.56	36	0.05	1.81	39
Round Tube	0.03	1.56	36	0.12	1.81	15

Based on Eq-8.1, *CF* represents a parameter that quantifies the compactness of the heat exchanger with respect to the heat transfer heating capacity of the coil. According to table 8.1, *CF* is 90 [m^2/ (kg/s)] for SMC and only 39 [m^2/ (kg/s)] for RMC. In addition,

with identical 10.3mm tube diameter, the ratio of tube surface heat transfer area on refrigerant flow rate within the tube is also 39 [m^2/ (kg/s)] for annular type microchannel (AMC) tube. The local Nusselt number of the AMC tube was found to be similar to RMC tube. Both AMC and RMC tubes have a CF that is about 57 % lower than SMC tube and this resulted in a decrease of the average Nusselt number of the tubes of approximately 15%. Finally, the round tube has the lowest ratio of secondary heat transfer area on refrigerant carried inside the tubes. This is only 15 [m^2/ (kg/s)] and the round tube has the lowest refrigerant side single phase convective Nusselt number.

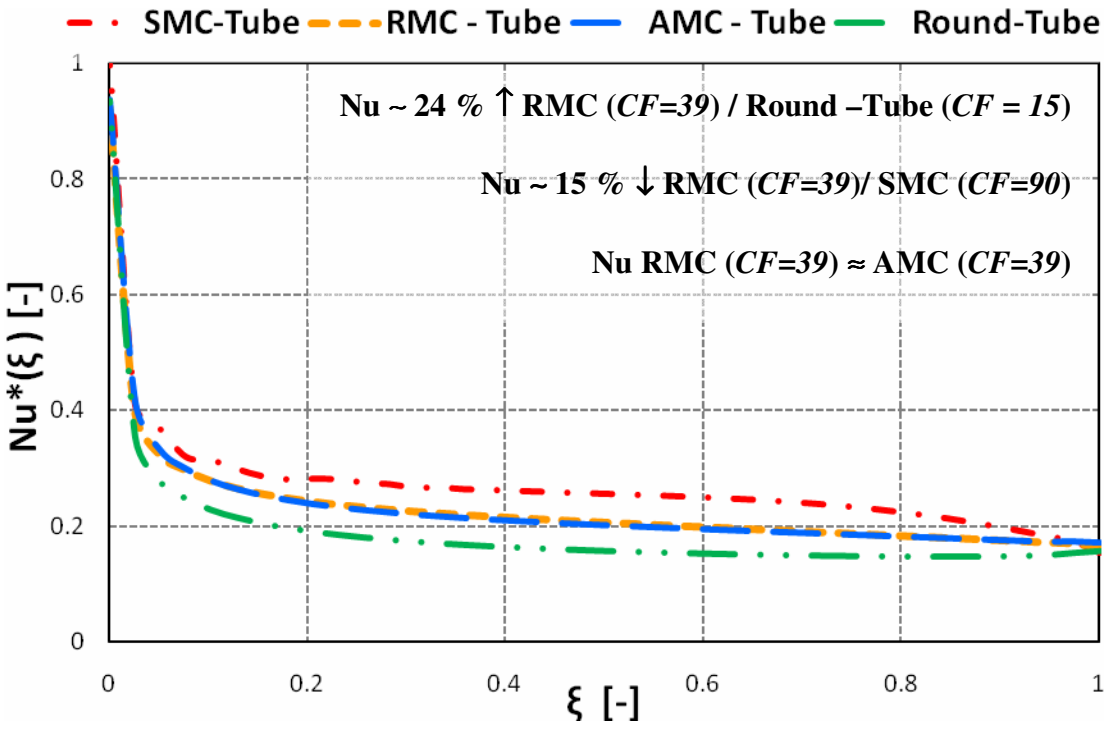

Figure 8.1: Convective Refrigerant Side Local Nusselt numbers (Non-dimensionlozed with respect to SMC) Comparison of Full Round Tube (Round-Tube), Straight Microchannel Tube (SMC), Round Microchannel Tube (RMC) and Annular type Microchannel Tube (AMC)

For an outdoor evaporator of about 4 tons of refrigeration capacity, the coil with vertical straight microchannel tubes would have typical dimensions of 1.5 m in height by 9.2 m in width. Thus the straight microchannel tube is only 1.5 m long. A similar coil using horizontal round tubes would have RMC tubes of about 9.6 m in length. All RMC tubes are designed to be circuited in parallel for the entire height of the coil and they slightly extend the straight microchannel tube coil dimensions. The major pressure drops were calculated by using Eq. 4-2 and results are summarized in figure 8.2.

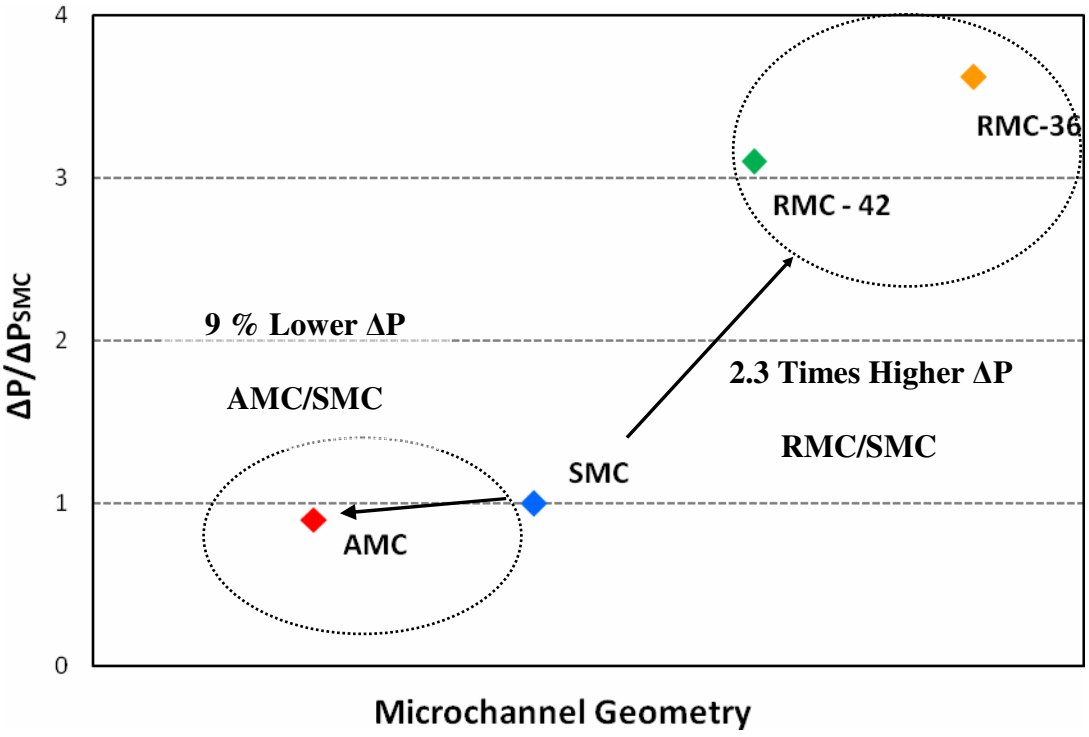

Figure 8.2: Refrigerant Side Major Pressure Drop
(Non-dimensionlozed with respect to SMC) Comparison
of Full Round Tube (Round-Tube), Straight Microchannel Tube (SMC),
Round Microchannel Tube (RMC) and Annular type Microchannel Tube (AMC)

A RMC tube coil would have an estimated refrigerant side pressure drop of about 2.3 times higher than the one in SMC coil. Surprisingly, an annular type micro tube coil with similar outer tube diameter of about 10.3mm and annular gap of about 1.6mm hydraulic diameter gives reduced pressure drop by about 9% with respect to SMC tube coil. The removal of the micro-ports in the tube increases the refrigerant flow area by about 54% and reduces significantly the frictional losses along the tube.

8.2 Results of Air Side Heat Transfer Analysis for Refrigerant to Air Cross Flow Heat Exchangers using Microchannel Tubes

In addition to refrigerant side analysis, I numerically studied the air side performance of RMC tubes by estimating the outside convective heat transfer rates of these tubes cooled by of dry air streams in cross flow heat exchangers. In should be noticed that only the tube surface area, which is the secondary heat transfer area of the coil, was considered in my study. The primary fin surface area was not considered here.

Within to tube spacing ($W_{s\,tube}$) between two straight microchannel tubes, only one RMC tube of outer diameter of 10.3 mm exists. The tube spacing comparison is graphically illustrated in figure 8.3. Based on this configuration, I compared the dry cooling performance of RMC tube geometry with SMC tube within individual coil configurations. The comparison is summarized in figure 8.4. The results show that, RMC coil has 3.4 % lower cooling capacity than SMC tube coil due to its wider tube spacing. Thus, reduction in round tube diameter from 10.3 mm to 5.15 mm was studied to investigate its effect on coil heat transfer performance and major refrigerant side pressure drop. Corresponding results are presented in the following section.

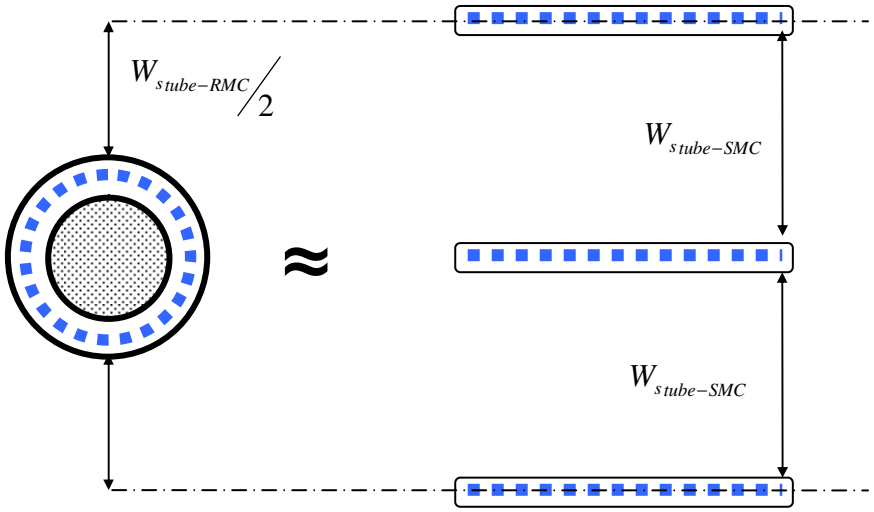

Figure 8.3: Comparison of Tube Spacing between Round Microchannel (D_o : 10.3mm) and Straight Microchannels

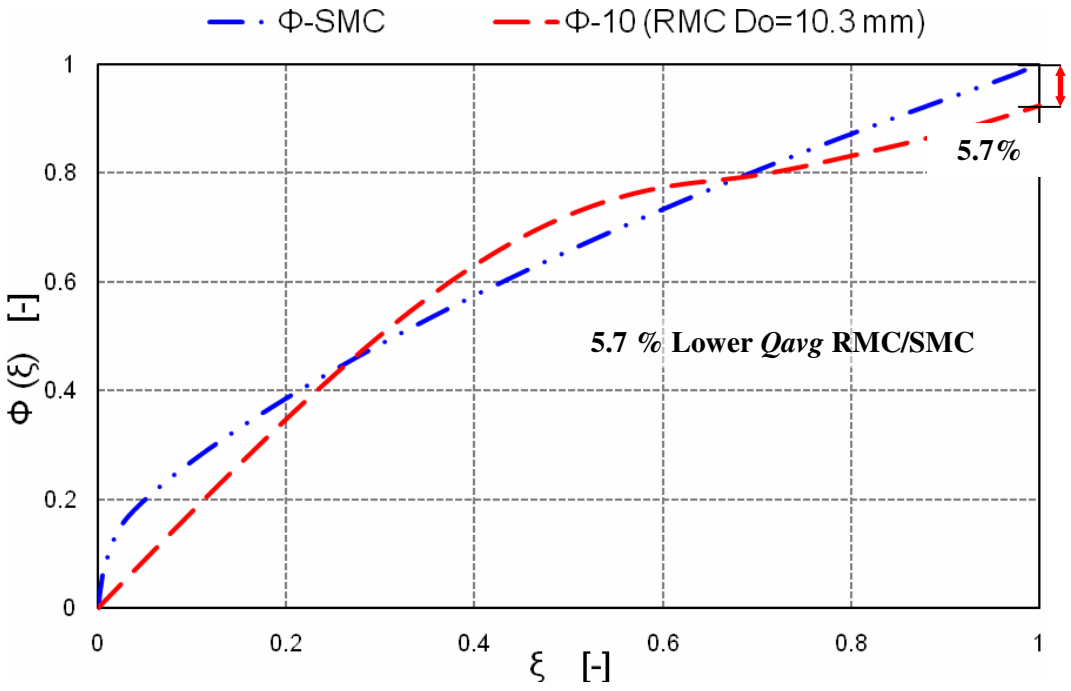

Figure 8.4: Comparison of Straight Microchannel Tube and 10.3 mm outer Diameter Round Micorchannel Tube Air Side Heat Transfer within Equavelent Coil size

8.3 Impact of the Microchannel Tube Size and Spacing on the Air Side Heat Transfer Rate and Refrigerant Side Pressure Drop

From the previous observations, it is desirable to develop a round tube with increased heat transfer performance and reduced refrigerant side pressure drop. Therefore, in order to investigate the effect of tube diameter and tube spacing on the coil thermal performance, the original 10.3mm round tube outer diameter was reduced by 50%, resulting in a much small tube of about 5.15 mm outer diameter. Annular type micro-tube was chosen because of the aim to limit the refrigerant side pressure drop, as it was observed in Figure 8.2. Corresponding geometric specifications and cross-sectional schematic are given in table 8.2 and figure 8.5, respectively.

Table 8.2: Geometric Specifications of 5.15 mm Annular Round Microchannel (AMC)

D_o [mm]	D_i [mm]	D_h [mm]	R_1 [mm]	R_2 [mm]
5.15	2.54	1.64	1.51	2.33

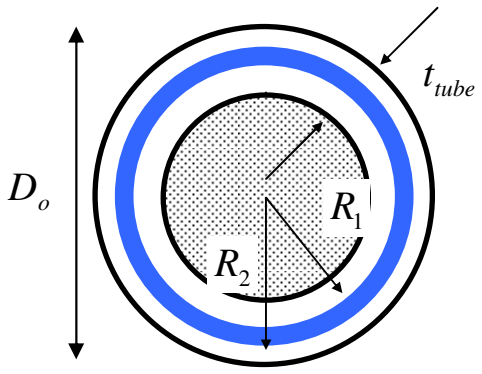

Figure 8.5: Single Round Annular Microchannel Tube Cross- sectional Geometry

By following the same iterative procedure with previous microchannel heat exchanger tube studies, fist the refrigerant side performance was analyzed in single phase laminar flow inside a counter flow tube heat exchanger simulation. In spite of its 18 % lower Nusselt number, based on straight microchannel tube pressure drop, 43 % lower major pressure reduction were obtained with 5.15mm outer diameter () AMC tube compared to 10.3mm D_o AMC, which was shown in figure 8.6 and 8.7, respectively.

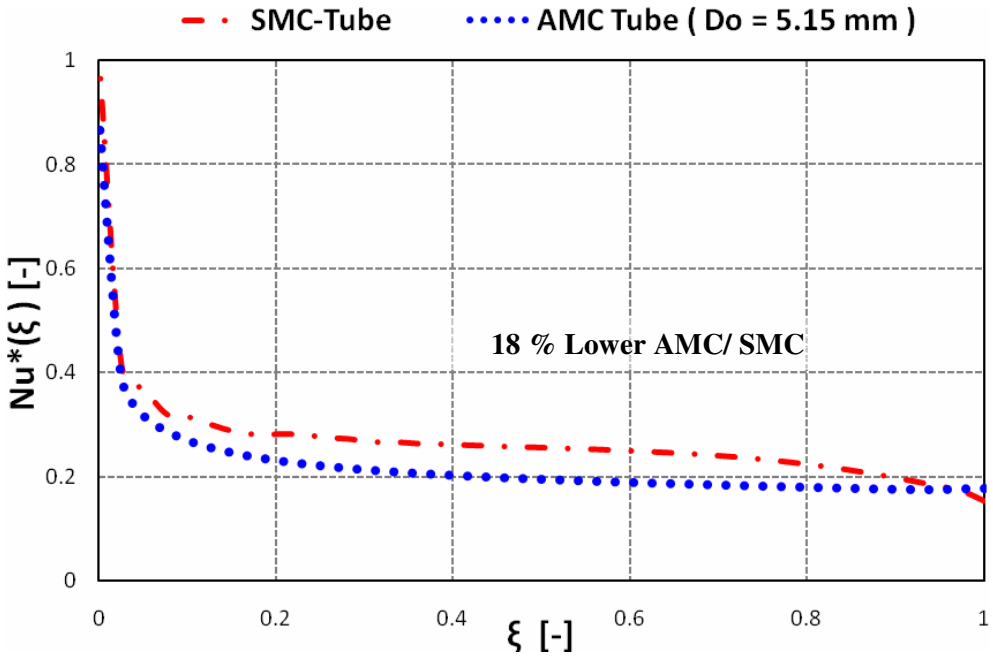

Figure 8.6: Comparison of Dimensionless Nusselt number between Straight Microchannel Tube (SMC) and D_o = 5.15 mm - Annular Microchannel (AMC) Tube

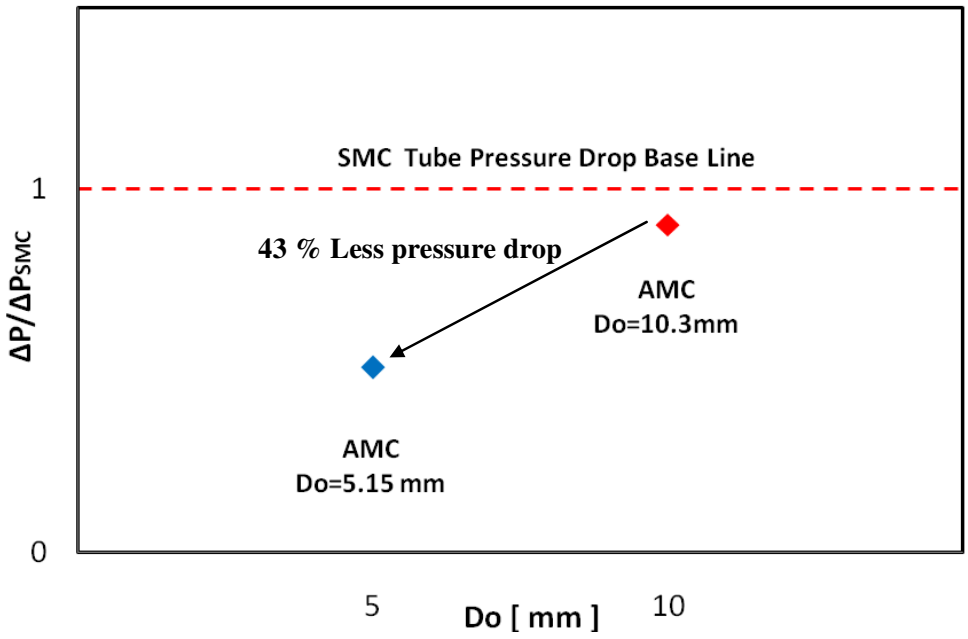

Figure 8.7: Comparison of Dimensionless Pressure Drop (based on SMC tube) between D_o: 10.3 mm and D_o: 5.15 mm Round Annular Microchannel (AMC) Tubes

Beside refrigerant side, I estimated the air side performance of 5.15mm D_o AMC tube with my 2D FLUENT code, which was explained previously in Chapter 7. Similar to RMC tube, sudden temperature increases were investigated at the flow downstream due to vortex formations in the vortex region. Resultant velocity, temperature and stream line maps are presented in figure 8.7, 8.8 and 8.9.

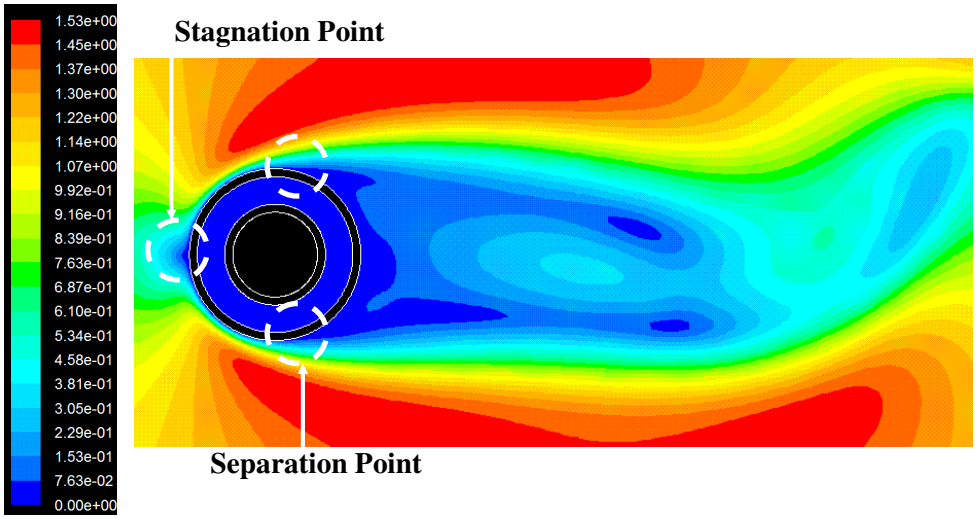

Figure 8.8: Velocity Profile of Air Cross Flow over D_o: 5.15mm AMC Tube

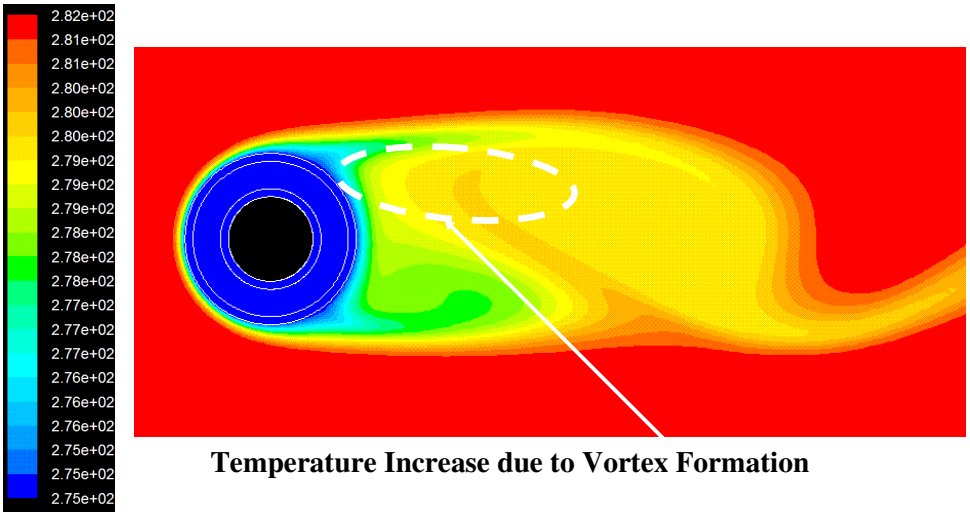

Figure 8.9: Temperature Map of Air Cross Flow over D_o: 5.15mm AMC Tube

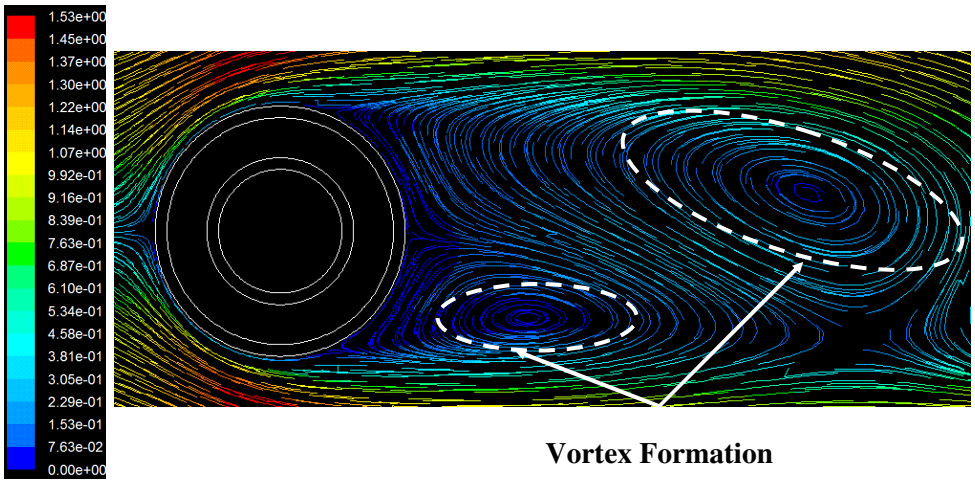

Figure 8.10: Stream Lines of Air Cross Flow over D_o: 5.15mm AMC Tube

Within an equivalent coil length of 17mm single tube spacing ($W_{s\,tube-Fin\&Tube}$), four 10.3 mm D_o RMC tubes correspond to five numbers of 5.15mm D_o AMC tube. In the same coil length, eight SMC tubes with 11mm straight microchannel coil tube spacing ($W_{s\,tube-SMC}$) exits. Figure 8.11 below graphically illustrate this case.

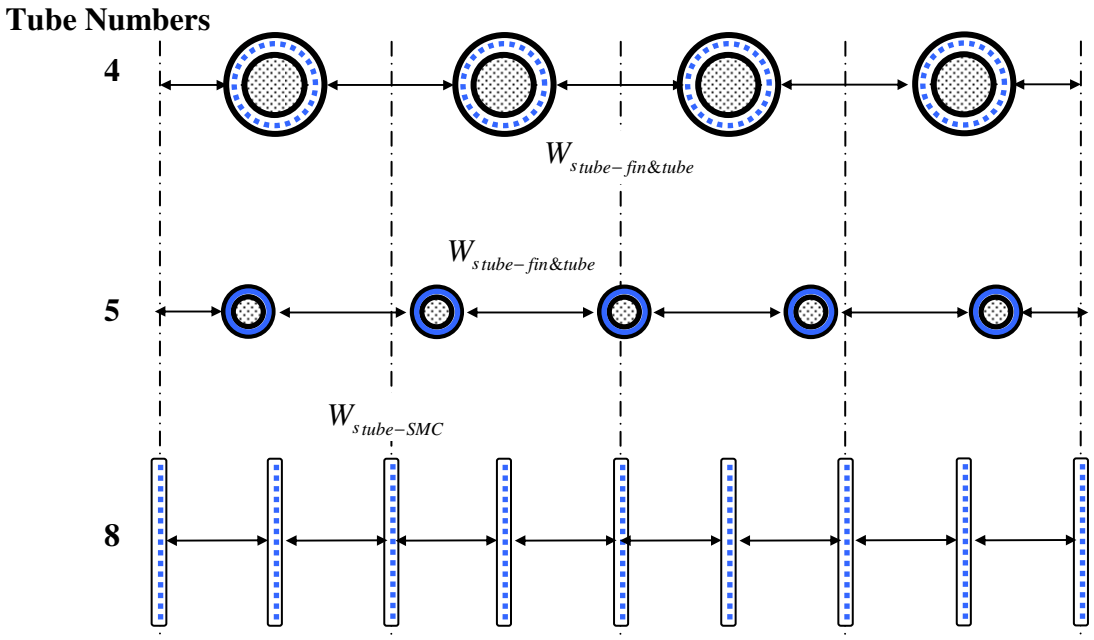

Figure 8.11: Comparison of Tube Spacing and Corresponded Number of Tubes between RMC (D_o: 10.3mm), AMC (D_o: 5.15mm) and SMC Tubes

According to figure 8.11, the number of tubes increased 25% in 5.15 mm D_o AMC and % 50 in SMC tube compared to 10.3 mm D_o RMC tube number. Assuming a uniform heat transfer rate in each tube, variations in dimensionless heat transfer capacity (Φ) of 10.3 mm D_o RMC tube and 5.15mm D_o AMC tube were calculated by dividing the actual capacity by the capacity of SMC tubes as follows:

$$\Phi = \frac{Q_{avg}}{Q_{avg\ SMC-coil}} \tag{8.1}$$

By doing so, comparative air side thermal performance of round microchannel geometry was evaluated with respect straight microchannel tube performance. Additionally, reduction in tube spacing impact in coil heat transfer rate were investigated between current fin and tube spacing of 17mm and straight microchannel tube spacing of 11mm and results are presented in figure 8.12 .

In heat exchangers the primary heat transfer area between air stream and refrigerant flow is the fin surface area. The tube heat transfer area is a secondary effect to contribute to the heat transfer rate. In my study, I assumed that the primary heat transfer area acts the same way regardless of the tube type. This is not true for SMC tube coils, for which the primary heat transfer area in typical coils is at least 50% higher than the primary heat transfer area of round tube coils. However, my aim is to identify tube diameters and tube profiles that have superior performance with respect to conventional type round tube coils (for which the primary heat transfer area is indeed the same as RMC and AMC tubes) and possibly meet the performance standards of straight microchannel tubes. The effect of the primary heat transfer area, i.e., the fin design, is proposed as future expansion of this work. Here, I calculated the heat transfer capacity of each coil configuration by only considering the secondary heat transfer area, which is the total tube surface area. As a result, since reduction in round tube diameter decreased the heat transfer area of 5.15 mm D_o AMC tube coil, less heat transfer capacity were obtained compared to 10.3 mm D_o RMC tube within current fin and tube spacing of 17mm. By decreasing the tube distance 12 % the similar SMC tube heat transfer capacity

was obtained with RMC tube. For 5.15 mm D_o AMC tube, similar air side performance was reached when the tube spacing was 11mm which is equal to SMC tube spacing.

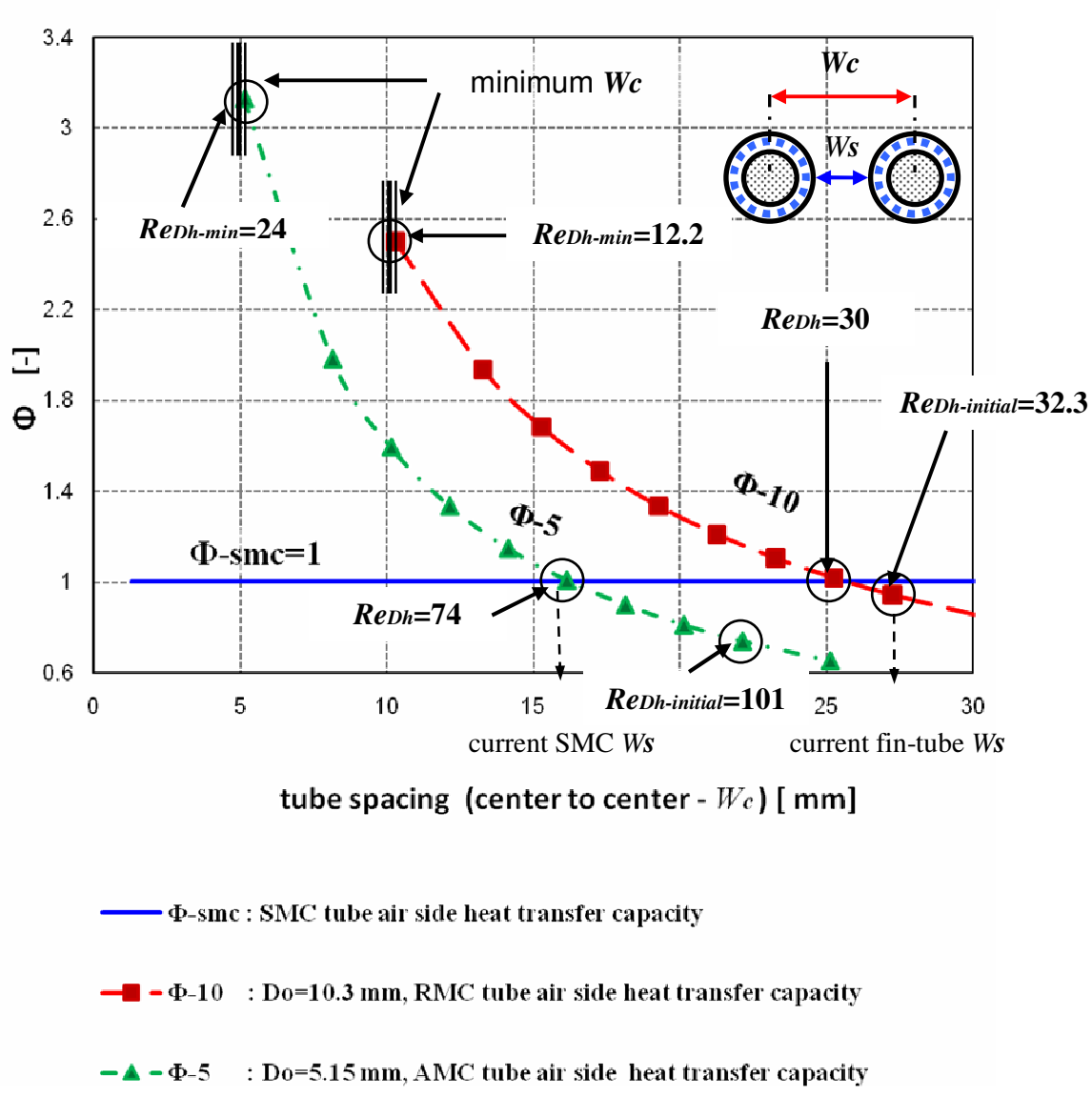

Figure 8.12: Dimensionless Heat Transfer Capacity (Φ) Performance Analysis of RMC (D_o : 10.3 mm) and AMC (D_o : 5.15 mm) based on SMC tube

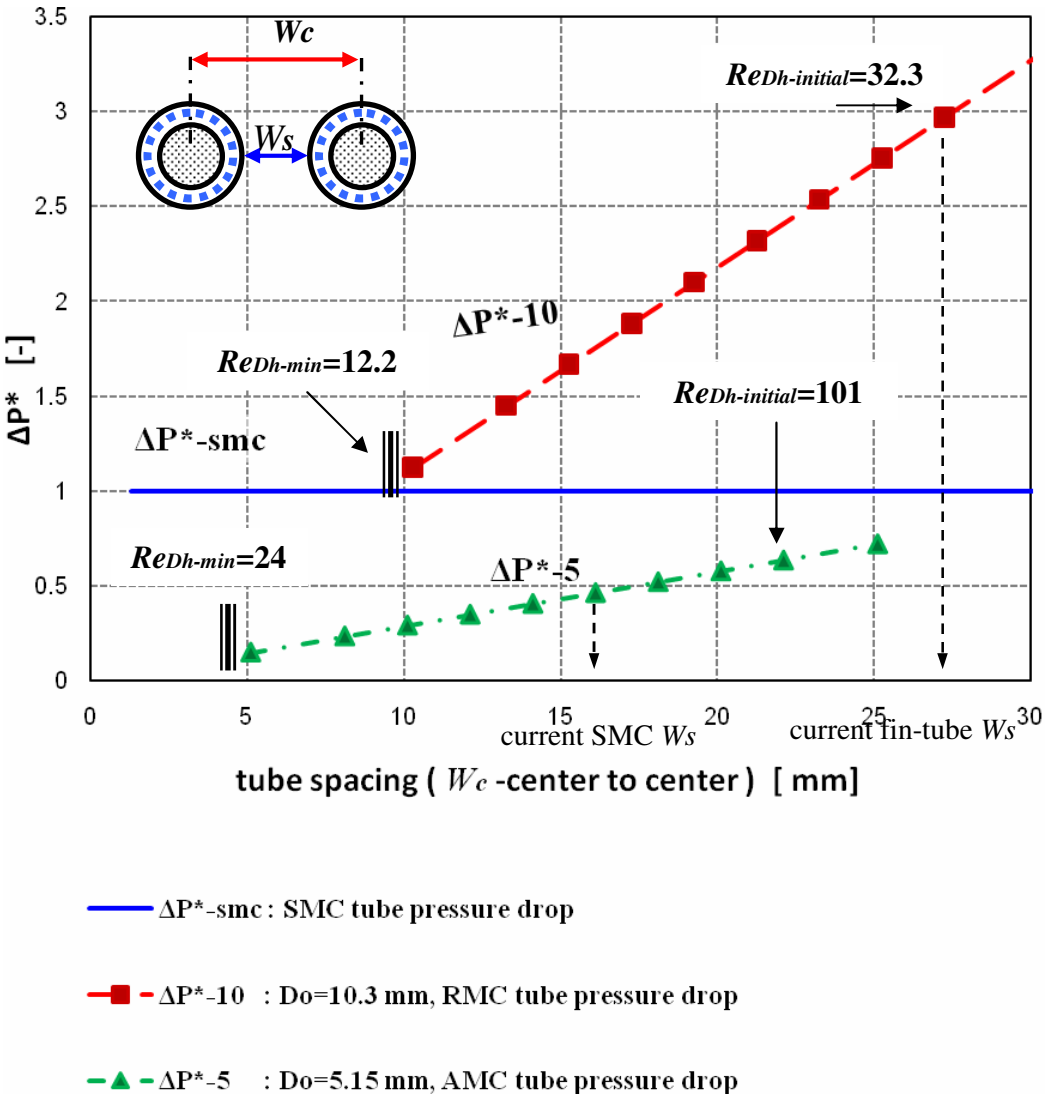

Figure 8.13: Dimensionless Pressure Drop (ΔP*) Performance Analysis of RMC (D_o : 10.3 mm) and AMC (D_o : 5.15 mm) based on SMC tube

Finally, effect of tube spacing on major coil pressure drop was further studied by using Eq-4.2. Since number of tubes was increased by decreasing tube spacing, refrigerant flow rate in each tube diminished which decreased the velocity of the fluid

flow in each channel. As a result, decrease in tube spacing reduced the pressure drop in each coil which is shown in figure 8.13. Compared to SMC tube, % 50 less pressure drop were obtained by using 5.15 mm D_o AMC tube at the same tube spacing, due to its larger flow area. For 10.3 mm D_o RMC tube, however, desired lower pressure loss couldn't achieve.

Additionally, decreasing tube spacing reduced the round microchannel port Reynolds number at the same time due to decrease in mass flow rate at each port. As it shown in figure 8.12 and 8.13, this variation was evaluated between $24 \leq \mathrm{Re}_{Dh} \leq 101$ for 5.15 mm outer diameter round annular microchannel tube and $12 \leq \mathrm{Re}_{Dh} \leq 32$ for 10.3 mm outer diameter multiple port round microchannel tube.

CHAPTER IX

Conclusion

The main objective of this study was to explore alternative design to straight microchannel tube geometry in outdoor evaporator of heat pump systems. The aim is to provide insights for new microtubes profiles that could perform as efficient as conventional fin and tubes during wet and cold operating conditions (heating periods) and maintains high heat transfer performance during dry cooling conditions (summer periods). The approach was to apply the microchannel features on a round tube based heat exchanger and compare the heat transfer and pressure drop characteristics by numerical methods. The refrigerant side and air side behaviors of the tubes were individually and independently investigated in this thesis. The results highlight the limitations and potential benefits of a novel round microchannel tube concept. According to the work presented in the previous sections, the specific conclusions are as follows:

1. A numerical model was created by using the FLUENT CFD solver and it was validated against data available in the literature. In order to verify the accuracy from the numerical predictions of my model, small diameter tubes and microchannel tubes were chosen from papers in the open literature as case studies. Their geometries and operating

conditions were reproduced using my CFD program, including the pre-processor, equation solving scheme, and post-processor techniques used in my study. The case studies used for the model validation were close, but not identical, to the actual geometry and operating conditions of the round tube microchannels, for which experimental data were not found in the public domain. The simulations predicted the data from the literature within an error in the range from 0.1 to 7.8%.

2. The refrigerant side heat transfer capacity of round tubes of 10.3mm outer diameter with 42 microports of about 0.6 mm port diameter distributed around the tube perimeter (round tube microchannel) was estimated to be about 24% higher than conventional round tube (with no microchannel ports in them) and about 15% lower than conventional straight microchannel tube heat exchangers used in outdoor evaporators. Additionally, compared to conventional fin and tube coils, straight microchannel tube coils have more micro-tubes which help to reduce the major refrigerant side pressure drop. In spite of its higher refrigerant flow area, a 10.3mm outer diameter round tube microchannel had about 2.3 times higher pressure loss compared to straight microchannel.

In order to reach similar thermal and hydraulic performances, increasing the refrigerant flow area is the key to reduce the refrigerant side pressure losses. Within similar heat transfer ratio to multiple micro-ports, annular flow type microtube could be designed and the pressure drop was estimated to be about 9 % lower than straight microchannel tubes. As a result, it was concluded that a micro annulus ring of about 1.6 mm hydraulic diameter reduces the refrigerant side flow pressure losses and still maintains high refrigerant side heat transfer coefficients.

3. To investigate how efficient the new geometry compares to straight microchannel tube, I performed a parametric study to measure the performance of 10.3 mm outer diameter round (microchannel) tubes (multi port and annular) under cross flow configuration with dry air streams and I compared the air side heat transfer capacity with SMC tubes. The predictions shows that the RMC and AMC tube coils have about 5.7 % lower air side heat transfer rate compared to SMC tube coil due to their lower heat transfer area.

4. A 50 % tube diameter reduction could increase the number of round tubes per unit length by about 20%. This would reduce further the refrigerant side pressure drops by about 43 % due to a significantly increase of the ratio of refrigerant side flow area on the refrigerant flow rate per unit length. However, compared to the 0.375 inches (10.3 mm) round (microchannel) tube, diameter reduction diminished the air side heat transfer performance in my predictions, since only the tube surface area (and not the fin surface area) was accounted for.

5. In order to explore the diameter of the round tube that could achieve similar air side thermal and hydraulic capacity of straight microchannel tube coil, I conduct a parametric investigation of the tube diameter and tube spacing with round tube microchannel. The minimum outer diameter of the tube was about 0.25 inches (5.15mm) and the tube has a micro-annulus of about 1.6 mm hydraulic diameter. Based on straight microchannel (SMC) tube coil, I estimated that the heat exchanger tube spacing has marked impacts on the heat transfer capacity and pressure drops. According to the simulations, a 12 % decrease in tube spacing of a 0.375 inches (10.3 mm) outer diameter

RMC tubes, that is reducing the tube spacing from 17 mm to 15mm, provides very similar air side heat transfer capacity with respect to the secondary heat transfer area of SMC tube coils. A 50 % smaller tube outer diameter with annular type micro tube could achieve similar heat transfer performance if the tube spacing is 11 mm. In other words, a 0.25 inches (5.15mm) outer tube diameter with a micro-annulus ring around its perimeter and straight microchannel tubes have similar air side heat transfer capacity if the tube spacing is also the same. This is because the ratio of the secondary heat transfer area to the refrigerant flow rate per unit length is close to each other. At this tube spacing, using 5.15mm diameter round (annular) tube in a fin and tube coil configuration could reduce the pressure drop by about 50 % lower than SMC tube level.

In summary, during this study I provided two alternative round micorchannel tube design and heat exchanger coil configuration guidelines with respect to heat transfer capacity, major pressure drop and Reynold's number variation of the microchannel fluid flow comparisions between straight microchannel tube heat exchanger. According to figure 8.12 and 8.13:

1. The round tube design of 5.15 mm outer diameter having an annular port of 1.6mm hydraulic diameter within 11mm edge to edge tube spacing of vertically parallel fin and tube coil configuration can provide similar air side heat transfer capacity of straight microchannel coil based on its secondary heat transfer area. Additionally, this configuration can provide 50 % better pressure drop performance compared to conventional straight microchannel tube coil.

2. The round tube design of 10.3mm outer diameter having multiple (42 in numbers) trapezoidal port of 0.6mm hydraulic diameter within 15 mm edge to edge tube

spacing of vertically parallel fin and tube coil configuration can provide similar airside heat transfer capacity of straight microchannel coil based on its secondary heat transfer area. However, this coil configuration has 1.75 times higher pressure drop than straight microchannel coil.

Future Work:

Based on the findings presented in this thesis, possible extensions of this work might include areas as indeicated next:

- Experimental Validation: It is desirable to provide experimental studies, which could measure the single phase laminar fluid flow thermal performances inside microchannels. A counter flow tube in tube calorimeter would be an applicable experimental set up in order to measure the tube surface temperature and microchannel refrigerant side temperature variations. By doing so, a strong assurance of my FLUENT CFD code accuracy would be provided corresponding to its calculation methodology, iterative procedure and applicable assumptions.

- Improved Model Configurations (Multiple Port – Multiple Tube Simulation): In this work, complete heat exchanger coil cooling performances were estimated based on single microchannel tube- single port section's numerical simulations and uniformity in each port and tube assumptions were applied due to computational limitations. In the future works, first a complete tube and then complete coil model simulations should be applied to investigate tube to tube and port to port effects on frost growth and pressure drop within round microchannel heat exchangers.

- Advance Model Configurations (Fin Effect): In my study, the main objective was to identify the advantageous of tube diameters and tube profiles' effect on microchannel heat exchangers thermal performance and impose to the new round microchannel design. Thus, I only include the secondary heat transfer area, which is the heat exchanger tube surface area in my thermal performance analysis. In order to have a complete coil performance, there should be additional studies which include the effect of the primary heat transfer area, i.e., the fin design to conclude the horizontally parallel heat exchanger configuration of round microchannel coil design.

- Multi-Phase Refrigerant Laminar/Transient/Turbulent Flow Simulations: Since two phase flow boiling of refrigerants (or refrigerant mixtures) occurs inside the actual outdoor evaporators, in the future studies multi-phase and multi-components fluid flow simulators in microstructures should be considered as well as data from suitable experiments. Additionally, since the viscosity of refrigerants, such as R22, is lower compared to water viscosity, flow reaches to transition/turbulent region earlier. Therefore, in addition to laminar flow, turbulent flow analysis should be applied.

References

Adams, T. M., Abdel-Khalik, S. I., Jeter, S. M., & Qureshi, Z. H. (1997). An experimental investigation of single-phase forced convection in microchannels. *International Journal of Heat and Mass Transfer, 41*(6-7), 851-857.

Adams, T. M., Dowling, M. F., Abdel-Khalik, S. I., & Jeter, S. M. (1999). Applicability of traditional turbulent single-phase forced convection correlations to non-circular microchannels. *International Journal of Heat and Mass Transfer, 42*(23), 4411-4415.

Ambatipudi, K. K., & Rahman, M. M. (2000). Analysis of conjugate heat transfer in microchannel heat sinks. *Numerical Heat Transfer; Part A: Applications, 37*(7), 711-731.

Bandhauer, T. M., Agarwal, A., & Garimella, S. (2006). *Measurement and modeling of condensation heat transfer coefficients in circular microchannels*.

Bhaskaran, R., & Collins, L. (2002). *Introduction to CFD Basics*, electronic source: http://instruct1.cit.cornell.edu/courses/fluent/cfd/intro.pdf

Celata, G. P., Cumo, M., Marconi, V., McPhail, S. J., & Zummo, G. (2006). Microtube liquid single-phase heat transfer in laminar flow. *International Journal of Heat and Mass Transfer, 49*(19-20), 3538-3546.

Cengel, Y. A., Turner, H.T. (2004). Fundamentals of Thermal–Fluid Sciences. McGraw-Hill.

Colebrook, C. F. (1939). Turbulent flow in pipes, with particular reference to the transition region between smooth and rough pipe laws. *Journal of the Institution of Civil Engineers (London).*

Dirker, J., & Meyer, J. P. (2005). Convective heat transfer coefficients in concentric annuli. *Heat Transfer Engineering, 26*(2), 38-44.

Fedorov, A. G., & Viskanta, R. (2000). Three-dimensional conjugate heat transfer in the microchannel heat sink for electronic packaging. *International Journal of Heat and Mass Transfer, 43*(3), 399-415.

FLUENT 6.3 Text Command List (2006). NH: Fluent Inc., Lebanon.

FLUENT 6.3 User's Guide (2006). NH: Fluent Inc., Lebanon.

Harms, T. M., Kazmierczak, M., Gerner, F. M., Holke, A., Henderson, H. T., Pilchowski, J., et al. (1997). Experimental investigation of heat transfer and pressure drop trough deep microchannelsin a (110) silicon substrate. *ASME HTD, 351*(1), 347-357.

Heun, M. K., & Dunn, W. E. (1996). Princinples of refrigerant circuiting with applications to microchannel condensers : part 1 - problem formulation and the effects of port diamter and port shape. *ASHRAE Transactions : Symposia*, 382-393.

Incropera, F.P., DeWitt, D.P., Bergman, T. L., Lavine, A. S. (2007). Introduction to Heat Transfer. Fifth edition. Wiley , Newyork

Keogh, A. (2007). Microchannel heat exchangers. *IEA Heat Pump Centre, 25*(3), 15-17.

Kim, J. H., & Groll, E. A. (2003). Performance comparisons of a unitary split system using microchannel and fin-tube outdoor coils. *ASHRAE Transactions : Research*, 219-229.

Lee, P.-S., Garimella, S. V., & Liu, D. (2005). Investigation of heat transfer in rectangular microchannels. *International Journal of Heat and Mass Transfer, 48*(9), 1688-1704.

Lelea, D., Nishio, S., & Takano, K. (2004). The experimental research on microtube heat transfer and fluid flow of distilled water. *International Journal of Heat and Mass Transfer, 47*(12-13), 2817-2830.

Li, Z., Tao, W.-Q., & He, Y.-L. (2005). *A numerical study of laminar convective heat transfer in microchannel with non-circular cross-section*, Toronto, ON, Canada.

Liu, D., & Garimella, S. V. (2005). Analysis and optimization of the thermal performance of microchannel heat sinks. *International Journal of Numerical Methods for Heat and Fluid Flow, 15*(1), 7-26.

Maranzana, G., Perry, I., & Maillet, D. (2004). Mini- and micro-channels: Influence of axial conduction in the walls. *International Journal of Heat and Mass Transfer, 47*(17-18), 3993-4004.

Mokrani, O., Bourouga, B., Castelain, C., & Peerhossaini, H. (2009). Fluid flow and convective heat transfer in flat microchannels. *International Journal of Heat and Mass Transfer, 52*(5-6), 1337-1352.

Monrad, C. C., & Pelton, J. F. (1942). Heat transfer by convective annular spaces. *American Institute of Chemical Engineers, 38*, 593-611.

Muzychka, Y. S. (2005). Constructal design of forced convection cooled microchannel heat sinks and heat exchangers. *International Journal of Heat and Mass Transfer, 48*(15), 3119-3127.

Owhaib, W., & Palm, B. (2004). Experimental investigation of single-phase convective heat transfer in circular microchannels. *Experimental Thermal and Fluid Science, 28*(2-3), 105-110.

Padhmanabhan, S., Cremaschi, L., Fisher, D., & Knight, J. (2008). Comparison of frost and defrost performance between microchannel coil and fin and tube coil for heat pump systems. *International Refrigerant and Air Conditioning Conference at Purdue, July 14-17 2008*, 1-8.

Peng, X. F., & Peterson, G. P. (1995). The effect of thermofluid and geometrical parameters on convection of liquids trough rectangular microchannels *International Journal of Heat and Mass Transfer, 38*(4), 755-758.

Peng, X. F., & Peterson, G. P. (1996a). Convective heat transfer and flow friction for water flow in microchannel structures. *International Journal of Heat and Mass Transfer, 39*(12), 2599-2608.

Peng, X. F., & Peterson, G. P. (1996b). Forced convection heat transfer of single-phase binary mixtures through microchannels. *Experimental Thermal and Fluid Science, 12*(1), 98-104.

Peng, X. F., Piao, Y., & Jia, L. (2002). Single-phase convective heat transfer in microchannels. *Progress in Natural Science, 12*(10), 721-728.

Peng, X. F., Wang, B. X., Peterson, G. P., & Ma, H. B. (1995). Experimental investigation of heat-tranfer in flat plates with rectengular microchannels. *International Journal of Heat and Mass Transfer, 38*(1), 127-137.

Qu, W., & Mudawar, I. (2002). Analysis of three-dimensional heat transfer in micro-channel heat sinks. *International Journal of Heat and Mass Transfer, 45*(19), 3973-3985.

Rahman, M. M. (2000). Measurements of heat transfer in microchannel heat sinks. *International Communications in Heat and Mass Transfer, 27*(4), 495-506.

Rahman, M. M., & Gui, F. J. (1993). Design fabrication and testing of microchannel heat sink for aircraft avionics cooling. *Proceedings of the 28th Intersociety Energy Conversion Engineering Conference, 1*, 1-6.

Saidi, M. H., & Khiabani, R. H. (2007). Forced convective heat transfer in parallel flow multilayer microchannels. *Journal of Heat Transfer, 129*(9), 1230-1236.

Tuckerman, D. B., & Pease, R. F. W. (1981). High-performance heat sinking for VLSI. *Electron Device Letters, 2*(5), 126-129.

Wang, B. X., & Peng, X. F. (1994). Experimental investigation on liquid forced - convection heat-transfer trough microchannels. *International Journal of Heat and Mass Transfer, 37*, 73-82.

Wang, G., Hao, L., & Cheng, P. (2009). An experimental and numerical study of forced convection in a microchannel with negligible axial heat conduction. *International Journal of Heat and Mass Transfer, 52*(3-4), 1070-1074.

Webb, R. L., & Jung, S. H. (1992). Air-side performance of enhanced brazed aluminum heat exchangers. *ASHRAE Transactions : Symposia*, 391-401.

Xia, Y., Zhong, Y., Hrnjak, P. S., & Jacobi, A. M. (2006). Frost, defrost, and refrost and its impact on the air-side thermal-hydraulic performance of louvered-fin, flat-tube heat exchangers. *International Journal of Refrigeration-Revue Internationale Du Froid, 29*(7), 1066-1079.

Xie, X. L., Tao, W. Q., & He, Y. L. (2007). Numerical study of turbulent heat transfer and pressure drop characteristics in a water-cooled minichannel heat sink. *Journal of Electronic Packaging, Transactions of the ASME, 129*(3), 247-255.

Zhigang, L., Ning, G., & Takei, M. (2007). An experimental investigation of single-phase heat transfer in 0.045mm to 0.141mm microtubes. *Nanoscale and Microscale Thermophysical Engineering, 11*(3-4), 333-349.

APPENDIX A

Validation Models' Gambit Journal Files

A-1: Tube in Tube Validation Model Gambit Journal File

```
//Identifier "Journal File -Annular Tube in Tube Validation"

//Starting Point Inlet Section
$si=0.0
//Internal brass pipe radius at the inner channel [mm]
$rb=6.86
//Internal channel radius at the inlet and outlet sections [mm]
$ri=15.88
//Length of tube and tube [mm]
$lt=1714.5
//Outer radius of the jacket[mm]
$rj=38.89

//Creating geometry
vertex create "O" coordinates $si $si $si
vertex create "A" coordinates $si $rb $si
vertex create "B" coordinates $rb $si $si
vertex create "AA" coordinates $si $ri $si
vertex create "BB" coordinates $ri $si $si
vertex create "AAA" coordinates $si $rj $si
vertex create "BBB" coordinates $rj $si $si
edge create "Brass-Arc" center2points "O" "A" "B" minarc arc
edge create "Channel-Arc" center2points "O" "AA" "BB" minarc arc
edge create "Jacket-Arc" center2points "O" "AAA" "BBB" minarc arc
edge create "sym-JC-Y" straight "AAA" "AA"
edge create "sym-CB-Y" straight "AA" "A"
edge create "sym-BO-Y" straight "A" "O"
edge create "sym-JC-X" straight "BBB" "BB"
edge create "sym-CB-X" straight "BB" "B"
edge create "sym-BO-X" straight "B" "O"

//Create faces
face create "brass pipe inlet" wireframe "Brass-Arc" "sym-BO-X" "sym-
BO-Y" real
face create "channel inlet" wireframe "Channel-Arc" "sym-CB-X" "Brass-
Arc" "sym-CB-Y" real
face create "jacket inlet" wireframe "Jacket-Arc" "sym-JC-X" "Channel-
```

```
Arc" "sym-JC-Y" real
//Create solid 3D volume
volume create "Brass-Volume" translate "brass pipe inlet" vector $si
$si $lt
volume create "Channel-Volume" translate "channel inlet" vector $si $si
$lt
volume create "Jacket-Volume" translate "jacket inlet" vector $si $si
$lt
//Mesh edges
undo begingroup
edge picklink "Jacket-Arc" "Channel-Arc" "Brass-Arc"
edge mesh "Brass-Arc" "Channel-Arc" "Jacket-Arc" successive ratio1 1
intervals 30
undo endgroup
undo begingroup
edge picklink "sym-BO-X" "sym-BO-Y"
edge mesh "sym-BO-Y" "sym-BO-X" successive ratio1 1 intervals 10
undo endgroup
undo begingroup
edge picklink "sym-CB-Y" "sym-CB-X"
edge mesh "sym-CB-X" "sym-CB-Y" successive ratio1 1 intervals 26
undo endgroup
undo begingroup
edge picklink "sym-JC-Y" "sym-JC-X"
edge mesh "sym-JC-X" "sym-JC-Y" successive ratio1 1 intervals 67
undo endgroup

//mesh faces
face mesh "brass pipe inlet" pave intervals 10
face mesh "channel inlet" map intervals 10
face mesh "jacket inlet" map intervals 10

//Mesh volumes
volume mesh "Brass-Volume" cooper source "face.7" "brass pipe inlet"
intervals 72
volume mesh "Channel-Volume" cooper source "channel inlet" "face.12"
intervals 72
volume mesh "Jacket-Volume" cooper source "jacket inlet" "face.17"
intervals  72

//Scale the geometry from mm to m
model scale factor 0.001 origin  0 0 0

//Select Solver
solver select "FLUENT 5/6"

//Define Boundaries
physics create "BP-InletWall" btype "WALL" face "brass pipe inlet"
physics create "BP-OuterWall" btype "WALL" face "face.7"
physics create "BP-InnerWall" btype "WALL" face "face.6"
physics create "BP-Symmetry-Y" btype "SYMMETRY" face "face.5"
physics create "BP-Symmetry-X" btype "SYMMETRY" face "face.4"
physics create "Channel-Inlet" btype "MASS_FLOW_INLET" face "channel
inlet"
physics create "Channel-Outlet" btype "PRESSURE_OUTLET" face "face.12"
physics create "Channel-Wall" btype "WALL" face "face.10"
physics create "Channel-Symmetry-Y" btype "SYMMETRY" face "face.11"
```

```
physics create "Channel-Symmetry-X" btype "SYMMETRY" face "face.8"
physics create "Jacket-Inlet" btype "MASS_FLOW_INLET" face "jacket
inlet"
physics create "Jacket-Outlet" btype "PRESSURE_OUTLET" face "face.17"
physics create "Jacket-Wall" btype "WALL" face "face.16"
physics create "Jacket-Symmetry-Y" btype "SYMMETRY" face "face.15"
physics create "Jacket-Symmetry-X" btype "SYMMETRY" face "face.13"
physics create "Brass Pipe " ctype "SOLID" volume "Brass-Volume"
physics create "Channel-Cold-Water" ctype "FLUID" volume "Channel-
Volume"
physics create "Jacket-Hot-Water" ctype "FLUID" volume "Jacket-Volume"

//Check Topology and Geometry
check topology
check geometry

//Export Mesh

export fluent5 "TinT-V.msh"

save
```

A-2: Microchannel Heat Exchanger Validation Model Gambit Journal File

```
//Identifier " Journal File -Microchannel Heat Exchanger Validation"
//Create the geometry
vertex create "O" coordinates 0 0 0
vertex create "A" coordinates 0 1.7 0
vertex create "B" coordinates 0 2.0 0
vertex create "C" coordinates 5.8 2.0 0
vertex create "D" coordinates 5.8 1.7 0
vertex create "E" coordinates 6.2 1.7 0
vertex create "F" coordinates 6.2 2.0 0
vertex create "G" coordinates 7.8 2.0 0
vertex create "H" coordinates 7.8 1.7 0
vertex create "I" coordinates 8.2 1.7 0
vertex create "J" coordinates 8.2 2.0 0
vertex create "K" coordinates 9.0 2.0 0
vertex create "L" coordinates 9.0 1.7 0
vertex create "M" coordinates 9.0 0 0
edge create "OA" straight "O" "A"
edge create "AB" straight "A" "B"
edge create "BC" straight "B" "C"
edge create "CD" straight "C" "D"
edge create "DE" straight "D" "E"
edge create "EF" straight "E" "F"
edge create "FG" straight "F" "G"
edge create "GH" straight "G" "H"
edge create "HI" straight "H" "I"
edge create "IJ" straight "I" "J"
edge create "JK" straight "J" "K"
edge create "KL" straight "K" "L"
```

```
edge create "LM" straight "L" "M"
edge create "CF" straight "C" "F"
edge create "GJ" straight "G" "J"
edge create "OM" straight "O" "M"

//Face geometry
face create "STEEL-CHANNEL" wireframe "OA" "AB" "BC" "CD" "DE" "EF"
"FG" "GH" "HI" "IJ" "JK" "KL" "LM" "OM" real
face create "PORT-1-INLET" wireframe "CD" "DE" "EF" "CF" real
face create "PORT-2-INLET" wireframe "GH" "HI" "IJ" "GJ" real

//Volume geometry
volume create "STELL-CHANNEL-VOLUME" translate "STEEL-CHANNEL" vector 0
0 50
volume create "PORT 1-VOLUME" translate "PORT-1-INLET" vector 0 0 50
volume create "PORT 2-VOLUME" translate "PORT-2-INLET" vector 0 0 50

//Mesh edges
undo begingroup
edge picklink "DE" "CF"
edge mesh "CF" "DE" successive ratio1 1 intervals 12
undo endgroup
undo begingroup
edge picklink "HI" "GJ"
edge mesh "GJ" "HI" successive ratio1 1 intervals 12
undo endgroup
undo begingroup
edge picklink "BC"
edge mesh "BC" successive ratio1 1 intervals 174
undo endgroup
undo begingroup
edge picklink "FG"
edge mesh "FG" successive ratio1 1 intervals 48
undo endgroup
undo begingroup
edge picklink "JK"
edge mesh "FG" successive ratio1 1 intervals 24
undo endgroup
undo begingroup
edge picklink "OM"
edge mesh "OM" successive ratio1 1 intervals 270
undo endgroup
undo begingroup
edge picklink "LM" "OA"
edge mesh "OA" "LM" successive ratio1 1 intervals 36
undo endgroup
undo begingroup
edge picklink "KL" "IJ" "GH" "EF" "CD" "AB"
edge mesh "AB" "CD" "EF" "GH" "IJ" "KL" successive ratio1 1 intervals
24
undo endgroup

//Mesh face
face mesh "PORT-1-INLET" "PORT-2-INLET" map intervals 10
face mesh "STEEL-CHANNEL" submap intervals 10

//Mesh volume
```

```
volume mesh "STELL-CHANNEL-VOLUME" cooper source "STEEL-CHANNEL"
"face.18" intervals 25
volume mesh "PORT 1-VOLUME" cooper source "PORT-1-INLET" "face.23"
intervals 25
volume mesh "PORT 2-VOLUME" cooper source "PORT-2-INLET" "face.28"
intervals 25

//Scale the model mm to m
model scale factor 0.001 origin 0 0 0

//Select Solver
solver select "FLUENT 5/6"

//Define Boundaries
physics create "steel-inlet-wall" btype "WALL" face "STEEL-CHANNEL"
physics create "steel-outlet-wall" btype "WALL" face "face.18"
physics create "steel-side-wall-1" btype "WALL" face "face.9"
physics create "steel-side wall-2" btype "WALL" face "face.5"
physics create "steel-btm-wall" btype "WALL" face "face.4"
physics create "steel-top-wall-1" btype "WALL" face "face.15"
physics create "steel-top-wall-2" btype "WALL" face "face.22"
physics create "steel-top-wall-3" btype "WALL" face "face.16"
physics create "steel-top-wall-4" btype "WALL" face "face.27"
physics create "steel-top-wall-5" btype "WALL" face "face.17"
physics create "port-1-btm-wall" btype "WALL" face "face.7"
physics create "port-1-side-wall-1" btype "WALL" face "face.10"
physics create "port-1-side-wall-2" btype "WALL" face "face.11"
physics create "port-2-btm-wall" btype "WALL" face "face.8"
physics create "port-2-side-wall-1" btype "WALL" face "face.12"
physics create "port-2-side-wall-2" btype "WALL" face "face.13"
physics create "ststeel-tube-sym-1" btype "SYMMETRY" face "face.14"
physics create "steel-tube-sym-2" btype "SYMMETRY" face "face.6"
physics create "port-1-inlet" btype "MASS_FLOW_INLET" face "PORT-1-
INLET"
physics create "port-2-inlet" btype "MASS_FLOW_INLET" face "PORT-2-
INLET"
physics create "port-1-outlet" btype "PRESSURE_OUTLET" face "face.23"
physics create "port-2-outlet" btype "PRESSURE_OUTLET" face "face.28"
physics create "steel-solid" ctype "SOLID" volume "STELL-CHANNEL-
VOLUME"
physics create "port-1-fluid" ctype "FLUID" volume "PORT 1-VOLUME"
physics create "port-2-fluid" ctype "FLUID" volume "PORT 2-VOLUME"

//Check Topology and Geometry
check topology
check geometry

//Export Mesh
export fluent5 "MCHEX-V.msh"

save
```

APPENDIX B

3D Gambit Journal Files

B-1: Simulation Model 1 Round Tube in Tube Heat Exchanger

Gambit Journal File

```
// Identifier "Journal File-3D-Round Tube (medium mesh)"
//Round tube geometry [mm]
$Do=0.010287*1000
$Di=0.0096774*1000
$Dj=0.03*1000
$si=0.0
// Internal Channel radius at the Inlet and Outlet Sections
$ri=$Di/2
// Outer Channel radius at the Inlet and Outlet Sections
$ro=$Do/2
// Length of tube and tube [m]
$lt=1200
// Outer radius of the jacket
$rj=$Dj/2

//Create edges
vertex create "O" coordinates $si $si $si
vertex create "AI" coordinates $si $ri $si
vertex create "BI" coordinates $ri $si $si
vertex create "AO" coordinates $si $ro $si
vertex create "BO" coordinates $ro $si $si
vertex create "AJ" coordinates $si $rj $si
vertex create "BJ" coordinates $rj $si $si
edge create "Channel-I-Arc" center2points "O" "AI" "BI" minarc arc
edge create "Channel-O-Arc" center2points "O" "AO" "BO" minarc arc
edge create "Jacket-Arc" center2points "O" "AJ" "BJ" minarc arc
edge create "sym-J-Y" straight "AJ" "AO"
edge create "sym-O-Y" straight "AO" "AI"
edge create "sym-I-Y" straight "AI" "O"
edge create "sym-J-X" straight "BJ" "BO"
edge create "sym-O-X" straight "BO" "BI"
edge create "sym-I-X" straight "BI" "O"
```

```
//Create faces
face create "channel inlet" wireframe "Channel-I-Arc" "sym-I-X" "sym-I-
Y" real
face create "channel thickness" wireframe "Channel-O-Arc" "sym-O-X"
"Channel-I-Arc"  "sym-O-Y" real
face create "jacket outlet" wireframe "Jacket-Arc" "sym-J-X" "Channel-
O-Arc" "sym-J-Y" real

//Create volume
volume create "Channel-Volume" translate "channel inlet" vector $si $si
$lt
volume create "Channel-Thickness-Volume" translate "channel thickness"
vector $si $si $lt
volume create "Jacket-Volume" translate "jacket outlet" vector $si $si
$lt

// Mesh edges
undo begingroup
edge picklink "sym-I-X" "sym-I-Y"
edge mesh "sym-I-Y" "sym-I-X" successive ratio1 1 intervals 64
undo endgroup
undo begingroup
edge picklink "sym-O-X" "sym-O-Y"
edge mesh "sym-O-Y" "sym-O-X" successive ratio1 1 intervals 4
undo endgroup
undo begingroup
edge picklink "sym-J-X" "sym-J-Y"
edge mesh "sym-J-Y" "sym-J-X" successive ratio1 1 intervals 130
undo endgroup
undo begingroup
edge picklink "Jacket-Arc" "Channel-O-Arc" "Channel-I-Arc"
edge mesh "Channel-I-Arc" "Channel-O-Arc" "Jacket-Arc" successive
ratio1 1 intervals 32

// Mesh face
face mesh "channel inlet" triprimitive intervals 10
face mesh "channel thickness" map intervals 10
face mesh "jacket outlet" map intervals 10

// Mesh volume
volume mesh "Channel-Volume" cooper source "face.7" "channel inlet"
intervals 40
volume mesh "Channel-Thickness-Volume" cooper source "channel
thickness" "face.12" intervals 40
volume mesh "Jacket-Volume" cooper source "jacket outlet" "face.17"
intervals 40

//Scale the Geometry from mm to m
model scale factor 0.001 origin  0 0 0

// Select Solver
solver select "FLUENT 5/6"

// Define Boundaries
physics create "channel-inlet" btype "MASS_FLOW_INLET" face "channel
inlet"
physics create "channel-outlet" btype "PRESSURE_OUTLET" face "face.7"
```

```
physics create "jacket-inlet" btype "MASS_FLOW_INLET" face "face.17"
physics create "jacket-outlet" btype "PRESSURE_OUTLET" face "jacket
outlet"
physics create "thickness-inlet" btype "WALL" face "channel thickness"
physics create "thickness-outlet" btype "WALL" face "face.12"
physics create "channel-inner-wall" btype "WALL" face "face.6"
physics create "channel-outer-wall" btype "WALL" face "face.10"
physics create "jacket-wall" btype "WALL" face "face.16"
physics create "channel -sym-y" btype "SYMMETRY" face "face.5"
physics create "channel-sym-x" btype "SYMMETRY" face "face.4"
physics create "thickness-sym-y" btype "SYMMETRY" face "face.11"
physics create "thickness-sym-x" btype "SYMMETRY" face "face.8"
physics create "jacket-sym-y" btype "SYMMETRY" face "face.15"
physics create "jacket-sym-x" btype "SYMMETRY" face "face.13"
physics create "cold-water-fluid" ctype "FLUID" volume "Channel-Volume"
physics create "copper-solid" ctype "SOLID" volume "Channel-Thickness-
Volume"
physics create "hot-water-fluid" ctype "FLUID" volume "Jacket-Volume"
default set "GRAPHICS.GENERAL.CONNECTIVITY_BASED_COLORING" numeric 1

//Check Topology and Geometry
check topology
check geometry

// Export Mesh

export fluent5 "3D-RT-M.msh"
save
```

B-2: Simulation Model 2 SMC Tube in Tube Heat Exchanger

Gambit Journal File

```
//Journal File for GAMBIT 2.4.6, Database 2.4.4, ntx86 SP2007051421
//Identifier “Journal File-3D-SMC Tube (medium mesh)”
//Starting Point
$s=0.0
//Rectangular microchannel width and height [mm]
$w=0.41
$h=0.255
/ Length of tube [m]
$lt=1200.0
//Outer radius of the water jacket
$rj=15.0
//t is the tube thickness and k is the sectional length [mm]
$t=0.65
$k=0.385625

//Creating geometry
```

```
vertex create "O" coordinates $s $s $s
vertex create "A" coordinates $s $h $s
vertex create "A'" coordinates $s -$h $s
vertex create "B" coordinates $s $k $s
vertex create "B'" coordinates $s -$k $s
vertex create "C" coordinates $w $h $s
vertex create "C'" coordinates $w -$h $s
vertex create "D" coordinates $t $k $s
vertex create "D'" coordinates $t -$k $s
vertex create "E" coordinates $rj $k $s
vertex create "E'" coordinates $rj -$k $s
edge create "AA'" straight "A" "A'"
edge create "AB" straight "A" "B"
edge create "A'B'" straight "A'" "B'"
edge create "CC'" straight "C" "C'"
edge create "DD'" straight "D" "D'"
edge create "AC" straight "A" "C"
edge create "BD" straight "B" "D"
edge create "DE" straight "D" "E"
edge create "A'C'" straight "A'" "C'"
edge create "B'D'" straight "B'" "D'"
edge create "D'E'" straight "D'" "E'"
edge create "EE'" center2points "O" "E'" "E" minarc arc

//Creating face
face create "port-face" wireframe "AA'" "AC" "CC'" "A'C'" real
face create "channel-face" wireframe "AB" "BD" "DD'" "B'D'" "A'B'"
"A'C'" "CC'" "AC" real
face create "jacket-face" wireframe "DD'" "D'E'" "EE'" "DE" real

//Creating volume
volume create "port-volume" translate "port-face" vector $s $s $lt
volume create "channel-volume" translate "channel-face" vector $s $s
$lt
volume create "jacket-volume" translate "jacket-face" vector $s $s $lt

//Mesh port
undo begingroup
edge picklink "AA'" "CC'"
edge mesh "CC'" "AA'" successive ratio1 1 intervals 19
undo endgroup
undo begingroup
edge picklink "A'C'" "AC"
edge mesh "AC" "A'C'" successive ratio1 1 intervals 15
undo endgroup
undo begingroup

//Mesh channel
undo begingroup
edge picklink "A'B'" "AB"
edge mesh "AB" "A'B'" successive ratio1 1 intervals 5
undo endgroup
undo begingroup
edge picklink "DD'"
edge mesh "DD'" successive ratio1 1 intervals 29
undo endgroup
edge picklink "BD" "B'D'"
```

```
edge mesh "B'D'" "BD" successive ratio1 1 intervals 24
undo endgroup

//Mesh Jacket
undo begingroup
edge picklink "EE'"
edge mesh "EE'" successive ratio1 1 intervals 29
undo endgroup
undo begingroup
edge picklink "DE" "D'E'"
edge mesh "D'E'" "DE" successive ratio1 1 intervals 525
undo endgroup
//Mesh face
face mesh "port-face" map intervals 10
face mesh "channel-face" submap intervals 10
face mesh "jacket-face" map intervals 10

//Mesh volume
volume mesh "port-volume" cooper source "port-face" "face.8" intervals
40
volume mesh "jacket-volume" cooper source "jacket-face" "face.22"
intervals 40
volume mesh "channel-volume" cooper source "channel-face" "face.17"
intervals 40

//Scale the model
model scale factor 0.001 origin 0 0 0

//Select Solver
solver select "FLUENT 5/6"

//Boundary Conditions
physics create "port-inlet" btype "MASS_FLOW_INLET" face "port-face"
physics create "channel-wall-front" btype "WALL" face "channel-face"
physics create "jacket-outlet" btype "PRESSURE_OUTLET" face "jacket-
face"
physics create "port-innerwall-btm" btype "WALL" face "face.4"
physics create "port-symetry" btype "SYMMETRY" face "face.5"
physics create "port-innerwall-side" btype "WALL" face "face.6"
physics create "port-innerwall-top" btype "WALL" face "face.7"
physics create "port-outlet" btype "PRESSURE_OUTLET" face "face.8"
physics create "port-symetry-bttm" btype "SYMMETRY" face "face.9"
physics create "port-symetry-sideL" btype "SYMMETRY" face "face.10"
physics create "channel-wall" btype "WALL" face "face.13"
physics create "port-symetry-sideT" btype "WALL" face "face.15"
physics create "port-symetry-top" btype "SYMMETRY" face "face.16"
physics create "port-outlet-wall" btype "WALL" face "face.17"
physics create "jacket-symetry-bttm" btype "SYMMETRY" face "face.18"
physics create "jacket-wall" btype "WALL" face "face.20"
physics create "jacket-symetry-top" btype "SYMMETRY" face "face.21"
physics create "Jacket-Inlet" btype "MASS_FLOW_INLET" face "face.22"
physics create "port-cold-water" ctype "FLUID" volume "port-volume"
physics create "aluminum-channel" ctype "SOLID" volume "channel-volume"
physics create "jacket-hot-water" ctype "FLUID" volume "jacket-volume"
default set "GRAPHICS.GENERAL.CONNECTIVITY_BASED_COLORING" numeric 1

//Check Topology and Geometry
```

```
check topology
check geometry
//Export Mesh
export fluent5 "3D-SMC-M.msh"
save
```

B-3: Simulation Model 3 RMC Tube in Tube Heat Exchanger

Gambit Journal File

```
//Identifier “Journal File-3D-RMC Tube (medium mesh)"
//starting point
$o=0
//Tube length [mm]
$L=1200
//Water jacket radius [mm]
$Rj=15
//tube thickness [mm]
$t=1.3
//microchannel port thickness [mm]
$ta=0.24

//microchannel outer and inner radius [ mm]
$Ro=5.1435
$Ri=$Ro-$t
//microchannel port radius 1 and 2 [mm]
$R1=$Ri+$ta
$R2=$Ro-$ta

//trapezoidal port upper and lower widths [mm]
$A=0.46
$B=0.56
//port number
$N=36
//sectional single port geometry angles
$tet=DEG2RAD*ATAN($A/(2*$R1))
$bet=(2*PI-(2*$tet*$N))/($N-1)
$teta=($tet*RAD2DEG)
$beta=($tet+(0.5*$bet))*RAD2DEG

//x points
$XA=$Ri*COS($beta)
$XAA=$Ri*COS($beta)
$XB=$R1
$XBB=$R1
$XC=$R2
$XCC=$R2
$XD=$Ro*COS($beta)
$XDD=$Ro*COS($beta)
$XE=$Rj*COS($beta)
$XEE=$Rj*COS($beta)
```

```
//y-points
$YA=$Ri*SIN($beta)
$YAA=-$Ri*SIN($beta)
$YB=($A/2)
$YBB=-($A/2)
$YC=($B/2)
$YCC=-($B/2)
$YD=$Ro*SIN($beta)
$YDD=-$Ro*SIN($beta)
$YE=$Rj*SIN($beta)
$YEE=-$Rj*SIN($beta)

//create edges
vertex create "O" coordinates $o $o $o
vertex create "A" coordinates $XA $YA $o
vertex create "B" coordinates $XB $YB $o
vertex create "C" coordinates $XC $YC $o
vertex create "D" coordinates $XD $YD $o
vertex create "E" coordinates $XE $YE $o
vertex create "AA" coordinates $XAA $YAA $o
vertex create "BB" coordinates $XBB $YBB $o
vertex create "CC" coordinates $XCC $YCC $o
vertex create "DD" coordinates $XDD $YDD $o
vertex create "EE" coordinates $XEE $YEE $o
edge create "A-D" straight "A" "D"
edge create "AA-DD" straight "AA" "DD"
edge create "D-E" straight "D" "E"
edge create "DD-EE" straight "DD" "EE"
edge create "B-C" straight "B" "C"
edge create "BB-CC" straight "BB" "CC"
edge create "INNER-CHAMBER" center2points "O" "A" "AA" minarc arc
edge create "OUTER-CHAMBER" center2points "O" "D" "DD" minarc arc
edge create "B-BB" straight "B" "BB"
edge create "C-CC" straight "C" "CC"
edge create "JACKET-CHAMBER" center2points "O" "E" "EE" minarc arc

//Face geometry
face create "Channel-Face" wireframe "INNER-CHAMBER" "A-D" "OUTER-
CHAMBER" \
  "AA-DD" real
face create "Port-Face" wireframe "B-BB" "B-C" "C-CC" "BB-CC" real
face create "Jacket-Face" wireframe "OUTER-CHAMBER" "D-E" "JACKET-
CHAMBER" \
  "DD-EE" real
face split "Channel-Face" connected faces "Port-Face"

//Volume geometry
volume create "channel-volume" translate "Channel-Face" vector 0 0 1200
volume create "port-volume" translate "Port-Face" vector 0 0 1200
volume create "jacket-volume" translate "Jacket-Face" vector 0 0 1200

//Mesh geometry
undo begingroup
edge picklink "JACKET-CHAMBER" "INNER-CHAMBER" "OUTER-CHAMBER"
edge mesh "OUTER-CHAMBER" "INNER-CHAMBER" "JACKET-CHAMBER" successive
ratio1 1 intervals 27
undo endgroup
```

```
undo begingroup
edge delete "edge.13" "edge.14" keepsettings onlymesh
edge picklink "edge.14" "edge.13"
edge mesh "edge.13" "edge.14" successive ratio1 1 intervals 15
undo endgroup
undo begingroup
edge delete "edge.12" "edge.15" keepsettings onlymesh
edge picklink "edge.15" "edge.12"
edge mesh "edge.12" "edge.15" successive ratio1 1 intervals 30
undo endgroup
undo begingroup
edge delete "AA-DD" "A-D" keepsettings onlymesh
edge picklink "A-D" "AA-DD"
edge mesh "AA-DD" "A-D" successive ratio1 1 intervals 48
undo endgroup
undo begingroup
edge picklink "D-E" "DD-EE"
edge mesh "DD-EE" "D-E" successive ratio1 1 intervals 360
undo endgroup

//Mesh face
face mesh "Channel-Face" submap intervals 10
face mesh "Port-Face" map intervals 10
face mesh "Jacket-Face" map intervals 10

//Mesh volume
volume mesh "channel-volume" cooper source "Channel-Face" "face.13"
intervals 40
volume mesh "port-volume" cooper source "Port-Face" "face.18" intervals
40
volume mesh "jacket-volume" cooper source "Jacket-Face" "face.23"
intervals 40

//Smooth volume mesh
volume smooth "jacket-volume" "port-volume" "channel-volume" fixed
lwlaplacian
//Scale the model mm to m
model scale factor 0.001 origin 0 0 0

//Select Solver
solver select "FLUENT 5/6"

//Boundary conditions
physics create "channel-wall-front" btype "WALL" face "Channel-Face"
physics create "jacket-outlet" btype "PRESSURE_OUTLET" face "Jacket-
Face"
physics create "port-inlet" btype "MASS_FLOW_INLET" face "Port-Face"
physics create "channel-symetry-btm" btype "SYMMETRY" face "face.5"
physics create "port-inner-wall-b" btype "WALL" face "face.6"
physics create "channel-adiabatic-wall" btype "WALL" face "face.7"
physics create "port-inner-wall-side-adb" btype "WALL" face "face.8"
physics create "port-inner-wall-jckt" btype "WALL" face "face.9"
physics create "channel-outer-wall-jck" btype "WALL" face "face.10"
physics create "port-inner-wall-top" btype "WALL" face "face.11"
physics create "channel-symmetry-top" btype "SYMMETRY" face "face.12"
physics create "channel-wall-back" btype "WALL" face "face.13"
physics create "port-outlet" btype "PRESSURE_OUTLET" face "face.18"
```

```
physics create "jacket-symetry-btm" btype "SYMMETRY" face "face.19"
physics create "jacket-wall" btype "WALL" face "face.21"
physics create "jacket-symmetry-top" btype "SYMMETRY" face "face.22"
physics create "jacket-inlet" btype "MASS_FLOW_INLET" face "face.23"
physics create "aluminum-channel" ctype "SOLID" volume "channel-volume"
physics create "port-cold-water" ctype "FLUID" volume "port-volume"
physics create "jacket-hot-water" ctype "FLUID" volume "jacket-volume"

default set "GRAPHICS.GENERAL.CONNECTIVITY_BASED_COLORING" numeric 1
//Check Topology and Geometry
check topology
check geometry
//Export Mesh
export fluent5 "3D-RMC-M.msh"
save
```

APPENDIX C

2 D Gambit Journal Files

C-1: Simulation Model 4 RMC Tube Heat Exchanger in Air Cross Flow

Gambit Journal File

```
/ Journal File for GAMBIT 2.4.6, Database 2.4.4, ntx86 SP2007051421
/ Identifier " Simulation Model 4: 2D RMC Air Cross Flow Journal File”
/ File opened for write Wed Jun 04 12:14:39 2008.
$t=1.3
$Rj=15
$Ro=5.1435
$Ri=$Ro-$t
$R1=$Ri+0.24
$R2=$Ro-0.24
$T=$Ro+(965-(36*2*$Ro))/(35*2)
$A=0.46
$B=0.56
$N=42
$tet=DEG2RAD*ATAN($A/(2*$R1))
$bet=(2*PI-(2*$tet*$N))/($N)
$o=0
$IN=50
$OUT=100
$ooo=$OUT+$T
$teta=($tet*RAD2DEG)
$beta=($bet*RAD2DEG)
//Angles
$tet01BC=$teta
$tet02AD=$tet01BC+$beta
$tet02BC=$tet02AD+(2*$teta)
$tet03AD=$tet02BC+$beta
$tet03BC=$tet03AD+(2*$teta)
$tet04AD=$tet03BC+$beta
$tet04BC=$tet04AD+(2*$teta)
$tet05AD=$tet04BC+$beta
$tet05BC=$tet05AD+(2*$teta)
// …… Repetition from 05 to 40
$tet40BC=$tet40AD+(2*$teta)
$tet41AD=$tet40BC+$beta
$tet41BC=$tet41AD+(2*$teta)
```

```
$tet42AD=$tet41BC+$beta
$tet42BC=$tet42AD+(2*$teta)
$tet01AD=$tet42BC+$beta

//Calculation of X location for each port edge
$X01A=($IN)+($R1/COS($tet01AD))*COS($tet01AD)
$X01B=($IN)+($R1/COS($tet01AD))*COS($tet01BC)
$X01C=($IN)+($R2/COS($tet01AD))*COS($tet01BC)
$X01D=($IN)+($R2/COS($tet01AD))*COS($tet01AD)
$X02A=($IN)+($R1/COS($tet01AD))*COS($tet02AD)
$X02B=($IN)+($R1/COS($tet01AD))*COS($tet02BC)
$X02C=($IN)+($R2/COS($tet01AD))*COS($tet02BC)
$X02D=($IN)+($R2/COS($tet01AD))*COS($tet02AD)
$X03A=($IN)+($R1/COS($tet01AD))*COS($tet03AD)
$X03B=($IN)+($R1/COS($tet01AD))*COS($tet03BC)
$X03C=($IN)+($R2/COS($tet01AD))*COS($tet03BC)
$X03D=($IN)+($R2/COS($tet01AD))*COS($tet03AD)
$X04A=($IN)+($R1/COS($tet01AD))*COS($tet04AD)
$X04B=($IN)+($R1/COS($tet01AD))*COS($tet04BC)
$X04C=($IN)+($R2/COS($tet01AD))*COS($tet04BC)
$X04D=($IN)+($R2/COS($tet01AD))*COS($tet04AD)
$X05A=($IN)+($R1/COS($tet01AD))*COS($tet05AD)
$X05B=($IN)+($R1/COS($tet01AD))*COS($tet05BC)
$X05C=($IN)+($R2/COS($tet01AD))*COS($tet05BC)
$X05D=($IN)+($R2/COS($tet01AD))*COS($tet05AD)
// …… Repetition from 5 to 40
$X40A=($IN)+($R1/COS($tet01AD))*COS($tet40AD)
$X40B=($IN)+($R1/COS($tet01AD))*COS($tet40BC)
$X40C=($IN)+($R2/COS($tet01AD))*COS($tet40BC)
$X40D=($IN)+($R2/COS($tet01AD))*COS($tet40AD)
$X41A=($IN)+($R1/COS($tet01AD))*COS($tet41AD)
$X41B=($IN)+($R1/COS($tet01AD))*COS($tet41BC)
$X41C=($IN)+($R2/COS($tet01AD))*COS($tet41BC)
$X41D=($IN)+($R2/COS($tet01AD))*COS($tet41AD)
$X42A=($IN)+($R1/COS($tet01AD))*COS($tet42AD)
$X42B=($IN)+($R1/COS($tet01AD))*COS($tet42BC)
$X42C=($IN)+($R2/COS($tet01AD))*COS($tet42BC)
$X42D=($IN)+($R2/COS($tet01AD))*COS($tet42AD)

//Calculation of Y location for each port edge
$Y01B=($R1/COS($tet01AD))*SIN($tet01BC)
$Y01C=($R2/COS($tet01AD))*SIN($tet01BC)
$Y02A=($R1/COS($tet01AD))*SIN($tet02AD)
$Y02B=($R1/COS($tet01AD))*SIN($tet02BC)
$Y02C=($R2/COS($tet01AD))*SIN($tet02BC)
$Y02D=($R2/COS($tet01AD))*SIN($tet02AD)
$Y03A=($R1/COS($tet01AD))*SIN($tet03AD)
$Y03B=($R1/COS($tet01AD))*SIN($tet03BC)
$Y03C=($R2/COS($tet01AD))*SIN($tet03BC)
$Y03D=($R2/COS($tet01AD))*SIN($tet03AD)
$Y04A=($R1/COS($tet01AD))*SIN($tet04AD)
$Y04B=($R1/COS($tet01AD))*SIN($tet04BC)
$Y04C=($R2/COS($tet01AD))*SIN($tet04BC)
$Y04D=($R2/COS($tet01AD))*SIN($tet04AD)
$Y05A=($R1/COS($tet01AD))*SIN($tet05AD)
$Y05B=($R1/COS($tet01AD))*SIN($tet05BC)
$Y05C=($R2/COS($tet01AD))*SIN($tet05BC)
```

```
$Y05D=($R2/COS($tet01AD))*SIN($tet05AD)
// …… Repetition from 5 to 40
$Y40A=($R1/COS($tet01AD))*SIN($tet40AD)
$Y40B=($R1/COS($tet01AD))*SIN($tet40BC)
$Y40C=($R2/COS($tet01AD))*SIN($tet40BC)
$Y40D=($R2/COS($tet01AD))*SIN($tet40AD)
$Y41A=($R1/COS($tet01AD))*SIN($tet41AD)
$Y41B=($R1/COS($tet01AD))*SIN($tet41BC)
$Y41C=($R2/COS($tet01AD))*SIN($tet41BC)
$Y41D=($R2/COS($tet01AD))*SIN($tet41AD)
$Y42A=($R1/COS($tet01AD))*SIN($tet42AD)
$Y42B=($R1/COS($tet01AD))*SIN($tet42BC)
$Y42C=($R2/COS($tet01AD))*SIN($tet42BC)
$Y42D=($R2/COS($tet01AD))*SIN($tet42AD)
$Y01A=($R1/COS($tet01AD))*SIN($tet01AD)
$Y01D=($R2/COS($tet01AD))*SIN($tet01AD)

//Calculationof air inlet and exit location
$X0=$IN
$XA=$IN+$Ri
$XB=$IN
$XC=$IN-$Ri
$XD=$IN+$Ro
$XE=$IN
$XF=$IN-$Ro
$X01S1=$IN+$R1
$X01S2=$IN+$R2
$X22S1=$IN-$R1
$X22S2=$IN-$R2
$Y01S1=$o
$Y01S2=$o
$Y22S1=$o
$Y22S2=$o
$YIN=$Ro
$YOUT=$Ro
$YA=$o
$YB=$Ri
$YC=$o
$YD=$o
$YE=$Ro
$YF=$o
$XXD=$IN+$T
$XXF=$IN-$T
$XYE=$T

//Create edges
vertex create "A" coordinates $XA $YA
vertex create "B" coordinates $XB $YB
vertex create "BB" coordinates $XB -$YB
vertex create "C" coordinates $XC $YC
vertex create "D" coordinates $XD $YD
vertex create "E" coordinates $XE $YE
vertex create "EE" coordinates $XE -$YE
vertex create "F" coordinates $XF $YF
vertex create "DX" coordinates $XXD $o
vertex create "EX" coordinates $XE $XYE
vertex create "EEX" coordinates $XE -$XYE
```

```
vertex create "FX" coordinates $XXF $o
vertex create "O" coordinates $IN $o
vertex create "L-IN" coordinates $o -$T
vertex create "U-IN" coordinates $o $T
vertex create "L-OUT" coordinates $OUT -$T
vertex create "U-OUT" coordinates $OUT $T
vertex create "01S1" coordinates $X01S1 $Y01S1
vertex create "01S2" coordinates $X01S2 $Y01S2
vertex create "22S1" coordinates $X22S1 $Y22S1
vertex create "22S2" coordinates $X22S2 $Y22S2
//port geometry
vertex create "01A" coordinates $X01A $Y01A
vertex create "01B" coordinates $X01B $Y01B
vertex create "01C" coordinates $X01C $Y01C
vertex create "01D" coordinates $X01D $Y01D
vertex create "02A" coordinates $X02A $Y02A
vertex create "02B" coordinates $X02B $Y02B
vertex create "02C" coordinates $X02C $Y02C
vertex create "02D" coordinates $X02D $Y02D
vertex create "03A" coordinates $X03A $Y03A
vertex create "03B" coordinates $X03B $Y03B
vertex create "03C" coordinates $X03C $Y03C
vertex create "03D" coordinates $X03D $Y03D
vertex create "04A" coordinates $X04A $Y04A
vertex create "04B" coordinates $X04B $Y04B
vertex create "04C" coordinates $X04C $Y04C
vertex create "04D" coordinates $X04D $Y04D
vertex create "05A" coordinates $X05A $Y05A
vertex create "05B" coordinates $X05B $Y05B
vertex create "05C" coordinates $X05C $Y05C
vertex create "05D" coordinates $X05D $Y05D
// …… Repetition 5 to 40
vertex create "40A" coordinates $X40A $Y40A
vertex create "40B" coordinates $X40B $Y40B
vertex create "40C" coordinates $X40C $Y40C
vertex create "40D" coordinates $X40D $Y40D
vertex create "41A" coordinates $X41A $Y41A
vertex create "41B" coordinates $X41B $Y41B
vertex create "41C" coordinates $X41C $Y41C
vertex create "41D" coordinates $X41D $Y41D
vertex create "42A" coordinates $X42A $Y42A
vertex create "42B" coordinates $X42B $Y42B
vertex create "42C" coordinates $X42C $Y42C
vertex create "42D" coordinates $X42D $Y42D
//Airflow edges
edge create "LT-ARCIN" threepoints "A" "B" "C" arc
edge create "LT-ARCINN" threepoints "A" "BB" "C" arc
edge create "LT-OUTARC" threepoints "D" "E" "F" arc
edge create "LT-OUTARCC" threepoints "D" "EE" "F" arc
edge create "LT-R-SYM1" straight "D" "01S2"
edge create "LT-R-SYM2" straight "01S1" "A"
edge create "LT-L-SYM1" straight "C" "22S1"
edge create "LT-L-SYM2" straight "22S2" "F"
edge create "THR-UP-1" center2points "O" "EX" "FX" minarc arc
edge create "THR-DWN-1" center2points "O" "FX" "EEX" minarc arc
edge create "THR-UP-2" center2points "O" "EX" "DX" minarc arc
edge create "THR-DWN-2" center2points "O" "DX" "EEX" minarc arc
```

```
edge create "THR-INT-1" straight "FX" "F"
edge create "THR-INT-2" straight "D" "DX"
edge create "LT-IN-SYM" straight "L-IN" "EEX"
edge create "LT-OUT-SYM" straight "L-OUT" "EEX"
edge create "UP-IN-SYM" straight "U-IN" "EX"
edge create "UP-OUT-SYM" straight "U-OUT" "EX"

//Create Port Edges
edge create "LT-P01-R1" straight "01S2" "01C"
edge create "LT-P01-T" straight "01C" "01B"
edge create "LT-P01-L1" straight "01B" "01S1"
edge create "LT-P02-R" straight "02D" "02C"
edge create "LT-P02-T" straight "02C" "02B"
edge create "LT-P02-L" straight "02B" "02A"
edge create "LT-P02-B" straight "02A" "02D"
edge create "LT-P03-R" straight "03D" "03C"
edge create "LT-P03-T" straight "03C" "03B"
edge create "LT-P03-L" straight "03B" "03A"
edge create "LT-P03-B" straight "03A" "03D"
edge create "LT-P04-R" straight "04D" "04C"
edge create "LT-P04-T" straight "04C" "04B"
edge create "LT-P04-L" straight "04B" "04A"
edge create "LT-P04-B" straight "04A" "04D"
edge create "LT-P05-R" straight "05D" "05C"
edge create "LT-P05-T" straight "05C" "05B"
edge create "LT-P05-L" straight "05B" "05A"
edge create "LT-P05-B" straight "05A" "05D"
// …… Repetition 5 to 40
edge create "UT-P40-R" straight "40D" "40C"
edge create "UT-P40-T" straight "40C" "40B"
edge create "UT-P40-L" straight "40B" "40A"
edge create "UT-P40-B" straight "40A" "40D"
edge create "UT-P41-R" straight "41D" "41C"
edge create "UT-P41-T" straight "41C" "41B"
edge create "UT-P41-L" straight "41B" "41A"
edge create "UT-P41-B" straight "41A" "41D"
edge create "UT-P42-R" straight "42D" "42C"
edge create "UT-P42-T" straight "42C" "42B"
edge create "UT-P42-L" straight "42B" "42A"
edge create "UT-P42-B" straight "42A" "42D"
edge create "UT-P01-R2" straight "01S1" "01A"
edge create "UT-P01-B" straight "01A" "01D"
edge create "UT-P01-L2" straight "01D" "01S2"
//Create Edges Air Inlet and Exit
edge create "FLOW-IN" straight "U-IN" "L-IN"
edge create "FLOW-OUT" straight "U-OUT" "L-OUT"

//Create Edges for Ports
edge create "LT-01B-02A" straight "01B" "02A"
edge create "LT-02B-03A" straight "02B" "03A"
edge create "LT-03B-04A" straight "03B" "04A"
edge create "LT-04B-05A" straight "04B" "05A"
edge create "LT-05B-06A" straight "05B" "06A"
// …… Repetition 5 to 40
edge create "UT-40C-41D" straight "40C" "41D"
edge create "UT-41C-42D" straight "41C" "42D"
edge create "UT-42C-01D" straight "42C" "01D"
```

```
edge create "UT-42B-01A" straight "42B" "01A"
//Face geometry
face create "LT-MID-01-02" wireframe "LT-P01-T" "LT-01B-02A" "LT-P02-B"
"LT-01C-02D" real
face create "LT-MID-02-03" wireframe "LT-P02-T" "LT-02B-03A" "LT-P03-B"
"LT-02C-03D" real
face create "LT-MID-03-04" wireframe "LT-P03-T" "LT-03B-04A" "LT-P04-B"
"LT-03C-04D" real
face create "LT-MID-04-05" wireframe "LT-P04-T" "LT-04B-05A" "LT-P05-B"
"LT-04C-05D" real
face create "LT-MID-05-06" wireframe "LT-P05-T" "LT-05B-06A" "LT-P06-B"
"LT-05C-06D" real
// …… Repetition 5 to 40
face create "UT-MID-40-41" wireframe "UT-P40-T" "UT-40B-41A" "UT-P41-B"
"UT-40C-41D" real
face create "UT-MID-41-42" wireframe "UT-P41-T" "UT-41B-42A" "UT-P42-B"
"UT-41C-42D" real
face create "UT-MID-42-01" wireframe "UT-P42-T" "UT-42B-01A" "UT-P01-B"
"UT-42C-01D" real

face create "LT-UP" wireframe "LT-R-SYM1" "LT-P01-R1" "LT-01C-02D" "LT-
P02-R" \
  "LT-02C-03D" "LT-P03-R" "LT-03C-04D" "LT-P04-R" "LT-04C-05D" "LT-P05-
R" \
  "LT-05C-06D" "LT-P06-R" "LT-06C-07D" "LT-P07-R" "LT-07C-08D" "LT-P08-
R" \
  "LT-08C-09D" "LT-P09-R" "LT-09C-10D" "LT-P10-R" "LT-10C-11D" "LT-P11-
R" \
  "LT-11C-12D" "LT-P12-R" "LT-12C-13D" "LT-P13-R" "LT-13C-14D" "LT-P14-
R" \
  "LT-14C-15D" "LT-P15-R" "LT-15C-16D" "LT-P16-R" "LT-16C-17D" "LT-P17-
R" \
  "LT-17C-18D" "LT-P18-R" "LT-18C-19D" "LT-P19-R" "LT-19C-20D" "LT-P20-
R" \
  "LT-20C-21D" "LT-P21-R" "LT-21C-22D" "LT-P22-L1" "LT-L-SYM2" "LT-
OUTARC" \
  real
face create "LT-DOWN" wireframe "LT-R-SYM2" "LT-P01-L1" "LT-01B-02A" \
  "LT-P02-L" "LT-02B-03A" "LT-P03-L" "LT-03B-04A" "LT-P04-L" "LT-04B-
05A" \
  "LT-P05-L" "LT-05B-06A" "LT-P06-L" "LT-06B-07A" "LT-P07-L" "LT-07B-
08A" \
  "LT-P08-L" "LT-08B-09A" "LT-P09-L" "LT-09B-10A" "LT-P10-L" "LT-10B-
11A" \
  "LT-P11-L" "LT-11B-12A" "LT-P12-L" "LT-12B-13A" "LT-P13-L" "LT-13B-
14A" \
  "LT-P14-L" "LT-14B-15A" "LT-P15-L" "LT-15B-16A" "LT-P16-L" "LT-16B-
17A" \
  "LT-P17-L" "LT-17B-18A" "LT-P18-L" "LT-18B-19A" "LT-P19-L" "LT-19B-
20A" \
  "LT-P20-L" "LT-20B-21A" "LT-P21-L" "LT-21B-22A" "LT-P22-R1" "LT-L-
SYM1" \
  "LT-ARCIN" real
face create "UT-UP" wireframe "LT-OUTARCC" "LT-R-SYM1" "UT-P01-L2" \
  "UT-42C-01D" "UT-P42-R" "UT-41C-42D" "UT-P41-R" "UT-40C-41D" "UT-P40-
R" \
```

```
  "UT-39C-40D" "UT-P39-R" "UT-38C-39D" "UT-P38-R" "UT-37C-38D" "UT-P37-
R" \
  "UT-36C-37D" "UT-P36-R" "UT-35C-36D" "UT-P35-R" "UT-34C-35D" "UT-P34-
R" \
  "UT-33C-34D" "UT-P33-R" "UT-32C-33D" "UT-P32-R" "UT-31C-32D" "UT-P31-
R" \
  "UT-30C-31D" "UT-P30-R" "UT-29C-30D" "UT-P29-R" "UT-28C-29D" "UT-P28-
R" \
  "UT-27C-28D" "UT-P27-R" "UT-26C-27D" "UT-P26-R" "UT-25C-26D" "UT-P25-
R" \
  "UT-24C-25D" "UT-P24-R" "UT-23C-24D" "UT-P23-R" "UT-22C-23D" "UT-P22-
L2" \
  "LT-L-SYM2" real
face create "UT-DOWN" wireframe "LT-L-SYM1" "UT-P22-R2" "UT-22B-23A" \
  "UT-P23-L" "UT-23B-24A" "UT-P24-L" "UT-24B-25A" "UT-P25-L" "UT-25B-
26A" \
  "UT-P26-L" "UT-26B-27A" "UT-P27-L" "UT-27B-28A" "UT-P28-L" "UT-28B-
29A" \
  "UT-P29-L" "UT-29B-30A" "UT-P30-L" "UT-30B-31A" "UT-P31-L" "UT-31B-
32A" \
  "UT-P32-L" "UT-32B-33A" "UT-P33-L" "UT-33B-34A" "UT-P34-L" "UT-34B-
35A" \
  "UT-P35-L" "UT-35B-36A" "UT-P36-L" "UT-36B-37A" "UT-P37-L" "UT-37B-
38A" \
  "UT-P38-L" "UT-38B-39A" "UT-P39-L" "UT-39B-40A" "UT-P40-L" "UT-40B-
41A" \
  "UT-P41-L" "UT-41B-42A" "UT-P42-L" "UT-42B-01A" "UT-P01-R2" "LT-R-
SYM2" \
  "LT-ARCINN" real
face create "INLET-FACE" wireframe "FLOW-IN" "UP-IN-SYM" "THR-UP-1" \
  "THR-DWN-1" "LT-IN-SYM" real
face create "OUTLET-FACE" wireframe "FLOW-OUT" "LT-OUT-SYM" "THR-DWN-2"
\
  "THR-UP-2" "UP-OUT-SYM" real
face create "THR-UP-FACE" wireframe "THR-UP-1" "THR-UP-2" "THR-INT-2" \
  "LT-OUTARC" "THR-INT-1" real
face create "THR-DWN-FACE" wireframe "THR-INT-2" "THR-DWN-2" "THR-DWN-
1" \
  "THR-INT-1" "LT-OUTARCC" real
face create "PORT-01" wireframe "LT-P01-L1" "LT-P01-T" "LT-P01-R1" \
  "UT-P01-L2" "UT-P01-B" "UT-P01-R2" real
face create "PORT-02" wireframe "LT-P02-B" "LT-P02-R" "LT-P02-T" "LT-
P02-L" real
face create "PORT-03" wireframe "LT-P03-B" "LT-P03-R" "LT-P03-T" "LT-
P03-L" real
face create "PORT-04" wireframe "LT-P04-B" "LT-P04-R" "LT-P04-T" "LT-
P04-L" real
face create "PORT-05" wireframe "LT-P05-B" "LT-P05-R" "LT-P05-T" "LT-
P05-L" real
// …… Repetition 5 to 40
face create "PORT-40" wireframe "UT-P40-R" "UT-P40-T" "UT-P40-L" "UT-
P40-B" real
face create "PORT-41" wireframe "UT-P41-R" "UT-P41-T" "UT-P41-L" "UT-
P41-B" real
face create "PORT-42" wireframe "UT-P42-R" "UT-P42-T" "UT-P42-L" "UT-
P42-B" real
```

```
//Mesh Edges
//connection - 21x2
undo begingroup
edge picklink "LT-21C-22D" "LT-21B-22A" "LT-20C-21D" "LT-20B-21A" \
  "LT-19C-20D" "LT-19B-20A" "LT-18C-19D" "LT-18B-19A" "LT-17C-18D" \
  "LT-17B-18A" "LT-16C-17D" "LT-16B-17A" "LT-15C-16D" "LT-15B-16A" \
  "LT-14C-15D" "LT-14B-15A" "LT-13C-14D" "LT-13B-14A" "LT-12C-13D" \
  "LT-12B-13A" "LT-11C-12D" "LT-11B-12A" "LT-10C-11D" "LT-10B-11A" \
  "LT-09C-10D" "LT-09B-10A" "LT-08C-09D" "LT-08B-09A" "LT-07C-08D" \
  "LT-07B-08A" "LT-06C-07D" "LT-06B-07A" "LT-05C-06D" "LT-05B-06A" \
  "LT-04C-05D" "LT-04B-05A" "LT-03C-04D" "LT-03B-04A" "LT-02C-03D" \
  "LT-02B-03A" "LT-01C-02D" "LT-01B-02A"
edge mesh "LT-01B-02A" "LT-01C-02D" "LT-02B-03A" "LT-02C-03D" "LT-03B-
04A" \
  "LT-03C-04D" "LT-04B-05A" "LT-04C-05D" "LT-05B-06A" "LT-05C-06D" \
  "LT-06B-07A" "LT-06C-07D" "LT-07B-08A" "LT-07C-08D" "LT-08B-09A" \
  "LT-08C-09D" "LT-09B-10A" "LT-09C-10D" "LT-10B-11A" "LT-10C-11D" \
  "LT-11B-12A" "LT-11C-12D" "LT-12B-13A" "LT-12C-13D" "LT-13B-14A" \
  "LT-13C-14D" "LT-14B-15A" "LT-14C-15D" "LT-15B-16A" "LT-15C-16D" \
  "LT-16B-17A" "LT-16C-17D" "LT-17B-18A" "LT-17C-18D" "LT-18B-19A" \
  "LT-18C-19D" "LT-19B-20A" "LT-19C-20D" "LT-20B-21A" "LT-20C-21D" \
  "LT-21B-22A" "LT-21C-22D" successive ratio1 1 intervals 2
undo endgroup
//ports - 20 x 6
undo begingroup
edge picklink "LT-P21-R" "LT-P21-L" "LT-P20-R" "LT-P20-L" "LT-P19-R" \
  "LT-P19-L" "LT-P18-R" "LT-P18-L" "LT-P17-R" "LT-P17-L" "LT-P16-R" \
  "LT-P16-L" "LT-P15-R" "LT-P15-L" "LT-P14-R" "LT-P14-L" "LT-P13-R" \
  "LT-P13-L" "LT-P12-R" "LT-P12-L" "LT-P11-R" "LT-P11-L" "LT-P10-R" \
  "LT-P10-L" "LT-P09-R" "LT-P09-L" "LT-P08-R" "LT-P08-L" "LT-P07-R" \
  "LT-P07-L" "LT-P06-R" "LT-P06-L" "LT-P05-R" "LT-P05-L" "LT-P04-R" \
  "LT-P04-L" "LT-P03-R" "LT-P03-L" "LT-P02-R" "LT-P02-L"
edge mesh "LT-P02-L" "LT-P02-R" "LT-P03-L" "LT-P03-R" "LT-P04-L" "LT-
P04-R" \
  "LT-P05-L" "LT-P05-R" "LT-P06-L" "LT-P06-R" "LT-P07-L" "LT-P07-R" \
  "LT-P08-L" "LT-P08-R" "LT-P09-L" "LT-P09-R" "LT-P10-L" "LT-P10-R" \
  "LT-P11-L" "LT-P11-R" "LT-P12-L" "LT-P12-R" "LT-P13-L" "LT-P13-R" \
  "LT-P14-L" "LT-P14-R" "LT-P15-L" "LT-P15-R" "LT-P16-L" "LT-P16-R" \
  "LT-P17-L" "LT-P17-R" "LT-P18-L" "LT-P18-R" "LT-P19-L" "LT-P19-R" \
  "LT-P20-L" "LT-P20-R" "LT-P21-L" "LT-P21-R" successive ratio1 1
intervals 6
undo endgroup
//connection - 2 x 21
undo begingroup
edge picklink "UT-42C-01D" "UT-42B-01A" "UT-41C-42D" "UT-41B-42A" \
  "UT-40C-41D" "UT-40B-41A" "UT-39C-40D" "UT-39B-40A" "UT-38C-39D" \
  "UT-38B-39A" "UT-37C-38D" "UT-37B-38A" "UT-36C-37D" "UT-36B-37A" \
  "UT-35C-36D" "UT-35B-36A" "UT-34C-35D" "UT-34B-35A" "UT-33C-34D" \
  "UT-33B-34A" "UT-32C-33D" "UT-32B-33A" "UT-31C-32D" "UT-31B-32A" \
  "UT-30C-31D" "UT-30B-31A" "UT-29C-30D" "UT-29B-30A" "UT-28C-29D" \
  "UT-28B-29A" "UT-27C-28D" "UT-27B-28A" "UT-26C-27D" "UT-26B-27A" \
  "UT-25C-26D" "UT-25B-26A" "UT-24C-25D" "UT-24B-25A" "UT-23C-24D" \
  "UT-23B-24A" "UT-22C-23D" "UT-22B-23A"
edge mesh "UT-22B-23A" "UT-22C-23D" "UT-23B-24A" "UT-23C-24D" "UT-24B-
25A" \
  "UT-24C-25D" "UT-25B-26A" "UT-25C-26D" "UT-26B-27A" "UT-26C-27D" \
  "UT-27B-28A" "UT-27C-28D" "UT-28B-29A" "UT-28C-29D" "UT-29B-30A" \
```

```
  "UT-29C-30D" "UT-30B-31A" "UT-30C-31D" "UT-31B-32A" "UT-31C-32D" \
  "UT-32B-33A" "UT-32C-33D" "UT-33B-34A" "UT-33C-34D" "UT-34B-35A" \
  "UT-34C-35D" "UT-35B-36A" "UT-35C-36D" "UT-36B-37A" "UT-36C-37D" \
  "UT-37B-38A" "UT-37C-38D" "UT-38B-39A" "UT-38C-39D" "UT-39B-40A" \
  "UT-39C-40D" "UT-40B-41A" "UT-40C-41D" "UT-41B-42A" "UT-41C-42D" \
  "UT-42B-01A" "UT-42C-01D" successive ratio1 1 intervals 2
undo endgroup
//ports - 20x6
undo begingroup
edge picklink "UT-P42-R" "UT-P42-L" "UT-P41-R" "UT-P41-L" "UT-P40-R" \
  "UT-P40-L" "UT-P39-R" "UT-P39-L" "UT-P38-R" "UT-P38-L" "UT-P37-R" \
  "UT-P37-L" "UT-P36-R" "UT-P36-L" "UT-P35-R" "UT-P35-L" "UT-P34-R" \
  "UT-P34-L" "UT-P33-R" "UT-P33-L" "UT-P32-R" "UT-P32-L" "UT-P31-R" \
  "UT-P31-L" "UT-P30-R" "UT-P30-L" "UT-P29-R" "UT-P29-L" "UT-P28-R" \
  "UT-P28-L" "UT-P27-R" "UT-P27-L" "UT-P26-R" "UT-P26-L" "UT-P25-R" \
  "UT-P25-L" "UT-P24-R" "UT-P24-L" "UT-P23-R" "UT-P23-L"
edge mesh "UT-P23-L" "UT-P23-R" "UT-P24-L" "UT-P24-R" "UT-P25-L" "UT-
P25-R" \
  "UT-P26-L" "UT-P26-R" "UT-P27-L" "UT-P27-R" "UT-P28-L" "UT-P28-R" \
  "UT-P29-L" "UT-P29-R" "UT-P30-L" "UT-P30-R" "UT-P31-L" "UT-P31-R" \
  "UT-P32-L" "UT-P32-R" "UT-P33-L" "UT-P33-R" "UT-P34-L" "UT-P34-R" \
  "UT-P35-L" "UT-P35-R" "UT-P36-L" "UT-P36-R" "UT-P37-L" "UT-P37-R" \
  "UT-P38-L" "UT-P38-R" "UT-P39-L" "UT-P39-R" "UT-P40-L" "UT-P40-R" \
  "UT-P41-L" "UT-P41-R" "UT-P42-L" "UT-P42-R" successive ratio1 1
intervals 6
undo endgroup
//half ports -  2x 3
undo begingroup
edge picklink "LT-P22-R1" "LT-P22-L1" "LT-P01-L1" "LT-P01-R1"
edge mesh "LT-P01-R1" "LT-P01-L1" "LT-P22-L1" "LT-P22-R1" successive
ratio1 1 \
  intervals 3
undo endgroup

undo begingroup
edge picklink "UT-P01-L2" "UT-P01-R2" "UT-P22-R2" "UT-P22-L2"
edge mesh "UT-P22-L2" "UT-P22-R2" "UT-P01-R2" "UT-P01-L2" successive
ratio1 1 \
  intervals 3
undo endgroup
//port sides - 8
undo begingroup
edge picklink "LT-P22-B" "LT-P21-T" "LT-P21-B" "LT-P20-T" \
  "LT-P20-B" "LT-P19-T" "LT-P19-B" "LT-P18-T" "LT-P18-B" "LT-P17-T" \
  "LT-P17-B" "LT-P16-T" "LT-P16-B" "LT-P15-T" "LT-P15-B" "LT-P14-T" \
  "LT-P14-B" "LT-P13-T" "LT-P13-B" "LT-P12-T" "LT-P12-B" "LT-P11-T" \
  "LT-P11-B" "LT-P10-T" "LT-P10-B" "LT-P09-T" "LT-P09-B" "LT-P08-T" \
  "LT-P08-B" "LT-P07-T" "LT-P07-B" "LT-P06-T" "LT-P06-B" "LT-P05-T" \
  "LT-P05-B" "LT-P04-T" "LT-P04-B" "LT-P03-T" "LT-P03-B" "LT-P02-T" \
  "LT-P02-B" "LT-P01-T"
edge mesh "LT-P01-T" "LT-P02-B" "LT-P02-T" "LT-P03-B" \
  "LT-P03-T" "LT-P04-B" "LT-P04-T" "LT-P05-B" "LT-P05-T" "LT-P06-B" \
  "LT-P06-T" "LT-P07-B" "LT-P07-T" "LT-P08-B" "LT-P08-T" "LT-P09-B" \
  "LT-P09-T" "LT-P10-B" "LT-P10-T" "LT-P11-B" "LT-P11-T" "LT-P12-B" \
  "LT-P12-T" "LT-P13-B" "LT-P13-T" "LT-P14-B" "LT-P14-T" "LT-P15-B" \
  "LT-P15-T" "LT-P16-B" "LT-P16-T" "LT-P17-B" "LT-P17-T" "LT-P18-B" \
  "LT-P18-T" "LT-P19-B" "LT-P19-T" "LT-P20-B" "LT-P20-T" "LT-P21-B" \
```

```
  "LT-P21-T" "LT-P22-B" successive ratio1 1 intervals 8
undo endgroup
undo begingroup
edge picklink "UT-P01-B" "UT-P42-T" "UT-P41-T" "UT-P42-B" \
  "UT-P40-T" "UT-P41-B" "UT-P39-T" "UT-P40-B" "UT-P38-T" "UT-P39-B" \
  "UT-P37-T" "UT-P38-B" "UT-P36-T" "UT-P37-B" "UT-P36-B" "UT-P35-T" \
  "UT-P35-B" "UT-P34-T" "UT-P34-B" "UT-P33-T" "UT-P33-B" "UT-P32-T" \
  "UT-P32-B" "UT-P31-T" "UT-P31-B" "UT-P30-T" "UT-P30-B" "UT-P29-T" \
  "UT-P29-B" "UT-P28-T" "UT-P28-B" "UT-P27-T" "UT-P27-B" "UT-P26-T" \
  "UT-P26-B" "UT-P25-T" "UT-P25-B" "UT-P24-T" "UT-P24-B" "UT-P23-T" \
  "UT-P23-B" "UT-P22-T"
edge mesh "UT-P22-T" "UT-P23-B" "UT-P23-T" "UT-P24-B" \
  "UT-P24-T" "UT-P25-B" "UT-P25-T" "UT-P26-B" "UT-P26-T" "UT-P27-B" \
  "UT-P27-T" "UT-P28-B" "UT-P28-T" "UT-P29-B" "UT-P29-T" "UT-P30-B" \
  "UT-P30-T" "UT-P31-B" "UT-P31-T" "UT-P32-B" "UT-P32-T" "UT-P33-B" \
  "UT-P33-T" "UT-P34-B" "UT-P34-T" "UT-P35-B" "UT-P35-T" "UT-P36-B" \
  "UT-P37-B" "UT-P36-T" "UT-P38-B" "UT-P37-T" "UT-P39-B" "UT-P38-T" \
  "UT-P40-B" "UT-P39-T" "UT-P41-B" "UT-P40-T" "UT-P42-B" "UT-P41-T" \
  "UT-P42-T" "UT-P01-B" successive ratio1 1 intervals 8
undo endgroup
undo begingroup
edge picklink "LT-L-SYM2" "LT-L-SYM1" "LT-R-SYM2" "LT-R-SYM1"
edge mesh "LT-R-SYM1" "LT-R-SYM2" "LT-L-SYM1" "LT-L-SYM2" successive
ratio1 1 \
  intervals 4
undo endgroup
undo begingroup
edge picklink "THR-DWN-2" "THR-UP-1"
edge mesh "THR-UP-1" "THR-DWN-2" successive ratio1 1 intervals 84
undo endgroup
undo begingroup
edge picklink "THR-DWN-1" "THR-UP-2"
edge mesh "THR-UP-2" "THR-DWN-1" successive ratio1 1 intervals 84
undo endgroup
undo begingroup
edge picklink "FLOW-OUT" "FLOW-IN"
edge mesh "FLOW-IN" "FLOW-OUT" successive ratio1 1 intervals 168
undo endgroup
undo begingroup
edge picklink "LT-ARCINN" "LT-OUTARCC" "LT-ARCIN" "LT-OUTARC"
edge mesh "LT-OUTARC" "LT-ARCIN" "LT-OUTARCC" "LT-ARCINN" successive
ratio1 1 \
  intervals 168
undo endgroup

undo begingroup
edge picklink "THR-INT-2" "THR-INT-1"
edge mesh "THR-INT-1" "THR-INT-2" successive ratio1 1 intervals 60
undo endgroup
undo begingroup
edge picklink "LT-OUT-SYM" "UP-OUT-SYM" "LT-IN-SYM" "UP-IN-SYM"
edge mesh "UP-IN-SYM" "LT-IN-SYM" "UP-OUT-SYM" "LT-OUT-SYM" successive
ratio1 \
  1 intervals 242
undo endgroup
//Face Mesh
face mesh "PORT-01" "LT-MID-01-02" "PORT-02" "LT-MID-02-03" "PORT-03" \
```

```
  "LT-MID-03-04" "PORT-04" "LT-MID-04-05" "PORT-05" "LT-MID-05-06"
"PORT-06" \
  "LT-MID-06-07" "PORT-07" "LT-MID-07-08" "PORT-08" "LT-MID-08-09"
"PORT-09" \
  "LT-MID-09-10" "PORT-10" "LT-MID-10-11" "PORT-11" "LT-MID-11-12"
"PORT-12" \
  "LT-MID-12-13" "PORT-13" "LT-MID-13-14" "PORT-14" "LT-MID-14-15"
"PORT-15" \
  "LT-MID-15-16" "PORT-16" "LT-MID-16-17" "PORT-17" "LT-MID-17-18"
"PORT-18" \
  "LT-MID-18-19" "PORT-19" "LT-MID-19-20" "PORT-20" "LT-MID-20-21"
"PORT-21" \
  "LT-MID-21-22" "PORT-22" "UT-MID-22-23" "PORT-23" "UT-MID-23-24"
"PORT-24" \
  "UT-MID-24-25" "PORT-25" "UT-MID-25-26" "PORT-26" "UT-MID-26-27"
"PORT-27" \
  "UT-MID-27-28" "PORT-28" "UT-MID-28-29" "PORT-29" "UT-MID-29-30"
"PORT-30" \
  "UT-MID-30-31" "PORT-31" "UT-MID-31-32" "PORT-32" "UT-MID-32-33"
"PORT-33" \
  "UT-MID-33-34" "PORT-34" "UT-MID-34-35" "PORT-35" "UT-MID-35-36"
"PORT-36" \
  "UT-MID-36-37" "PORT-37" "UT-MID-37-38" "PORT-38" "UT-MID-38-39"
"PORT-39" \
  "UT-MID-39-40" "PORT-40" "UT-MID-40-41" "PORT-41" "UT-MID-41-42"
"PORT-42" \
  "UT-MID-42-01" map intervals 10
face mesh "LT-UP" "UT-UP" map intervals 10
face mesh "LT-DOWN" "UT-DOWN" map intervals 10
face mesh "INLET-FACE" "OUTLET-FACE" map intervals 10
undo begingroup
face delete "THR-UP-FACE" "THR-DWN-FACE" onlymesh
face mesh "THR-UP-FACE" "THR-DWN-FACE" map
undo endgroup

//Scale the model mm to m
model scale factor 0.001 origin 0 0 0

//Select Solver
solver select "FLUENT 5/6"

//Boundary Conditions
physics create "Air-Inlet" btype "VELOCITY_INLET" edge "FLOW-IN"
physics create "Air-Outlet" btype "PRESSURE_OUTLET" edge "FLOW-OUT"
physics create "Air-Sym-1" btype "SYMMETRY" edge "UP-IN-SYM"
physics create "Air-Sym-2" btype "SYMMETRY" edge "UP-OUT-SYM"
physics create "Air-Sym-3" btype "SYMMETRY" edge "LT-OUT-SYM"
physics create "Air-Sym-4" btype "SYMMETRY" edge "LT-IN-SYM"
physics create "Air-Intr-1" btype "INTERIOR" edge "THR-UP-1"
physics create "Air-Intr-2" btype "INTERIOR" edge "THR-UP-2"
physics create "Air-Intr-3" btype "INTERIOR" edge "THR-DWN-2"
physics create "Air-Intr-4" btype "INTERIOR" edge "THR-DWN-1"
physics create "Air-Intr-5" btype "INTERIOR" edge "THR-INT-1"
physics create "LT-P01-R1" btype "WALL" edge "LT-P01-R1"
physics create "LT-P01-T" btype "WALL" edge "LT-P01-T"
physics create "LT-P01-L1" btype "WALL" edge "LT-P01-L1"
physics create "LT-P02-R" btype "WALL" edge "LT-P02-R"
```

```
physics create "LT-P02-T" btype "WALL" edge "LT-P02-T"
physics create "LT-P02-L" btype "WALL" edge "LT-P02-L"
physics create "LT-P02-B" btype "WALL" edge "LT-P02-B"
physics create "LT-P03-R" btype "WALL" edge "LT-P03-R"
physics create "LT-P03-T" btype "WALL" edge "LT-P03-T"
physics create "LT-P03-L" btype "WALL" edge "LT-P03-L"
physics create "LT-P03-B" btype "WALL" edge "LT-P03-B"
physics create "LT-P04-R" btype "WALL" edge "LT-P04-R"
physics create "LT-P04-T" btype "WALL" edge "LT-P04-T"
physics create "LT-P04-L" btype "WALL" edge "LT-P04-L"
physics create "LT-P04-B" btype "WALL" edge "LT-P04-B"
physics create "LT-P05-R" btype "WALL" edge "LT-P05-R"
physics create "LT-P05-T" btype "WALL" edge "LT-P05-T"
physics create "LT-P05-L" btype "WALL" edge "LT-P05-L"
physics create "LT-P05-B" btype "WALL" edge "LT-P05-B"
// …… Repetition 5 to 40
physics create "UT-P40-R" btype "WALL" edge "UT-P40-R"
physics create "UT-P40-T" btype "WALL" edge "UT-P40-T"
physics create "UT-P40-L" btype "WALL" edge "UT-P40-L"
physics create "UT-P40-B" btype "WALL" edge "UT-P40-B"
physics create "UT-P41-R" btype "WALL" edge "UT-P41-R"
physics create "UT-P41-T" btype "WALL" edge "UT-P41-T"
physics create "UT-P41-L" btype "WALL" edge "UT-P41-L"
physics create "UT-P41-B" btype "WALL" edge "UT-P41-B"
physics create "UT-P42-R" btype "WALL" edge "UT-P42-R"
physics create "UT-P42-T" btype "WALL" edge "UT-P42-T"
physics create "UT-P42-L" btype "WALL" edge "UT-P42-L"
physics create "UT-P42-B" btype "WALL" edge "UT-P42-B"
physics create "UT-P01-R2" btype "WALL" edge "UT-P01-R2"
physics create "UT-P01-B" btype "WALL" edge "UT-P01-B"
physics create "UT-P01-L2" btype "WALL" edge "UT-P01-L2"
/SYM-TUBEWALLS
physics create "LT-OuterWall"  btype "WALL" edge "LT-OUTARC"
physics create "LT-AdbWall" btype "WALL" edge "LT-ARCIN"
physics create "UT-OuterWall"  btype "WALL" edge "LT-OUTARCC"
physics create "UT-AdbWall" btype "WALL" edge "LT-ARCINN"
//ALUMINUM
physics create "Solid-LT-MID-01-02" ctype "SOLID" face "LT-MID-01-02"
physics create "Solid-LT-MID-02-03" ctype "SOLID" face "LT-MID-02-03"
physics create "Solid-LT-MID-03-04" ctype "SOLID" face "LT-MID-03-04"
physics create "Solid-LT-MID-04-05" ctype "SOLID" face "LT-MID-04-05"
physics create "Solid-LT-MID-05-06" ctype "SOLID" face "LT-MID-05-06"
physics create "Solid-LT-MID-06-07" ctype "SOLID" face "LT-MID-06-07"
physics create "Solid-LT-MID-07-08" ctype "SOLID" face "LT-MID-07-08"
physics create "Solid-LT-MID-08-09" ctype "SOLID" face "LT-MID-08-09"
physics create "Solid-LT-MID-09-10" ctype "SOLID" face "LT-MID-09-10"
physics create "Solid-LT-MID-10-11" ctype "SOLID" face "LT-MID-10-11"
physics create "Solid-LT-MID-11-12" ctype "SOLID" face "LT-MID-11-12"
physics create "Solid-LT-MID-12-13" ctype "SOLID" face "LT-MID-12-13"
physics create "Solid-LT-MID-13-14" ctype "SOLID" face "LT-MID-13-14"
physics create "Solid-LT-MID-14-15" ctype "SOLID" face "LT-MID-14-15"
// …… Repetition 5 to 40
physics create "Solid-UT-MID-39-40" ctype "SOLID" face "UT-MID-39-40"
physics create "Solid-UT-MID-40-41" ctype "SOLID" face "UT-MID-40-41"
physics create "Solid-UT-MID-41-42" ctype "SOLID" face "UT-MID-41-42"
physics create "Solid-UT-MID-42-01" ctype "SOLID" face "UT-MID-42-01"
physics create "Solid-LT-UP" ctype "SOLID" face "LT-UP"
```

```
physics create "Solid-LT-DOWN" ctype "SOLID" face "LT-DOWN"
physics create "Solid-UT-UP" ctype "SOLID" face "UT-UP"
physics create "Solid-UT-DOWN" ctype "SOLID" face "UT-DOWN"
//FLUID
physics create "Fluid-PORT-01" ctype "FLUID" face "PORT-01"
physics create "Fluid-PORT-02" ctype "FLUID" face "PORT-02"
physics create "Fluid-PORT-03" ctype "FLUID" face "PORT-03"
physics create "Fluid-PORT-04" ctype "FLUID" face "PORT-04"
physics create "Fluid-PORT-05" ctype "FLUID" face "PORT-05"
// …… Repetition 5 to 40
physics create "Fluid-PORT-40" ctype "FLUID" face "PORT-40"
physics create "Fluid-PORT-41" ctype "FLUID" face "PORT-41"
physics create "Fluid-PORT-42" ctype "FLUID" face "PORT-42"
physics create "Fluid-Air-Inlet" ctype "FLUID" face "INLET-FACE"
physics create "Fluid-Air-Thr-up" ctype "FLUID" face "THR-UP-FACE"
physics create "Fluid-Air-Thr-Dwn" ctype "FLUID" face "THR-DWN-FACE"
physics create "Fluid-Air-Exit" ctype "FLUID" face "OUTLET-FACE"
default set "GRAPHICS.GENERAL.CONNECTIVITY_BASED_COLORING" numeric 1
//Check Topology and Geometry
check topology
check geometry
//Export Mesh
export fluent5 "2DRMC-M.msh" nozval
save
```

C-2: Simulation Model 5: SMC Tube Heat Exchanger in Air Cross Flow

Gambit Journal File

```
//Identifier "Simulation Model 4: 2D RMC Air Cross Flow Journal File"
//half tube thickness [mm]
$t=1.3/2
//Half tube spacing [mm]
$T=(12.7)/2
//Port Geometry [mm]
$H=0.51
$W=0.41
//Port Number [mm]
$N=23
//Tube Geometry [mm]
$tt=18
$a=0.24
$b=0.26125
$o=0
$IN=50-($tt/2)
$OUT=100

// X Points
$XA=($IN)
```

```
$XAB=($XA)
$XAA=$XA-5
$XB=($XA+$b)
$XD=$XA+$tt
$XDD=$XD+5
$XC=($XD-$b)
$XCD=$XD

// Port X points
$X01A=($XA+$b)
$X01B=($X01A)
$X01C=($X01B+$H)
$X01D=($X01C)
$X02A=($X01C+$b)
$X02B=($X02A)
$X02C=($X02B+$H)
$X02D=($X02C)
$X03A=($X02C+$b)
$X03B=($X03A)
$X03C=($X03B+$H)
$X03D=($X03C)
$X04A=($X03C+$b)
$X04B=($X04A)
$X04C=($X04B+$H)
$X04D=($X04C)
$X05A=($X04C+$b)
$X05B=($X05A)
$X05C=($X05B+$H)
$X05D=($X05C)
// …… Repetition 5 to 20
$X20B=($X20A)
$X20C=($X20B+$H)
$X20D=($X20C)
$X21A=($X20C+$b)
$X21B=($X21A)
$X21C=($X21B+$H)
$X21D=($X21C)
$X22A=($X21C+$b)
$X22B=($X22A)
$X22C=($X22B+$H)
$X22D=($X22C)
$X23A=($X22C+$b)
$X23B=($X23A)
$X23C=($X23B+$H)
$X23D=($X23C)

//Port Y Points
$Y01A=(-$W)
$Y01B=($W)
$Y01C=($Y01B)
$Y01D=($Y01A)
$Y02A=($Y01A)
$Y02B=($Y01B)
$Y02C=($Y01C)
$Y02D=($Y01D)
$Y03A=($Y02A)
$Y03B=($Y02B)
```

```
$Y03C=($Y02C)
$Y03D=($Y02D)
$Y04A=($Y03A)
$Y04B=($Y03B)
$Y04C=($Y03C)
$Y04D=($Y03D)
$Y05A=($Y04A)
$Y05B=($Y04B)
$Y05C=($Y04C)
$Y05D=($Y04D)
// …… Repetition 5 to 20
$Y20B=($Y19B)
$Y20C=($Y19C)
$Y20D=($Y19D)
$Y21A=($Y20A)
$Y21B=($Y20B)
$Y21C=($Y20C)
$Y21D=($Y20D)
$Y22A=($Y21A)
$Y22B=($Y21B)
$Y22C=($Y21C)
$Y22D=($Y21D)
$Y23A=($Y22A)
$Y23B=($Y22B)
$Y23C=($Y22C)
$Y23D=($Y22D)

//Y Points
$YA=$Y01A
$YAB=$Y01B
$YB=$Y01B+$b
$YBB=$Y01A-$b
$YC=$YB
$YCC=$YBB
$YCD=$Y22C
$YD=$YA
$XIN=($XA-$b)
$XOUT=($XD+$b)

//Geometry
vertex create "A" coordinates $XA $YA
vertex create "AB" coordinates $XAB $YAB
vertex create "BB" coordinates $XB $YBB
vertex create "B" coordinates $XB $YB
vertex create "C" coordinates $XC $YC
vertex create "CC" coordinates $XC $YCC
vertex create "CD" coordinates $XCD $YCD
vertex create "D" coordinates $XD $YD
vertex create "L-IN" coordinates $o -$T
vertex create "U-IN" coordinates $o $T
vertex create "U-IN-A" coordinates $XAB $T
vertex create "L-IN-A" coordinates $XAB -$T
vertex create "U-OUT-D" coordinates $XCD $T
vertex create "U-OUT" coordinates $OUT $T
vertex create "L-OUT" coordinates $OUT -$T
vertex create "L-OUT-D" coordinates $XCD -$T
```

```
//Port Gometry
vertex create "01A" coordinates $X01A $Y01A
vertex create "01B" coordinates $X01B $Y01B
vertex create "01C" coordinates $X01C $Y01C
vertex create "01D" coordinates $X01D $Y01D
vertex create "02A" coordinates $X02A $Y02A
vertex create "02B" coordinates $X02B $Y02B
vertex create "02C" coordinates $X02C $Y02C
vertex create "02D" coordinates $X02D $Y02D
vertex create "03A" coordinates $X03A $Y03A
vertex create "03B" coordinates $X03B $Y03B
vertex create "03C" coordinates $X03C $Y03C
vertex create "03D" coordinates $X03D $Y03D
vertex create "04A" coordinates $X04A $Y04A
vertex create "04B" coordinates $X04B $Y04B
vertex create "04C" coordinates $X04C $Y04C
vertex create "04D" coordinates $X04D $Y04D
vertex create "05A" coordinates $X05A $Y05A
vertex create "05B" coordinates $X05B $Y05B
vertex create "05C" coordinates $X05C $Y05C
vertex create "05D" coordinates $X05D $Y05D
// …… Repetition 5 to 20
vertex create "20A" coordinates $X20A $Y20A
vertex create "20B" coordinates $X20B $Y20B
vertex create "20C" coordinates $X20C $Y20C
vertex create "20D" coordinates $X20D $Y20D
vertex create "21A" coordinates $X21A $Y21A
vertex create "21B" coordinates $X21B $Y21B
vertex create "21C" coordinates $X21C $Y21C
vertex create "21D" coordinates $X21D $Y21D
vertex create "22A" coordinates $X22A $Y22A
vertex create "22B" coordinates $X22B $Y22B
vertex create "22C" coordinates $X22C $Y22C
vertex create "22D" coordinates $X22D $Y22D
vertex create "23A" coordinates $X23A $Y23A
vertex create "23B" coordinates $X23B $Y23B
vertex create "23C" coordinates $X23C $Y23C
vertex create "23D" coordinates $X23D $Y23D
edge create "LT-P01-R" straight "01D" "01C"
edge create "LT-P01-T" straight "01C" "01B"
edge create "LT-P01-L" straight "01B" "01A"
edge create "LT-P01-B" straight "01A" "01D"
edge create "LT-P02-R" straight "02D" "02C"
edge create "LT-P02-T" straight "02C" "02B"
edge create "LT-P02-L" straight "02B" "02A"
edge create "LT-P02-B" straight "02A" "02D"
edge create "LT-P03-R" straight "03D" "03C"
edge create "LT-P03-T" straight "03C" "03B"
edge create "LT-P03-L" straight "03B" "03A"
edge create "LT-P03-B" straight "03A" "03D"
edge create "LT-P04-R" straight "04D" "04C"
edge create "LT-P04-T" straight "04C" "04B"
edge create "LT-P04-L" straight "04B" "04A"
edge create "LT-P04-B" straight "04A" "04D"
edge create "LT-P05-R" straight "05D" "05C"
edge create "LT-P05-T" straight "05C" "05B"
edge create "LT-P05-L" straight "05B" "05A"
```

```
edge create "LT-P05-B" straight "05A" "05D"
// …… Repetition 5 to 20
edge create "LT-P20-R" straight "20D" "20C"
edge create "LT-P20-T" straight "20C" "20B"
edge create "LT-P20-L" straight "20B" "20A"
edge create "LT-P20-B" straight "20A" "20D"
edge create "LT-P21-R" straight "21D" "21C"
edge create "LT-P21-T" straight "21C" "21B"
edge create "LT-P21-L" straight "21B" "21A"
edge create "LT-P21-B" straight "21A" "21D"
edge create "LT-P22-R" straight "22D" "22C"
edge create "LT-P22-T" straight "22C" "22B"
edge create "LT-P22-L" straight "22B" "22A"
edge create "LT-P22-B" straight "22A" "22D"
edge create "LT-P23-R" straight "23D" "23C"
edge create "LT-P23-T" straight "23C" "23B"
edge create "LT-P23-L" straight "23B" "23A"
edge create "LT-P23-B" straight "23A" "23D"

// Geometry of air flow inlet and outlet
edge create "FLOW-IN" straight "U-IN" "L-IN"
edge create "FLOW-OUT" straight "U-OUT" "L-OUT"
edge create "FLOW-UT-TH-IN" straight "U-IN-A" "AB"
edge create "FLOW-UT-TH-OUT" straight "U-OUT-D" "CD"
edge create "FLOW-LT-TH-IN" straight "A" "L-IN-A"
edge create "FLOW-LT-TH-OUT" straight "D" "L-OUT-D"
edge create "sym-top-1" straight "U-IN" "U-IN-A"
edge create "sym-top-2" straight "U-IN-A" "U-OUT-D"
edge create "sym-top-3" straight "U-OUT-D" "U-OUT"
edge create "sym-bttm-1" straight "L-IN" "L-IN-A"
edge create "sym-bttm-2" straight "L-IN-A" "L-OUT-D"
edge create "sym-bttm-3" straight "L-OUT-D" "L-OUT"
edge create "tb-wall-1" straight "A" "AB"
edge create "tb-wall-2" center2points "01B" "AB" "B" minarc arc
edge create "tb-wall-3" straight "B" "C"
edge create "tb-wall-4" center2points "23C" "C" "CD" minarc arc
edge create "tb-wall-5" straight "CD" "D"
edge create "tb-wall-6" center2points "23D" "D" "CC" minarc arc
edge create "tb-wall-7" straight "CC" "BB"
edge create "tb-wall-8" center2points "01A" "BB" "A" minarc arc
edge merge "tb-wall-2" "tb-wall-3" "tb-wall-4" forced
edge merge "tb-wall-8" "tb-wall-7" "tb-wall-6" forced
//Face ports
face create "PORT-01" wireframe "LT-P01-L" "LT-P01-T" "LT-P01-R" "LT-
P01-B" real
face create "PORT-02" wireframe "LT-P02-L" "LT-P02-T" "LT-P02-R" "LT-
P02-B" real
face create "PORT-03" wireframe "LT-P03-L" "LT-P03-T" "LT-P03-R" "LT-
P03-B" real
face create "PORT-04" wireframe "LT-P04-L" "LT-P04-T" "LT-P04-R" "LT-
P04-B" real
face create "PORT-05" wireframe "LT-P05-L" "LT-P05-T" "LT-P05-R" "LT-
P05-B" real
// …… Repetition 5 to 20
face create "PORT-20" wireframe "LT-P20-L" "LT-P20-T" "LT-P20-R" "LT-
P20-B" real
```

```
face create "PORT-21" wireframe "LT-P21-L" "LT-P21-T" "LT-P21-R" "LT-
P21-B" real
face create "PORT-22" wireframe "LT-P22-L" "LT-P22-T" "LT-P22-R" "LT-
P22-B" real
face create "PORT-23" wireframe "LT-P23-L" "LT-P23-T" "LT-P23-R" "LT-
P23-B" real
//Face Gometry
face create "TUBE-FACE" wireframe "tb-wall-1" "v_edge.113" "tb-wall-5"
\
  "v_edge.114" real
face split "TUBE-FACE" connected faces "PORT-01" "PORT-02" "PORT-03" \
  "PORT-04" "PORT-05" "PORT-06" "PORT-07" "PORT-08" "PORT-09" "PORT-10"
\
  "PORT-11" "PORT-12" "PORT-13" "PORT-14" "PORT-15" "PORT-16" "PORT-17"
\
  "PORT-18" "PORT-19" "PORT-20" "PORT-21" "PORT-22" "PORT-23"
face create "UT-THR-FACE" wireframe "FLOW-UT-TH-IN" "sym-top-2" "FLOW-
UT-TH-OUT" \
  "edge.113" real
face create "LT-THR-FACE" wireframe "FLOW-LT-TH-IN" "edge.114" "FLOW-
LT-TH-OUT" \
  "sym-bttm-2" real
face create "IN-FACE" wireframe "FLOW-IN" "sym-top-1" "FLOW-UT-TH-IN"
"tb-wall-1" \
  "FLOW-LT-TH-IN" "sym-bttm-1" real
face create "OUT-FACE" wireframe "sym-top-3" "FLOW-OUT" "sym-bttm-3" \
  "FLOW-LT-TH-OUT" "tb-wall-5" "FLOW-UT-TH-OUT" real
//Mesh Edges
undo begingroup
edge picklink "tb-wall-5" "edge.183" "edge.182" "edge.181" "edge.180" \
  "edge.179" "edge.178" "edge.177" "edge.176" "edge.175" "edge.174" \
  "edge.173" "edge.172" "edge.171" "edge.170" "edge.169" "edge.168" \
  "edge.167" "edge.166" "edge.165" "edge.164" "edge.163" "edge.162" \
  "edge.161" "edge.160" "edge.159" "edge.158" "edge.157" "edge.156" \
  "edge.155" "edge.154" "edge.153" "edge.152" "edge.151" "edge.150" \
  "edge.149" "edge.148" "edge.147" "edge.146" "edge.145" "edge.144" \
  "edge.143" "edge.142" "edge.141" "edge.140" "edge.139" "edge.138" \
  "tb-wall-1"
edge mesh "tb-wall-1" "edge.138" "edge.139" "edge.140" "edge.141"
"edge.142" \
  "edge.143" "edge.144" "edge.145" "edge.146" "edge.147" "edge.148" \
  "edge.149" "edge.150" "edge.151" "edge.152" "edge.153" "edge.154" \
  "edge.155" "edge.156" "edge.157" "edge.158" "edge.159" "edge.160" \
  "edge.161" "edge.162" "edge.163" "edge.164" "edge.165" "edge.166" \
  "edge.167" "edge.168" "edge.169" "edge.170" "edge.171" "edge.172" \
  "edge.173" "edge.174" "edge.175" "edge.176" "edge.177" "edge.178" \
  "edge.179" "edge.180" "edge.181" "edge.182" "edge.183" "tb-wall-5" \
  successive ratio1 1 intervals 8
undo endgroup
undo begingroup
edge delete "edge.115" "edge.116" "edge.117" "edge.118" "edge.119"
"edge.120" \
  "edge.121" "edge.122" "edge.123" "edge.124" "edge.125" "edge.126" \
  "edge.127" "edge.128" "edge.129" "edge.130" "edge.131" "edge.132" \
  "edge.133" "edge.134" "edge.135" "edge.136" "edge.137" "edge.206" \
  "edge.205" "edge.204" "edge.203" "edge.202" "edge.201" "edge.200" \
  "edge.199" "edge.198" "edge.197" "edge.196" "edge.195" "edge.194" \
```

```
  "edge.193" "edge.192" "edge.191" "edge.190" "edge.189" "edge.188" \
  "edge.187" "edge.186" "edge.185" "edge.184" keepsettings onlymesh
edge picklink "edge.184" "edge.185" "edge.186" "edge.187" "edge.188" \
  "edge.189" "edge.190" "edge.191" "edge.192" "edge.193" "edge.194" \
  "edge.195" "edge.196" "edge.197" "edge.198" "edge.199" "edge.200" \
  "edge.201" "edge.202" "edge.203" "edge.204" "edge.205" "edge.206" \
  "edge.137" "edge.136" "edge.135" "edge.134" "edge.133" "edge.132" \
  "edge.131" "edge.130" "edge.129" "edge.128" "edge.127" "edge.126" \
  "edge.125" "edge.124" "edge.123" "edge.122" "edge.121" "edge.120" \
  "edge.119" "edge.118" "edge.117" "edge.116" "edge.115"
edge mesh "edge.115" "edge.116" "edge.117" "edge.118" "edge.119"
"edge.120" \
  "edge.121" "edge.122" "edge.123" "edge.124" "edge.125" "edge.126" \
  "edge.127" "edge.128" "edge.129" "edge.130" "edge.131" "edge.132" \
  "edge.133" "edge.134" "edge.135" "edge.136" "edge.137" "edge.206" \
  "edge.205" "edge.204" "edge.203" "edge.202" "edge.201" "edge.200" \
  "edge.199" "edge.198" "edge.197" "edge.196" "edge.195" "edge.194" \
  "edge.193" "edge.192" "edge.191" "edge.190" "edge.189" "edge.188" \
  "edge.187" "edge.186" "edge.185" "edge.184" successive ratio1 1
intervals 5
undo endgroup
undo begingroup
edge delete "edge.113" "edge.114" "sym-top-2" "sym-bttm-2" keepsettings
onlymesh
edge picklink "sym-bttm-2" "sym-top-2" "edge.114" "edge.113"
edge mesh "edge.113" "edge.114" "sym-top-2" "sym-bttm-2" successive
ratio1 1 \
  intervals 180
undo endgroup
undo begingroup
edge delete "FLOW-UT-TH-IN" "FLOW-UT-TH-OUT" "FLOW-LT-TH-IN" "FLOW-LT-
TH-OUT" \
  keepsettings onlymesh
edge picklink "FLOW-LT-TH-OUT" "FLOW-LT-TH-IN" "FLOW-UT-TH-OUT" \
  "FLOW-UT-TH-IN"
edge mesh "FLOW-UT-TH-IN" "FLOW-UT-TH-OUT" "FLOW-LT-TH-IN" "FLOW-LT-TH-
OUT" \
  successive ratio1 1 intervals 50
undo endgroup
undo begingroup
edge delete "sym-top-1" "sym-top-3" "sym-bttm-1" "sym-bttm-3"
keepsettings onlymesh
edge picklink "sym-bttm-3" "sym-bttm-1" "sym-top-3" "sym-top-1"
edge mesh "sym-top-1" "sym-top-3" "sym-bttm-1" "sym-bttm-3" successive
ratio1 \
  1 intervals 410
undo endgroup
undo begingroup
edge delete "FLOW-IN" "FLOW-OUT" keepsettings onlymesh
edge picklink "FLOW-OUT" "FLOW-IN"
edge mesh "FLOW-IN" "FLOW-OUT" successive ratio1 1 intervals 108
undo endgroup
//Mesh Faces
face mesh "TUBE-FACE" pave intervals 10
face mesh "PORT-01" "PORT-02" "PORT-03" "PORT-04" "PORT-05" "PORT-06" \
  "PORT-07" "PORT-08" "PORT-09" "PORT-10" "PORT-11" "PORT-12" "PORT-13"
\
```

```
  "PORT-14" "PORT-15" "PORT-16" "PORT-17" "PORT-18" "PORT-19" "PORT-20"
\
  "PORT-21" "PORT-22" "PORT-23" map intervals 10
face mesh "UT-THR-FACE" "LT-THR-FACE" map intervals 10
face mesh "IN-FACE" "OUT-FACE" map intervals 10
//Scale the model mm to m
model scale factor 0.001 origin 0 0 0
//Select Solver
solver select "FLUENT 5/6"
//BC
physics create "P01-R" btype "WALL" edge "edge.138"
physics create "P01-T" btype "WALL" edge "edge.184"
physics create "P01-L" btype "WALL" edge "edge.139"
physics create "P01-B" btype "WALL" edge "edge.115"
physics create "P02-R" btype "WALL" edge "edge.140"
physics create "P02-T" btype "WALL" edge "edge.185"
physics create "P02-L" btype "WALL" edge "edge.141"
physics create "P02-B" btype "WALL" edge "edge.116"
physics create "P03-R" btype "WALL" edge "edge.142"
physics create "P03-T" btype "WALL" edge "edge.186"
physics create "P03-L" btype "WALL" edge "edge.143"
physics create "P03-B" btype "WALL" edge "edge.117"
physics create "P04-R" btype "WALL" edge "edge.144"
physics create "P04-T" btype "WALL" edge "edge.187"
physics create "P04-L" btype "WALL" edge "edge.145"
physics create "P04-B" btype "WALL" edge "edge.118"
physics create "P05-R" btype "WALL" edge "edge.146"
physics create "P05-T" btype "WALL" edge "edge.188"
physics create "P05-L" btype "WALL" edge "edge.147"
physics create "P05-B" btype "WALL" edge "edge.119"
// …… Repetition5 to 20
physics create "P20-R" btype "WALL" edge "edge.176"
physics create "P20-T" btype "WALL" edge "edge.203"
physics create "P20-L" btype "WALL" edge "edge.177"
physics create "P20-B" btype "WALL" edge "edge.134"
physics create "P21-R" btype "WALL" edge "edge.178"
physics create "P21-T" btype "WALL" edge "edge.204"
physics create "P21-L" btype "WALL" edge "edge.179"
physics create "P21-B" btype "WALL" edge "edge.135"
physics create "P22-R" btype "WALL" edge "edge.180"
physics create "P22-T" btype "WALL" edge "edge.205"
physics create "P22-L" btype "WALL" edge "edge.181"
physics create "P22-B" btype "WALL" edge "edge.136"
physics create "P23-R" btype "WALL" edge "edge.182"
physics create "P23-T" btype "WALL" edge "edge.206"
physics create "P23-L" btype "WALL" edge "edge.183"
physics create "P23-B" btype "WALL" edge "edge.137"
physics create "flow-sym-top-01" btype "SYMMETRY" edge "sym-top-1"
physics create "flow-sym-top-02" btype "SYMMETRY" edge "sym-top-2"
physics create "flow-sym-top-03" btype "SYMMETRY" edge "sym-top-3"
physics create "flow-sym-btm-01" btype "SYMMETRY" edge "sym-bttm-1"
physics create "flow-sym-btm-02" btype "SYMMETRY" edge "sym-bttm-2"
physics create "flow-sym-btm-03" btype "SYMMETRY" edge "sym-bttm-3"
physics create "ch-in-wall" btype "WALL" edge "tb-wall-1"
physics create "ch-top-wall" btype "WALL" edge "edge.113"
physics create "ch-btm-wall" btype "WALL" edge "edge.114"
physics create "ch-ext-wall" btype "WALL" edge "tb-wall-5"
```

```
physics create "Flow-Inlet" btype "VELOCITY_INLET" edge "FLOW-IN"
physics create "Flow-Outlet" btype "PRESSURE_OUTLET" edge "FLOW-OUT"
physics create "Interior-inlet-1" btype "INTERIOR" edge "FLOW-LT-TH-IN"
physics create "Interior-inlet-2" btype "INTERIOR" edge "FLOW-UT-TH-IN"
physics create "interior-outlet-1" btype "INTERIOR" edge "FLOW-LT-TH-
OUT"
physics create "interior-outlet-2" btype "INTERIOR" edge "FLOW-UT-TH-
OUT"
physics create "Fluid-PORT-01" ctype "FLUID" face "PORT-01"
physics create "Fluid-PORT-02" ctype "FLUID" face "PORT-02"
physics create "Fluid-PORT-03" ctype "FLUID" face "PORT-03"
physics create "Fluid-PORT-04" ctype "FLUID" face "PORT-04"
physics create "Fluid-PORT-05" ctype "FLUID" face "PORT-05"
// …… Repetition 5 to 20
physics create "Fluid-PORT-20" ctype "FLUID" face "PORT-20"
physics create "Fluid-PORT-21" ctype "FLUID" face "PORT-21"
physics create "Fluid-PORT-22" ctype "FLUID" face "PORT-22"
physics create "Fluid-PORT-23" ctype "FLUID" face "PORT-23"
physics create "INLET-FLUID" ctype "FLUID" face "IN-FACE"
physics create "THROAT-FLUID-1" ctype "FLUID" face "UT-THR-FACE"
physics create "THROAT-FLUID-2" ctype "FLUID" face "LT-THR-FACE"
physics create "OUTLET-FLUID" ctype "FLUID" face "OUT-FACE"
physics create "TUBE-SOLID" ctype "SOLID" face "TUBE-FACE"
default set "GRAPHICS.GENERAL.CONNECTIVITY_BASED_COLORING" numeric 1

//Check Topology and Geometry
check topology
check geometry

//Export Mesh
export fluent5 "2DSMC-M.msh" nozval
save
```

APPENDIX D

D-1: Water Thermal Properties

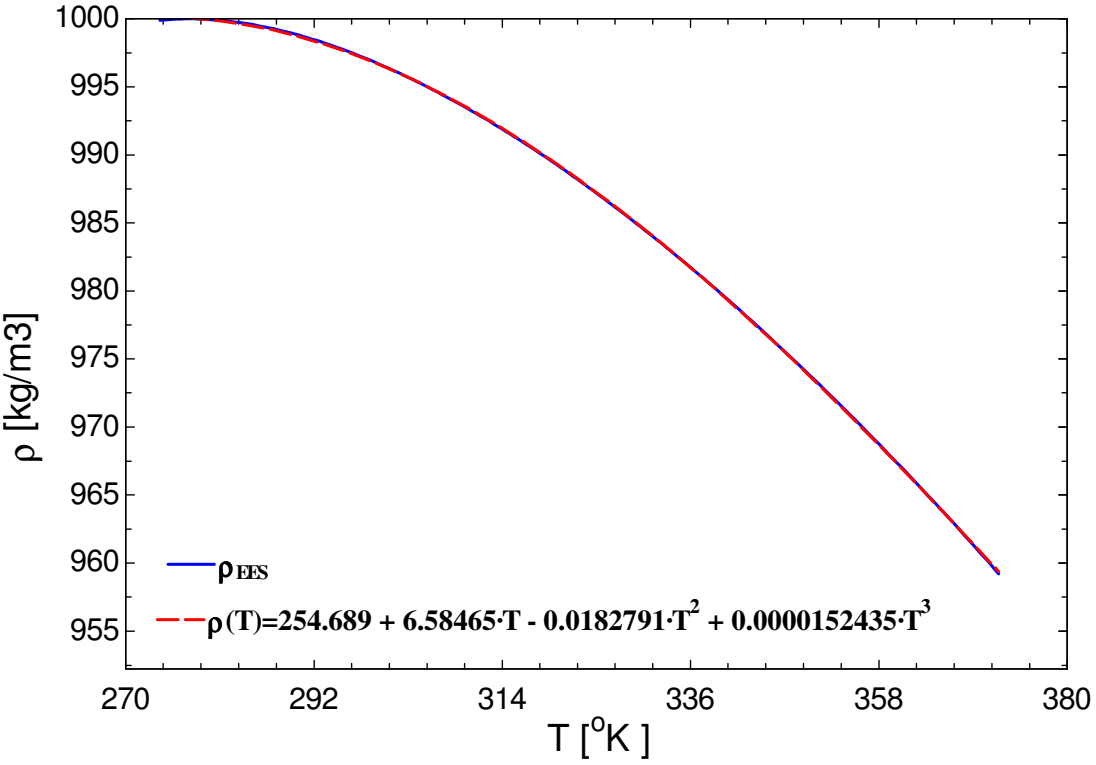

Figure D.1: Temperature Dependent Water Density Variation (Eq-3.7)

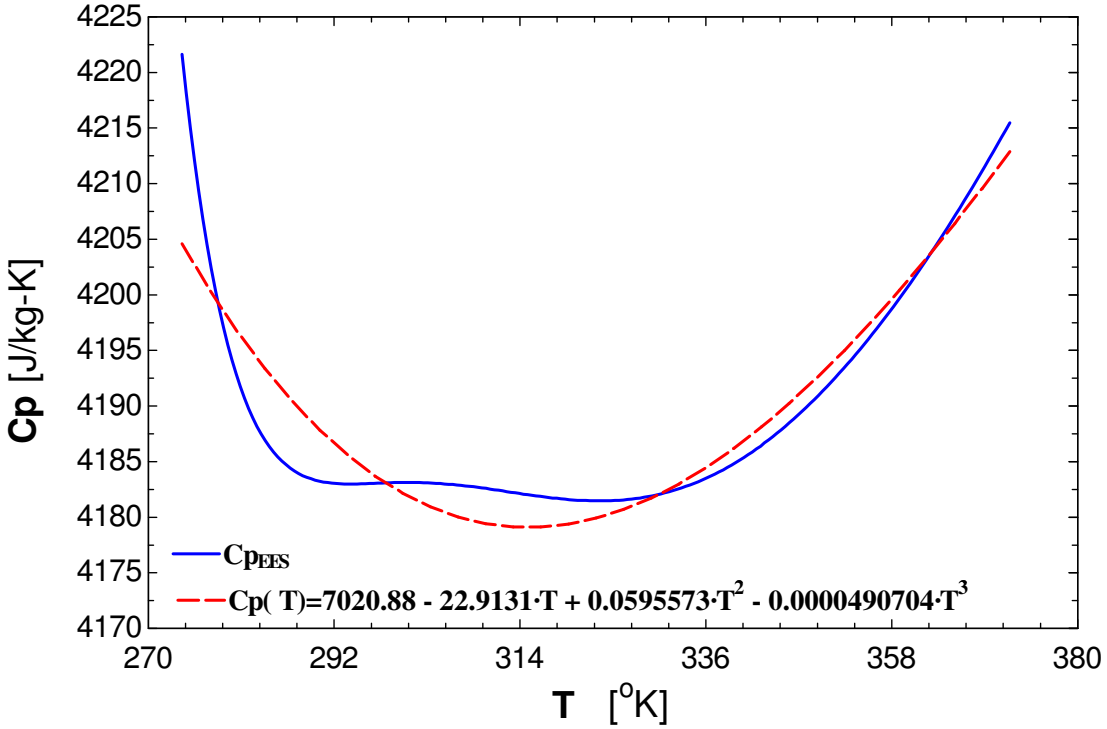

Figure D.2: Temperature Dependent Water Specific Heat Variation (Eq-3.8)

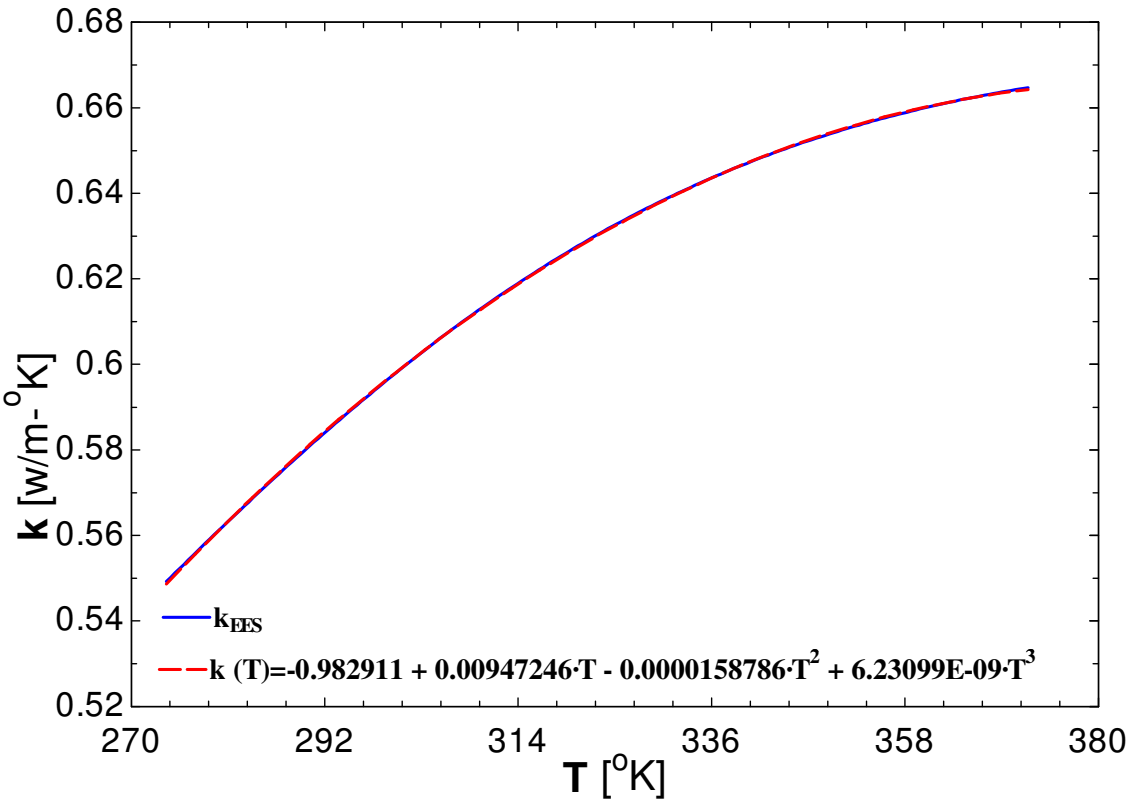

Figure D.3: Temperature Dependent Water Conductivity Variation (Eq-3.9)

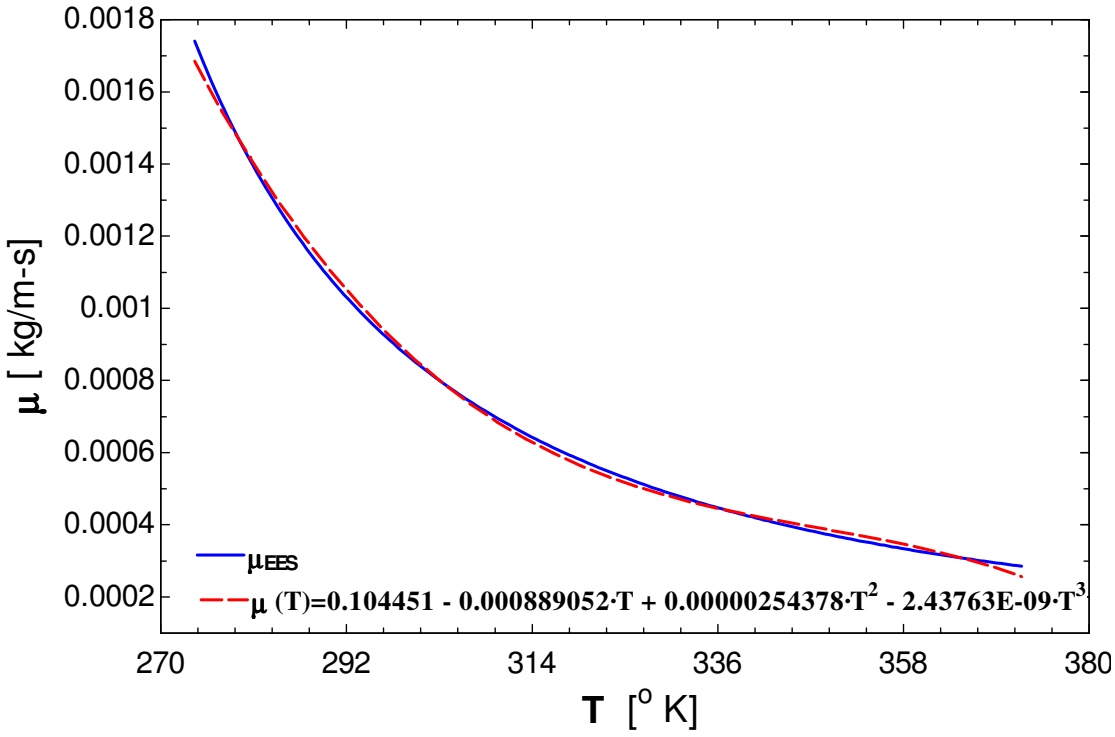

Figure D.4: Temperature Dependent Water Viscosity Variation (Eq -3.10)

D-2: Air Thermal Properties

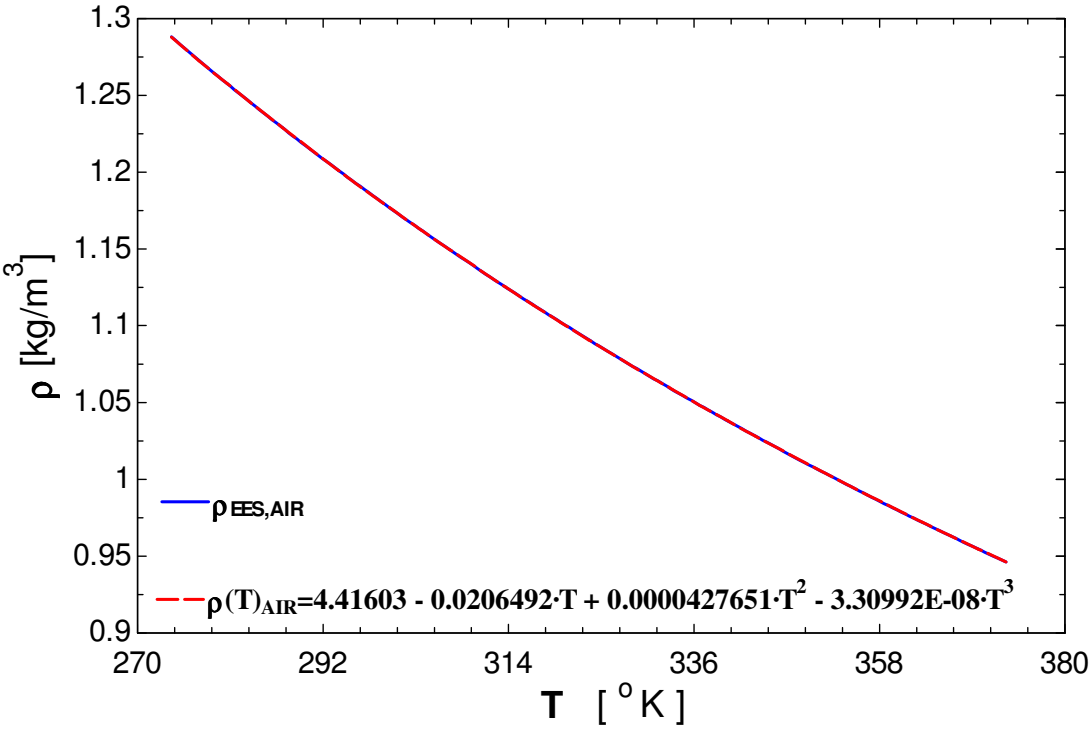

Figure D.5: Temperature Dependent Air Density Variation (Eq-3.11)

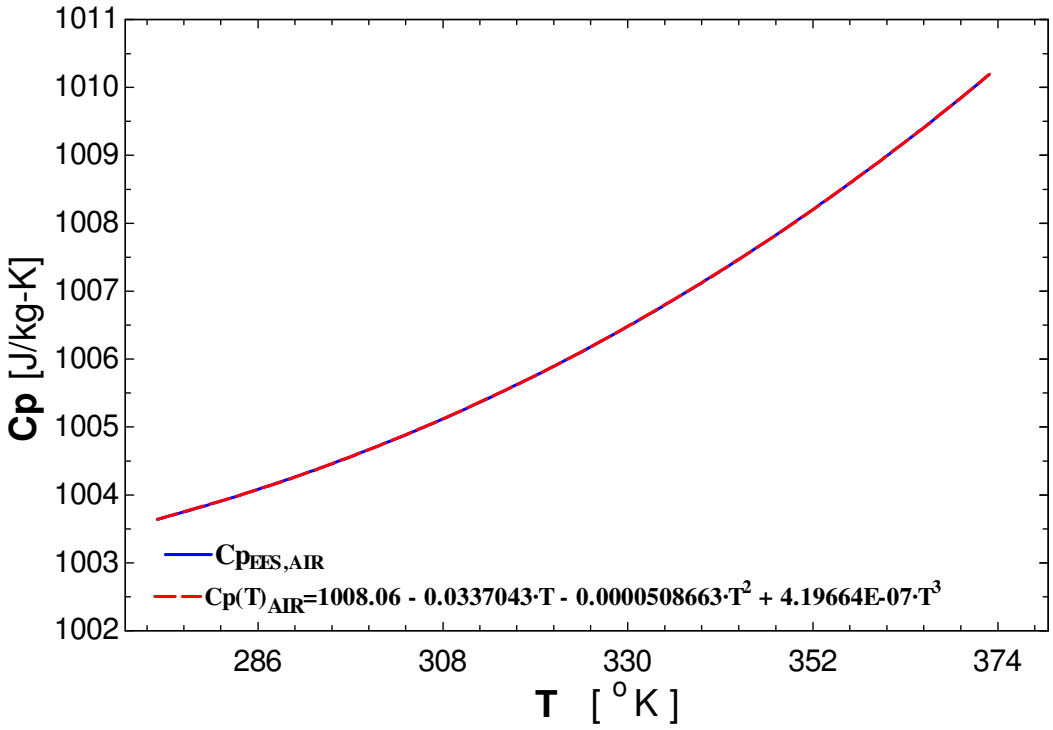

Figure D.6: Temperature Dependent Air Specific Heat Variation (Eq-3.12)

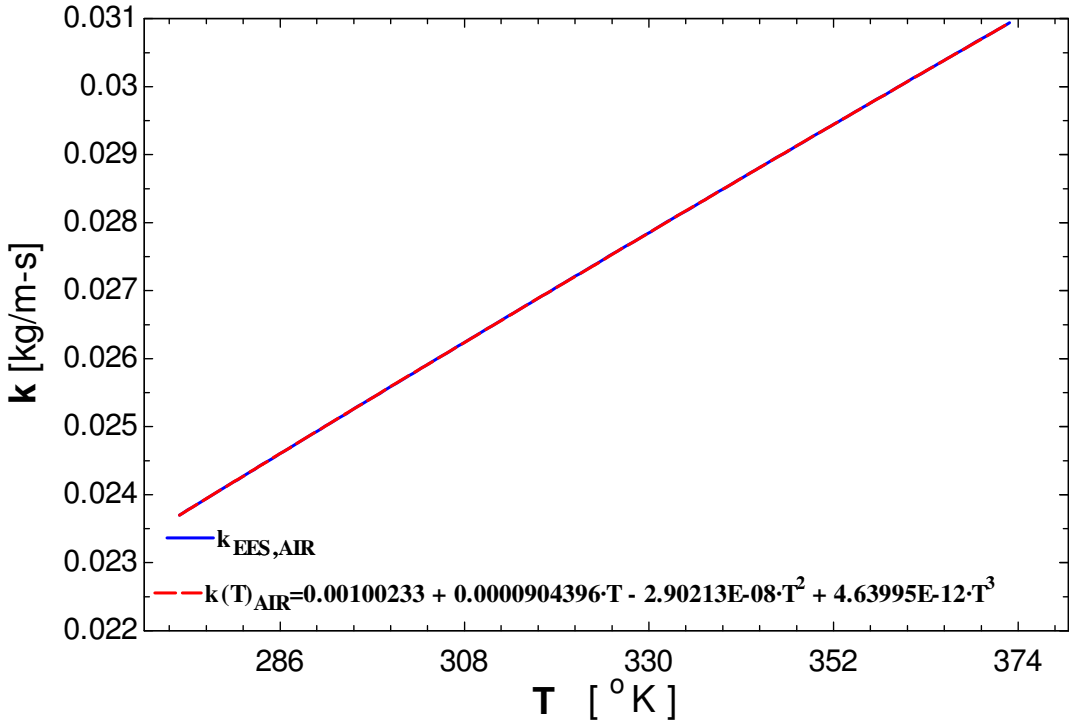

Figure D.7: Temperature Dependent Air Conductivity Variation (Eq-3.13)

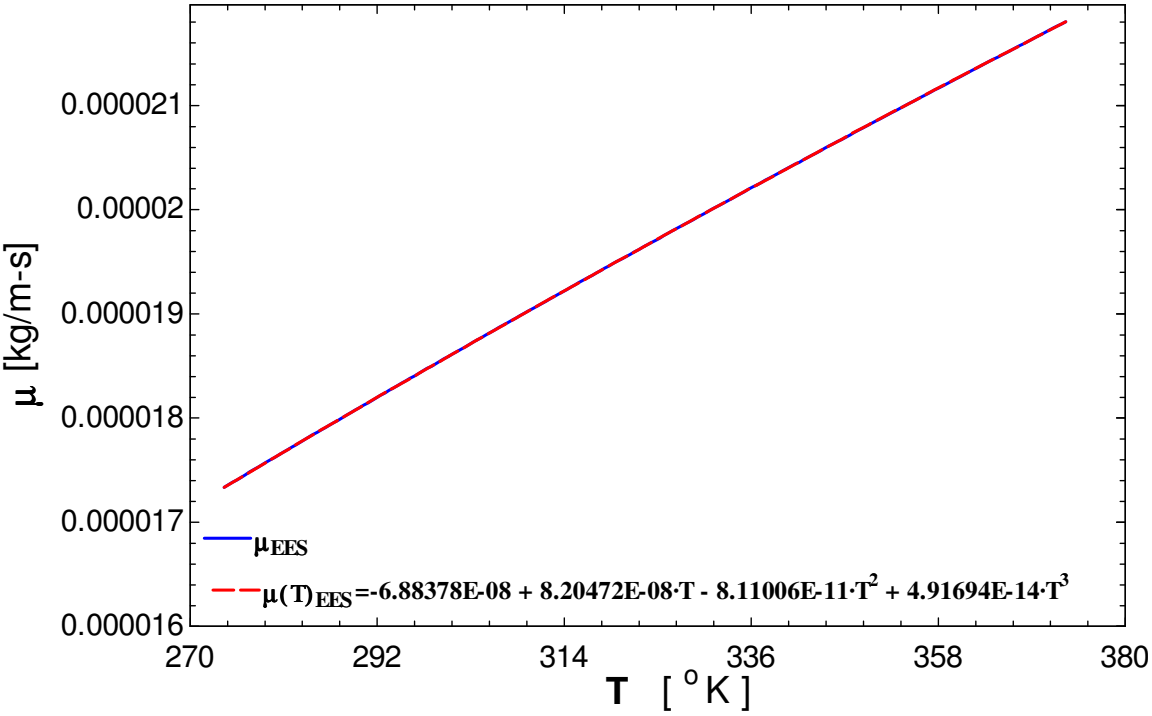

Figure D.8: Temperature Dependent Air Viscosity Variation (Eq -3.14)

APPANDIX E

3D FLUENT Journal Files

E-1: Simulation Model 1 Round Tube in Tube Heat Exchanger

3D FLUENT Journal File

```
file rc C:\3D-RT-M.msh
define materials change-create air water y polynomial 4 254.689 6.58465
-0.0182791 1.52435E-05 y polynomial 4 7020.88 -22.9131 0.0595573 -
4.90704E-05 y polynomial 4 -0.9829 0.009472 -1.58786E-05 6.23E-09  y
polynomial 4 0.104451 -0.00089 2.54378E-06 -2.44E-09 y 18.0152 y 0 n n
n n y
define materials change-create aluminum copper y constant 8978 y
constant 381 y constant 387.6 n
define boundary-conditions mass-flow-inlet channel-inlet y 0.004988 n
274.6 n 0 y y y n 0 n 0 n 1
define boundary-conditions mass-flow-inlet jacket-inlet y 0.005 n 323 n
0 y y y n 0 n 0 n -1
define boundary-conditions pressure-outlet channel-outlet n 187.1689 n
300 n y n n
define boundary-conditions pressure-outlet jacket-outlet n 1.75883 n
300 n y n n
define boundary-conditions wall channel-inner-wall 0 n 0 y copper n n
define boundary-conditions wall channel-outer-wall 0 n 0 y copper n n n
n
define boundary-conditions wall thickness-inlet 0 n 0 y copper n n 0 n
define boundary-conditions wall thickness-outlet 0 n 0 y copper n n 0 n
define boundary-conditions solid copper-solid y copper n n y 0 0 0 0 0
1 n
solve initialize compute-defaults mass-flow-inlet channel-inlet
solve initialize initialize-flow
solve patch (2) z-velocity n -0.032451
solve monitors residual convergence-criteria 1.0e-6 1.0e-6 1.0e-6 1.0e-
6 1.0e-6
solve set equations temp n
solve iterate 1000
file write-case-data RT-G1-Conv.cas
solve monitors residual convergence-criteria 1.0e-7 1.0e-6 1.0e-6 1.0e-
6 1.0e-6
solve set equations temp y
```

```
solve iterate 5
solve monitors residual convergence-criteria 1.0e-6 1.0e-6 1.0e-6 1.0e-
6 1.0e-6
solve iterate 1000
file write-case-data RT-G1-0.cas
solve set under-relaxation mom 0.6
solve iterate 100
file write-case-data RT-G1-1.cas
solve set under-relaxation mom 0.5
solve iterate 100
file write-case-data RT-G1-2.cas
solve set under-relaxation mom 0.4
solve iterate 100
file write-case-data RT-G1-3.cas
solve set under-relaxation pressure 0.2
solve iterate 100
file write-case-data RT-G1-4.cas
solve set discretization-scheme mom 1
solve set discretization-scheme temp 1
solve monitors residual convergence-criteria 1.0e-7 1.0e-6 1.0e-6 1.0e-
6 1.0e-6
solve iterate 5
solve monitors residual convergence-criteria 1.0e-6 1.0e-6 1.0e-6 1.0e-
6 1.0e-6
solve iterate 2000
file write-case-data RT-G1-2nd.cas
```

E-2: Simulation Model 2 SMC Tube in Tube Heat Exchanger

3D FLUENT Journal File

```
file rc C:\SMC-M.msh
define materials change-create air water y polynomial 4 254.689 6.58465
-0.0182791 1.52435E-05 y polynomial 4 7020.88 -22.9131 0.0595573 -
4.90704E-05 y polynomial 4 -0.9829 0.009472 -1.58786E-05 6.23E-09  y
polynomial 4 0.104451 -0.00089 2.54378E-06 -2.44E-09 y 18.0152 y 0 n n
n n y
define boundary-conditions mass-flow-inlet port-inlet y 8.75657E-06 n
274.6 n 0 y y y n 0 n 0 n 1
define boundary-conditions mass-flow-inlet jacket-inlet y 0.000323768 n
323 n 0 y y y n 0 n 0 n -1
define boundary-conditions pressure-outlet port-outlet n 6843.381691 n
300 n y n n
define boundary-conditions pressure-outlet jacket-outlet n 1.446009696
n 300 n y n n
solve initialize compute-defaults mass-flow-inlet port-inlet
solve initialize initialize-flow
solve patch (2) z-velocity n -0.029599655
solve monitors residual convergence-criteria 1.0e-6 1.0e-6 1.0e-6 1.0e-
6 1.0e-6
```

```
solve set equations temp n
solve iterate 15000
file write-case-data SMC-M-Conv.cas
solve monitors residual convergence-criteria 1.0e-7 1.0e-6 1.0e-6 1.0e-
6 1.0e-6
solve set equations temp y
solve iterate 5
solve monitors residual convergence-criteria 1.0e-6 1.0e-6 1.0e-6 1.0e-
6 1.0e-6
solve iterate 5000
file write-case-data SMC-M-0.cas
solve set under-relaxation mom 0.6
solve iterate 1000
file write-case-data SMC-M-1.cas
solve set under-relaxation mom 0.5
solve iterate 1000
file write-case-data SMC-M-2.cas
solve set under-relaxation mom 0.4
solve iterate 1000
file write-case-data SMC-M-3.cas
solve set under-relaxation pressure 0.2
solve iterate 1000
file write-case-data SMC-M-4.cas
solve set under-relaxation pressure 0.1
solve iterate 5000
file write-case-data SMC-M-5.cas
solve set discretization-scheme mom 1
solve set discretization-scheme temp 1
solve monitors residual convergence-criteria 1.0e-7 1.0e-6 1.0e-6 1.0e-
6 1.0e-6
solve iterate 5
solve monitors residual convergence-criteria 1.0e-6 1.0e-6 1.0e-6 1.0e-
6 1.0e-6
solve iterate 10000
file write-case-data SMC-M-2nd.cas
```

E-3: Simulation Model 3 RMC Tube in Tube Heat Exchanger

3D FLUENT Journal File

```
file rc C:\RMC-M.msh
define materials change-create air water y polynomial 4 254.689 6.58465
-0.0182791 1.52435E-05 y polynomial 4 7020.88 -22.9131 0.0595573 -
4.90704E-05 y polynomial 4 -0.9829 0.009472 -1.58786E-05 6.23E-09  y
polynomial 4 0.104451 -0.00089 2.54378E-06 -2.44E-09 y 18.0152 y 0 n n
n n y
define boundary-conditions mass-flow-inlet port-inlet y 3.59722E-05 n
274.6 n 0 y y y n 0 n 0 n 1
define boundary-conditions mass-flow-inlet jacket-inlet y 8.67E-04 n
323 n 0 y y y n 0 n 0 n -1
```

```
define boundary-conditions pressure-outlet port-outlet n 15803.2057 n
300 n y n n
define boundary-conditions pressure-outlet jacket-outlet n 2.638245682
n 300 n y n n
solve initialize compute-defaults mass-flow-inlet port-inlet
solve initialize initialize-flow
solve patch (2) z-velocity n -0.048675769
solve monitors residual convergence-criteria 1.0e-6 1.0e-6 1.0e-6 1.0e-
6 1.0e-6
solve set equations temp n
solve iterate 15000
file write-case-data RMC-M-Conv.cas
solve monitors residual convergence-criteria 1.0e-7 1.0e-6 1.0e-6 1.0e-
6 1.0e-6
solve set equations temp y
solve iterate 5
solve monitors residual convergence-criteria 1.0e-5 1.0e-6 1.0e-6 1.0e-
6 1.0e-6
solve iterate 5000
file write-case-data RMC-M-0.cas
solve set under-relaxation mom 0.6
solve iterate 1000
file write-case-data RMC-M-1.cas
solve set under-relaxation mom 0.5
solve iterate 1000
file write-case-data RMC-M-2.cas
solve set under-relaxation mom 0.4
solve iterate 1000
file write-case-data RMC-M-3.cas
solve set under-relaxation pressure 0.2
solve iterate 1000
file write-case-data RMC-M-4.cas
solve set under-relaxation pressure 0.1
solve iterate 5000
file write-case-data RMC-M-5.cas
solve set discretization-scheme mom 1
solve set discretization-scheme temp 1
solve monitors residual convergence-criteria 1.0e-7 1.0e-6 1.0e-6 1.0e-
6 1.0e-6
solve iterate 5
solve monitors residual convergence-criteria 1.0e-6 1.0e-6 1.0e-6 1.0e-
6 1.0e-6
solve iterate 10000
file write-case-data RMC-M-2nd.cas
```

APPENDIX F

2D FLUENT Journal Files

F-1: Simulation Model 4 RMC Tube Heat Exchanger in Air Cross Flow

2D FLUENT Journal File

```
file rc C:\2DRMC-M.msh
define models energy y n n n y
define materials change-create air air y polynomial 4 1.18247 -
0.00295682 4.40414E-06 -2.82E-09 y polynomial 4 1004.92 -0.00450201
0.000607344 -5.016834E-07 y polynomial 4 -0.023635 7.56238E-05 -2.52E-
08 4.64E-12 y polynomial 4 1.75E-05 4.59E-08 -2.47E-11 1.08E-14 n n n n
n n
define materials change-create air air y polynomial 4 4.41603 -
0.0206492 0.0000427651 -3.30992E-08 y polynomial 4 1008.06 -0.0337043 -
0.0000508663 4.19664E-07 y polynomial 4 0.00100233 0.0000904396 -
2.90213E-08 4.63995E-12 y polynomial 4 -6.88378E-08 8.20472E-08 -
8.11006E-11 4.91694E-14 n n n n n n
define boundary-conditions fluid fluid-port-01 y water n y n n y
274.8167 y 0 0 n n
define boundary-conditions fluid fluid-port-02 y water n y n n y
274.8167 y 0 0 n n
define boundary-conditions fluid fluid-port-03 y water n y n n y
274.8167 y 0 0 n n
define boundary-conditions fluid fluid-port-04 y water n y n n y
274.8167 y 0 0 n n
define boundary-conditions fluid fluid-port-05 y water n y n n y
274.8167 y 0 0 n n
define boundary-conditions fluid fluid-port-06 y water n y n n y
274.8167 y 0 0 n n
define boundary-conditions fluid fluid-port-07 y water n y n n y
274.8167 y 0 0 n n
define boundary-conditions fluid fluid-port-08 y water n y n n y
274.8167 y 0 0 n n
define boundary-conditions fluid fluid-port-09 y water n y n n y
274.8167 y 0 0 n n
define boundary-conditions fluid fluid-port-10 y water n y n n y
274.8167 y 0 0 n n
define boundary-conditions fluid fluid-port-11 y water n y n n y
274.8167 y 0 0 n n
```

```
define boundary-conditions fluid fluid-port-12 y water n y n n y
274.8167 y 0 0 n n
define boundary-conditions fluid fluid-port-13 y water n y n n y
274.8167 y 0 0 n n
define boundary-conditions fluid fluid-port-14 y water n y n n y
274.8167 y 0 0 n n
define boundary-conditions fluid fluid-port-15 y water n y n n y
274.8167 y 0 0 n n
define boundary-conditions fluid fluid-port-16 y water n y n n y
274.8167 y 0 0 n n
define boundary-conditions fluid fluid-port-17 y water n y n n y
274.8167 y 0 0 n n
define boundary-conditions fluid fluid-port-18 y water n y n n y
274.8167 y 0 0 n n
define boundary-conditions fluid fluid-port-19 y water n y n n y
274.8167 y 0 0 n n
define boundary-conditions fluid fluid-port-20 y water n y n n y
274.8167 y 0 0 n n
define boundary-conditions fluid fluid-port-21 y water n y n n y
274.8167 y 0 0 n n
define boundary-conditions fluid fluid-port-22 y water n y n n y
274.8167 y 0 0 n n
define boundary-conditions fluid fluid-port-23 y water n y n n y
274.8167 y 0 0 n n
define boundary-conditions fluid fluid-port-24 y water n y n n y
274.8167 y 0 0 n n
define boundary-conditions fluid fluid-port-25 y water n y n n y
274.8167 y 0 0 n n
define boundary-conditions fluid fluid-port-26 y water n y n n y
274.8167 y 0 0 n n
define boundary-conditions fluid fluid-port-27 y water n y n n y
274.8167 y 0 0 n n
define boundary-conditions fluid fluid-port-28 y water n y n n y
274.8167 y 0 0 n n
define boundary-conditions fluid fluid-port-29 y water n y n n y
274.8167 y 0 0 n n
define boundary-conditions fluid fluid-port-30 y water n y n n y
274.8167 y 0 0 n n
define boundary-conditions fluid fluid-port-31 y water n y n n y
274.8167 y 0 0 n n
define boundary-conditions fluid fluid-port-32 y water n y n n y
274.8167 y 0 0 n n
define boundary-conditions fluid fluid-port-33 y water n y n n y
274.8167 y 0 0 n n
define boundary-conditions fluid fluid-port-34 y water n y n n y
274.8167 y 0 0 n n
define boundary-conditions fluid fluid-port-35 y water n y n n y
274.8167 y 0 0 n n
define boundary-conditions fluid fluid-port-36 y water n y n n y
274.8167 y 0 0 n n
define boundary-conditions fluid fluid-port-37 y water n y n n y
274.8167 y 0 0 n n
define boundary-conditions fluid fluid-port-38 y water n y n n y
274.8167 y 0 0 n n
define boundary-conditions fluid fluid-port-39 y water n y n n y
274.8167 y 0 0 n n
```

```
define boundary-conditions fluid fluid-port-40 y water n y n n y
274.8167 y 0 0 n n
define boundary-conditions fluid fluid-port-41 y water n y n n y
274.8167 y 0 0 n n
define boundary-conditions fluid fluid-port-42 y water n y n n y
274.8167 y 0 0 n n
define boundary-conditions velocity-inlet air-inlet y y n 1 n 1 n 0 n
281.5
solve initialize compute-defaults velocity-inlet air-inlet
solve initialize initialize-flow
solve monitors residual convergence-criteria 1.0e-7 1.0e-6 1.0e-6 1.0e-
6 1.0e-6
solve monitors residual monitor y n n n
solve monitors residual check-convergence y
solve monitors residual plot y
solve set equations temp n
solve iterate 100
file write-case-data 2DRMC-M-M0.cas
solve set under-relaxation mom 0.6
solve iterate 1000
file write-case-data 2DRMC-M-M1.cas
solve set under-relaxation mom 0.5
solve iterate 1000
file write-case-data 2DRMC-M-M2.cas
solve set equations temp y
solve iterate 2500
file write-case-data 2DRMC-M-1st-1.cas
solve set under-relaxation mom 0.4
solve iterate 2500
file write-case-data 2DRMC-M-1st-2.cas
solve set discretization-scheme mom 1
solve set discretization-scheme temp 1
solve iterate 2500
file write-case-data 2DRMC-M-2nd-1.cas
solve iterate 2500
file write-case-data 2DRMC-M-2nd-2.cas
solve set under-relaxation mom 0.3
solve iterate 5000
file write-case-data 2DRMC-M-3rd-2.cas
```

F-2: Simulation Model 5 SMC Tube Heat Exchanger in Air Cross Flow

2D FLUENT Journal File

```
file rc C:\2DSMC-M.msh
define models energy y n n n y
define materials change-create air air y polynomial 4 1.18247 -
0.00295682 4.40414E-06 -2.82E-09 y polynomial 4 1004.92 -0.00450201
0.000607344 -5.016834E-07 y polynomial 4 -0.023635 7.56238E-05 -2.52E-
08 4.64E-12 y polynomial 4 1.75E-05 4.59E-08 -2.47E-11 1.08E-14 n n n n
n n
```

```
define materials change-create air air y polynomial 4 4.41603 -
0.0206492 0.0000427651 -3.30992E-08 y polynomial 4 1008.06 -0.0337043 -
0.0000508663 4.19664E-07 y polynomial 4 0.00100233 0.0000904396 -
2.90213E-08 4.63995E-12 y polynomial 4 -6.88378E-08 8.20472E-08 -
8.11006E-11 4.91694E-14 n n n n n n
define boundary-conditions fluid fluid-port-01 y water n y n n y
274.8167 y 0 0 n n
define boundary-conditions fluid fluid-port-02 y water n y n n y
274.8167 y 0 0 n n
define boundary-conditions fluid fluid-port-03 y water n y n n y
274.8167 y 0 0 n n
define boundary-conditions fluid fluid-port-04 y water n y n n y
274.8167 y 0 0 n n
define boundary-conditions fluid fluid-port-05 y water n y n n y
274.8167 y 0 0 n n
define boundary-conditions fluid fluid-port-06 y water n y n n y
274.8167 y 0 0 n n
define boundary-conditions fluid fluid-port-07 y water n y n n y
274.8167 y 0 0 n n
define boundary-conditions fluid fluid-port-08 y water n y n n y
274.8167 y 0 0 n n
define boundary-conditions fluid fluid-port-09 y water n y n n y
274.8167 y 0 0 n n
define boundary-conditions fluid fluid-port-10 y water n y n n y
274.8167 y 0 0 n n
define boundary-conditions fluid fluid-port-11 y water n y n n y
274.8167 y 0 0 n n
define boundary-conditions fluid fluid-port-12 y water n y n n y
274.8167 y 0 0 n n
define boundary-conditions fluid fluid-port-13 y water n y n n y
274.8167 y 0 0 n n
define boundary-conditions fluid fluid-port-14 y water n y n n y
274.8167 y 0 0 n n
define boundary-conditions fluid fluid-port-15 y water n y n n y
274.8167 y 0 0 n n
define boundary-conditions fluid fluid-port-16 y water n y n n y
274.8167 y 0 0 n n
define boundary-conditions fluid fluid-port-17 y water n y n n y
274.8167 y 0 0 n n
define boundary-conditions fluid fluid-port-18 y water n y n n y
274.8167 y 0 0 n n
define boundary-conditions fluid fluid-port-19 y water n y n n y
274.8167 y 0 0 n n
define boundary-conditions fluid fluid-port-20 y water n y n n y
274.8167 y 0 0 n n
define boundary-conditions fluid fluid-port-21 y water n y n n y
274.8167 y 0 0 n n
define boundary-conditions fluid fluid-port-22 y water n y n n y
274.8167 y 0 0 n n
define boundary-conditions fluid fluid-port-23 y water n y n n y
274.8167 y 0 0 n n
define boundary-conditions velocity-inlet flow-inlet y y n 1 n 1 n 0 n
281.5
solve initialize compute-defaults velocity-inlet flow-inlet
solve initialize initialize-flow
solve monitors residual convergence-criteria 1.0e-12 1.0e-6 1.0e-6
1.0e-6 1.0e-6
```

```
solve monitors residual monitor y n n n
solve monitors residual check-convergence y
solve monitors residual plot y
solve set equations temp n
solve iterate 2500
file write-case-data 2DSMC-M-M.cas
solve monitors residual convergence-criteria 1.0e-13 1.0e-6 1.0e-6
1.0e-6 1.0e-6
solve set equations temp y
solve iterate 10
solve monitors residual convergence-criteria 1.0e-12 1.0e-6 1.0e-6
1.0e-6 1.0e-6
solve iterate 2500
file write-case-data 2DSMC-M-1st-1.cas
solve set under-relaxation mom 0.6
solve iterate 2500
file write-case-data 2DSMC-M-1st-2.cas
solve monitors residual convergence-criteria 1.0e-13 1.0e-6 1.0e-6
1.0e-6 1.0e-6
solve set discretization-scheme mom 1
solve set discretization-scheme temp 1
solve iterate 10
solve monitors residual convergence-criteria 1.0e-12 1.0e-6 1.0e-6
1.0e-6 1.0e-6
solve iterate 2500
file write-case-data 2DSMC-M-2nd-1.cas
solve set under-relaxation mom 0.5
solve iterate 2500
file write-case-data 2DSMC-M-2nd-2.cas
solve set under-relaxation mom 0.4
solve iterate 2500
file write-case-data 2DSMC-M-2nd-3.cas
```

APPENDIX G

Excel Spreadsheet Example

	A	B	C	D	E	F	G	H	I	J	M	N	O	P	Q	R
1	Round Microchannel Heat Exchanger 3D Refrigerant Side Heat Transfer Performance Analysis															
2	z	ξ	T_jacket	Θ-Tj	T_wall	Θ-Tw	q"	q"*(ξ)	Nu(z)	Nu*(ξ)	RESULTS					∫Nu*(ξ)dξ
3	0.015	1	314.954	0.828	276.947	0.000	-11478.8	1.000	9.446	0.176						0
4	0.045	0.974	315.520	0.840	279.233	0.050	-11363.7	0.990	9.794	0.182						0.247
5	0.075	0.949	315.912	0.849	281.168	0.092	-10986.9	0.957	9.890	0.184						0.499
6	0.105	0.923	316.296	0.857	283.056	0.133	-10639.1	0.927	10.010	0.186						0.754
7	0.135	0.897	316.662	0.865	284.883	0.173	-10291.3	0.897	10.128	0.189						1.012
8	0.165	0.872	317.012	0.872	286.657	0.211	-9940.6	0.866	10.242	0.191						1.274
9	0.195	0.846	317.348	0.880	288.367	0.249	-9598.3	0.836	10.358	0.193						1.538
10	0.225	0.821	317.668	0.887	290.020	0.285	-9256.2	0.806	10.471	0.195						1.805
11	0.255	0.795	317.974	0.893	291.612	0.319	-8922.4	0.777	10.585	0.197						2.075
12	0.285	0.769	318.265	0.900	293.147	0.353	-8590.8	0.748	10.697	0.199						2.347
13	0.315	0.744	318.543	0.906	294.623	0.385	-8267.7	0.720	10.810	0.201						2.623
14	0.345	0.718	318.807	0.912	296.045	0.416	-7948.4	0.692	10.921	0.203						2.902
15	0.375	0.692	319.059	0.917	297.410	0.446	-7637.9	0.665	11.034	0.205						3.183
16	0.405	0.667	319.298	0.922	298.722	0.474	-7332.3	0.639	11.145	0.208						3.468
17	0.435	0.641	319.526	0.927	299.980	0.502	-7035.8	0.613	11.258	0.210						3.755
18	0.465	0.615	319.742	0.932	301.187	0.528	-6745.1	0.588	11.370	0.212						4.045
19	0.495	0.590	319.948	0.936	302.344	0.553	-6464.0	0.563	11.484	0.214						4.338
20	0.525	0.564	320.143	0.941	303.452	0.577	-6189.1	0.539	11.597	0.216						4.634
21	0.555	0.538	320.329	0.945	304.513	0.600	-5924.0	0.516	11.715	0.218						4.933
22	0.585	0.513	320.505	0.949	305.528	0.622	-5665.7	0.494	11.831	0.220						5.235
23	0.615	0.487	320.672	0.952	306.498	0.644	-5417.5	0.472	11.954	0.223						5.540
24	0.645	0.462	320.831	0.956	307.425	0.664	-5176.4	0.451	12.077	0.225						5.848
25	0.675	0.436	320.982	0.959	308.311	0.683	-4945.7	0.431	12.208	0.227						6.159
26	0.705	0.410	321.125	0.962	309.157	0.701	-4722.2	0.411	12.341	0.230						6.474
27	0.735	0.385	321.261	0.965	309.965	0.719	-4509.5	0.393	12.486	0.233						6.792
28	0.765	0.359	321.391	0.968	310.737	0.736	-4304.2	0.375	12.635	0.235						7.114
29	0.795	0.333	321.514	0.971	311.473	0.752	-4110.1	0.358	12.802	0.238						7.440
30	0.825	0.308	321.632	0.973	312.177	0.767	-3923.5	0.342	12.978	0.242						7.771
31	0.855	0.282	321.744	0.976	312.849	0.782	-3748.5	0.327	13.180	0.245						8.106
32	0.885	0.256	321.851	0.978	313.491	0.796	-3581.5	0.312	13.399	0.250						8.447
33	0.915	0.231	321.954	0.980	314.106	0.809	-3427.1	0.299	13.657	0.254						8.794
34	0.945	0.205	322.053	0.982	314.695	0.822	-3281.7	0.286	13.949	0.260						9.148
35	0.975	0.179	322.148	0.984	315.261	0.834	-3151.2	0.275	14.309	0.266						9.510
36	1.005	0.154	322.241	0.986	315.805	0.846	-3032.4	0.264	14.738	0.274						9.882
37	1.035	0.128	322.331	0.988	316.333	0.858	-2934.4	0.256	15.300	0.285						10.267
38	1.065	0.103	322.420	0.990	316.847	0.869	-2854.6	0.249	16.019	0.298						10.669
39	1.095	0.077	322.510	0.992	317.353	0.880	-2817.3	0.245	17.086	0.318						11.093
40	1.125	0.051	322.602	0.994	317.870	0.891	-2812.1	0.245	18.588	0.346						11.551
41	1.155	0.026	322.705	0.996	318.387	0.902	-3172.7	0.276	22.985	0.428						12.084
42	1.185	0.000	322.868	1.000	319.856	0.934	-5171.6	0.451	53.701	1.000						13.067

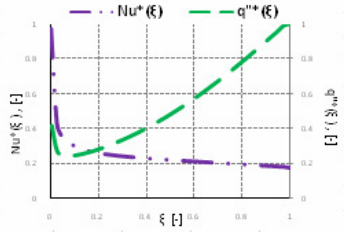

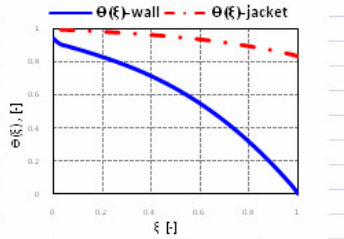

FLUENT | DIRKER-MAYER | Sheet3

VITA

Ozkan Emre Ozdemir

Candidate for the Degree of

Master of Science

Thesis: THERMAL PERFORMANCE COMPARISON BETWEEN MICROCHANNEL AND ROUND TUBE HEAT EXCHANGERS

Major Field: Mechanical Engineering

Biographical:

Personal Data:

Born in Ankara, Turkey on March 07, 1983

Education:

Recived the B.S. degree from Middle East Technical University, Ankara , Turkey, 2006, in Aerospace Engineering

Completed the requirements for the degree of Master of Science with a major in Mechanical Engineering at Oklahoma State University in July 2009.

Experience:

During graduate school, worked as a research assistant in Building and Environmental Thermal System Research Group and performined computational simulations of different type of heat exchangers in FLUENT CFD solver including microchannel heat exchangers.

Worked as a teaching assistant for the the courses of Thermodynmamics, Heat Tranfer and Gas Power Systems and led weekly discussion sections, held office hours, assisted students individually, graded weekly assignments, proctored exams and quizzes.

Professional Memberships:

ASHRAE student member

Name: Ozkan Emre Ozdemir Date of Degree: July, 2009

Institution: Oklahoma State University Location: Stillwater, Oklahoma

Title of Study: THERMAL PERFORMANCE COMPARISON BETWEEN MICROCHANNEL AND ROUND TUBE HEAT EXCHANGERS

Pages in Study: 225 Candidate for the Degree of Master of Science

Major Field: Mechanical Engineering

Alternative round tube profiles to straight microchannel (SMC) tube geometry was explored by gradually applying the microchannel features to fin and tube type heat exchangers. First, previous experimental and computational works related to design and heat transfer analysis of microchannel heat exchanger tubes and testing was reviewed and then a numerical CFD model in FLUENT solver was developed, which was experimentally validated within an error range of 0.1 to 7.8 % based on available data in literature. Single phase, water to water, laminar, counter fluid flow of tube in shell calorimeter heat transfer experiments were numerically simulated to analyze the refrigerant side heat transfer enhancement if round microchannel tubes are used as outdoor coil. According to numerical results, the refrigerant side heat transfer capacity of round tubes of 10.3mm outer diameter with 42 microports of about 0.6 mm port diameter distributed around the tube perimeter (round tube microchannel) was estimated to be about 24% higher than conventional round tube (with no microchannel ports in them) and about 15% lower than conventional straight microchannel tube heat exchangers used in outdoor evaporators. In addition to refrigerant side, parametric studies were performed to investigate the heat transfer effectiveness of 10.3 mm and 5.15 mm outer diameter round (microchannel) tubes (multi port and annular) under cross flow configuration with dry air streams and results were compared with straight microchannel tubes in terms of tube diameter tube spacing effect. It was obtained that the round tube design of 5.15 mm outer diameter having an annular port of 1.6mm hydraulic diameter within 11mm edge to edge tube spacing of vertically parallel fin and tube coil configuration can provide similar air side heat transfer capacity of straight microchannel coil based on its secondary heat transfer area. Additionally, this configuration can provide 50 % better pressure drop performance compared to conventional straight microchannel tube coil.

ADVISER'S APPROVAL: Type Adviser's Name Here